

# **Processing and Structure of High Strength Steels**

**Erfan Abbasi**



**Department of Materials Science and Engineering**

**The University of Sheffield**

**A thesis submitted for the degree of Doctor of Philosophy**

**April 2015**





The  
University  
Of  
Sheffield.

Access  
To  
Thesis.

**This thesis is protected by the Copyright, Designs and Patents Act 1988. No reproduction is permitted without consent of the author. It is also protected by the Creative Commons Licence allowing Attributions-Non-commercial-No derivatives.**

- A bound copy of every thesis which is accepted as worthy for a higher degree, must be deposited in the University of Sheffield Library, where it will be made available for borrowing or consultation in accordance with University Regulations.
- All students registering from 2008–09 onwards are also required to submit an electronic copy of their final, approved thesis. Students who registered prior to 2008–09 may also submit electronically, but this is not required.

Author: Erfan Abbasi Dept: Materials Science and Engineering

Thesis Title: Processing and Structure of High Strength Steels Registration No: 100256215

**For completion by all students:**

Submit in print form only (for deposit in the University Library):

Submit in print form and also upload to the *White Rose eTheses Online* server: In full ☒  
Edited eThesis ☐

**Please indicate if there are any embargo restrictions on this thesis. Please note that if no boxes are ticked, you will have consented to your thesis being made available without any restrictions.**

Embargo details: (complete only if requesting an embargo to either your print and/or eThesis) Embargo required? Length of embargo (in years)

Print Thesis	Yes <input type="checkbox"/>	No <input checked="" type="checkbox"/>	_____
eThesis	Yes <input type="checkbox"/>	No <input checked="" type="checkbox"/>	_____

**Supervisor:** I, the supervisor, agree to the named thesis being made available under the conditions specified above.

Name: Prof. W M Rainforth Dept: Materials Science and Engineering

Signed: [Signature] Date: 21/3/15

**Student:** I, the author, agree to the named thesis being made available under the conditions specified above.

I give permission to the University of Sheffield to reproduce the print thesis in whole or in part in order to supply single copies for the purpose of research or private study for a non-commercial purpose.

I confirm that this thesis is my own work, and where materials owned by a third party have been used copyright clearance has been obtained. I am aware of the University's *Guidance on the Use of Unfair Means* ([www.sheffield.ac.uk/lets/design/unfair](http://www.sheffield.ac.uk/lets/design/unfair))

I confirm that all copies of the thesis submitted to the University (including electronic copies on CD/DVD) are identical in content.

Name: Erfan Abbasi Dept: Materials Science and Engineering

Signed: [Signature] Date: 01/04/2015

**For completion by students also submitting an electronic thesis (eThesis):**

I, the author, agree that the University of Sheffield's eThesis repository (currently WREO) will make my eThesis available over the internet via an entirely non-exclusive agreement and that, without changing content, WREO may convert my thesis to any medium or format for the purpose of future preservation and accessibility.

I, the author, agree that the metadata relating to the eThesis will normally appear on both the University's eThesis server and the British Library's EThOS service, even if the thesis is subject to an embargo. I agree that a copy of the eThesis may be supplied to the British Library.

I confirm that the upload is identical to the final, examined and awarded version of the thesis as submitted in print to the University for deposit in the Library (unless edited as indicated above).

Name: Erfan Abbasi Dept: Materials Science and Engineering

Signed: [Signature] Date: 01/04/2015

**THIS SHEET MUST BE BOUND IN THE FRONT OF THE PRINTED THESIS BEFORE IT IS SUBMITTED**

# Abstract

There is currently an extensive effort to develop new steels with a better combination of strength and ductility, the so-called Ultra-High Strength Steels (UHSS) and Advanced High Strength Steels (AHSS). The new steels must be able to be manufactured using existing plant and at the same time meet ever decreasing cost demands. This study looks at developing AHSS, with a focus primarily on the microalloying precipitation behaviour and microstructural evolution during thermomechanical processing of transformation induced plasticity (TRIP) assisted steels. This approach combines two mechanisms that are known to enhance properties, namely the TRIP effect and precipitation hardening arising from strain induced precipitation. In respect of the TRIP effect, a detailed investigation was undertaken to look at the effect of the intercritical anneal on strength and ductility. For the strain induced precipitation, the effect of combined microalloy additions was investigated.

Initially, the effect of intercritical annealing was studied using a trial as-cold rolled multiphase V microalloyed TRIP assisted steel with a polygonal ferrite matrix (1.5Mn C+Si+Al+N $\approx$ 1.0 (C 0.2) and V<0.2 wt%) focusing on the isothermal bainite transformation at 460°C. The V(C,N) precipitates were extensively observed in all phases (ferrite, retained austenite, martensite and bainitic ferrite) after isothermal bainite transformation in a random manner. The tensile testing suggested considerable improvements in yield, ultimate tensile strengths and elongation after 180s isothermal bainite holding time. According to SEM/TEM observations, these effects were attributed to the evolution of retained austenite from block to film morphology, and possible interaction between microalloying precipitates and newly formed dislocations as a result of bainite transformation. The average density of V(C,N) slightly increased after intercritical annealing, though it did not show a significant variation during the isothermal bainite transformation. Nevertheless, the size distribution of V(C,N) precipitates did not change significantly.

The effect of a combined addition of Nb, Mo and V was investigated in TRIP multiphase steel (0.12C 1.50Mn 1.50Si and NbVTiMo $\leq$ 0.20 wt%), which was compared to a V single addition steel with otherwise matched composition. A comparative study was undertaken using intercritical annealing after ~20% cold-rolled deformation of the rough rolled specimens. The resulting microstructure in both alloys comprised acicular/bainitic ferrite with an uneven proportion of allotriomorphic ferrite and retained

austenite and martensite. An average density of precipitates increased in both alloys after intercritical annealing, with an average of 137 and 219 precipitate/ $\mu\text{m}^2$  in NbVMo and V steels, respectively. NbV(C,N), NbVMo(C,N) and V(C,N) were observed in the NbVMo steel. In both alloys, precipitates with different morphologies were observed, located in the matrix, on dislocations and at grain boundaries. The results suggested that the NbMo addition retarded the growth/coarsening of precipitates with a size of lower than 15nm. Also, much greater precipitation strengthening was observed in the NbVMo steel after intercritical annealing compared to the V steel.

The last part of the project was to systematically study the effect of Nb and Mo on the V steel as a function of thermomechanical processing. Laboratory simulations were developed by plane strain compression testing which accurately replicate the whole thermomechanical process route from the hot rolling through intercritical annealing, followed by the bainite transformation. After hot and controlled rolling at intercritical annealing range the resulting microstructure was acicular/bainitic ferrite, retained austenite and martensite surrounded by allotriomorphic ferrite in both alloys. The TEM observations suggested that a noticeable number of precipitates were formed in the NbVMo steel up to the finishing stage (i.e. average of 112 precipitate/ $\mu\text{m}^2$  in NbVMo containing steels). It was also found that the V(C,N) precipitation occurred in austenite and ferrite below the finishing stage (i.e.  $\leq 830^\circ\text{C}$ ) with an average cooling rate of  $\sim 12^\circ\text{C/s}$ . The overall findings suggest that the high dislocation density in the  $\sim 20\%$  cold rolled acicular/bainitic ferrite could lead to an intense precipitation and coarsening of V(C,N) during the intercritical annealing.

# Contents

<b>Abstract.....</b>	<b>I</b>
<b>Contents .....</b>	<b>III</b>
<b>List of Figures.....</b>	<b>VII</b>
<b>List of Tables.....</b>	<b>XXI</b>
<b>Nomenclature.....</b>	<b>XXIII</b>
<b>Acknowledgements .....</b>	<b>XXVI</b>
<b>Chapter 1. Introduction .....</b>	<b>1</b>
1.1 Advanced High Strength Steels Assisted by TRIP Effect .....	1
1.2 Outline and Objectives of the Thesis.....	3
<b>Chapter 2. Literature Review .....</b>	<b>4</b>
2.1. Background of Advanced High Strength Steels (AHSS).....	4
2.1.1. AHSS Steels Assisted by TRIP Effect .....	6
2.2. Effect of Chemical Composition .....	12
2.2.1. Carbon and Nitrogen .....	13
2.2.2. Microalloying Elements .....	15
2.2.3. Other Alloying Elements .....	20
2.2.3.1. Silicon, Aluminium, Phosphorus and Sulphur.....	20
2.2.3.2. Manganese and Molybdenum.....	21
2.3. Evolution of Microstructure during Thermomechanical Processing .....	24
2.3.1. Reheating Stage.....	26
2.3.2. Roughing .....	28
2.3.3. Finishing.....	32

2.3.4.	Run-out Table and Coiling Stage .....	33
2.3.4.1.	Bainite Transformation .....	36
2.3.5.	Cold Rolling and Intercritical Annealing .....	40
2.3.5.1.	Stage 1- Fast Heating Up to $A_{c1}$ Range .....	41
2.3.5.2.	Stages 2 and 3- Slow Heating ( $T > A_{c1}$ ) and Isothermal Annealing....	42
2.3.5.3.	Stage 4- Rapid Cooling and Isothermal Holding Stage.....	43
2.3.5.4.	Stage 5- Isothermal Bainite Transformation.....	43
2.3.5.5.	Stage 6- Final Quenching .....	43
<b>Chapter 3.</b>	<b>Experimental Procedure .....</b>	<b>44</b>
3.1.	Material .....	45
3.2.	Sample Preparation .....	46
3.2.1.	Alloy 1: Isothermal Bainite Transformation after Intercritical Annealing....	48
3.2.2.	Alloys 2 and 3; Roughing, Cold Rolling and Intercritical Annealing.....	51
3.2.3.	Alloys 2 and 3; Controlled Rolling .....	53
3.2.3.1.	Plane Strain Compression (PSC) Testing.....	54
3.2.3.2.	The Analysis and Correction of the PSC Data .....	59
3.3.	Characterization Techniques .....	60
3.3.1.	X-Ray Diffraction Analysis (XRD) .....	60
3.3.2.	Optical Microscopy and Quantitative Metallography.....	62
3.3.3.	Scanning Electron Microscopy (SEM) .....	63
3.3.4.	Transmission Electron Microscopy (TEM) .....	63
3.3.4.1.	Carbon Extraction Replica .....	64
3.3.4.2.	Thin Foil Sample .....	65
3.3.4.3.	Electron Energy Loss Spectroscopy (EELS) .....	65
3.3.5.	Vickers Hardness and Microhardness Testing .....	65
3.3.6.	Tensile Testing .....	66
<b>Chapter 4.</b>	<b>Results and Discussion: Alloy 1; Intercritical Annealing.....</b>	<b>68</b>
4.1.	Introduction.....	68
4.2.	Results .....	69
4.2.1.	Microstructural Characterizations .....	69
4.2.2.	Precipitation Behaviour.....	78
4.2.3.	Retained Austenite Content.....	86

4.2.4.	Hardness Testing.....	89
4.2.5.	Tensile Testing.....	90
4.2.	Discussion .....	92
4.2.1.	Characterization of Microstructure .....	92
4.2.2.	Microalloying Precipitation .....	95
4.2.3.	Mechanical Testing .....	96
<b>Chapter 5. Results and Discussion: Alloys 2 and 3; Intercritical Annealing.....</b>		<b>100</b>
5.1.	Introduction .....	100
5.2.	Results .....	101
5.2.1.	Microstructural Characterizations.....	101
5.2.1.1.	Rough Rolled Structure .....	101
5.2.1.2.	Cold Rolled and Intercritical Annealed Structure.....	108
5.2.2.	Grain Size Measurements and Retained Austenite Content .....	116
5.2.3.	Precipitation Behaviour.....	118
5.2.3.1.	TEM Thin Foil Analysis .....	118
5.2.3.2.	TEM Carbon Extraction Replica Analysis .....	126
5.2.4.	Hardness Testing.....	137
5.3.	Discussion .....	138
5.3.1.	Evolution of Microstructure during Rough Rolling (Rolling Mill) .....	138
5.3.2.	Evolution of Microstructure during Cold Rolling.....	139
5.3.3.	Evolution of Microstructure during Intercritical Annealing Range .....	140
5.3.4.	TEM Thin Foil Analysis of Precipitate.....	142
5.3.5.	TEM Carbon Extraction Replica Analysis of Precipitates.....	144
5.3.6.	Hardness Testing.....	146
<b>Chapter 6. Results and Discussion: Alloys 2 and 3; Controlled Rolling.....</b>		<b>148</b>
6.1.	Introduction .....	148
6.2.	Results .....	149
6.2.1.	PSC Stress-Strain Curves.....	149
6.2.2.	Microstructural Characterizations.....	150
6.2.3.	Retained Austenite Content.....	160
6.2.4.	TEM Thin Foil Analysis .....	163
6.2.5.	TEM Carbon Extraction Replica Analysis.....	173

6.2.6.	Hardness Testing.....	190
6.3.	Discussion .....	191
6.3.1.	Microstructural Characterizations.....	191
6.3.2.	Retained Austenite .....	193
6.3.3.	TEM Thin Foil Analysis of Precipitate.....	194
6.3.4.	TEM Carbon Extraction Replica Analysis of Precipitates.....	195
6.3.5.	PSC Stress-Strain Curves.....	197
6.3.6.	Hardness Testing.....	199
<b>Chapter 7. Conclusions.....</b>		<b>201</b>
<b>Chapter 8. Future Work .....</b>		<b>205</b>
<b>References.....</b>		<b>207</b>
<b>Appendix A. Analysis and Corrections of PSC Data .....</b>		<b>221</b>

# List of Figures

Fig. 2.1, An overview of typical car body components which are made from different groups of AHSS steels with respect to their effect on the final weight reduction [7].....	4
Fig. 2.2, A comparison of tensile strength against elongation for different groups of HSS and AHSS steels. IF, Interstitial free steel; BH, Bake hardening steel; C-Mn, carbon manganese containing steel; HSLA, High strength low alloy steel; DP, Dual phase steel; CP, Complex phase steel; TRIP, Transformation induced plasticity steel; Mart, Martensitic steel, (A80 (%): maximum of uniform elongation) [8]. ....	5
Fig. 2.3, True stress strain curves for different groups of AHSS steels. Curves are plotted approximately up to the necking point [6]. ....	6
Fig. 2.4, Effect of cooling rate on the evolution of microstructure in steels [14]. ....	7
Fig. 2.5, Schematic illustration of carbon concentration distribution in retained austenite ( $C_{\gamma 0}$ ) in TRIP assisted steels, $\gamma_R$ ; retained austenite, $\alpha_{am}$ ; annealed martensitic ferrite, $\alpha_{bf}$ ; bainitic ferrite [3]. ....	8
Fig. 2.6, Schematic of microstructure effect on the propagation of crack in TRIP assisted AHSS steels, (a) Polygonal ferrite matrix, (b) Bainitic matrix with the presence of quasi cleavage crack at plastic zone i.e. a localized, often isolated feature on a fracture surface that exhibits characteristics of both cleavage and plastic deformation [3, 18]. ....	9
Fig. 2.7, The interaction between dislocation slipping and precipitates, (a) The balance of resistance forces against the dislocation movement, (b) Releasing the dislocation during meeting hard nonshearable precipitates by looping or cross slip, (c) Shearing the precipitates by the dislocation motion [21]. ....	10
Fig. 2.8, Particle radius versus number density of NbC precipitates as function of number density required to pin subgrain structure. Three different techniques, including modelling, TEM and atom probe field ion microscopy (APFIM) were applied. The full line representing dislocation density of $\rho=8 \times 10^{14} \text{ m}^{-2}$ according to their observations and the dotted line from the estimated work by Burk et al. ( $\rho=4 \times 10^{15} \text{ m}^{-2}$ ). ●, modelling; ■, TEM; ▲, APFIM [22]. ....	11
Fig. 2.9, Comparison between two conventional production processes of AHSS steels assisted by TRIP effect, (a) Hot rolling-cold rolling and intercritical annealing, (b) Controlled rolling. $\alpha$ ; Ferrite, $\gamma$ ; Austenite, $\alpha_b$ ; Bainite, $\alpha'$ ; Martensite [25]. ....	12



Fig. 2.10, The carbon content of steel types used in car body applications. DP; Dual phase, DC; Cold rolled low carbon steel, BH; Bake hardening steel, TRIP; Polygonal ferrite transformation induced plasticity assisted steel, FB; Ferrite-bainite steel; IF; Interstitial free steel, HSLA; High strength low alloy steel [30].	13
Fig. 2.11, Effect of individual elements on the $M_s$ temperature of Fe-base binary alloys [37].	14
Fig. 2.12, Comparison among equilibrium solubility of microalloyed (C,N) precipitates in austenite and ferrite [39].	15
Fig. 2.13, Effect of Nb precipitation at different ranges of temperature on the evolution of microstructure, showing the positive impact of Nb precipitates on controlling the austenite recrystallization/growth and consequently ferrite refinement, and precipitation strengthening [14].	19
Fig. 2.14, Binary Fe-Mn equilibrium phase diagram, showing the presence of different meta-stable allotropies of Fe-Mn at different temperatures [68].	22
Fig. 2.15, Hardness versus isothermal holding time at austenite to ferrite transformation range of temperature [75].	23
Fig. 2.16, Effect of controlled rolling on the microstructure in terms of temperature [42].	24
Fig. 2.17, Schematic of thermomechanical processing of AHSS steels assisted by TRIP effect and the influence of alloying elements on transformation behaviour during cooling [6, 76].	25
Fig. 2.18, A comparison of roughing and finishing temperature ranges based on critical austenite temperatures for the different types of thermomechanical treatment. A, conventional hot rolling; B, conventional controlled rolling; C, intensified (intercritical) controlled rolling; D, recrystallization controlled rolling. T, temperature; $T_{AC3}$ , stands for the temperature ferrite fully transformed into austenite during heating; $T_{Ar3}$ , the temperature at which austenite starts transforming to ferrite during cooling; $T_{Ar1}$ , the temperature at which the transformation of austenite to ferrite and probable cementite is completed; $T_{GC}$ , grain coarsening temperature; $T_{rs}$ , recrystallization stop temperature. $T_{GC}$ stands for the temperature above which grain coarsening starts by secondary recrystallization and the precipitates do not suppress grain growth [42].	26
Fig. 2.19, (a) TEM micrograph of carbon extraction replica corresponding a complex precipitate in a typical V-Nb-Ti steel, (b) and (c) EDS spectrum of shell and core of duplex precipitate, respectively [5].	28

Fig. 2.20, The variation of austenite grain size during a simplified controlled rolling schedule of C-Mn and 0.04 % Nb steels [62].	30
Fig. 2.21, The precipitation-time-temperature diagram of a Nb-Ti-V microalloyed steel, $P_s$ and $P_f$ stand for the 5% start and 95% finish times as function of strain ( $\epsilon$ ) in austenite [86].	31
Fig. 2.22, The variation of final ferrite grain size in terms of finishing temperature for a typical microalloyed steel [67].	33
Fig. 2.23, Ferrite grain size versus prior austenite grain size illustrating the importance of austenite grain size in prediction of ferrite grain size during cooling stage [62].	34
Fig. 2.24, The micrograph of austenite grain interior features after final cooling to room temperature of low carbon Nb microalloyed steel, (a) Optical micrograph, (b) SEM micrograph, (c) and (d) TEM micrographs, MA/M, martensite; $\Theta$ , cementite; BF/B, bainitic ferrite; $\alpha$ , ferrite; P, pearlite; PF, polygonal ferrite [95].	35
Fig. 2.25, Illustration of retained austenite volume fraction as a function of prior austenite grain size and volume fraction of allotriomorphic ferrite, (a) 70 $\mu\text{m}$ and (b) 230 $\mu\text{m}$ [96].	36
Fig. 2.26, Schematic representation of temperature versus time of bainite formed in the Cu-Ni-Cr-Mo-V steel during continuous cooling. Three paths illustrate the schematic cooling conditions for the formation of bainite with different morphologies, (I); granular bainite, (II); upper bainite, (III); lower bainite [100, 101].	37
Fig. 2.27, Evolution of the volume fraction of retained austenite as function of isothermal bainite holding time at 375°C for three types of steels [60].	38
Fig. 2.28, Schematic representation of retained austenite morphology in bainitic microstructure [107].	39
Fig. 2.29, Schematic of the intercritical annealing treatment for cold rolled AHSS steels assisted by TRIP effect. Six stages represent the effect of heating/cooling rate on the evolution of microstructure [2].	40
Fig. 2.30, Schematic illustration of mechanisms of austenite formation from cold rolled initial microstructure in terms of heating rate i.e. 10 and 50 K/s [112].	41
Fig. 3.1, (a) Thermomechanical compression test machine (Servotest, UK), (b) Induction furnace equipped by fast air cooling system which is called FTTU [117].	47

Fig. 3.2, Illustration of intercritical annealing schedule suggested by Tata Steel for the vanadium microalloyed multiphase steel with different holding times at isothermal bainite transformation temperature, $\gamma$ ; austenite, $\alpha$ ; : ferrite, $\alpha_b$ ; bainite.....	49
Fig. 3.3, Holder used in order to simulate the intercritical annealing followed by isothermal bainite transformation in Alloy 1 (dimensions are in mm with general tolerance: $\pm 0.5\text{mm}$ ). .....	50
Fig. 3.4, (a) Slab used for hot rolling, (b) Hot rolled plate. ....	51
Fig. 3.5, Thermomechanical processing profile in studying Alloys 2 and 3, including roughing stage, cold rolling and intercritical annealing, followed by isothermal bainite transformation. ....	52
Fig. 3.6, The Hille rolling mill and muffle furnace.....	53
Fig. 3.7, Illustration of plane strain compression test. ....	55
Fig. 3.8, Illustration of thermomechanical schedules which were simulated by PSC machine, (a) Hot rolling, (b) Controlled rolling, (c) Water quenched after finishing, ( $\dot{\epsilon}=10\text{s}^{-1}$ ). ....	56
Fig. 3.9, Typical PSC standard specimen, (a) and (b) Pre and post deformation, respectively, (c) Sketch of PSC standard specimen with relevant dimensions (mm)....	58
Fig. 3.10, Schematic illustration of critical dimensional points for measurement in PSC specimen, (a) Before deformation, (b) After plane strain compression test [118].....	59
Fig 3.11, Illustration of sectioned area from the deformed PSC sample for characterization. ....	60
Fig. 3.12, Carbon extraction replication, (a) particles embedded in the microstructure, (b) revealing the particles in the microstructure by etching, (c) coating the surface by a thin amorphous carbon film, (d) extracting the particles adhering to the carbon film [127].	64
Fig. 3.13, Dog bone shape standard sample for the tensile testing, (a) The selected direction for the sample preparation, (b) Sub size sample dimensions according ASTM E8/E8M and illustration of sample holder used to heat treat the sample by FTTU.....	67
Fig. 4.1, The micrographs of starting microstructure, (a) and (b) Optical micrograph and SEM image, representing the secondary phase inside the ferritic matrix, (c) and (d) Optical and SEM micrographs of structure in rolling direction, (e) and (f) BF/DF, TEM micrographs, showing the pearlite. ....	70

Fig. 4.2, Selected micrographs after the intercritical annealing, (a) and (b) Optical and SEM micrographs corresponding to the normal direction plane, respectively, (c) and (d) Optical and SEM micrographs corresponding to the rolling direction plane, respectively, RA; retained austenite, M; martensite.....	71
Fig. 4.3, Variation of ferrite grain size versus isothermal bainite holding time, measured by intercept method from the SEM micrographs. ....	72
Fig. 4.4, SEM and TEM micrographs of the samples prepared by 5s IBT, (a) and (b) SEM images with two different magnifications, showing a substructure in the block of austenite, (c) and (d) TEM micrograph and corresponding electron diffraction pattern in zone axis [100] of retained austenite, showing different constituents, similar to that shown in (a) and (b), (e) Schematic of observed block shape feature in (c). ....	74
Fig. 4.5, Selected SEM and TEM micrographs of heat treated samples, (a) and (b) SEM micrographs of sample prepared by 30s and 180s holding time at IBT, respectively, (c) Bright field image of a given secondary phase from the sample prepared by 180s holding time.....	75
Fig. 4.6, (a) and (b) Thin-foil TEM micrographs of samples prepared by 40s holding at IBT, showing the bainitic ferrite growth into the blocks of austenite, (c) and (d) BF/DF micrographs, illustrating the film shape retained austenite.....	76
Fig. 4.7, Selected TEM micrographs and corresponding EDS spectrum of thin foil samples prepared by 180s holding, illustrating the presence of dislocations and microalloying precipitates at regions adjacent to the interfaces of retained austenite and bainitic ferrite. ....	77
Fig. 4.8, Selected carbon extraction replica micrograph, showing the V/Ti(C,N) precipitates, (a) Different morphologies of precipitates in the microstructure, A, complex; B, spherical; C, oval, (b) Typical distribution of precipitates in the microstructure.....	79
Fig. 4.9, (a) Selected carbon extraction replica micrographs, showing the distribution of precipitates in the microstructure, (b) A typical complex precipitate and corresponding EDS spectra for each cap, (c) Typical spherical precipitates and corresponding EDS spectra. ....	80
Fig. 4.10, Bright and dark field carbon extraction replica micrographs corresponding to the sample prepared by 30s holding time, (a) An AlN particle in the vicinity of microalloying precipitates, (b) Corresponding EELS spectrum, (c) Corresponding EDS spectrum. ....	81

Fig. 4.11, Bright field TEM images of carbon extraction replica and corresponding EELS spectra, showing the existence of nitrogen in precipitates, (a) With N, (b) Without N, (c) Without N.....	82
Fig. 4.12, Bright and dark field carbon extraction replica micrographs, showing two typical V precipitates with two different morphologies, (a) An oval shape and corresponding EDS spectrum, (b) A complex shape and corresponding EDS spectra for each cap.....	83
Fig. 4.13, Area density of precipitates versus isothermal bainite transformation holding time, measured from the TEM micrographs of the carbon extraction replica samples. .	84
Fig. 4.14, Precipitate size distribution of samples prepared with different holding times at IBT, measured from carbon extraction replica samples, (a) Before intercritical annealing (cold rolled structure), (b) 5s holding time, (c) 30s holding time, (d) 40s holding time, (e) 180s holding time.....	85
Fig. 4.15, A selected graphical representation of Rietveld analysis for X-ray diffraction pattern of the intercritical annealed sample, followed by the subsequent IBT. ....	86
Fig. 4.16, Evolution of the volume fraction of retained austenite in terms of IBT holding time in the studied steels measured by XRD method. ....	87
Fig. 4.17, (a) Carbon content of retained austenite after different IBT holding times, measured from the lattice parameter (b) The best fit line, showing the linear trend of variation for the longer holding time $\geq 40$ s in (a). ....	88
Fig. 4.18, Optical micrographs showing hardness and microhardness indentations, (a) A typical Vickers hardness indentation, (b) Microhardness indentations, M/RA/B; martensite/retained austenite/bainite.....	89
Fig. 4.19, Variation of hardness values as a function of IBT holding time. ....	89
Fig. 4.20, (a) Engineering tensile stress-strain curve of samples in terms of IBT holding time, (b) Trend of yield strength and UTS versus isothermal bainite holding time.....	91
Fig. 4.21, Ideal schematic representation of the polygonal ferrite TRIP assisted steels with the presence of retained austenite and bainitic ferrite at the junctions of grain boundaries. ....	98
Fig. 5.1, Optical micrographs of as-cast and rough rolled samples, (a) and (b) As cast of Alloys 2 and 3, respectively, (c) and (d) Normal and rolling direction planes of rough rolled Alloy 2, respectively, (e) and (f) Normal and rolling direction planes of rough rolled Alloy 3, respectively. ....	102

Fig. 5.2, Typical optical micrograph of the rough rolled Alloy 3, showing the presence of widmanstatten ferrite.....	103
Fig. 5.3, Scanning electron micrographs of as-cast and rough rolled samples, (a) and (b) As-cast of Alloys 2 and 3, respectively, (c) Rough rolled Alloy 2 and a magnified image, (d) Rough rolled Alloy 3 and a magnified image, respectively. ....	104
Fig. 5.4, Selected transmission electron micrographs of thin-foil samples of Alloys 2 and 3 before and after the rough rolling, showing different features as secondary phases in the microstructure, (a) As-cast Alloy 2, (b) Rough rolled Alloy 2 and corresponding electron diffraction pattern with bcc structure in zone axis [111], (c) Rough rolled Alloy 2, (d) Rough rolled Alloy 3.....	105
Fig. 5.5, Selected transmission electron micrographs of thin-foil sample of Alloys 3 after rough rolling, (a) Showing a bainitic ferritic feature, (b) Showing a feature similar to pearlite.....	106
Fig. 5.6, Bright field TEM image of thin foil from the rough rolled Alloy 3, showing the partial decomposition of a block shape retained austenite with features similar to martensite. ....	107
Fig. 5.7, (a) and (b) Optical micrographs of the normal direction plane of cold rolled Alloys 2 and 3, respectively (c) and (d) Optical micrographs of the rolling direction plane of cold rolled Alloys 2 and 3, respectively, (e) and (f) Scanning electron micrographs of cold rolled Alloys 2 and 3 in normal direction with two different magnifications, respectively. ....	109
Fig. 5.8, Micrographs corresponding the normal direction plane of the intercritical annealed samples, (a) and (b) Optical micrographs of Alloys 2 and 3, respectively, (c) Scanning electron micrographs of Alloy 2 with two different magnifications, (d) Scanning electron micrographs of Alloy 3 with two different magnifications.....	110
Fig. 5.9, Scanning electron micrographs, showing the microstructure of interrupted quench samples at the end of isothermal intercritical annealing, (a) Alloy 2 with two different magnifications, (b) Alloy 3 with two different magnifications.....	111
Fig. 5.10, (a) Scanning electron micrograph of the cold rolled Alloy 3 after the intercritical annealing, showing features similar to the precipitates, (b) EDS spectrum corresponding to these precipitates. ....	112

Fig. 5.11, (a) Scanning electron micrograph of the cold rolled Alloy 2 after the intercritical annealing, showing features similar to the precipitates, (b) EDS spectrum corresponding to these precipitates. ....	113
Fig. 5.12, Selected thin-foil transmission electron micrographs of cold rolled Alloy 3 after the intercritical annealing, (a) and (b) Bright and dark field images, showing the presence of precipitates adjacent to retained austenite, respectively, (c) Corresponding SAED pattern ([100] zone axis), (d) A typical EDS spectrum, showing the presence of Nb and V in the observed precipitates in (a). ....	114
Fig. 5.13, Two selected bright field images of thin-foil transmission electron micrographs of cold rolled Alloy 3 after intercritical annealing, (a) A typical twinning structure and corresponding SAED pattern, showing the presence of martensite, (b) Showing a bainitic feature and the presence of dislocations in the vicinity of interfaces. ....	115
Fig. 5.14, Variation of ferrite grain size versus different thermomechanical processing, measured by intercept method from the SEM micrographs, $\gamma$ ; austenite, $\alpha$ ; ferrite, CR; cold rolled, IA; intercritical annealed.....	116
Fig. 5.15, Selected graphical representation of X-ray diffraction pattern of Alloy 2, (a) Showing the peaks corresponding to the ferrite, retained austenite and cementite in the rough rolled sample, (b) A selected graphical representation of Rietveld analysis for X-ray diffraction pattern of the intercritical annealed sample. ....	117
Fig. 5.16, Thin-foil transmission electron micrographs of rough rolled Alloy 3 (a) and (b) Bright and dark field images, showing the presence of precipitates at grain boundary and interior of ferrite, (c) Showing the presence of precipitates along grain boundary and a typical corresponding EDS spectrum.....	120
Fig. 5.17, Typical thin-foil transmission electron micrographs of cold rolled sample after the intercritical annealing, (a) Showing the presence of fine precipitates in the ferrite in Alloy 3 and corresponding typical EDS spectrum, (b) Showing the presence of fine precipitates in the vicinity of grain boundary of the ferrite in Alloy 2 and corresponding typical EDS spectrum.....	122
Fig. 5.18, Selected thin-foil transmission electron micrographs of Alloy 3 after the intercritical annealing, (a) and (b) Bright and dark field images, showing the presence of V precipitates inside the martensite, respectively, (c) SAED pattern corresponding martensite region (zone axis [111]), (d) Corresponding typical EDS spectrum of precipitates shown by arrows. ....	123

Fig. 5.19, Typical thin-foil transmission electron micrographs of cold rolled Alloy 3 after the intercritical annealing, (a) Showing the presence of a small feature similar to retained austenite, (b) Showing the presence of high density of dislocation inside the feature, (c) Showing the presence of fine precipitates in the vicinity of the intersection of two martensite twins after slight tilting of the sample, (d) Corresponding EDS spectrum from the observed precipitates. ....	124
Fig. 5.20, Thin-foil transmission electron micrographs of rough rolled Alloy 2 after the intercritical annealing, showing the block shape retained austenite with annealing twin and corresponding electron diffraction ([111] zone axis). ....	125
Fig. 5.21, Selected carbon extraction replica micrograph of Alloy 2 after the intercritical annealing, showing different morphologies of the microalloying precipitates and a typical EDS spectrum, A; complex shape, B; round shape, C; square shape; D; small precipitates, E; cuboid. ....	127
Fig. 5.22, Selected carbon extraction replica micrograph of rough rolled Alloy 2 and a typical EDS spectrum from the fine precipitates and electron diffraction pattern from a selected spherical precipitate in zone axis [100] FCC. ....	128
Fig. 5.23, Selected carbon extraction replica micrograph of rough rolled Alloy 2, (a) Bright field image of a complex NbV precipitate, (b) and (c) Showing the dark field images of upper and lower caps and corresponding EDS spectra, respectively, (d) Electron diffraction pattern showing the relevant variants of each cap. ....	130
Fig. 5.24, Selected carbon extraction replica micrograph of rough rolled Alloy 2, (a) Showing a wide range of size and shape distribution of precipitates with different chemical compositions and morphologies, (b) A typical oval shape precipitate and corresponding EDS spectrum. ....	131
Fig. 5.25, Selected carbon extraction replica micrograph of rough rolled Alloy 2, (a) Bright field image, showing colony of precipitates which can be related to the effect of etching, (b) Dark field image illustrates very fine precipitates through the microstructure. ....	132
Fig. 5.26, Bright and dark field TEM images of Alloy 3 after the rough rolling and corresponding EDS spectrum, showing a triangle like precipitate. ....	132
Fig. 5.27, Bright and dark field TEM images and corresponding EDS spectra of the intercritical annealed samples, (a) Showing an oval shape precipitate in Alloy 2, (b) Showing a cuboidal shape precipitate in Alloy 2, (c) Showing an irregular shape precipitate in Alloy 3. ....	133



Fig. 5.28, Bright and dark field TEM images of Alloy 2 after the intercritical annealing, showing a distribution of precipitates along a boundary shape feature. ....	134
Fig. 5.29, Area density of precipitates versus thermomechanical processing, measured from the carbon extraction replica samples of Alloys 2 and 3.....	135
Fig. 5.30, Precipitate size distribution of rough rolled, intercritical annealed samples of Alloys 2 and 3, measured from carbon extraction, (a) Rough rolled Alloy 2, (b) Intercritical annealed Alloy 2, (c) Combined rough rolled and intercritical annealed Alloy 2, (d) Rough rolled Alloy 3, (e) Intercritical annealed Alloy 3, (f) Combined rough rolled and intercritical annealed Alloy 3. ....	136
Fig. 5.31, Vickers hardness versus the thermomechanical processing used for Alloys 2 and 3, CR; cold rolled, IA; intercritical annealed. ....	137
Fig. 5.32, Comparative histograms corresponding to the precipitate size distributions of Alloys 2 and 3 after the intercritical annealing. ....	146
Fig. 6.1, Flow curves corresponding to the hot rolling and controlled rolling simulations using Alloys 2 and 3.....	150
Fig. 6.2, Optical micrographs of hot rolled and controlled rolled samples, (a) and (b). Deformation area of the hot rolled and controlled rolled Alloy 2, respectively, (c) and (d). Deformation area of the hot rolled and controlled rolled Alloy 3, respectively, (e) and (f). Un-deformed area of the hot rolled and controlled rolled Alloys 2 and 3, respectively. ....	151
Fig. 6.3, Optical micrographs, illustrating the effect of deformation on the microstructural evolution in Alloy 2 after the hot rolling and controlled rolling, (a) Hot rolled, (b) Controlled rolled, (c) Schematic of the selected area for the observation. ....	152
Fig. 6.4, Optical micrographs, illustrating the effect of deformation on the microstructural evolution in Alloy 3 after the hot rolling and controlled rolling, (a) Hot rolled, (b) Controlled rolled, (c) Schematic of the selected area for the observation. ....	153
Fig. 6.5, Volume fraction of allotriomorphic ferrite versus the thermomechanical processing condition.....	154
Fig. 6.6, Optical micrographs of interrupted quench specimen of Alloy 3, showing the effect of deformation on the prior austenite grains and corresponding magnified images (average grain size of 38 $\mu$ m).....	155

Fig. 6.7, (a) Optical micrograph illustrating the effect of deformation on the prior austenite grains in Alloy 3 after the controlled rolling, (b) The highlighted grain boundaries of micrograph in (a) with average grain size of 121 $\mu$ m. ....	156-157
Fig. 6.8, Selected scanning electron microscopy micrographs from Alloys 2 and 3, (a) and (b) After the hot rolling of Alloys 2 and 3, respectively, (c) and (d) After the controlled rolling of Alloys 2 and 3, respectively, (e) and (f) Interrupted quench samples of Alloys 2 and 3, respectively.....	159
Fig. 6.9, Selected graphical representation of X-ray diffraction pattern of the hot rolled Alloy 2, (a) Showing the peaks corresponding to the ferrite, retained austenite and cementite, (b) A selected graphical representation of Rietveld analysis for X-ray diffraction pattern.....	160
Fig. 6.10, (a) Volume fraction of retained austenite in terms of thermomechanical processing for Alloys 2 and 3, measured by XRD method, (b) Carbon content of retained austenite, measured from the lattice parameter.....	162
Fig. 6.11, Selected transmission electron micrographs of a thin-foil sample of Alloy 3 after the hot rolling, (a) and (b) The presence of precipitates and dislocations in the ferrite after the hot rolling and controlled rolling, respectively, (c) and (d) Typical EDS spectra acquired from the precipitates inside the tangle of dislocations after the hot rolling and controlled rolling, respectively. ....	164
Fig. 6.12, Selected transmission electron micrographs of a thin-foil sample of Alloy 3 after the hot rolling, (a) Bainitic ferrite lath adjacent to retained austenite, (b) SAED pattern of the selected area, (c) and (d) Bright and dark field images of a given retained austenite lath, respectively. ....	165
Fig. 6.13, Selected transmission electron micrographs of a thin-foil sample of Alloy 3 after the hot rolling, showing the presence of microalloying precipitates in the vicinity of dislocations, (a) and (b) Bright and dark field images of lath ferrite and corresponding SAED pattern, (c) and (d) Tangle of dislocation in lath ferrite and typical EDS from the microalloying precipitates in these area, arrows indicating features similar to cementite. ....	166
Fig. 6.14, Selected transmission electron micrographs of a thin-foil sample of Alloy 3 after the controlled rolling, (a) and (b) Bright and dark field images of bainite adjacent to retained austenite, respectively, (arrows indicating particle similar to cementite), (c) Corresponding SAED pattern. ....	167

Fig. 6.15, Selected thin-foil transmission electron micrographs of Alloy 3 after the controlled rolling, (a) and (b) Bright and dark field images of ferrite with the presence of V precipitates at grain boundaries, respectively, (c) SAED pattern corresponding precipitates, (d) A typical EDS spectrum of precipitates located at grain boundary. ... 168

Fig. 6.16, Bright field TEM image of a thin foil from a sample of Alloy 3 after the controlled rolling, (a) Illustrating a very fine scale bainite, (b) Showing the presence of dislocations in bainitic ferrite adjacent to retained austenite, (c) A typical EDS spectrum of precipitates located in bainitic ferrite in (b). ..... 169

Fig. 6.17, Selected thin-foil transmission electron micrographs of Alloy 3 after the controlled rolling, (a) and (b) Bright and dark field images of a ferrite grain and the presence of V precipitates, respectively, (c) SAED pattern corresponding to the observed ferrite, (d) Corresponding EDS spectrum of the shown precipitates by arrows in (a).. 170

Fig. 6.18, Bright field TEM image of a thin foil sample of the interrupted quench Alloy 2, indicating the lath ferritic constituents with a high density of dislocations. .... 171

Fig. 6.19, (a) and (b) Bright and dark field TEM images of a thin foil and SAED pattern from a sample of interrupted quench Alloy 2, showing the presence of dislocations in lath ferrite structure, (c) and (d) Bright and dark field TEM images of a thin foil and SAED pattern from a sample of interrupted quench Alloy 2, showing the precipitates in regions close to grain boundaries of lath ferrite, (e) Corresponding EDS of precipitates located in the lath ferrite. .... 172

Fig. 6.20, (a) Bright field TEM image of a carbon extraction replica from a sample of Alloy 2 after the hot rolling, showing a typical needle like precipitate, (b) and (c) Corresponding EDS and EELS spectra, respectively, (d) Bright field TEM image of an carbon extraction replica from a sample of Alloy 2 after the hot rolling, showing a typical triangle precipitate, (e) and (f) Corresponding EDS and EELS spectra, respectively.. 174

Fig. 6.21, (a) Bright field TEM image of a carbon extraction replica from a sample of Alloy 3 after the hot rolling, showing a typical spherical precipitate, (b) and (c) Corresponding EDS and EELS spectra, respectively, (d) Bright field TEM image of a carbon extraction replica from a sample of Alloy 2 after the hot rolling, showing a typical rectangle precipitate, (e) and (f) Corresponding EDS and EELS spectra, respectively. .... 175

Fig. 6.22, (a) Bright field TEM image of a carbon extraction replica from a sample of Alloy 2 after the controlled rolling, showing a typical complex precipitate, (b) and (c) Corresponding EDS and EELS spectra, respectively, (d) Inverse Fourier images from the red dashed line rectangles in (a), (e) Reflections corresponding to the main precipitate i.e. red dash-rectangle in zone axis [110] FCC, (f) Corresponding graphical contrast between lattice fringes in (d), with a lattice parameter of  $\approx 4.82 \text{ \AA}$ . .... 176

Fig. 6.23, (a) and (b) Bright and dark field TEM micrographs of a carbon extraction replica from a sample of Alloy 2 after the hot rolling, showing typical distribution of fine precipitates, (c) Corresponding EDS in (a), (d) Bright field TEM micrograph of a carbon extraction replica from a sample of Alloy 2 after the hot rolling, showing a typical precipitate distribution, (e) Corresponding a typical EDS spectrum from a given precipitate in (d). .....	178
Fig. 6.24, (a) Bright field TEM micrograph of a carbon extraction replica from a sample of Alloy 2 after hot rolling, showing typical distribution of precipitates along a line, (b) Corresponding EDS, (c) TEM micrograph and EDS of hot rolled Alloy 3, showing a typical irregular precipitate, (d) TEM micrograph and EDS of hot rolled Alloy 3, showing a typical spherical precipitate. ....	179
Fig. 6.25, (a) Selected bright field TEM micrograph of a carbon extraction replica from a sample of Alloy 3 after the hot rolling, showing typical distribution of precipitates, (b) Corresponding EDS spectra, showing the high level of V precipitates throughout a grain boundary shape alignment, (c) Bright and dark field TEM micrographs of a carbon extraction replica from a sample of Alloy 3 after the hot rolling, showing typical distribution of fine precipitates. ....	180
Fig. 6.26, (a) and (b) Bright and dark field TEM images of a carbon extraction replica from a sample of Alloy 3 after the controlled rolling, showing a typical complex shape precipitate, (c) Corresponding EDS spectra from upper and lower caps, (d) Corresponding SAED pattern. ....	181
Fig. 6.27, Bright and dark field TEM images of a carbon extraction replica and a typical EDS spectrum from a sample of Alloy 2 after the controlled rolling, showing typical distributions of precipitates. ....	182
Fig. 6.28, Bright and dark field TEM images of a carbon extraction replica and a typical EDS spectrum from a sample of Alloy 3 after the controlled rolling, showing typical distributions of precipitates. ....	183
Fig. 6.29, (a) and (b) Bright and dark field TEM images of extraction replica with corresponding SAED pattern and EDS from the interrupted quench sample of Alloy 3, showing very few precipitates. ....	184
Fig. 6.30, (a) and (b) Bright and dark field TEM images of an extraction replica, corresponding EDS from the interrupted quench sample of Alloy 2. ....	185

Fig. 6.31, Precipitate size distribution of hot rolled, controlled rolled and interrupted quench samples of Alloys 2 and 3, measured from carbon extraction, (a) Hot rolled Alloy 2, (b) Controlled rolled Alloy 2, (c) Interrupted quench Alloy 2, (d) Combined hot rolled and controlled rolled Alloy 2, (e) Hot rolled Alloy 3, (f) Controlled rolled Alloy 3, (g) Interrupted quench Alloy 3, (h) Combined hot rolled and controlled rolled Alloy 3... 188

Fig. 6.32, Density of precipitates versus thermomechanical processing, measured from the carbon extraction replica samples of Alloys 2 and 3. .... 189

Fig. 6.33, Variation of hardness values as a function of thermomechanical processing condition..... 190

Fig. 6.34, Typical temperature versus time curves, indicating the variation of temperature in the specimens within the hot rolling and controlled rolling. .... 198

Fig. A.1, Schematic diagram of load-displacement illustrating origin correction [118].....222

# List of Tables

Table 2.1, Effect of microalloying and other conventional substitutional elements on development of microscopic features and macroscopic properties of AHSS and HSLA steels [6, 28, 40]. .....	16
Table 3.1, Chemical composition of steels used, wt.% .....	45
Table 3.2, Equilibrium temperatures (°C) of transformation.....	46
Table 3.3, The specifications of the TMC machine [117, 118]. .....	48
Table 3.4, Intercritical annealing schedule for Alloy 1; simulated by FTTU.....	49
Table 3.5, Schedule variables of the rough rolling process followed by cold rolling and standard intercritical annealing for Alloys 2 and 3. ....	52
Table 3.6, The characteristics of the rolling mill machine.....	53
Table 3.7, Hot rolling and controlled rolling schedules for Alloys 2 and 3; simulated by TMC machine.....	57
Table 3.8, Specifications of the XRD machine; D5000 Siemens. ....	61
Table 4.1, The retained austenite parameters examined by XRD.....	86
Table 4.2, The result of Vickers hardness measurements.....	90
Table 4.3, Tensile properties in terms of isothermal bainite holding time. ....	91
Table 5.1, The grain size of ferrite and prior austenite measured by intercept method.....	116
Table 5.2, The retained austenite characteristics and Fe <sub>3</sub> C, examined by XRD.....	118
Table 5.3, The result of Vickers hardness measurements.....	137
Table 6.1, Volume fraction of allotriomorphic ferrite. ....	154

Table 6.2, The retained austenite parameters and cementite examined by XRD. ....	161
Table 6.3, The existence of nitrogen in precipitates as a function of their morphologies and thermomechanical processing. ....	186
Table 6.4, Average density of precipitates as a function of thermomechanical processing condition, measured from the carbon extraction replica samples of Alloys 2 and 3. ...	189
Table A.1, Nomenclature [118]. ....	221

# Nomenclature

$A_{c1}$	Austenite start temperature during heating
$A_{c3}$	Temperature at which ferrite completely transforms into austenite during heating
AHSS	Advanced high strength steel
APFIM	Atom probe field ion microscopy
APT	Atom probe tomography
$A_{r1}$	Temperature at which austenite completely transforms into ferrite or ferrite/cementite during cooling
ASTM	American Society for Testing and Materials
B	Bainite
BF	Bright field image
BH	Bake hardening
$B_s$	Bainite start temperature
CP	Complex phase steel
CTRL rolled	Controlled rolled
DC	Cold rolled low carbon steel
DF	Dark field image
DP	Dual phase steel
ED	Elongation direction
EDS	Electron dispersive X-Ray spectroscopy
EELS	Electron energy loss spectroscopy
El%	Percent elongation
ESI	Energy spectroscopic imaging
ev	Electron-volt
F	Ferrite
FB	Ferritic bainitic steel
FEG	Field emission gun
FTTU	Fast thermal treatment unit
GOF	Goodness of fit
HR	Hot rolled



HSLA	High strength low alloy steel
HSS	High strength steel
HV	Vickers hardness
IBT	Isothermal bainite transformation
IF	Interstitial free steel
IFFT	Inverse fast Fourier transform
JCPDS	Joint committee on powder diffraction standard
M	Martensite
M steel	Martensitic steel
MAX.	Maximum
$M_f$	Martensite finish temperature
MIN.	Minimum
$M_s$	Martensite start temperature
ND	Normal direction
PH	Press hardening steel
PSC	Plane strain compression
Q & T	Quenching and tempering
RA	Retained austenite
$R_{exp}$	Expected error
RPM	Rotation per minute
$R_{wp}$	Weighted error
SAED	Selected area electron diffraction pattern
SEM	Scanning electron microscopy
SFE	Stacking fault energy
TD	Traverse direction
TEM	Transmission electron microscopy
TMC	Thermomechanical compression test
$T_{nr}$	Non-recrystallization temperature
TRIP	Transformation induced plasticity steel
$T_{rs}$	Recrystallization temperature
TWIP	Twinning induced plasticity steel
UHSS	Ultra high strength steel
UTS	Ultimate tensile strength
XRD	X-Ray diffraction

$\alpha$	Ferrite
$\alpha'$	Martensite
$\alpha_b$	Bainite
$\gamma$	Austenite
$\theta$	Cementite
$\sigma_f$	Flow stress
$\sigma_y$	Yield Strength

# Acknowledgments

First of all, I would like to express my special appreciation and thanks to my supervisor Prof. W Mark Rainforth for the supervision of this project. I would like to thank you for all your support and advice.

Many thanks are extended to Dr. Peter Korgul, Dr. Nik Reeves, Dr. Peng Zeng, Dr. Cheryl Shaw, Dr. Le Ma and other staffs of Sorby centre for their advice, training, provision of the laboratory facilities, their help and technical support. I am also grateful to Dr. Jo Sharp for performing electron energy loss spectroscopy (EELS) and high resolution TEM using FEG-TEM.

Also, I am very thankful to the staff of the University of Sheffield, in particular, Ann Newbould, Karen Burton, Vanessa Dalton, Dean Haylock, Richard Kangley, Ian Watts, Kyle Arnold, Michael Bell, and others, for their friendly and invaluable assistance contributed to this project.

Finally, I would like to express my gratitude to my beloved parents and siblings, and my friends for their love and support.

Many thanks to all of you and to those I might have forgotten.

# Chapter 1. Introduction

## 1.1 Advanced High Strength Steels Assisted by TRIP Effect

Climate change, depletion of fossil fuels and increasing numbers of cars in the world has driven the need for the reduction in consumption of fossil fuels. A key driving factor in the automotive industry has been the need to reduce exhaust emissions. There are a number of strategies to do this, but one major objective has been to decrease the weight of cars. This can be achieved by developing higher strength steels that allow the use of thinner steel sections.

The necessary crashworthiness has been obtained through using high strength steels with hybrid properties of different soft and hard phases. Generally, a combination of the effect of the high strength martensitic or bainitic constituent in addition to carbo/nitride precipitation in a soft, ductile ferritic or austenitic matrix results in a steel with high ductility and high strength. In this way, the advent of advanced high strength steels (AHSS) has brought a remarkable improvement in strength with acceptable formability.

In the family of AHSS steels, different types of steels have been introduced by researchers and steel makers. In 1967, Zackay and co-workers were the pioneering researchers who reported transformation induced plasticity (TRIP) effect in high strength steel [1]. It was further developed by many other researchers in the advanced high strength steels. It is now well established that the presence of retained austenite in the multiphase structure of these steels leads to a significant improvement in the mechanical properties due to the TRIP effect [2].

The AHSS steels assisted by the TRIP effect are generally classified in three main groups based on their matrix structure: polygonal ferrite, bainitic/acicular ferrite and martensite [3]. The microstructure of these steels is adjusted either through hot rolling or intercritical annealing after cold rolling. The targeted microstructure of the polygonal ferrite TRIP steels consists of ferrite separated by the retained austenite, martensite and bainite. The microstructure of bainitic ferrite TRIP steels mainly consists of fine lath bainitic ferrite separated by lath shape retained austenite [3, 4].

It is believed that the retention of austenite, apart from the effect of substitutional elements, is strongly dependent upon the bainite transformation during the cooling stage from the intercritical anneal. The displacive transformation of bainite is associated with carbon partitioning into the austenite. This increases the mechanical/thermal stability of austenite against martensite transformation. It is widely accepted that in TRIP assisted steels the cooling stage after intercritical annealing or finishing stage should be sufficiently rapid to minimize the possible transformations except the transformation to bainite.

Significant improvements in the mechanical properties of TRIP assisted steels have been achieved by the addition of microalloying elements. Although many investigations have been done to analyze the interaction between phase transformations during thermomechanical processing in these groups of steels, there are few studies focused on the effect of microalloying elements. Research for over half a century on microalloyed steels has shown the noticeable effect of these elements in the microstructural evolution both as a precipitate and solute. Niobium carbide/nitride and also titanium carbide/nitride precipitates are formed at higher temperatures compared to vanadium carbides/nitrides and strongly interact with the austenite during controlled rolling. In contrast, the effect of vanadium carbide precipitation is more pronounced at lower temperatures.

The precipitate strengthening is dependent on the microstructural evolution and chemical composition. For example, the ferrite recrystallization during an intercritical annealing annihilates a large amount of dislocations. Perhaps this reduces an intense precipitation and coarsening rate. Furthermore, since the diffusivity of vanadium is lower than carbon/nitrogen, the diffusion flux of vanadium is a rate controlling factor in the precipitate coarsening. The required level of carbon (i.e. generally 0.1 to 0.3 wt%) in TRIP assisted steels for securing a significant amount of retained austenite might lower the rate of coarsening of VC and encourage a homogeneous precipitation. However, no evidence could be found for the intense V(C,N) precipitation in a ferritic structure during an intercritical annealing process.

It has been documented in the literature that the multi-additions of microalloying elements can change the precipitation behaviour, particularly in terms of precipitate number density and precipitate size [5]. This is of particular importance in the context of microalloyed TRIP steels because of the interaction between strong microalloying

carbonitride formers and the evolution of microstructure. Thus, the question arises: to what extent can the initial microstructure change the precipitation behaviour.

## 1.2 Outline and Objectives of the Thesis

Three microalloyed TRIP assisted steels with different chemical compositions were studied in this research. The following objectives were defined, considering the hybrid influence of microalloying elements and microstructural evolution:

- The first alloy was a cold rolled V microalloyed TRIP steel with a polygonal ferrite matrix which is called in this report “Alloy 1”. The main objective of this chapter was to study the evolution of microstructure during the isothermal hold following the intercritical annealing, in which the bainite transformation occurs, with particular attention to the V(C,N) precipitation behaviour and the retained austenite.
- This initial research led to further investigations into the effect of the additional additions of Nb and Mo on the microstructural evolution following hot working, cold rolling and intercritical annealing. The driver for this was to establish whether further gains in strength could be achieved through additional microalloy additions and adjustments to the process route. The microstructure and precipitation behaviour of the Nb+Mo+V steel was compared to that of the V only steel after the rough rolling, cold rolling and intercritical annealing, and the evolution of this microstructure is discussed.
- In the final part of this PhD project, controlled rolling was simulated by a plane strain compression test. The effect of controlled rolling is compared with conventional rolling to interpret the effect of Nb+Mo+V additions on the microstructural evolution and precipitation behaviour of V microalloyed TRIP steels.

The following chapters detail the literature, the experimental procedure used to study the structure of the materials, discuss the results obtained, draw conclusions from this work and propose further research to investigate potential scientific ambiguities.

## Chapter 2. Literature Review

### 2.1. Background of Advanced High Strength Steels (AHSS)

Over the last few decades, rising fuel prices and more stringent requirements for safety and emission control have driven the automotive industry's interest in the development of AHSS. From the aspect of ecology, it is useful to limit the amount of greenhouse gas emitted into the environment by decreasing the fuel consumption of cars. This has been achieved by decreasing the weight of the car, for example, by reducing the thickness of steel sheets used in the car body [6].

These considerations resulted in pioneering efforts to increase the strength as well as formability. The introduction of high strength steels (HSS) was a first stage in this direction. The cornerstone of further developments for higher strength and ductility was laid by the introduction of a microstructure consisting of at least two different components. This enables the car makers to use thinner steel sheets, whilst still providing crash protection. A typical trend of high strength steels (HSS) and advanced high strength steels (AHSS) steels application in a car body is given in Fig. 2.1 [6, 7].

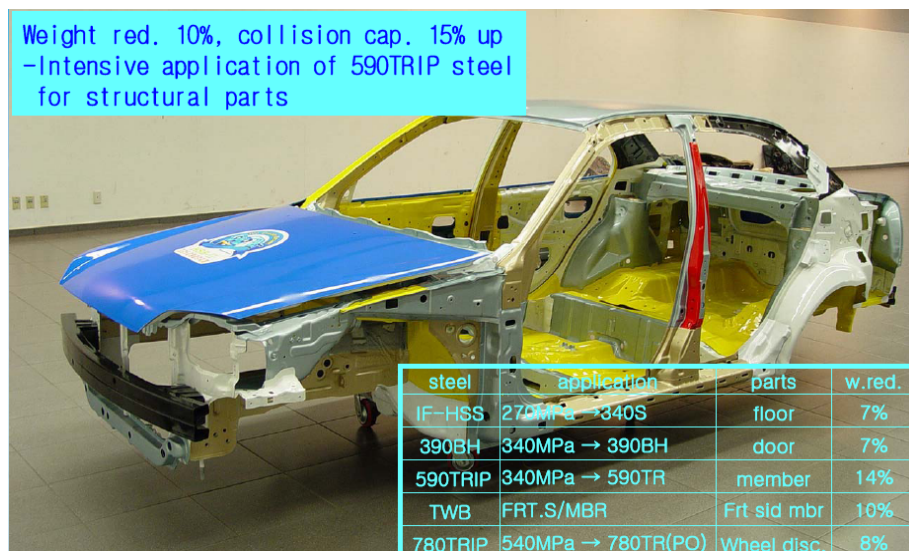


Fig. 2.1, An overview of typical car body components which are made from different groups of AHSS steels with respect to their effect on the final weight reduction [7].

AHSS are classified by their microstructure into dual phase (DP), transformation induced plasticity (TRIP), complex phase (CP), martensitic (M), twinning induced plasticity (TWIP), press hardening (PH) and also quenched and tempered (Q & T) steels. In these steels the combined effect of hard martensite, bainite, and the ductile ferrite and austenite phases improves the ductility-strength relationship of these steels compared to HSS. Fig. 2.2 compares tensile strength versus elongation for the conventional HSS and AHSS steels. It can be seen that AHSS steels have a significantly higher tensile strength i.e.  $\geq 300$  MPa [8, 9, 10].

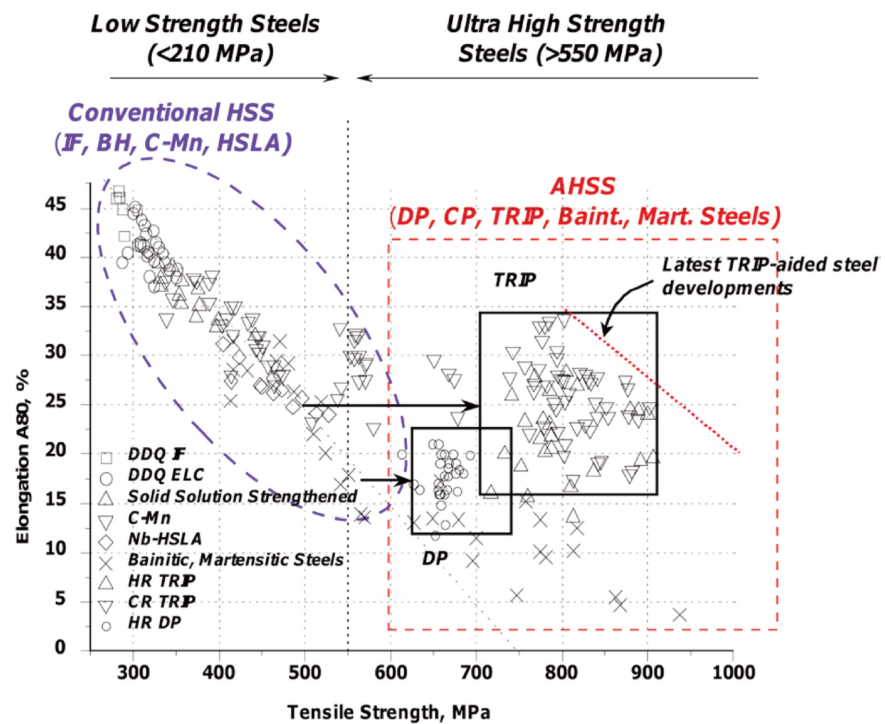


Fig. 2.2, A comparison of tensile strength against elongation for different groups of HSS and AHSS steels. IF, Interstitial free steel; BH, Bake hardening steel; C-Mn, carbon manganese containing steel; HSLA, High strength low alloy steel; DP, Dual phase steel; CP, Complex phase steel; TRIP, Transformation induced plasticity steel; Mart, Martensitic steel, (A80 (%): maximum of uniform elongation) [8].

Many studies have been conducted on the effect of microstructure evolution on the mechanical properties of AHSS. They indicate that the ductility and strength of these steels are dependent upon the morphology, distribution and volume fraction of martensite, bainite, retained austenite and nano scale precipitates in the microstructure. Fig. 2.3 shows an overview of flow curves under tensile deformation for different groups of conventional AHSS steels [6].



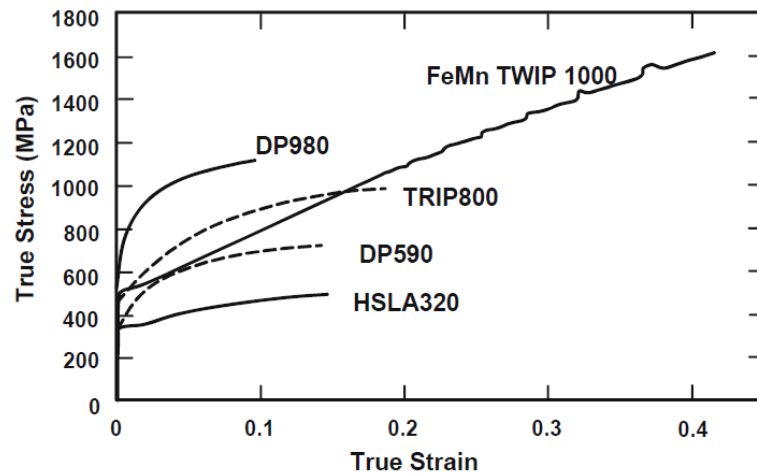


Fig. 2.3, True stress strain curves for different groups of AHSS steels. Curves are plotted approximately up to the necking point [6].

The main reason for the variation in yield and ultimate tensile strengths and the observed work hardening behaviour in these steels corresponds to the evolution of microstructure. These lead to variation in the mechanism of deformation, indicated by different stress-strain curves [6].

Further improvements to the mechanical properties of AHSS (strength and formability) are still sought, particularly to adiabatic deformation due to the high strain rate deformation commonly occurring during passenger car collision [2]. Attention has focussed on chemical composition and thermomechanical processing, in particular solid solution hardening and precipitation hardening, the objective being to increase strength without decreasing formability [2, 8].

### 2.1.1. AHSS Steels Assisted by TRIP Effect

In 1967 Zackay and co-workers reported a transformation induced plasticity (TRIP) effect in CrNiMoSi high strength steels [1]. Further substantial investigations into austempering after intercritical annealing confirmed the possibility of austenite retention in the microstructure at room temperature. It was found that the retained austenite in the microstructure leads to the TRIP effect during deformation. During deformation the retained austenite transforms to martensite which increases the work hardening and the formability of steels. Bainite transformation significantly increases the retention of austenite in the microstructure and its presence, obtained through the

TRIP effect, is essential in the production of AHSS. The presence of bainite stabilizes the austenite against martensite transformation through its increased carbon content.

In recent years, efforts have been made to increase the dynamic energy absorption during deformation with high strain rates [2]. Studies have concentrated mostly on the microstructural development of retained austenite and bainite but less so on the precipitation of microalloying elements [3, 4, 6]. Much work has been reported about controlling microstructure and precipitation behaviour during thermomechanical treatments as a function of chemical composition. Sugimoto in 2009, reported three generations of TRIP assisted steels. Their mechanical properties are strongly affected by the microstructure of the matrix. The development of the matrix in these steels is a function of thermomechanical processing and chemical composition and can be polygonal ferrite, bainitic ferrite or annealed martensite [3, 11, 12]. Among these steels the bainitic ferrite matrix is at the forefront of developments in the AHSS industry because of its favourable balance of strength, toughness and cost [13]. The coexistence of different phases requires an accurate production process and subtle design of chemical composition. Fig. 2.4 compares different commercial cooling scenarios in steels after the finish rolling stage. Many patents have been recorded which evidence that chemical composition is the priority factor in controlling the microstructure of the matrix in TRIP assisted steels [2, 13, 14].

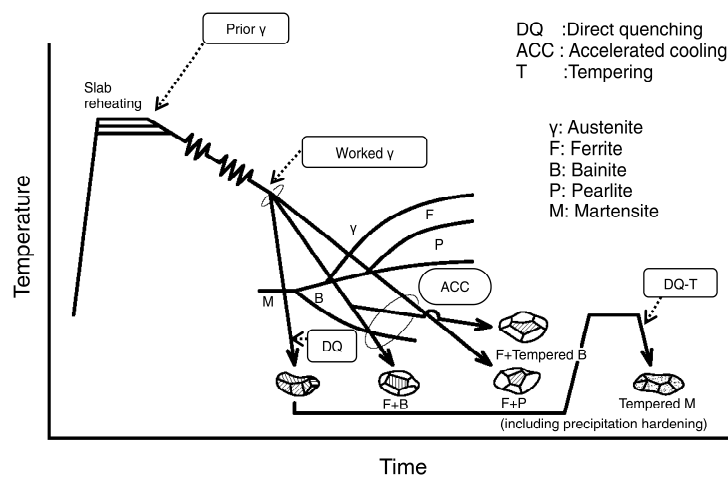


Fig. 2.4, Effect of cooling rate on the evolution of microstructure in steels [14].

A bainitic ferrite matrix can be achieved by relatively rapid cooling to the bainite transformation temperature. Rapid cooling suppresses the formation of pearlite

and other possible ferritic constituents and promotes the transformation of austenite to bainite [3, 4].

In 2007 a review paper [13] suggested quenching and tempering as an alternative cost effective approach to retaining significant austenite. It also highlighted the difficulty of controlling the formation of coarse cementite in bainitic steels even under rapid cooling conditions. However, the tempering stage favours the redistribution of carbon into the retained austenite which increases the stability of austenite against martensite transformation (Fig. 2.4). These steels look promising considering recent progress in the interaction between microalloying elements and cementite precipitation.

As pointed out earlier, the presence of retained austenite in this group of AHSS steel causes a TRIP effect and contributes greatly to enhanced ductility [15]. It is widely accepted that retained austenite with a film shape shows higher mechanical stability which leads to better formability (Fig. 2.5) [15, 16]. The generally accepted reason is that the film retained austenite has a higher level of carbon content compared to blocky morphology, stabilizing it against martensite transformation. Therefore, it is strongly desirable that the retained austenite be in the film shape morphology rather than the blocky shape. It has been reported that in both bainitic ferrite and martensite TRIP assisted steels the matrix has a fine lath type structure with a small interparticle path. This gives rise to the interfacial area between retained austenite and matrix, resulting in a high mean carbon concentration of retained austenite compared to the polygonal ferrite TRIP assisted steels (Fig. 2.5) [3].

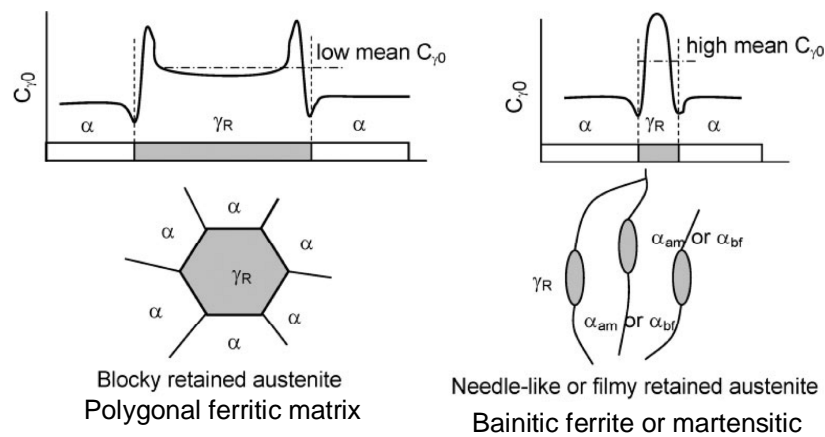


Fig. 2.5, Schematic illustration of carbon concentration distribution in retained austenite ( $C_{\gamma 0}$ ) in TRIP assisted steels,  $\gamma_R$ ; retained austenite,  $\alpha_{am}$ ; annealed martensitic ferrite,  $\alpha_{bf}$ ; bainitic ferrite [3].

The higher concentration of film shape retained austenite and smaller interlath bainitic ferrite in bainitic steels compared to polygonal ferritic TRIP assisted steels reduces the mean free path of austenite, which in turn suppresses the cleavage crack propagation (Fig. 2.6) [3, 17, 18]. This effect was studied by Sugimoto in 2009, who reported hydrogen embrittlement in this family of steels. More recently they have focussed on the effect of microstructure on this hydrogen embrittlement [3]. The coexistence of retained austenite and other constituents like bainitic ferrite, martensite and microalloying precipitates invites considerably more research.

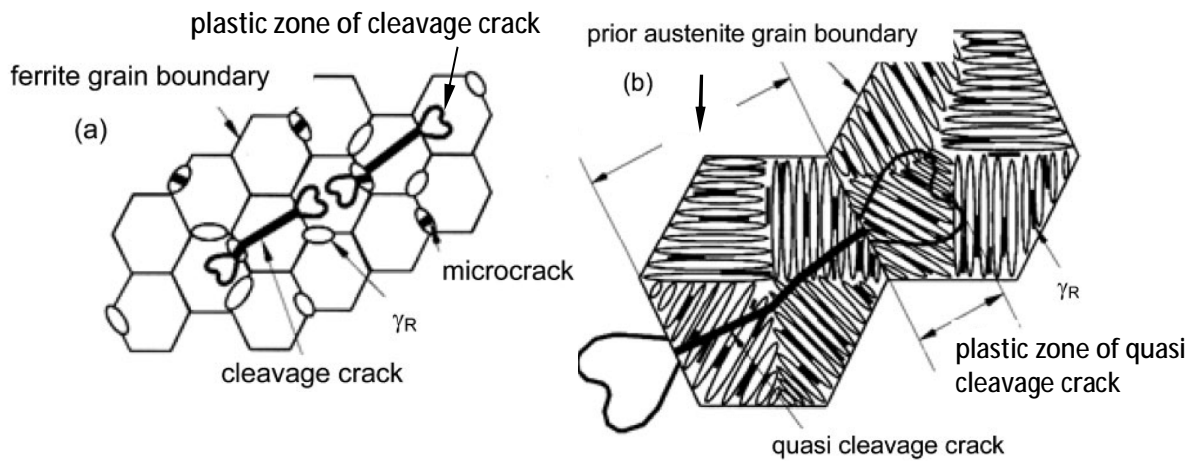


Fig. 2.6, Schematic of microstructure effect on the propagation of crack in TRIP assisted AHSS steels, (a) Polygonal ferrite matrix, (b) Bainitic matrix with the presence of quasi cleavage crack at plastic zone i.e. a localized, often isolated feature on a fracture surface that exhibits characteristics of both cleavage and plastic deformation [3, 18].

The literature evidences that multiple mechanisms contribute to the strengthening of AHSS steels and the following model has been proposed [19, 20]:

$$S_y = S_0 + S_{ss} + k.d^{-1/2} + S_r + S_{ppt} \quad (2.1)$$

where  $\sigma_0$  is the contribution from the matrix lattice friction stress,  $\sigma_{ss}$  corresponds to solid solution effect,  $d$  stands for the average grain size of the matrix structure,  $k$  is a constant value in the range of 15 to 18 ( $\text{MPa mm}^{0.5}$ ), and  $\sigma_p = M\alpha Gbp^{0.5}$ ,  $\sigma_{ppt}$  are related to the dislocation and precipitation effects, respectively.  $M$  stands for the Taylor factor,

which will be different for different phases (e.g. ferrite or austenite),  $\alpha$  is constant,  $G$  is shear modulus,  $b$  is Burgers vector and  $\rho$  is dislocation density.

However, the main interest of recent approaches is to increase the strength by the addition of microalloying elements. The effect of microalloying elements either in the form of precipitate or solute drag effect leads to grain refinements, solid solution hardening, dislocation density variations and precipitation hardening. It is noteworthy that the microalloying precipitation has shown a noticeable influence on controlling the microstructure at high temperature during hot roll processing. However, the precipitation strengthening can change the final mechanical properties of steels. This depends upon the strength of individual precipitates through interaction with dislocations either as shearable or non-shearable. Fig. 2.7 shows the balance of forces between a precipitate and a dislocation movement. As can be seen from Fig. 2.7 (b) and (c) the dislocation movement can be continued by either shearing the particle or by looping/cross-slip the non-shearable particles [21].

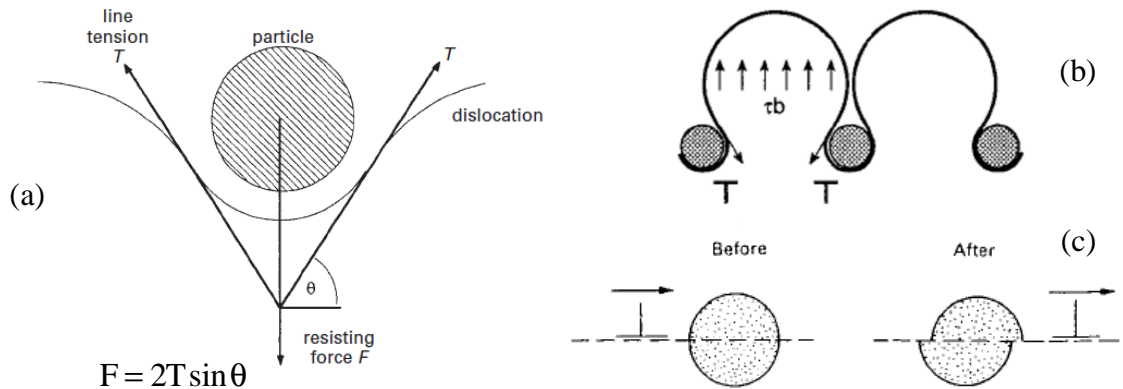


Fig. 2.7, The interaction between dislocation slipping and precipitates, (a) The balance of resistance forces against the dislocation movement, (b) Releasing the dislocation during meeting hard nonshearable precipitates by looping or cross slip, (c) Shearing the precipitates by the dislocation motion [21].

Gladman reported that there is a transition diameter for microalloying precipitates so that the precipitates with diameter exceeding approximately 5nm are more resistant to shearing mechanisms [21]. However, it has been accepted that the precipitation strengthening found in microalloyed steels is markedly consistent with the volume fraction, morphology and the average diameter of precipitates. In this sense, the development of microstructure as well as precipitation behaviour can retard the further

microstructure evolution by pinning the grain and sub grain boundaries. Rainforth et al. used electron spectroscopic imaging to provide strong evidence of subgrain structure pinning dependence on number density of precipitates and radius in Nb microalloyed steel (Fig. 2.8) [22].

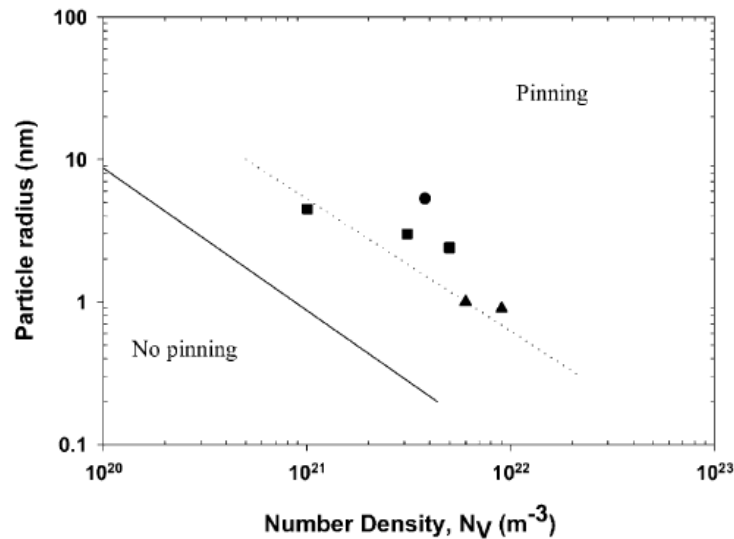


Fig. 2.8, Particle radius versus number density of NbC precipitates as function of number density required to pin subgrain structure. Three different techniques, including modelling, TEM and atom probe field ion microscopy (APFIM) were applied. The full line representing dislocation density of  $\rho=8 \times 10^{14} m^{-2}$  according to their observations and the dotted line from the estimated work by Burk et al. ( $\rho=4 \times 10^{15} m^{-2}$ ). ●, modelling; ■, TEM; ▲, APFIM [22].

In general, the evolution of microstructure and possible precipitation behaviour is controlled through thermomechanical processing, chemical composition and process parameters [23]. Fig. 2.9 shows two different methods of manipulating microstructure in TRIP assisted steels. These steels are produced either by hot rolling or annealing after cold rolling, followed by austempering in the range of bainite transformation temperature [24]. As can be seen from Fig. 2.9 (a), hot rolling followed by cold rolling is used to produce sheet steels for stamping applications. The necessary retained austenite is obtained by intercritical annealing after cold rolling [25]. As shown in Fig. 2.9 (b), the adjustment of microstructure in addition to thickness reduction can alternatively be produced by controlled rolling and cooling to the bainite transformation temperature range [25]. The alloying additions, strain rate, interpass interval and deformation temperature control the refinement of microstructure and precipitation

behaviour [26]. The presence of different elements can accelerate or retard the kinetics of transformation during the deformation and cooling stage, as will be described in a later section.

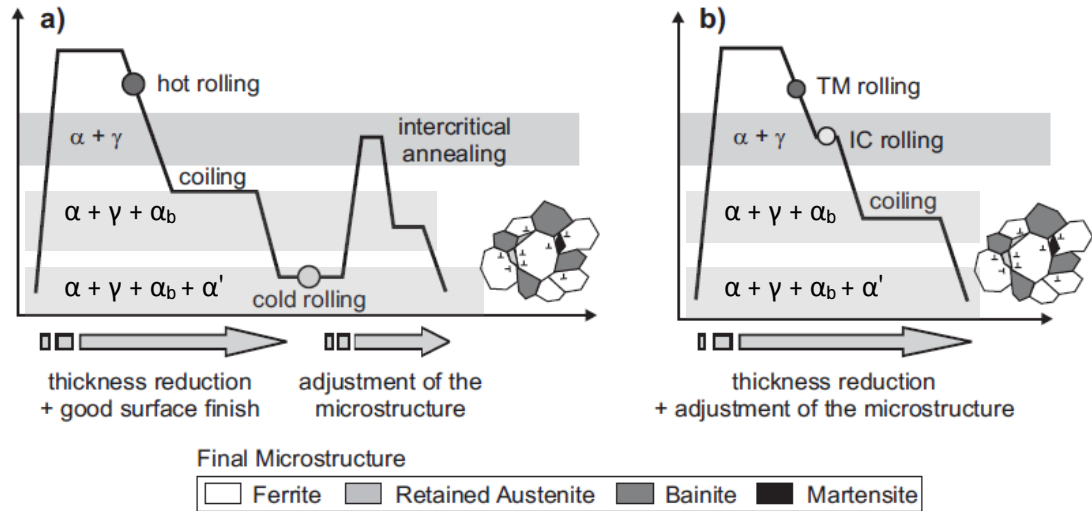


Fig. 2.9, Comparison between two conventional production processes of AHSS steels assisted by TRIP effect, (a) Hot rolling-cold rolling and intercritical annealing, (b) Controlled rolling.  $\alpha$ ; Ferrite,  $\gamma$ ; Austenite,  $\alpha_b$ ; Bainite,  $\alpha'$ ; Martensite [25].

## 2.2. Effect of Chemical Composition

The effect of chemical composition in microalloyed AHSS steels assisted by the TRIP effect is considered to be from two main aspects: the evolution of microstructure and precipitation behaviour. The chemical composition, thermomechanical process conditions and microalloying elements have a considerable influence on the determination of grain size and crystalline defects of austenite at elevated temperatures. Furthermore, the microalloying elements can control the kinetics of transformations and also the emergence of fine precipitates in the microstructure which leads to the significant improvement in strength. However, it is accepted that the effect of microalloying elements as solutes on the strengthening is attributed to the differences in electronegativity and radius of atoms compared to iron [27, 28, 29].

### 2.2.1. Carbon and Nitrogen

Fig. 2.10, displays a comparison between the average carbon content of different conventional AHSS and plain carbon steels which are commercially used in the automotive industry [30].

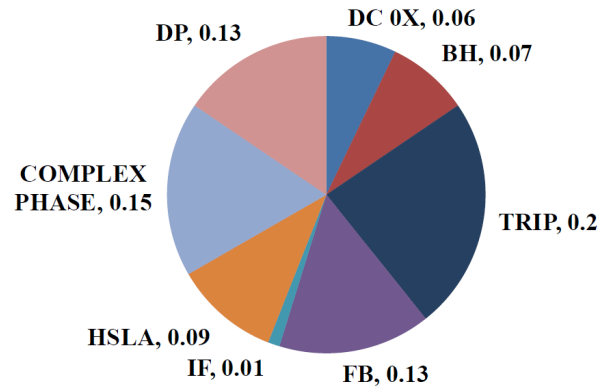


Fig. 2.10, The carbon content of steel types used in car body applications. DP; Dual phase, DC; Cold rolled low carbon steel, BH; Bake hardening steel, TRIP; Polygonal ferrite transformation induced plasticity assisted steel, FB; Ferrite-bainite steel; IF; Interstitial free steel, HSLA; High strength low alloy steel [30].

Fig. 2.2 indicated that decreasing carbon content increases ductility but reduces strength. However, carbon reduction also minimizes weldability and hot rolling problems [31]. Increasing the mechanical stability of austenite to martensite is important for a TRIP assisted steel and the presence of both carbon and nitrogen during cooling and mechanical deformation is key to this [32].

Many formulae have been published to predict the martensite start transformation ( $M_s$ ). However, the effect of carbon content on reduction of  $M_s$  shows a direct and similar trend in all formulae [33, 34].

It has often been reported that enhancing strain-induced martensite is facilitated by morphology and consequent crystal defects as well as by carbon/nitrogen content [35]. However, for a wide range of steels the  $M_s$  can reliably be calculated from chemical composition regardless of morphological effects. For example, using the following equation based on wt% of each element and assuming no interaction between them [36]:



$$M_s = 539 - 423[\% C] - 30.4[\% Mn] - 17.7[\% Ni] - 12.1[\% Cr] - 7.5[\% Mo] \quad (2.2)$$

Fig. 2.11 plots the impact of each alloying element on the  $M_s$  temperature of Fe-base binary alloys [37]. As can be seen from Fig. 2.11, the carbon and nitrogen are relatively more effective than all other given elements in reduction of the  $M_s$ .

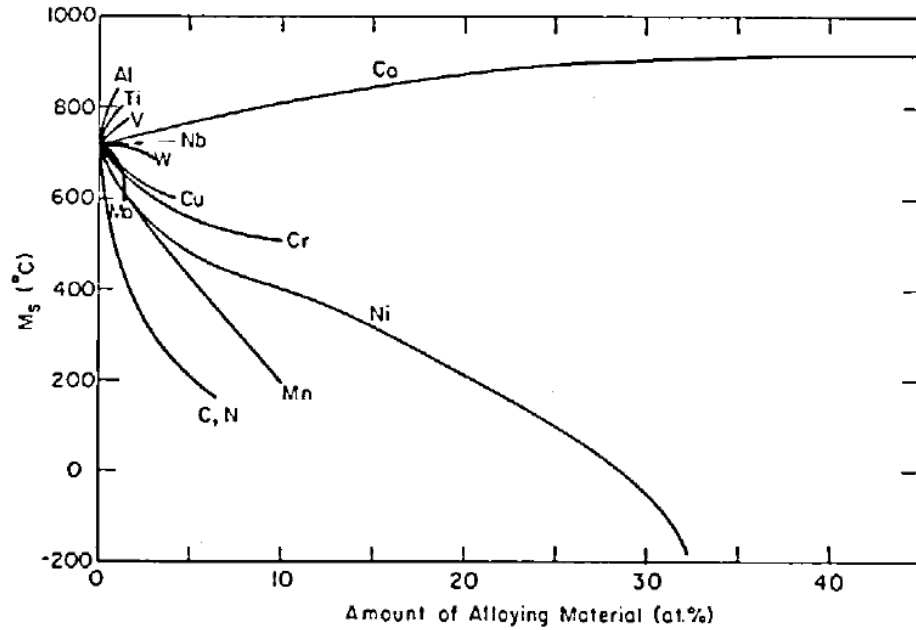


Fig. 2.11, Effect of individual elements on the  $M_s$  temperature of Fe-base binary alloys [37].

The presence of nitrogen can significantly influence the precipitation behaviour of microalloying elements, and the enhanced solubility of nitrogen in austenite compared to ferrite can intensify this behaviour. For instance, Bepari and Whitman reported the effect of N on Nb(C,N) precipitation in continuously cooled low carbon structural steels. They suggested that the presence of N leads to bulk precipitation of Nb(C,N) in austenite with little precipitation in ferrite, whereas in the absence of N the NbC occurred during and after  $\gamma \rightarrow \alpha$  transformation. It was also found that N is effective in altering the size and morphology of precipitates. This is thought to be because N increases the transformation temperature which enhances the growth of previously formed precipitates [38].

### 2.2.2. Microalloying Elements

Small additions to AHSS steels of Ti, V and Nb (microalloying) enhance their strength by grain refinement, precipitation hardening, acceleration/deceleration of transformations and also affecting the diffusion kinetics [6]. Whether solute or precipitate these microalloying elements can improve the mechanical properties according to the equation 2.1. The microalloying precipitates are formed at relatively high temperatures compared to cementite. Fig. 2.12 shows variable thermal stability of carbide and nitride precipitates for different microalloying elements under equilibrium conditions [39]. Lower thermal stability is associated with higher solubility which reduces precipitate formation. Variations in the kinetics of nucleation and growth for microalloying precipitation at different temperatures facilitate their control of microstructure development.

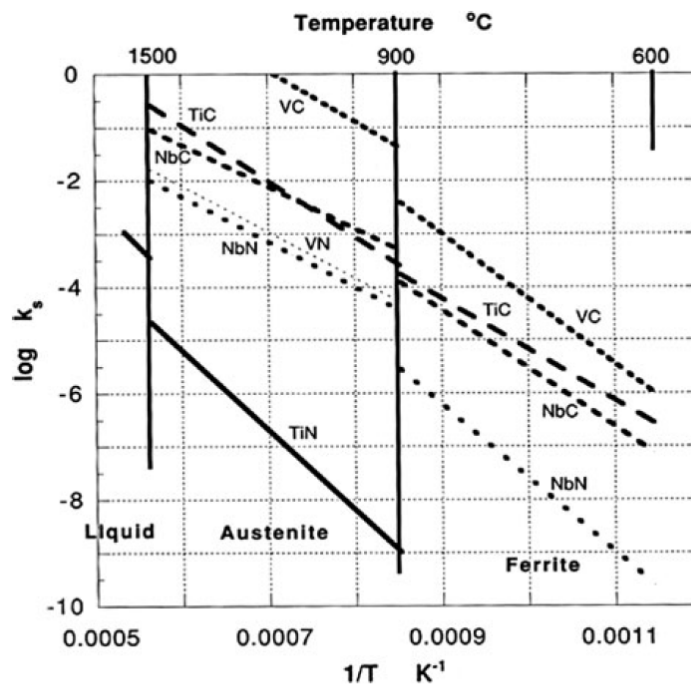


Fig. 2.12, Comparison among equilibrium solubility of microalloyed (C,N) precipitates in austenite and ferrite [39].

Table 2.1 provides a summary of microalloying and other conventional alloying elements effects on the microscopic/macroscopic behaviour of AHSS/HSLA steels [6].

Table 2.1, Effect of microalloying and other conventional substitutional elements on development of microscopic features and macroscopic properties of AHSS and HSLA steels [6, 28, 40].

Element	Microscopic effect			Macroscopic effect								
	Coarse precipitates	Fine precipitates	Precipitate coarsening resistance	Grain boundary segregation	Grain refinement	Cementite formation	C enrichment in austenite	Kinetics of recrystallization	Kinetics of $\alpha/\gamma$ transformation	Kinetics of bainite transformation	M <sub>s</sub> -temperature	Matrix strengthening
Al		+			+	-	+		+		+	
Si						-	+		+		-	+
Nb		+			++		+	--	-.+	-	-	++
Ti	+	+			+			-	+			
V		+			+			-	+			+
Mo			+						-	-	-	+
+ : promote/increase												
- : hinder/retard/reduce												

In general, precipitation at higher temperatures over the finish rolling stage is useful in controlling the microstructure, whilst precipitation at lower temperature enhances the strength of steels. Microalloying aims to develop precipitates which meet the following desirable requirements [41]:

- 1- The precipitates should be re-dissolved during the re-heating stage before hot rolling.
- 2- In AHSS steels assisted by the TRIP effect, the precipitates should not reduce the stability or volume fraction of retained austenite.
- 3- The number density of precipitates in terms of their mechanical properties and size should be as high as possible to raise the strength.
- 4- There should be no remarkable reduction of hot ductility due to higher hardness during hot rolling.
- 5- It should be possible to produce precipitates during continuous annealing.
- 6- In order to facilitate cold roll ability then there should be no significant formation of large precipitates during the finishing and coiling stage.

**Titanium** is mainly used to form fine TiN precipitates. The solubility of titanium nitrides is so low that the precipitates hardly re-dissolve in the subsequent stages of heat treatment. The Ti(N,C) precipitates effectively retard the recrystallization

and the growth of austenite at elevated temperatures, and can generate a pancaked structure at temperatures below the recrystallization start range [42]. Furthermore, the relatively high thermal stability of these precipitates makes it possible for them to act as nucleation sites for carbonitrides of other microalloying elements, accelerating the kinetics of their precipitation (Fig. 2.12). Titanium also promotes a bainitic microstructure leading to the refinement of bainitic ferrite [13].

**Vanadium** is widely used in AHSS steels as one of the most effective elements for the precipitation strengthening. This element can be completely dissolved at high temperatures (i.e. austenitising) before starting the hot rolling stage. So far, many investigations have estimated the dissolution temperature of VC and VN under equilibrium conditions. The following equations show the lowest temperatures for the dissolution of V(C,N) under equilibrium condition [43].

$$\log[\%V][\%N] = -8330/T + 3.40 \quad (2.3)$$

$$\log[\%V][\%C] = -9500/T + 6.72 \quad (2.4)$$

Balliger and Honeycombe in 1980 reported that the kinetics of vanadium precipitates varies with chemical composition. They studied the effect of N and carbon in three alloys, FeVC, FeVCN and FeVN with chemical composition of  $\approx 0.27\text{wt}\%$  V in addition to N maximum  $0.032\text{wt}\%$  and C maximum  $0.05\text{wt}\%$ . It was shown that the rate of VC coarsening in ferrite is around 50 times greater than VN and V(C,N) with ascending order  $VC > VN \approx V(C,N)$  [44]. At high temperatures the VN or V(C, N) are either in solute or small precipitates compared to other microalloying elements e.g. Nb [45, 46] which retards static recrystallization in austenite. Vanadium carbonitrides also markedly change the kinetics of bainite transformation at lower temperatures through interaction with dislocations and recovery of bainite [47, 48, 49].

**Niobium** is the most effective microalloying element which suppresses austenite recrystallization and recovery within thermomechanical processing. The soaking temperature ( $^{\circ}\text{K}$ ) in order to dissolve Nb(C,N) before hot rolling can be calculated by the following equations [27, 46]:

$$\log[\%Nb][\%C] = -7970/T + 3.31 + (1371/T - 0.900)[\%Mn] - (75/T - 0.0504)[\%Mn]^2 \quad (2.5)$$

$$\log[\% \text{Nb}][\% \text{N}] = -10230/T + 4.04 \quad (2.6)$$

Nb (0.03-0.09 wt%) at rolling temperatures below 1040°C is believed to suppress recrystallization and coarsening either by solute drag effect or by strain-induced Nb(C,N) precipitation on the deformed austenite and slip planes [42].

Nb(C,N) precipitate formation during thermomechanical processing is rare so the microalloying elements largely remain in solution [29]. Recrystallization and recovery are inhibited by the segregation of microalloying elements at the dislocations core which increases the driving force for the disengaging of dislocations from “Cottrell air mass”. In this way, the relative electronegativity and the radius of Nb atom compared to Fe determines its effectiveness on the evolution of microstructure [29].

In general, the strain induced precipitates are too large to provide precipitation strengthening. As shown in Fig. 2.12 the niobium carbonitrides have much lower solubility in austenite than vanadium precipitates. However, through thermomechanical processing at high temperatures the presence of Nb is associated with inhibition of austenite recrystallization, grain growth and recovery. By using Nb to suppress the growth of austenite grains during deformation pancake shaped austenite is formed with high accumulation of defects. This supplies potential sites for the nucleation of ferrite, leading to the refinement of ferrite at room temperature. The homogeneity of ferrite nucleation inhibits the probability of local coarsening (Fig. 2.13) [14].

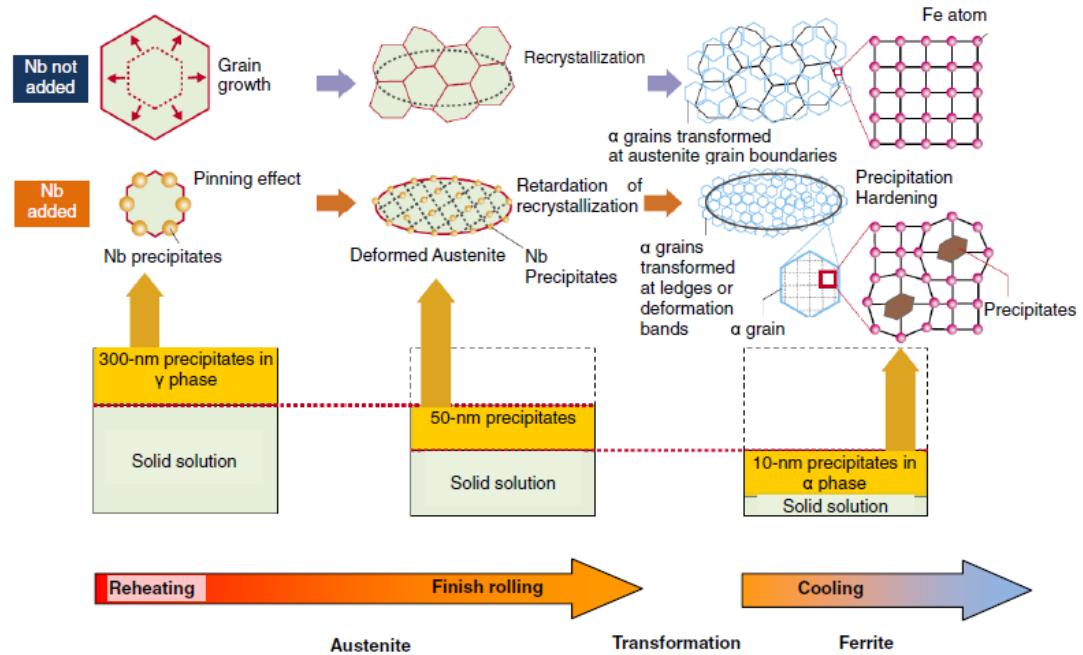


Fig. 2.13, Effect of Nb precipitation at different ranges of temperature on the evolution of microstructure, showing the positive impact of Nb precipitates on controlling the austenite recrystallization/growth and consequently ferrite refinement, and precipitation strengthening [14].

Nb offers outstanding benefits as a microalloying addition through its impact on thermomechanical processing, but its impact on microstructure through changing the kinetics of austenite to ferrite transformation is even more useful. The presence of Nb, whether as solute or precipitate changes the kinetics of austenite transformation to the other phases during cooling. Hong et al., studied the influence of Nb and the mechanical deformation at high temperatures on the grain growth of ferrite. He concluded that Nb significantly retards the strain induced ferrite transformation and also inhibits the grain growth of ferrite [50, 51]. Hinton et al. studied the effect of Nb and hot deformation at high temperatures on the ferrite transformation and proposed that Nb significantly reduces the kinetics of ferrite transformation regardless of any thermomechanical treatment [52]. The kinetics of polygonal ferrite transformation in Nb containing steels is relatively slow so requires either a slow cooling rate or an isothermal hold condition. Consequently, acicular/bainitic ferrite microstructure can be achieved by rapid cooling after finishing in Nb microalloyed steels [53].

Niobium in solid solution is able to lower the martensite start temperature and suppress cementite and pearlite formation. This promotes a higher volume fraction of austenite in the bainite temperature range [54, 55].

Several works have already been published on processing hot rolled microalloyed steels using V-Nb, Nb-Ti, Ti-Nb-V, etc. in alloys with similar carbon and manganese content. Five different morphologies of microalloying precipitates have been identified (complex, cuboid, spherical, irregular, oval/needle like shape). The morphology of precipitates is a function of chemical composition, microstructure and temperature, whereas their size is determined by nucleation time, nucleation temperature and chemical composition [5, 56]. Since the kinetics of transformation from multiple microalloying additions differs significantly from that of a single addition, the interaction between multiple microalloying elements in the microstructure is attracting considerable attention [27, 57, 58].

### **2.2.3. Other Alloying Elements**

#### **2.2.3.1. Silicon, Aluminium, Phosphorus and Sulphur**

**Silicon** increases the temperature of austenite to ferrite transformation and is effective in solid solution strengthening and decreases the stacking fault energy (SFE) of austenite. A high silicon content increases the bainite start temperature as well as the range of ferrite-bainite transformation [59]. Silicon and aluminium are both ferrite stabilizers which can restrict the loop of  $\gamma$ -field but their insolubility in cementite can lead to austenite retention by hindering the formation of cementite in the carbon enriched austenite within the bainite transformation temperature range [59]. Thus, the carbon can more readily partition into the austenite [60]. The formation of cementite in AHSS steels has two major detrimental effects in the evolution of microstructure: (a) cementite particles in the microstructure are responsible for stress concentration and crack initiation during mechanical deformation, and (b) a large amount of carbon is used by cementite reducing its availability for microalloying precipitation strengthening and austenite retention. An accumulation of silicon around a cementite nucleus can considerably increase the activity of C locally which prevents the diffusion of carbon to the nucleus. However, high levels of silicon promote the formation of an oxide film on the surface which reduces the wettability of steel sheet in the process of galvanizing [2].

**Aluminium** increases the SFE of austenite and can be used as an alternative to Si to avoid potential hot rolling or coating problems. Aluminium suppresses the austenite to martensite transformation during both cooling and mechanical deformation, whereas silicon decreases the stacking fault energy of austenite and sustains the strain induced martensite phase transformation [61]. The coexistence of aluminium and nitrogen significantly accelerates austenite recrystallization at the roughing stage [62]. Aluminium increases the mechanical stability of retained austenite through increasing the carbon concentration [63]. At high temperatures aluminium reduces free nitrogen by building up AlN precipitates, which in turn deters other microalloying precipitation e.g. VN [64, 65].

**Phosphorus** is a ferrite stabilizer and can drive transformation of austenite to bainite. It has been reported in the literature that the addition of phosphorus in Al-alloying steels delays cementite precipitation and enhances solid solution strengthening in the ferrite. In bainite it increases carbon activity encouraging its diffusion to austenite which accelerates the bainitic transformation and raises the carbon content in the retained austenite. Excess phosphorous causes grain boundary segregation and the formation of detrimental phases e.g. Fe<sub>3</sub>P phosphide reduces ductility [2, 24, 66].

**Sulphur** has a deleterious effect on the mechanical properties of steels. The interaction between Mn and S lowers the solubility of S in both austenite and ferrite encouraging grain boundary segregation at high temperatures, with a strong detrimental effect on the mechanical properties of steels. In AHSS steels the level of sulphur is relatively low, and consequently more manganese remains in the solid solution [67].

#### 2.2.3.2. Manganese and Molybdenum

**Manganese** directly impacts on the kinetics of austenite recrystallisation and has been used to improve the microstructure of AHSS steels throughout three generations of these steels. Manganese acts as an austenite stabilizer by slowing down the austenite to ferrite transformation. [62]. It lowers the activity coefficient of C in ferrite and austenite and also increases the C solubility in ferrite. Moreover, Mn is soluble in cementite [2].



The microstructural impact of varying Mn levels can be predicted from the schematic Fe-Mn binary diagram (Fig. 2.14) [68]. Adding small amounts of Mn to Fe, (5 to 25 mass%) at room temperature leads to the formation of cubic  $\alpha'$ -martensite at low Mn and hexagonal closed packed  $\epsilon$ -martensite at higher Mn content [69]. A large amount of manganese enhances the transformation of austenite into  $\epsilon$ -martensite during deformation. This is correlated with the dissociation of a perfect  $a/2\langle 011 \rangle \gamma$  dislocation into Shockley partial dislocations on a closed packed  $\{111\}\gamma$  plane. In the fault regions a reduction in the fault energy favours the formation of  $\epsilon$ -martensite (Fig. 2.14) [67].

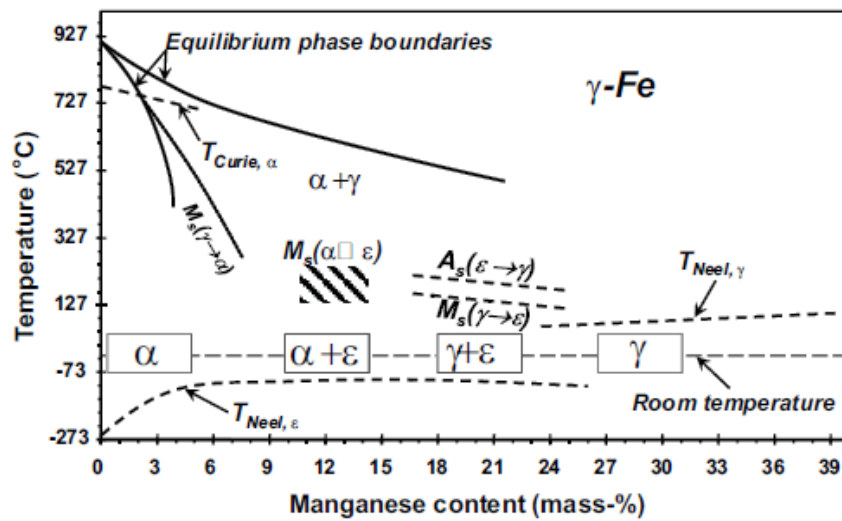


Fig. 2.14, Binary Fe-Mn equilibrium phase diagram, showing the presence of different meta-stable allotropies of Fe-Mn at different temperatures [68].

Mn also contributes to precipitation behaviour. For example, reducing the rate of dynamic precipitation by increasing the activity coefficient of Nb in austenite and significantly reducing the activity coefficient of C and N. Akben et al. reported an increase in necessary start time for Nb precipitation from 0.6 to 26s by increasing Mn from 0.42 to 1.90 wt% [28].

**Molybdenum** raises the hardenability and to a lesser extent strength through solid solution hardening. In general, Mo exerts considerable solute drag effect on austenite and reduces the activity coefficient of carbon [70]. Mo suppresses the kinetics of ferrite and pearlite formation [4, 6]. Compared with other microalloying elements Mo carbide and nitride are less readily formed than those of other microalloying elements and they do not precipitate under normal processing conditions. The thermomechanical

processing effects of Mo are similar to those of Mn, but Mn is considerably cheaper [42].

Mo impacts on dynamic precipitation and precipitate coarsening of microalloying elements. Various researchers, including Jiao et al. showed that Nb in solid solution improves the TRIP properties, therefore using Mo to retard the precipitation and coarsen Nb(C,N) enhances TRIP [28, 71]. Other investigators have reported the effect of Mo on the Nb precipitation at both austenite and ferrite ranges of temperature [58, 72, 73]. They suggest that two types of NbMo precipitates are generally formed, including MC and  $M_2C$ . Mo reduces the carbon activity in austenite increasing the solubility of Nb in austenite facilitating finer precipitation in the ferrite range of temperature [70, 74]. Higher precipitation at lower temperatures leads to denser and finer precipitates which enhances steel strength. These results have been corroborated by Cao et al. who evidenced that Nb-Mo gives higher yield strength compared to Nb-Ti due to finer and denser precipitates [70] and by Bhadeshia et al.'s work on interphase precipitation following Mo+Nb+Ti addition [75]. As can be seen from Fig. 2.15, the addition of Mo is associated with increasing the hardness.

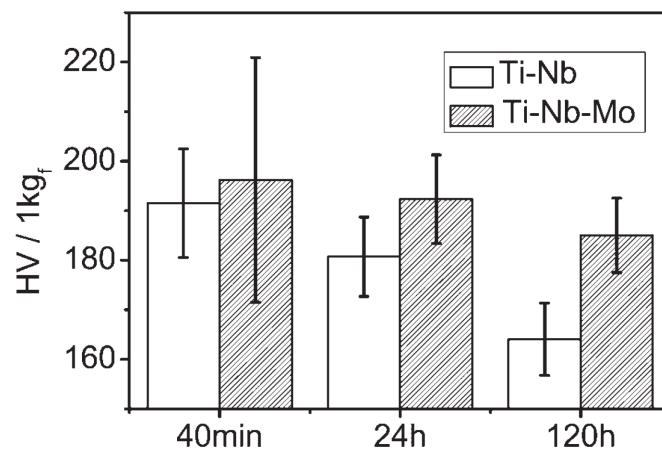


Fig. 2.15, Hardness versus isothermal holding time at austenite to ferrite transformation range of temperature [75].

### 2.3. Evolution of Microstructure during Thermomechanical Processing

Temperature, strain rate and magnitude of strain all impact on the route of diffusion or diffusionless mechanisms resulting in the evolution of different phases dependent on the thermomechanical processing applied.

For several decades at both the industrial and laboratory scale there has been considerable investment in controlling the deformation temperature and sequential cooling stages to optimise microstructure. Attention has been focussed on studying the C-curves of precipitation and other microstructural evolutions such as recrystallization, recovery, grain growth etc. Fig. 2.16 illustrates the contribution of deformation within the austenite range temperature to microstructure evolution. The rolling stage can basically be divided into three main stages in terms of working temperature with deformation stages occurring either above or below recrystallization temperature ( $T_{rs}$ ) or in the intercritical range up to  $A_{r1}$  (i.e. roughing or finishing respectively) [42].

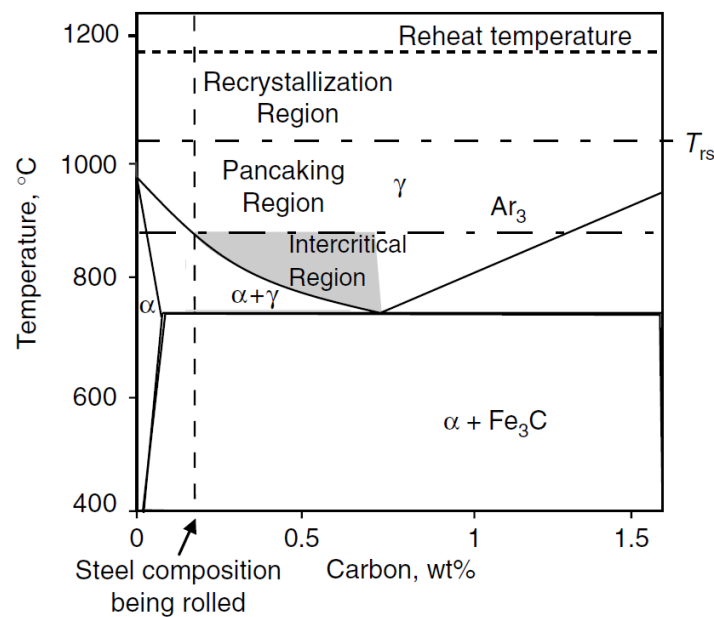


Fig. 2.16, Effect of controlled rolling on the microstructure in terms of temperature [42].

Fig. 2.16 shows the effect of temperature range and possible mechanical deformation at high temperatures on the microstructure of a typical hypoeutectoid steel [42]. In this case, the presence of alloying additions, in particular, microalloying

elements has shown a marked contribution at every stage indicating the effect of microalloying on the kinetics of transformation both as solute atoms and as precipitates.

Fig. 2.17 indicates an overview of industrial thermomechanical processing for AHSS steels. Regardless of the kinetics of transformations simultaneous or sequential transformations can be identified at every microstructure stage. The presence of different elements in solution also alters the kinetics of transformations at lower temperatures [6].

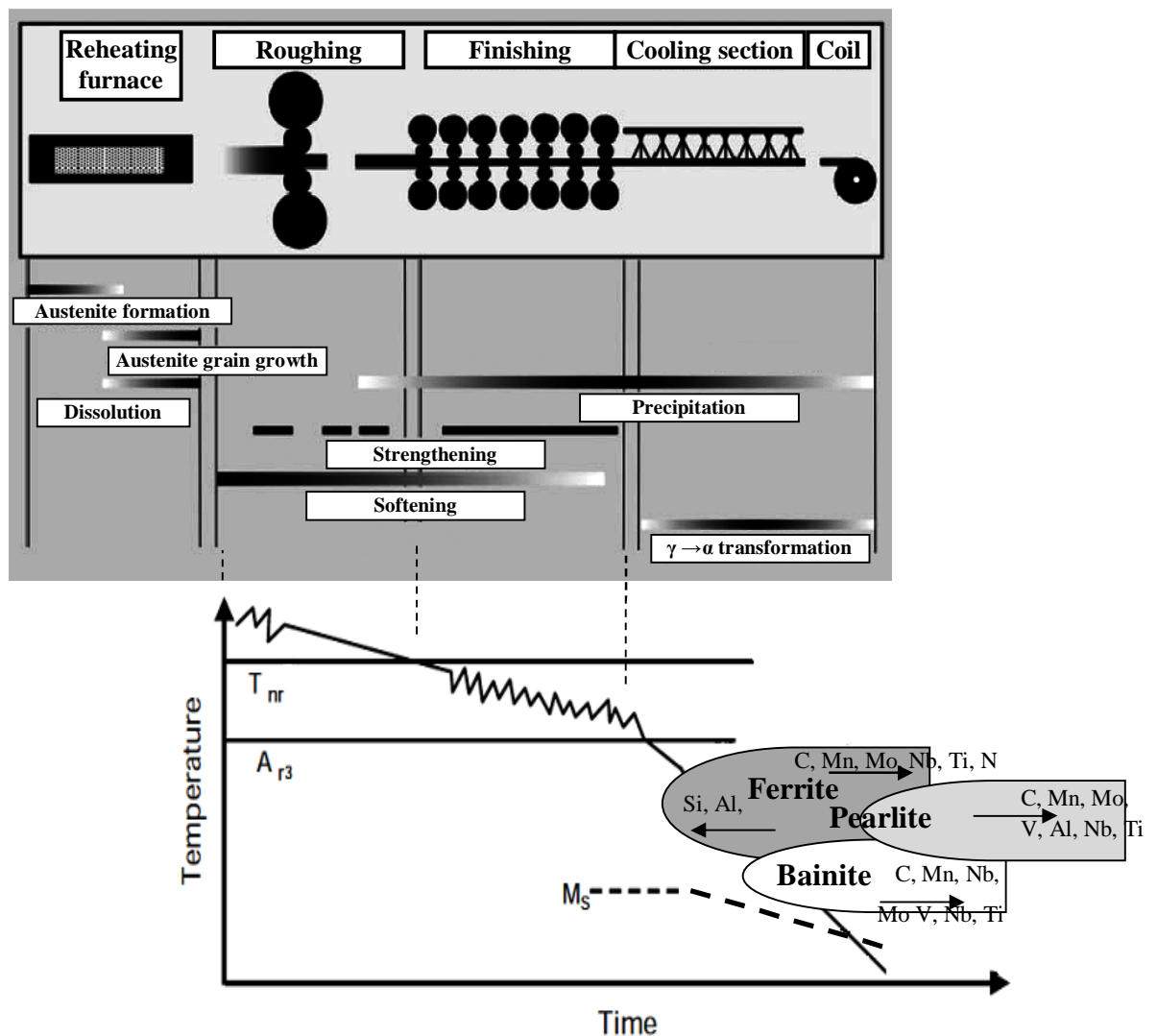


Fig. 2.17, Schematic of thermomechanical processing of AHSS steels assisted by TRIP effect and the influence of alloying elements on transformation behaviour during cooling [6, 76].

Thermomechanical treatments commonly applied in the production of AHSS steels are schematically reviewed in Fig. 2.18. The control of deformation temperature

is a significant factor in cases where different mechanisms such as recovery, recrystallization and precipitation occur simultaneously. Laboratory simulation of these conditions have been extensively reported elsewhere. For example, plane strain compression testing with controllable cooling systems has given outstanding results [77, 78].

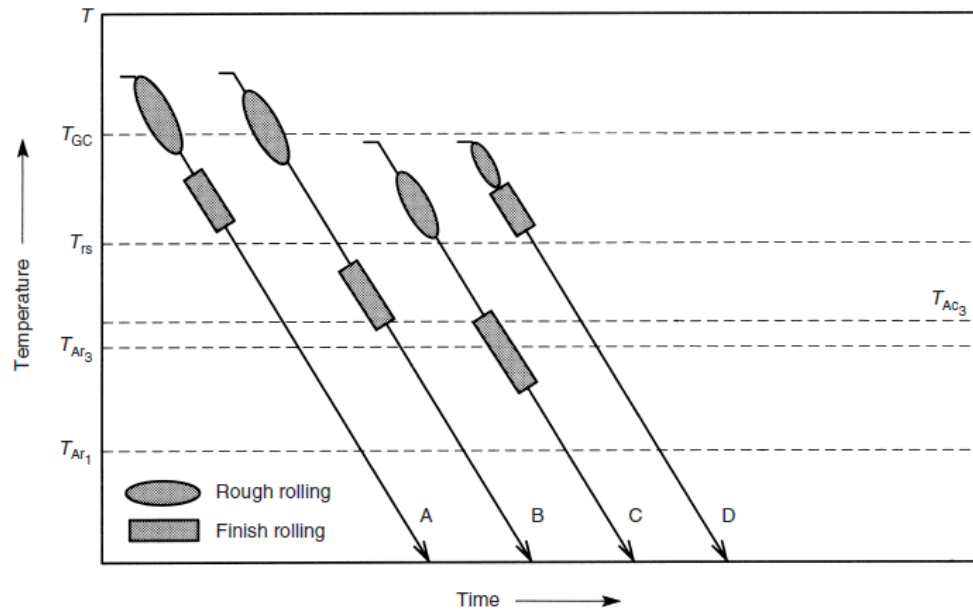


Fig. 2.18, A comparison of roughing and finishing temperature ranges based on critical austenite temperatures for the different types of thermomechanical treatment. A, conventional hot rolling; B, conventional controlled rolling; C, intensified (intercritical) controlled rolling; D, recrystallization controlled rolling.  $T$ , temperature;  $T_{AC3}$ , stands for the temperature ferrite fully transformed into austenite during heating;  $T_{Ar3}$ , the temperature at which austenite starts transforming to ferrite during cooling;  $T_{Ar1}$ , the temperature at which the transformation of austenite to ferrite and probable cementite is completed;  $T_{GC}$ , grain coarsening temperature;  $T_{RS}$ , recrystallization stop temperature.  $T_{GC}$  stands for the temperature above which grain coarsening starts by secondary recrystallization and the precipitates do not suppress grain growth [42].

### 2.3.1. Reheating Stage

Conventionally, slab preheating at temperatures  $\approx 1100-1250^{\circ}\text{C}$  before hot rolling is performed with the aim of austenitising and thereby dissolving most microalloying precipitates (i.e.  $\text{M}(\text{C},\text{N})$ , M represents microalloying elements) in the austenite. Increasing the temperature up to this range induces recrystallization and subsequent re-growth of austenite grains.

The interaction between precipitation behaviour and re-heating has been extensively researched now for a century. Sellars in 1979 reported that Nb was particularly effective at retarding grain growth in austenite at temperatures below 1200°C [62]. In 1980, White and Owen reported that raising the austenitizing temperature leads to a decrease in the rate of austenite recrystallization and that the higher solute concentration of V, Nb, C and N in austenite favours the faster carbonitride precipitation at 900°C [79]. They found that the higher austenitizing temperature increases the austenite grain size which reduces the potential sites for the recrystallization of austenite at grain boundaries, particularly at the early stages. Further investigations by Cuddy showed that the reheating stage in Nb microalloyed steels contributes to the recrystallization of austenite and the uniformity and grain size of the final product. He found that reducing the reheat temperature to restrict the austenite grain size below about 100µm provided complete recrystallization during the initial roughing pass [80].

One of the main objectives of reheating is to dissolve the microalloying precipitates by austenitizing. However, the coexistence of multiple microalloying elements can lead to co-precipitation of two or more microalloying elements as complex precipitates due to their different thermal stabilities (Fig. 2.19) [81, 82, 83]. Microalloying elements with higher thermal stability than the reheating temperature, such as TiN, undergo particle coarsening rather than dissolving and facilitate the precipitation of other microalloying elements by acting as nucleation sites (Fig. 2.19) [84].

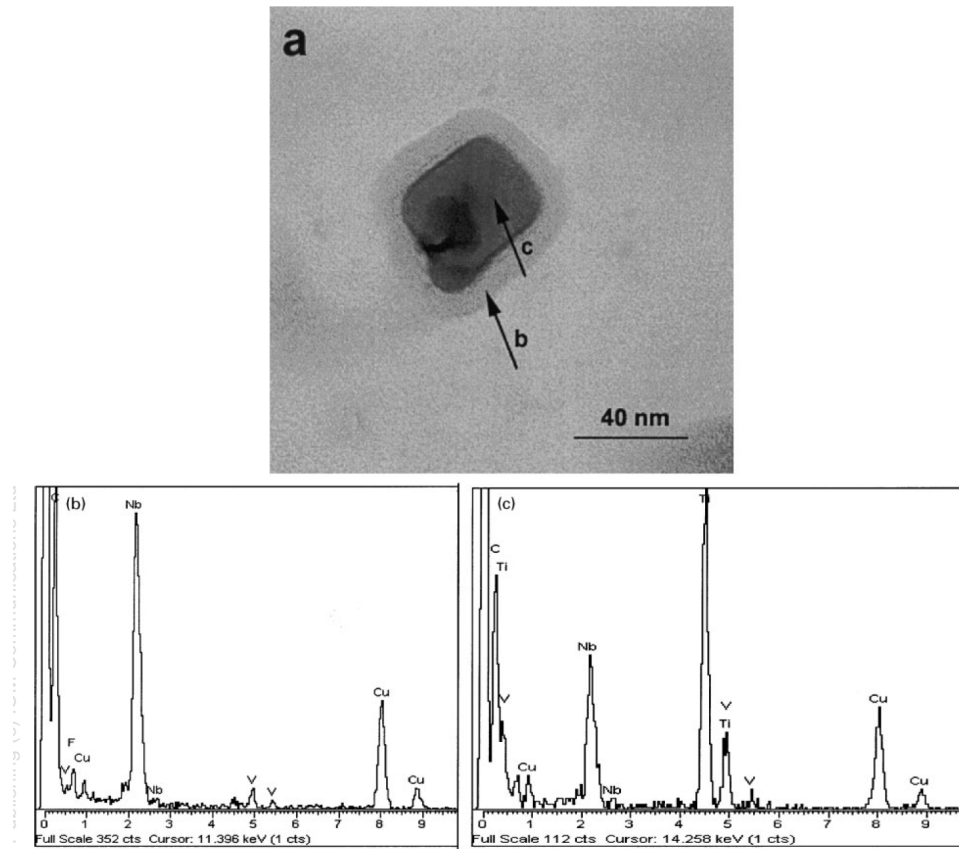


Fig. 2.19, (a) TEM micrograph of carbon extraction replica corresponding to a complex precipitate in a typical V-Nb-Ti steel, (b) and (c) EDS spectrum of shell and core of duplex precipitate, respectively [5].

The dissolution temperature of microalloying precipitates is challenging to model because it occurs over a wide range. For example, Palmiere et al.'s findings that Nb can be stable as a precipitate over dissolution temperatures calculated using published solubility data [81] are supported by Park's and Lee application of electrical resistivity techniques. They found that soaking time was a key parameter as well as temperature during the reheating stage [85].

### 2.3.2. Roughing

The rough rolling stage ("roughing") is also an important stage in the production process of AHSS steels. This stage involves a substantial deformation of austenite (generally >50% reduction) at temperatures above the non-recrystallization temperature ( $T_{nr}$ ) of austenite (Fig. 2.16).

The hot deformation for production of AHSS steels is usually short, and the extensive deformation arising during roughing is associated with the formation of micro bands and preferred crystallographic texture. The extent of deformation, deformation temperature, and interpass intervals all influence the microstructural evolution, including recrystallization and recovery behaviour of austenite.

In 1981, Akben et al. observed significant differences in rolling loads for a variety of chemical compositions of steels. They concluded that the differences in yield and flow stress were consistent with recrystallization and softening that could be directly ascribed to the solute alloying elements [27]. Understanding the interaction of microalloying elements with microstructure during roughing is important because of the widespread use of microalloying elements to control the kinetics of recrystallization and recovery.

During hot rolling many variables (dislocation density, clustering of atoms in the microstructure, overall diffusional conditions of substitutional and interstitial elements), significantly impact on the kinetics of precipitation. For example, the rolling process induces strain induced precipitation by providing more potential nucleation sites for M(C,N) resulting in austenite with a smaller grain size and higher dislocation density. As shown in Fig. 2.20, there is a considerable austenite refinement of Nb microalloyed steel by slightly decreasing the deformation temperature below approximately 1000°C, whereas Nb free steel exhibits much less refinement. It is clear that the presence of Nb inhibits the growth of grains after each deformation pass. This is believed to be due to precipitation being pinned at the boundaries at elevated temperatures resulting in sharp grain refinement [62].



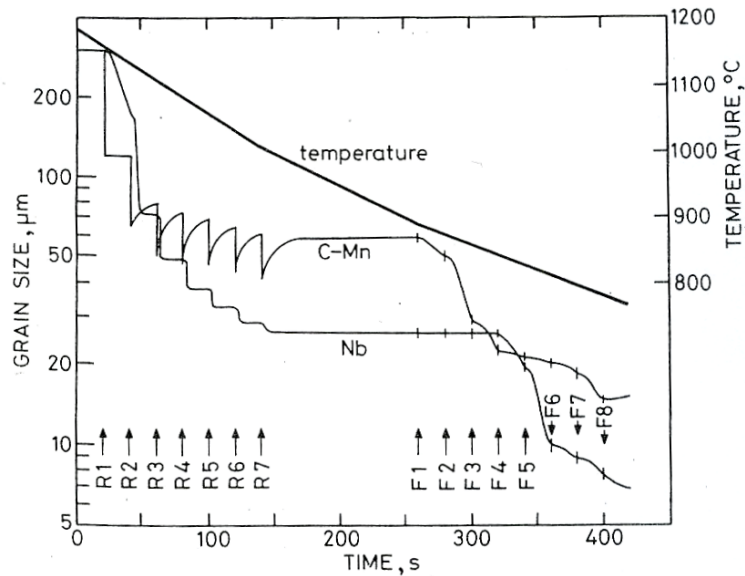


Fig. 2.20, The variation of austenite grain size during a simplified controlled rolling schedule of C-Mn and 0.04 % Nb steels [62].

The production of a very fine and uniform recrystallized structure arising from dramatic reduction at high temperatures during the recrystallization range is reported in several studies on various microalloyed steels [80].

As already reported by Valdes and Sellars [78], decreasing the reheating and roughing temperatures and increasing the roughing strain in the microalloyed steels significantly accelerates the strain induced precipitation. Jung et al. have reported the effect of straining on the precipitation of Nb-Ti-V steels under isothermal conditions. They identified a strong correlation between reheating temperature and rough strain to reach the optimum range of precipitate size. This optimum size of precipitates leads to peak strengthening in the final finishing deformation, indicating minimal recrystallization rate due to precipitation [86].

In 1980, Akben et al. examined dynamic precipitation and solute hardening in V and Nb microalloyed steel subjected to deformation at high temperatures. They showed that deformation increases the kinetics of precipitation in both Nb and V microalloyed steels, and extended their studies to multiple microalloying elements [27, 28]. From the C-curve of precipitation of Nb-Ti-V addition as a function of strain in Fig. 2.21, it can be seen that the deformation in the microstructure drastically increases the kinetics of precipitation [86]. This is exactly in agreement with other reports concerning single

addition of a microalloying element. However, the temperature of the nose of C-curve depends on the microalloying element [87]. For example, both Nb and Ti have higher nose temperatures than V. This infers that Nb and Ti additions allow the microstructure to be refined during roughing, whereas V is expected to be more efficient at lower temperatures [14, 20].

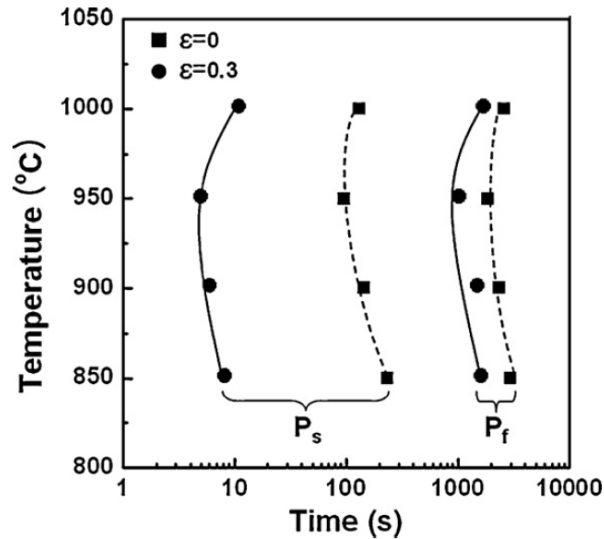


Fig. 2.21, The precipitation-time-temperature diagram of a Nb-Ti-V microalloyed steel,  $P_s$  and  $P_f$  stand for the 5% start and 95% finish times as function of strain ( $\epsilon$ ) in austenite [86].

It has been shown in the literature that the rate of Nb(C,N) precipitation at rolling temperatures over the recrystallization regime shows considerable localization. Systematic studies on microalloyed steels with a range of chemical compositions by Crooks et al. and Palmiere et al. have shown Nb supersaturation in proximity to planar crystalline defects. For example, volume fractions of Nb(C,N) precipitation at grain and subgrain boundaries is 1.5 - 2.0 times that of grain interiors. This phenomenon suggests that the recrystallization-stop temperature has been increased by a strong pinning force, inhibiting recrystallization and hardening of austenite [87, 88]. Rainforth et al.'s investigations into fully austenitic steels identified no NbC precipitation in the grain interiors at a deformation temperature of 950°C, providing desirable potential sites for strain induced precipitation during subsequent deformation at lower temperatures [22].

Katajarinne et al., reported non-uniform grain growth in Nb-Ti microalloyed steel during hot deformation. It was proposed that this could be avoided by modifying the interpass holding time and strain rates to promote repeated recrystallization and

subsequent grain growth [89]. Non-uniform grain growth of austenite in the microalloyed steel is therefore attributed to coarsened precipitates losing their effectiveness at pinning the grain boundaries [90].

Since the late 1970s, several workers have studied the influence of Mo on the retarding and coarsening of microalloying precipitates and on the evolution of microstructure, in particular, at roughing temperatures. Simultaneously adding Mo and V to Nb microalloyed steels retards the onset of recrystallization compared to single alloyed steels [28]. Mo bearing microalloyed steel showed Mo incorporation into Nb-rich carbonitrides in ferrite and very little incorporation into Nb-rich carbonitrides in austenite for the hot rolling and intercritical range. Enloe's et al. atom probe tomography (APT) studies have provided valuable data in analysing the distribution of Mo atoms in carbonitride precipitates. They found that the elements in the precipitates have an inhomogeneous distribution, with the size and morphology of precipitates affecting the retardation of coarsening [91].

### 2.3.3. Finishing

Conducting rolling at temperatures below the austenite recrystallization temperature and even within the ferrite-austenite regime (i.e. intercritical range) is known as finishing (Figs. 2.16 and 2.18). During the last 50 years considerable efforts have been made to understand the interaction between microalloying precipitation behaviour and microstructure evolution at the finishing stage, mainly by studying the mechanical properties, deformation induced precipitation, chemical composition and interpass intervals.

Gladman reported the following features of finishing [20]:

- 1- Depending upon the chemical composition and temperature range and also the amount of deformation, finishing can lead to the formation of pancaked austenite microstructure with high dislocation density. This enhances the formation of fine grain ferrite with a sub-grain structure. Fig. 2.22 shows the effect of finishing temperature on the final ferrite grain size for a given V/Nb microalloyed steel [67].

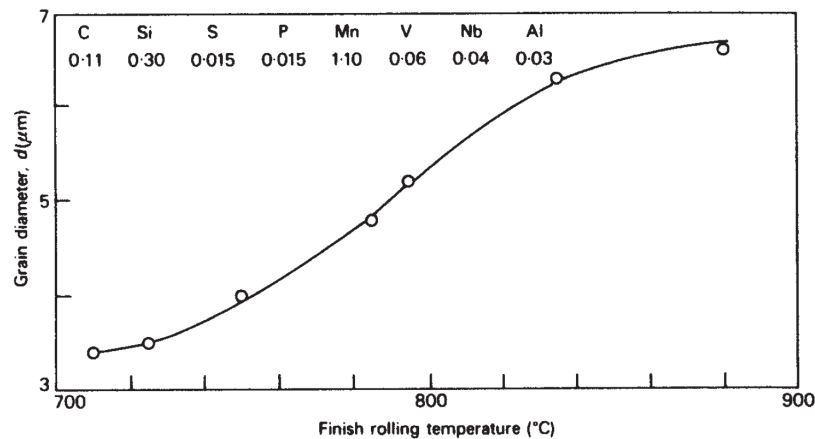


Fig. 2.22, The variation of final ferrite grain size in terms of finishing temperature for a typical microalloyed steel [67].

- 2- Deformation at this range brings about an obvious preferred orientation of the microstructure which can lead to an increase in strength, as well as influencing the texture of the ferrite and the toughness of the material.

Recent work by Vervynckt et al. have shown that the presence of small precipitates hinders the dislocation movement increasing strain hardening. Their results exhibited a reasonable evolution of precipitate size as a function of interpass intervals [92]. However, at short interpass times the small precipitates nucleate preferentially at dislocations and longer interpass times are required for growth and coarsening of precipitates. They also investigated the relationship between Zener force and recrystallization driving force in terms of interpass times, and concluded that interpass times which were too short or too long detrimentally affected control of austenite recrystallization [92].

#### 2.3.4. Run-out Table and Coiling Stage

The microstructure can still be significantly adjusted at the cooling stages below the finishing temperatures (Fig. 2.17). For example, decomposition of austenite to ferrite/pearlite and bainite occurs during the run out table and coiling stages and this can be accompanied by the formation of fine microalloyed precipitates. Formation of ferrite and bainite increases the density of carbon and nitrogen within the residual austenite, stabilizing against stress and strain induced martensite.

The direct correlation between prior austenite grain size and resultant ferrite grain size is well established in the literature, but alters in the presence of micro/alloying elements. It can be seen from Fig. 2.23, that there is a considerably more refinement of the ferrite grain size due to smaller prior austenite grain size in Nb free steel than when Nb is present [62]. Similar investigations on other microalloyed steel have also shown the interactive effect of cooling rate on the morphology of ferrite and bainite. For example, a high cooling rate from finishing stage to  $A_{r1}$  (i.e.  $25^{\circ}\text{C/s}$ ) decreases the chance of polygonal ferrite formation [93].

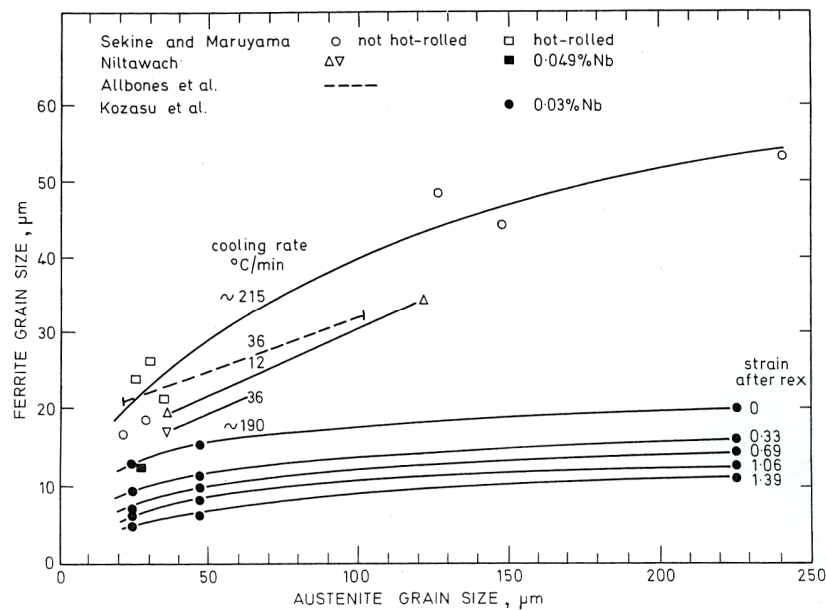


Fig. 2.23, Ferrite grain size versus prior austenite grain size illustrating the importance of austenite grain size in prediction of ferrite grain size during cooling stage [62].

Recent studies by Hinton et al. on the effect of thickness reduction in roughing for a given Nb added steel show good agreement with Sellar's overview [52, 62]. They also considered the effect of deformation on the kinetics of ferrite formation in the microstructure. Applying a double deformation at  $1050^{\circ}\text{C}$  caused an increase in the volume fraction and grain growth kinetics of ferrite at the austenite to ferrite transformation temperature range due to grain refinement of austenite and the increased grain boundary area accelerating the ferrite growth kinetics.

Liu et al.'s thermal analysis of chemical composition reported the effect of substitutional elements on the abnormal transformation of austenite to ferrite. Their

comparative studies of pure iron and alloyed steels indicated that this was due to the austenite grain size and rules out the solute drag effect of alloying elements [94].

Furuhara et al. in 2010, reported the role of Nb on the kinetics of bainite transformation in (0.15 or 0.05)C 0.2Si 1.5Mn (mass%) steel. Retardation of the proeutectoid ferrite transformation by Nb is due to the solute drag effect arising from Nb segregation at the austenite/ferrite interphase boundary [95]. They also pointed out that the interior austenite grains transform mainly to martensite with islands of bainite when cooled to room temperature (Fig. 2.24 (a) and (b)). The dark areas are clearly identifiable as martensite, bainite and retained austenite decorated by polygonal ferrite at grain boundaries. It is apparent from these micrographs that the kinetics of ferrite formation in Nb added steel is relatively low (Fig. 2.24 (c) and (d)). The presence of Nb has favoured the formation of a high volume fraction of bainite to obtain a bainitic matrix in TRIP assisted steels.

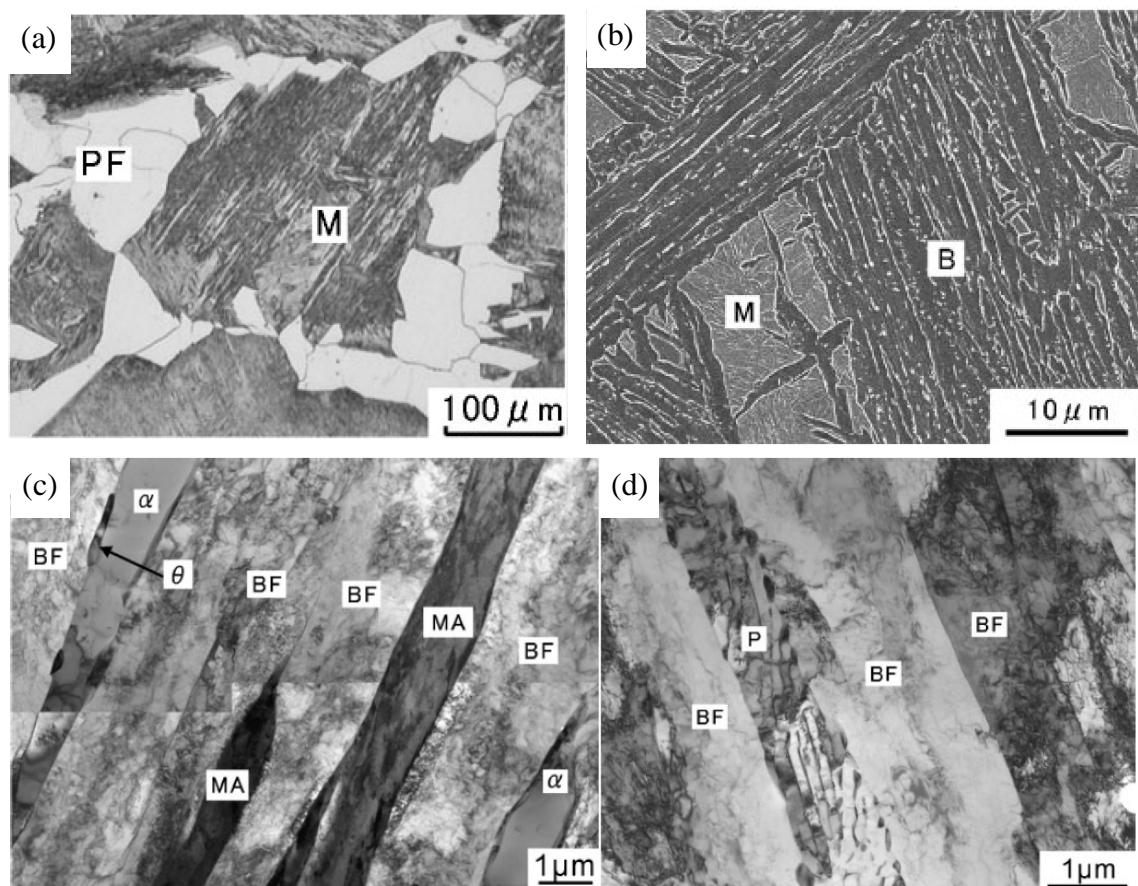


Fig. 2.24, The micrograph of austenite grain interior features after final cooling to room temperature of low carbon Nb microalloyed steel, (a) Optical micrograph, (b) SEM micrograph, (c) and (d) TEM micrographs, MA/M, martensite;  $\theta$ , cementite; BF/B, bainitic ferrite;  $\alpha$ , ferrite; P, pearlite; PF, polygonal ferrite [95].

Zarei-Hanzaki and Yue proposed that ferrite volume fraction and morphology also influence the proportion of retained austenite in bainitic TRIP assisted steels. Fig. 2.25 indicates maximum levels of volume fraction of retained austenite within allotriomorphic ferrite, irrespective of the presence of microalloying elements and better austenite retention in acicular ferrite than polygonal ferrite [40, 96].

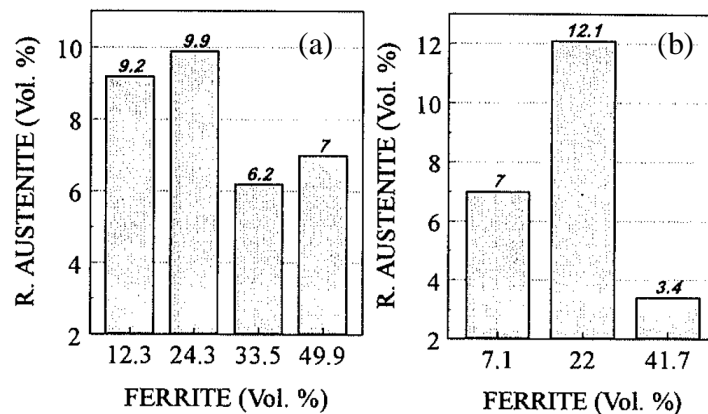


Fig. 2.25, Illustration of retained austenite volume fraction as a function of prior austenite grain size and volume fraction of allotriomorphic ferrite, (a) 70 μm and (b) 230 μm [96].

The interaction of microalloying elements with ferrite formation has been the main focus of many investigations. The precipitation of microalloying elements at the run out and coiling stage in terms of cooling rate can determine the precipitation behaviour whether they are in the form of interphase precipitates or preferentially located at dislocations inside the ferrite [97, 98].

The interphase precipitates are formed under slow cooling rates after finishing. Thus, the comparable kinetics of austenite to ferrite transformation and precipitation can determine the density and size of the precipitates [53].

#### 2.3.4.1. Bainite Transformation

Bainite is named after Edgar Bain who discovered its existence in 1930 [99]. Under different cooling conditions the decomposition of austenite to bainite evolves different morphologies - upper/lower bainite and/or a mixture of the two. Detailed studies by Ohmori et al. in 1971, provides valuable insight into this field [100]. Fig. 2.26, shows a schematic representation of the different types of bainite that can be

formed at temperatures lower than the bainite start temperature ( $B_s$ ) under different cooling rates [100, 101]. The  $B_s$  can be calculated using the empirical equation [32]:

$$B_s = 830 - 270[\% \text{C}] - 90[\% \text{Mn}] - 37[\% \text{Ni}] - 70[\% \text{Cr}] - 83[\% \text{Mo}] \quad (2.6)$$

where the elemental concentrations are in wt.%. Laboratory simulations can produce bainite morphologies under isothermal hold transformation conditions and coiling stage or galvanizing processes can produce it under industrial cooling conditions [101].

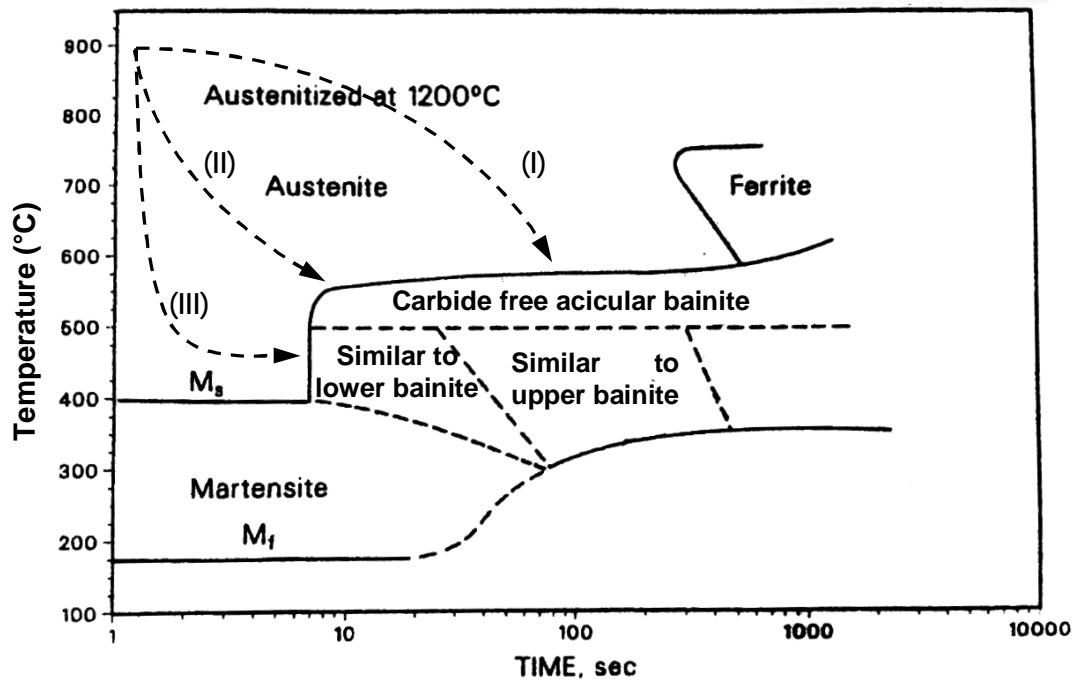


Fig. 2.26, Schematic representation of temperature versus time of bainite formed in the Cu-Ni-Cr-Mo-V steel during continuous cooling. Three paths illustrate the schematic cooling conditions for the formation of bainite with different morphologies, (I); granular bainite, (II); upper bainite, (III); lower bainite [100, 101].

A useful, detailed, and up to date review of the literature on bainite transformation in steels is provided by Fielding [102] in which the available mechanisms of bainite transformation are discussed. Two theories concerning acicular/bainitic transformation have been proposed, including reconstructive or diffusional, and displacive mechanisms. However, it is generally accepted that acicular/bainitic ferrite nucleation is associated with the diffusion of carbon. Thereafter, the growth of bainite is accompanied by a displacive transformation caused by movement of glissile interfaces until it is stopped by plastic relaxation in the adjacent



austenite. Dislocations, chemical composition, precipitation and etc can all change the kinetics of nucleation and growth in bainite [102, 103].

Investigations into the kinetics of isothermal bainite transformation were undertaken by Tomita in 1994 and Jun et al. in 2004. The evolution of isothermal bainite transformation in steels was found to depend on the proportion of retained austenite at room temperature. It has been established that the retention of austenite with different morphologies is attributed to the formation of bainitic ferrite and consequential carbon enrichment of austenite [104, 105, 106]. Similarly, Jacques et al. reported an optimum point in the amount of retained austenite as a function of isothermal bainite transformation. The trends of the three studied steels is consistent, even though the quantity of austenite depends upon chemical composition (Fig. 2.27) [60].

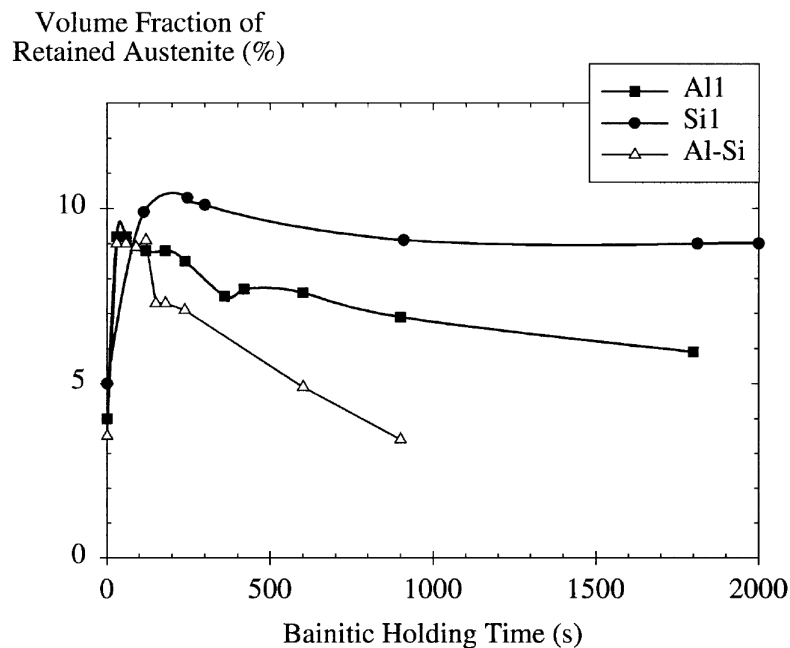


Fig. 2.27, Evolution of the volume fraction of retained austenite as function of isothermal bainite holding time at 375°C for three types of steels [60].

The dependence of austenite stability during final cooling on bainite transformation is well established. The growth of bainitic ferrite effectively partitions the carbon into untransformed austenitic regions. Fig. 2.28 shows the retained austenite with two different morphologies i.e. film shape and blocky. Lawrynowicz reported that the carbon concentration trapped between bainitic ferrite laths (i.e. film shape austenite) is much larger than blocky austenite [107]. Sugimoto et al. indicated that the bainitic

ferrite lath structure improves formability during deformation because of its uniform fine structure and lower microscopic stress concentration [54].

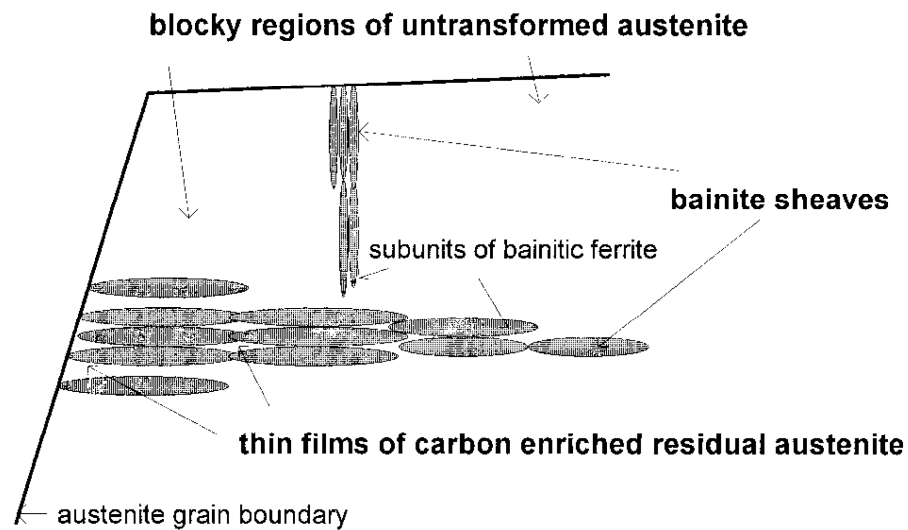


Fig. 2.28, Schematic representation of retained austenite morphology in bainitic microstructure [107].

The interaction between microalloying elements and bainite transformation has been intensely studied for some 50 years. Subject to chemical composition and thermomechanical processing in the fully austenite regime, some microalloying elements can remain in solution throughout finishing and the run out table, particularly if fast strain rates or rapid cooling are applied [53]. Experimental studies by Quidort et al. indicate that the presence of substitutional alloying elements can influence the carbon diffusivity which is able to alter the kinetics of transformation for a given steel through the solute drag effect [108].

The recovery and kinetics of bainite transformation are significantly affected by the vanadium carbonitrides,  $V(C,N)$ , preventing the recovery of the dislocation structure of bainite. [47, 64]. Few reports exist on the influence of  $Nb(C,N)$  precipitates on bainite transformation. Recent studies by Zuazo et al. show the Nb precipitates strongly retarding the softening of bainite on a typical Nb-added bainitic steel, and the formation of fine Nb precipitates after long isothermal bainite holding times, indicating very slow kinetics of precipitation [109]. This is in close agreement with findings by Rees et al., who found that increased Nb solute slightly retards bainite transformation, but  $Nb(C,N)$

precipitates in austenite markedly affect bainite formation during cooling [51]. Park et al. investigated Nb(C,N) precipitation during isothermal bainite transformation regime using electrical resistivity measurements and found that fine Nb(C,N) precipitates with diameter of less than 10 nm are mainly formed in the bainite matrix after cementite precipitation [85]. Hashimoto et al. pointed out the potential for considerable precipitation of NbMoC during cooling and coiling process [110].

### 2.3.5. Cold Rolling and Intercritical Annealing

As shown in Fig. 2.9 the microstructure of multiphase steels can also be manipulated by cold rolling and subsequent intercritical annealing, followed by austempering within the bainite temperature range. Fig. 2.29, represents a typical six stage standard intercritical annealing process, involving different heating and cooling scenarios.

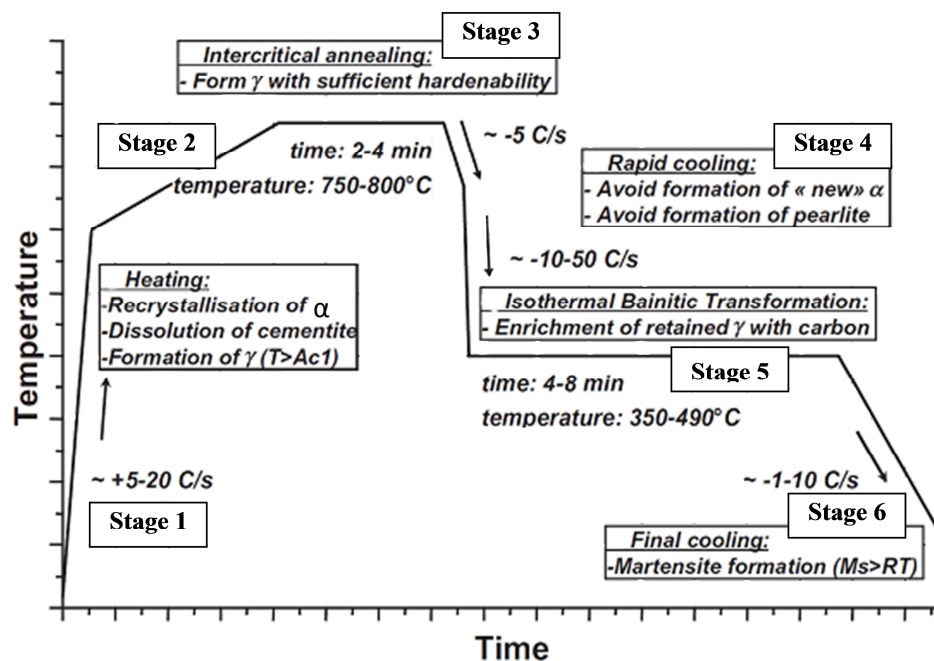


Fig. 2.29, Schematic of the intercritical annealing treatment for cold rolled AHSS steels assisted by TRIP effect. Six stages represent the effect of heating/cooling rate on the evolution of microstructure [2].

### 2.3.5.1. Stage 1- Fast Heating Up to $A_{c1}$ Range

In 1974, Matsuda and Okamura reported that the kinetics of austenite formation for low carbon boron-containing and boron-free steels strongly depends upon the initial microstructure [111]. They suggested that the mechanism of austenite formation depends on the heating rate and chemical composition. In fact, during heating up to  $A_{c1}$ , increasing the temperature causes the recrystallization and recovery of ferrite, followed by formation of austenite. Mohanty et al. recently reported on the effect of heating rate on austenite formation during both continuous heating and isothermal holding. They found that increasing the heating rate over the kinetics of recrystallization and growth of ferrite expanded the overlap of these two processes [112] and that by increasing the heating rate (e.g., 10 to 50 K/s) the  $A_{c1}$  slightly rises to higher temperatures (e.g., ~745 to ~755 °C). From the experimental results, it has been well established that the rate of austenite nucleation is enhanced by the presence of ferrite-ferrite grain boundaries. Thus, high heating rate partially suppresses the recovery, recrystallization and growth of ferrite and this facilitates the higher rate of austenite nucleation. Fig. 2.30, represents a schematic of austenite formation in terms of heating rate. It can be seen that by applying higher heating rate for a textured microstructure (i.e. cold rolled), the coarse inhomogeneous austenite is formed in the microstructure [112].

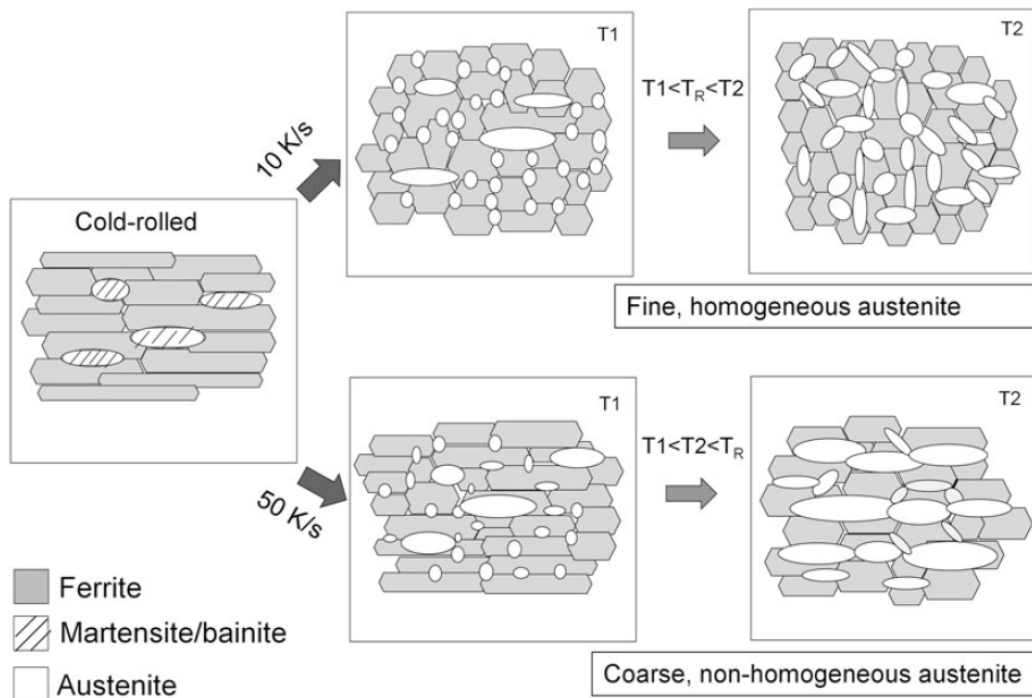


Fig. 2.30, Schematic illustration of mechanisms of austenite formation from cold rolled initial microstructure in terms of heating rate i.e. 10 and 50 K/s [112].

### 2.3.5.2. Stages 2 and 3- Slow Heating ( $T > A_{c1}$ ) and Isothermal Annealing

The standard intercritical annealing schedules proposed in the literature includes a deliberate reduction to the heating rate within the range  $A_{c1}$  - isothermal. This provides the condition for the recrystallization of ferrite and spheroidization of pearlite which can be followed by dissolution of pearlite and simultaneous formation of austenite [112, 113, 114].

A substantial work on austenite formation during intercritical annealing was reported by Speich et al. in 1981 [115]. Their investigations on the Dual Phase steels during intercritical annealing whilst using isothermal holding showed that the formation of austenite follows three main sequential stages: Very rapid growth of austenite into pearlite until the completion of pearlite dissolution, slower growth of austenite into ferrite under carbon diffusion controlled mechanism (or along ferrite grain boundaries), followed by very slow equilibration of austenite and ferrite.

Recent studies by Azizi et al. developed this approach by focusing on the cold and hot rolled plain low-carbon steels. The deformed grains due to cold rolling were found to bring about changes to the kinetics of austenite formation. The fragmented and spheroidized cementite resulting from cold rolling increased the nucleation density of austenite compared to that of hot rolled steels. The level of cold rolling and heating rate can change the morphology of austenite from randomly distributed to a banded structure [116].

Scott et al., proposed that  $V(C,N)$  precipitates can be stable in austenite during intercritical annealing provided that their radius exceeded a critical value which was higher than that needed in ferrite. The formation of austenite led to a partial dissolution of  $V(C,N)$  precipitates, potentially accompanied by increasing the mean radius of precipitates in ferrite and not coarsening. Recrystallization of ferrite facilitates further precipitation of  $V(C,N)$ . However, increasing the intercritical annealing temperature effectively coarsens the precipitates in ferrite, since the density of precipitates in austenite decreases, reducing the strengthening effect of the precipitates [31].

### **2.3.5.3. Stage 4- Rapid Cooling and Isothermal Holding Stage**

The cooling rates used in the intercritical annealing process need to be sufficiently fast to avoid any possible cementite formation arising from pearlite or upper bainite transformation. It has been shown that a slight reduction in cooling rate, even extending to short isothermal hold time under laboratory simulation conditions facilitates further carbon enrichment of austenite by the growth of newly formed ferrite [2].

### **2.3.5.4. Stage 5- Isothermal Bainite Transformation**

The process of rapid cooling up to bainite transformation, also known as austempering, was first pioneered by Bain et al. [32] and has since been further developed for application in intercritical annealing in TRIP assisted steels. This stage corresponds to transformation of austenite to bainite by isothermal hold treatment under laboratory simulation which is similar to the industrial processes of run out table/coiling. At this stage the transformation of austenite to bainite is accompanied by significant carbon enrichment of the austenite. As on a run-out table, all microstructural evolution and precipitation behaviour is controlled by bainite transformation.

### **2.3.5.5. Stage 6- Final Quenching**

Final quenching transforms austenite to martensite following quenching through the bainite range of transformation, or to acicular ferrite following slow cooling through this range. Stress induced transformation of austenite during cooling strongly depends on the shape and size of austenite grains, and on the distribution of alloying elements as well as dislocation density [35]. These factors are believed to inhibit the twinning and slip systems within the austenite and their manipulation during the final cooling stage can reduce stress induced transformation.

## Chapter 3. Experimental Procedure

The primary objective of this study was to investigate the interaction between microstructural evolution and precipitation behaviour of microalloyed TRIP assisted steels. Three steels with different chemical compositions were studied in this investigation.

As the first part of the PhD program, the effect of isothermal holding time in the temperature range for bainite transformation on the evolution of microstructure and microalloying precipitation behaviour for a given V-Ti ferritic TRIP-assisted steel was studied. Later, the effect of hot rolling on the evolution of microstructure for steels with further additions of Nb and Mo in a bainitic TRIP assisted steel was established. The samples were prepared in two main groups, firstly the intercritical annealing of cold rolled samples and secondly attempting to achieve the required microstructure applying controlled rolling. For the former, the rough rolling and cold rolling were carried out using a conventional rolling mill, whereas the fast thermal treatment unit (FTTU) of the thermomechanical compression (TMC) testing machine was used to simulate the intercritical annealing. For the second set of specimens, the controlled rolling schedule was simulated by plane strain compression tests at high temperatures using the TMC machine with subsequent fast cooling down to the temperature range of bainite formation.

A series of optical/electron microscopy, XRD analysis and mechanical testing were applied to characterize the evolution of microstructure as well as precipitation behaviour.

### 3.1. Material

The chemical compositions of the steels used in this investigation are given in Table 3.1. The amount of each element was measured at the Element Company (Sheffield, UK) using a spark optical emission spectroscopy technique (OES), where the amount of nitrogen was analyzed by a combustion/fusion technique due to poor precision of OES in detection of less than 0.02%. The studied steels were divided into two main groups. Alloy 1 was a commercial rolled ferritic TRIP assisted steel sheet supplied by Tata Steel in dimensions of 300x120x1 mm<sup>3</sup>. The key addition to the steel was the V microalloying addition, although the Ti content was also notably high. On the other hand, Alloys 2 and 3 were as-cast 15 kg ingots prepared by ArcelorMittal Metz. Alloy 3 had a similar composition to Alloy 2, but without the alloying additions of niobium and molybdenum. Alloy 3 composition was intentionally suggested in order to study the effect of Nb and Mo on the precipitation behaviour and the microstructure evolution. According to the recommended thermomechanical processing from ArcelorMittal and also the chemical composition, Alloys 2 and 3 were considered as bainitic TRIP assisted steels.

Table 3.1, Chemical composition of steels used, wt.%.

	Alloy	C	Mn	Si	Al	V	Mo	Nb	Ti	N	P	S	Ni	Fe
Commercial rolled (TATA)	1	0.20	1.52	0.38	0.31	0.12	-	-	0.0025	0.0091	0.090	<0.003	<0.01	Bal.
Laboratory cast (ArcelorMittal)	2	0.12	1.47	1.54	0.02	0.16	0.08	0.04	<0.01	0.0042	0.018	0.005	0.02	
	3	0.12	1.49	1.51	0.02	0.16	<0.01	<0.01	<0.01	0.0042	0.017	0.005	0.02	



### 3.2. Sample Preparation

Three different thermomechanical processing conditions were used to prepare the samples. The critical temperatures, including  $A_{c1}$ ,  $A_{c3}$  were calculated under equilibrium conditions from Thermo-Calc software using the TCEF6 database (Table 3.2).

Table 3.2, Equilibrium temperatures ( $^{\circ}\text{C}$ ) of transformation.

Alloy	$A_{c1}$	$A_{c3}$	$T_{\text{Cementite onset}}$
1	694	850	710
2 and 3	699	875	711

The thermomechanical compression (TMC) test machine supplied by Servotest Ltd. was used at the University of Sheffield to simulate the plane strain compression test (Fig. 3.1) [117]. In order to control the heating and cooling rates an external induction furnace equipped by controllable compressed air supply was used. This part of the TMC machine is connected to the deformation unit by the fully digitised control system, which is called fast thermal treatment unit (FTTU). The sample transfer between the FTTU and deformation unit was handled by a robot arm.

One of the most outstanding advantages of the TMC machine used in this research is the ability to control the test machine to give a constant strain rate. In fact, the velocity of the tool is controlled as a function of the instantaneous specimen thickness. In addition, the TMC machine is fully digitised and controlled by specific software designed to set up, run and record a plane strain compression test under a certain tolerance. Table 3.3 provides some practical specifications of the TMC machine.

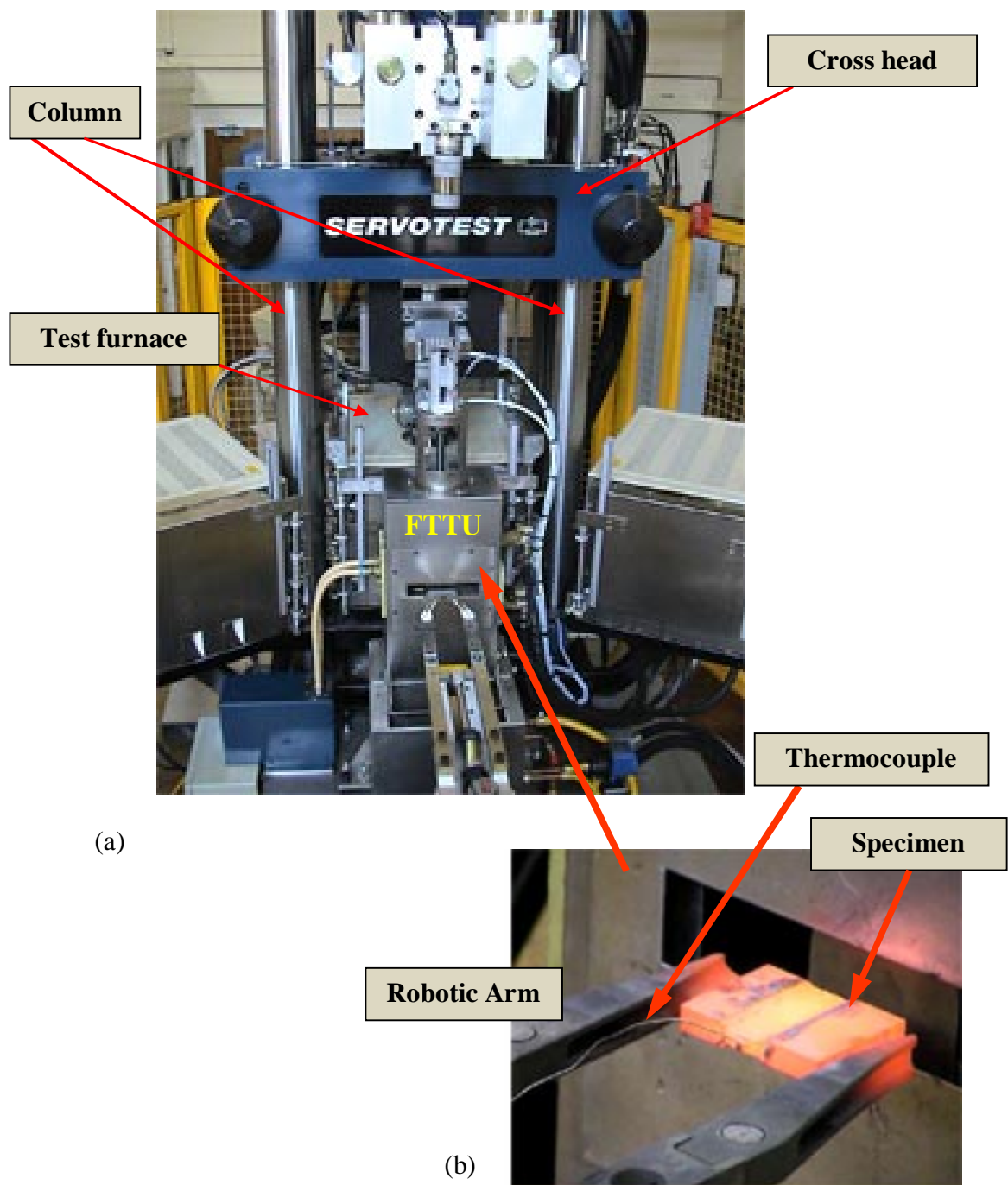


Fig. 3.1, (a) Thermomechanical compression test machine (Servotest, UK), (b) Induction furnace equipped by fast air cooling system which is called FTTU [117].

Table 3.3, The specifications of the TMC machine [117, 118].

	Machine characteristics
Maximum temperature	1250°C
Maximum cooling rate	15°C/s
Atmosphere control	Air
Maximum strain rate	150-200 s <sup>-1</sup>
Maximum load	500kN
Maximum strain	≈ 2
Quench	Air quenching / Water quenching
Cooling system	Air / Mist / Water
Temperature measurement	Up to three thermocouples in specimen

### 3.2.1. Alloy 1: Isothermal Bainite Transformation after Intercritical Annealing

During the first part of the project, the interaction between microstructural evolution and precipitation in Alloy 1 was studied. This part of PhD project was mainly focused on the isothermal bainite holding time after intercritical annealing. It is worth mentioning that the substantial work on the effect of intercritical annealing on this steel was carried out by a previous PhD student in 2009 [119], with a focus on simulating the industrial practice undertaken by Tata Steel. The current work extended this previous project to specifically look in much more detail at the bainite transformation part of the schedule.

Samples were cut from the commercial steel sheet in the dimension of 15x15x1 mm<sup>3</sup> using a conventional guillotine cutting machine. The fast thermal treatment unit (FTTU) of the TMC machine was used to simulate the schedule shown in Fig. 3.2. The heat treatment profile shown in Fig. 3.2, was similar to that suggested by Tata Steel for the heat treatment of this steel under industrial conditions. To conduct a systematic study on the bainite transformation in the final microstructure, eight different holding times at the isothermal bainite range were selected, which was followed by water quenching. Table 3.4 shows details of the heat treatment schedule.

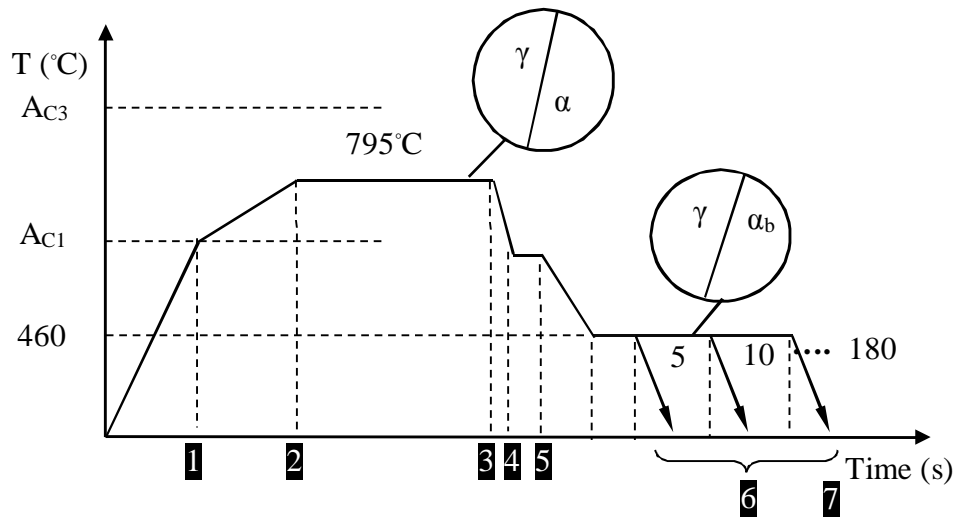


Fig. 3.2, Illustration of intercritical annealing schedule suggested by Tata Steel for the vanadium microalloyed multiphase steel with different holding times at isothermal bainite transformation temperature,  $\gamma$ ; austenite,  $\alpha$ ; : ferrite,  $\alpha_b$ ; bainite.

Table 3.4, Intercritical annealing schedule for Alloy 1; simulated by FTTU.

Stage	Temperature (°C)	Time (s)
1	695	50
2	795	90
3	795	20
4	670	10
5	670	12
5	460	34
6	460	Variable holding times, including 5, 10, 20, 30, 40, 60, 120 and 180 seconds
7	Room temperature	Water quenching

Due to relatively small sample size and the structure of the robot arms in the TMC machine, a holder was made in order to carry the sample inside the FTTU (Fig. 3.3). The temperature during heat treatment was controlled and recorded by a n-type thermocouple. The thermocouple was mechanically connected to the sample using the embedded hole inside the holder. The possible undesired overshooting of temperature and a temperature gradient inside the sample during the heat treatment was examined. Two thermocouples were simultaneously connected to the samples from the middle and end of the sample using embedded holes inside the holder. According to the monitored instantaneous temperature throughout the sample, it was found there was no significant gradient of temperature during heating and cooling stages in the sample.

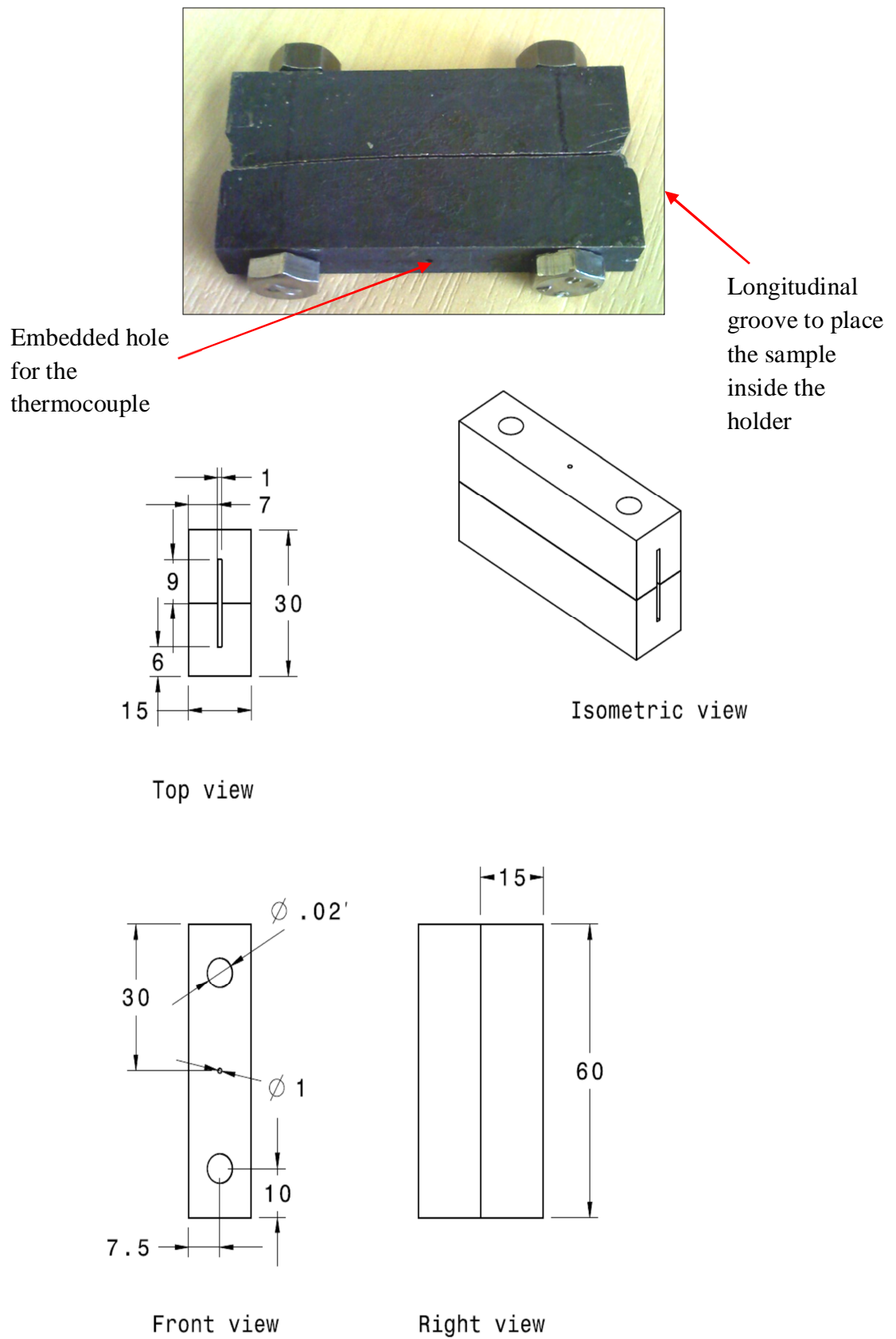


Fig. 3.3, Holder used in order to simulate the intercritical annealing followed by isothermal bainite transformation in Alloy 1 (dimensions are in mm with general tolerance:  $\pm 0.5\text{mm}$ ).

### 3.2.2. Alloys 2 and 3; Roughing, Cold Rolling and Intercritical Annealing

Before the roughing process the specimens were austenitised at high temperature for half an hour in an argon atmosphere. The soaking temperature was calculated under equilibrium conditions by the conventional equations in order to completely dissolve Nb and other microalloying elements (see equations 2.3-2.6). These calculations suggested a minimum solution temperature of 1185 °C for the Alloy 2. Therefore, the slabs with thickness of 20mm from Alloys 2 and 3 were soaked at a temperature of 1250°C for 30 minutes using a muffle furnace in an argon atmosphere (Fig. 3.6). To control the temperature of the furnace and sample two k-type thermocouples were individually used. One thermocouple was placed at the centre of furnace and another one inserted inside the slab (Fig. 3.4 (a)). The roughing (hot rolling) after austenitising was conducted using a rolling mill up to approximately 4.7mm thick plates within 7 or 5 passes (Fig. 3.5 and 3.6). The specifications concerning the rolling mill used are given in Table 3.6.

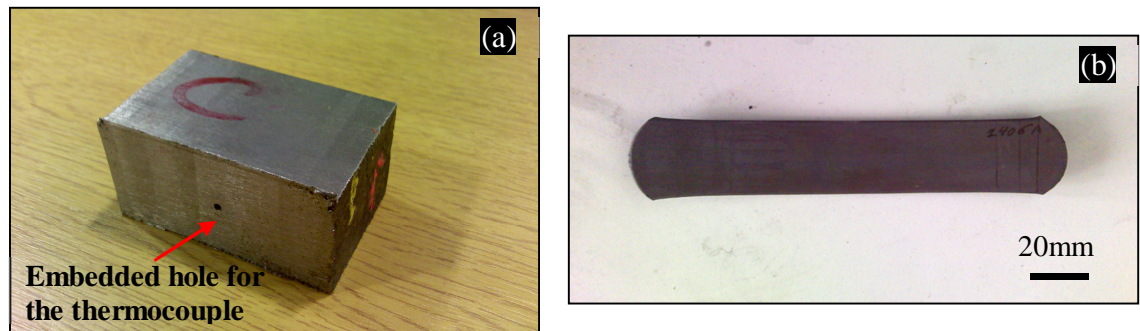


Fig. 3.4, (a) Slab used for hot rolling, (b) Hot rolled plate.

To minimize the undesirable temperature drop due to interaction between the workpiece, the rolling mill and the environment after each two or three rolling passes, the sample was returned into the furnace for around 4-5 minutes (Fig. 3.5). After hot rolling the hot rolled strips were cut using a Buehler ISOMET5000. Following this cold rolling was carried out with an average strain 0.08 for each pass for two groups of samples up to a thickness of ~3.7 mm.

The interaction between intercritical annealing and microstructural evolution were examined by applying a standard intercritical annealing schedule (Fig. 3.5). Plates with dimension of 15x15x1mm<sup>3</sup> were cut from the cold rolled specimens. The

intercritical annealing was simulated by means of the FTTU using the same holder as used for Alloy 1 (Fig. 3.3). Table 3.5 lists the details of hot/cold rolling and intercritical annealing.

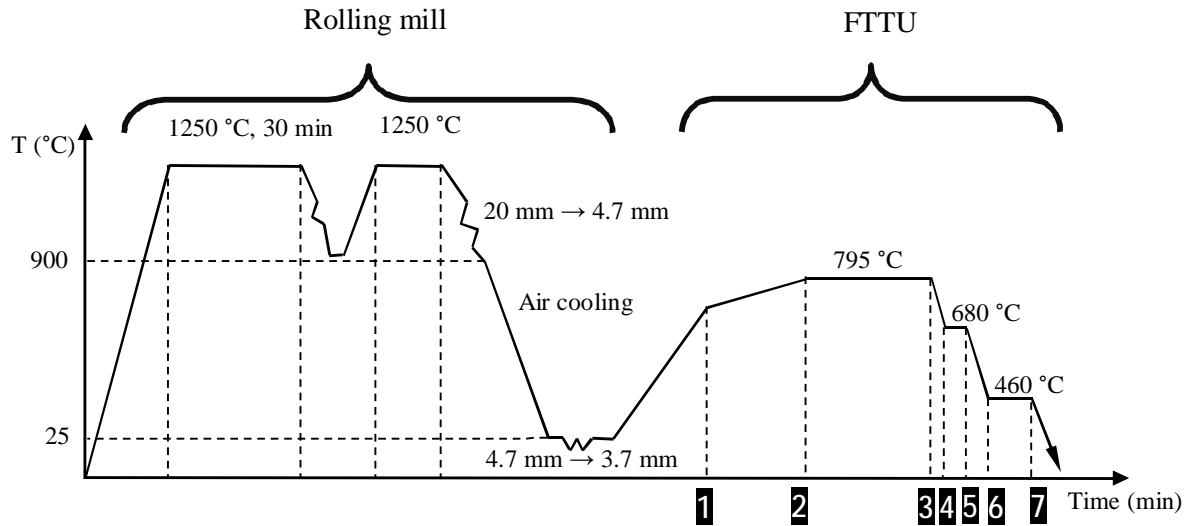


Fig. 3.5, Thermomechanical processing profile in studying Alloys 2 and 3, including roughing stage, cold rolling and intercritical annealing, followed by isothermal bainite transformation.

Table 3.5, Schedule variables of the rough rolling process followed by cold rolling and standard intercritical annealing for Alloys 2 and 3.

Stage	Temperature (°C)	Time (s)
<b>Roughing and cold rolling using rolling mill</b>		
1	1250-900	Roughing
2	Room temperature	Air cooling
3	Room temperature	Cold rolling
<b>Intercritical annealing using FTTU</b>		
1	695	50
2	795	90
3	795	20
4	680	10
5	680	12
6	460	20
7	460	10
8	Room temperature	Quenching



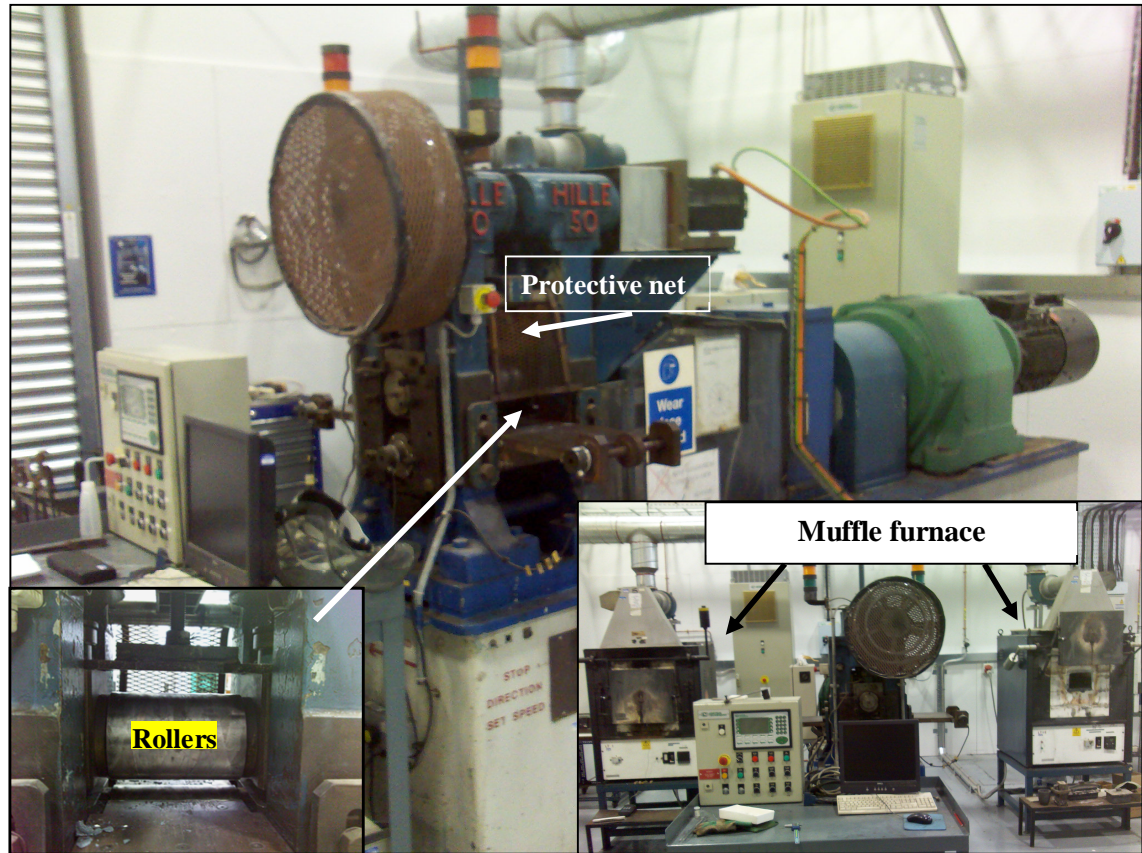


Fig. 3.6, The Hille rolling mill and muffle furnace.

Table 3.6, The characteristics of the rolling mill machine.

Width Max.(mm)	Height Max. (mm)	Diameter Max. (mm)	Speed (RPM)
120	40	136.08	20

### 3.2.3. Alloys 2 and 3; Controlled Rolling

In bainitic TRIP assisted steels, it is required that fast cooling be used after the finishing stage down to the temperature range of bainite formation, to minimize the ferrite or pearlite formation. However, the microalloying precipitation behaviour mainly occurs at the higher temperatures. Thus, it was decided to simulate controlled rolling to investigate the interaction between precipitation behaviour and microstructural evolution at high temperatures.



To simulate the thermomechanical processing with proper repeatability and reproducibility at high temperatures, three methods have been universally established, including axisymmetric compression, plane strain compression (PSC) and torsion testing [118]. Here, PSC testing was used to simulate the hot rolling condition similar to the industrial Steckel mills. Initially, the as-cast ingots of Alloys 2 and 3 were hot rolled up to  $\approx 13$ mm thickness using a rolling mill in order to minimize the segregation of alloying elements and dissolving the microalloying elements in the as-cast microstructure (Fig. 3.8). The standard specimens were machined from the rough rolled samples up to 10mm thickness.

### **3.2.3.1. Plane Strain Compression (PSC) Testing**

PSC testing is a well-established deformation testing method at high temperature in order to simulate the material behaviour during rolling under industrial condition. There has been extensive experience on this technique using different materials at the University of Sheffield over many years. This culminated in the production of a practical guide to PSC testing by Sellars et al., which gives the requirements for conducting PSC testing using a thermomechanical plane strain compression testing (TMC) machine [118].

Fig. 3.7 shows a schematic illustration of the PSC test. In a plane strain compression test the sample is deformed under compression with a load exerted by two flat tool surfaces. In this case it is important to use tools with narrow flat surfaces relative to the overall width of the specimen. This makes it possible to minimize the straining of the material in the lateral direction (i.e. retaining plane strain). Straining in one plane constrains the deformation of the specimen to two planes, i.e. the vertical plane, due to direction of tool motion, and the horizontal plane in the direction along the length of the specimen. This is similar to that which occurs in strip rolling. In the present study, the tools used to deform the specimens were flat and rectangular with 15mm in width and 100mm in breadth with a relatively smooth surface.

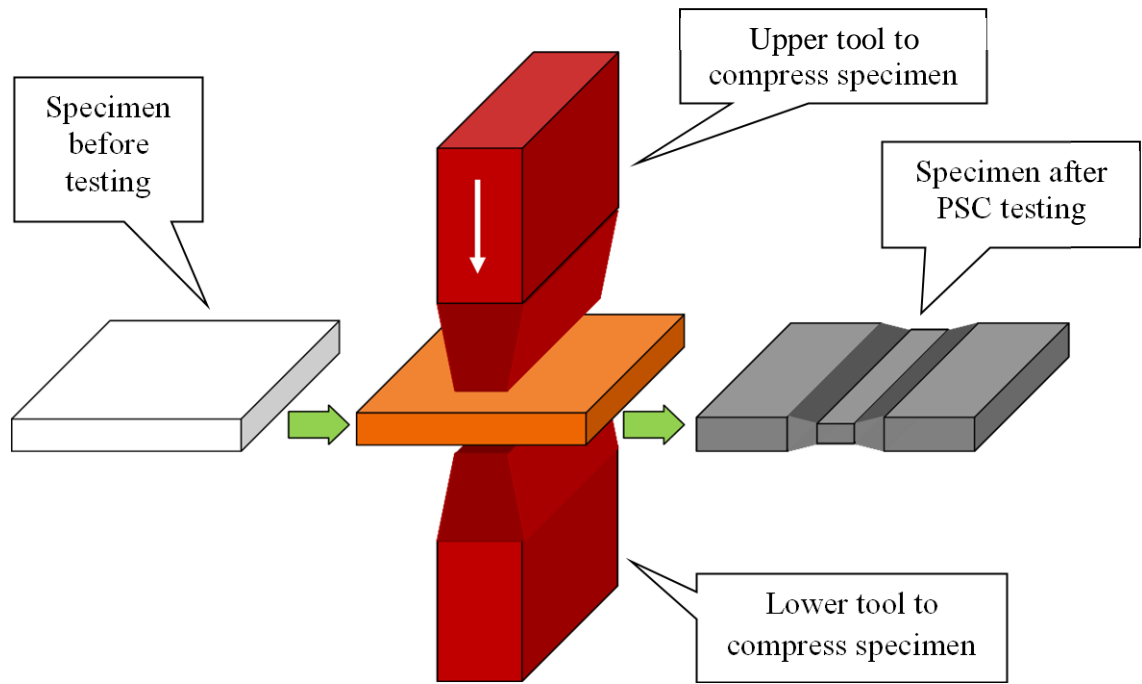


Fig. 3.7, Illustration of plane strain compression test.

Fig. 3.8 shows three different thermomechanical test conditions used at this stage. Five minutes soaking at 1250°C was conducted before PSC testing to obtain a similar initial structure in all samples, aiming at dissolving the precipitates. Moreover, since the quenched stage could not occur inside the deformation furnace, a short delay of approximately one second between the finishing stage and quenching was considered. Three deformation stages were selected at different temperatures with finish rolling at 830°C. In the second schedule the specimen was held for 50 seconds at 900°C to investigate the effect of precipitation behaviour at high temperature on the microstructural evolution for two different microalloyed steels. The precipitation behaviour at high temperature was studied by quenching the sample after the finishing stage. All three deformations were carried out at a strain rate of 10 s<sup>-1</sup>. The selection of the critical temperatures and holding times after finishing stage were those recommended by ArcelorMittal Company.

As can be seen from Fig. 3.8, the interaction of precipitation behaviour and microstructure evolution at high temperatures was investigated by applying 50s holding time at 900 °C. To subtract the effect of microstructural evolution at lower temperatures a pair of specimens were prepared by quenching after the final deformation stage i.e. 830 °C (Fig. 3.8 (c)).

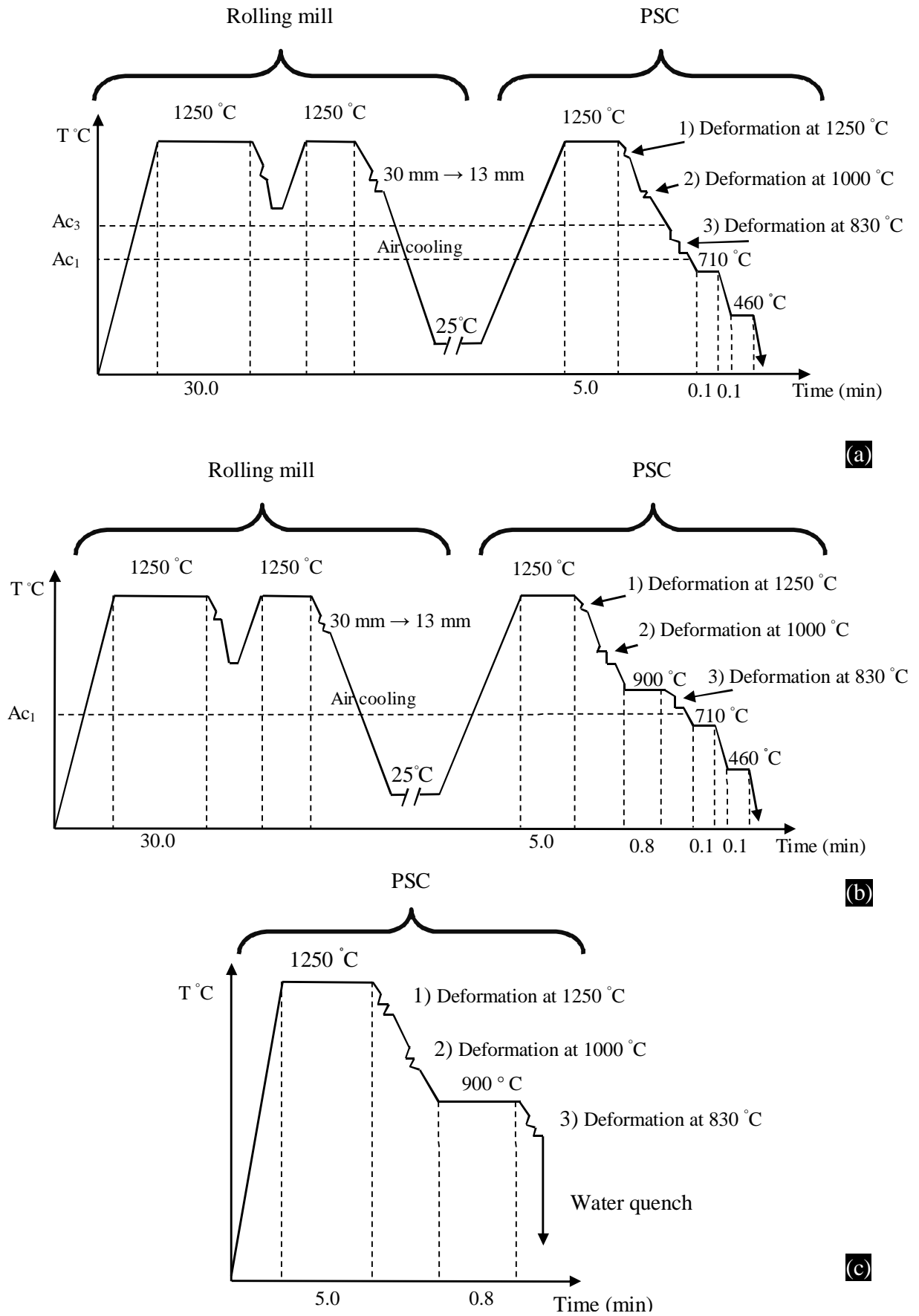


Fig. 3.8, Illustration of thermomechanical schedules which were simulated by PSC machine, (a) Hot rolling, (b) Controlled rolling, (c) Water quenched after finishing, ( $\dot{\epsilon}=10\text{s}^{-1}$ ).

Table 3.7, Hot rolling and controlled rolling schedules for Alloys 2 and 3; simulated by TMC machine.

Stage	Temperature (°C)	Time (s)
<b>Rough rolling using rolling mill</b>		
1	1250	Rough heating
2	25	Air cooling
<b>Hot rolling using PSC</b>		
1	1250	120
2	1250	300
3	1250	Deformation ( $\varepsilon = 20\%$ )
4	1000	17
5	1000	Deformation ( $\varepsilon = 20\%$ )
6	900	10
7*	900	50
8	830	10
9	830	Deformation ( $\varepsilon = 20\%$ )
10	710	10
11	710	10
12	460	20
13	460	10
14	25	Water quenching
* Holding time to control the precipitation (see Fig 3.8 (b))		

To control and record the temperature within the test, an n-type thermocouple was used. The thermocouple was inserted into the predrilled hole in the sample. Fig. 3.9 shows the standard specimen used in this research for PSC testing. Before testing the dimensions shown in Fig. 3.10 (a) were measured accurately with two or three decimal places (mm). As shown in Fig. 3.10 (b), after deformation the dimensions of the deformed area were measured.

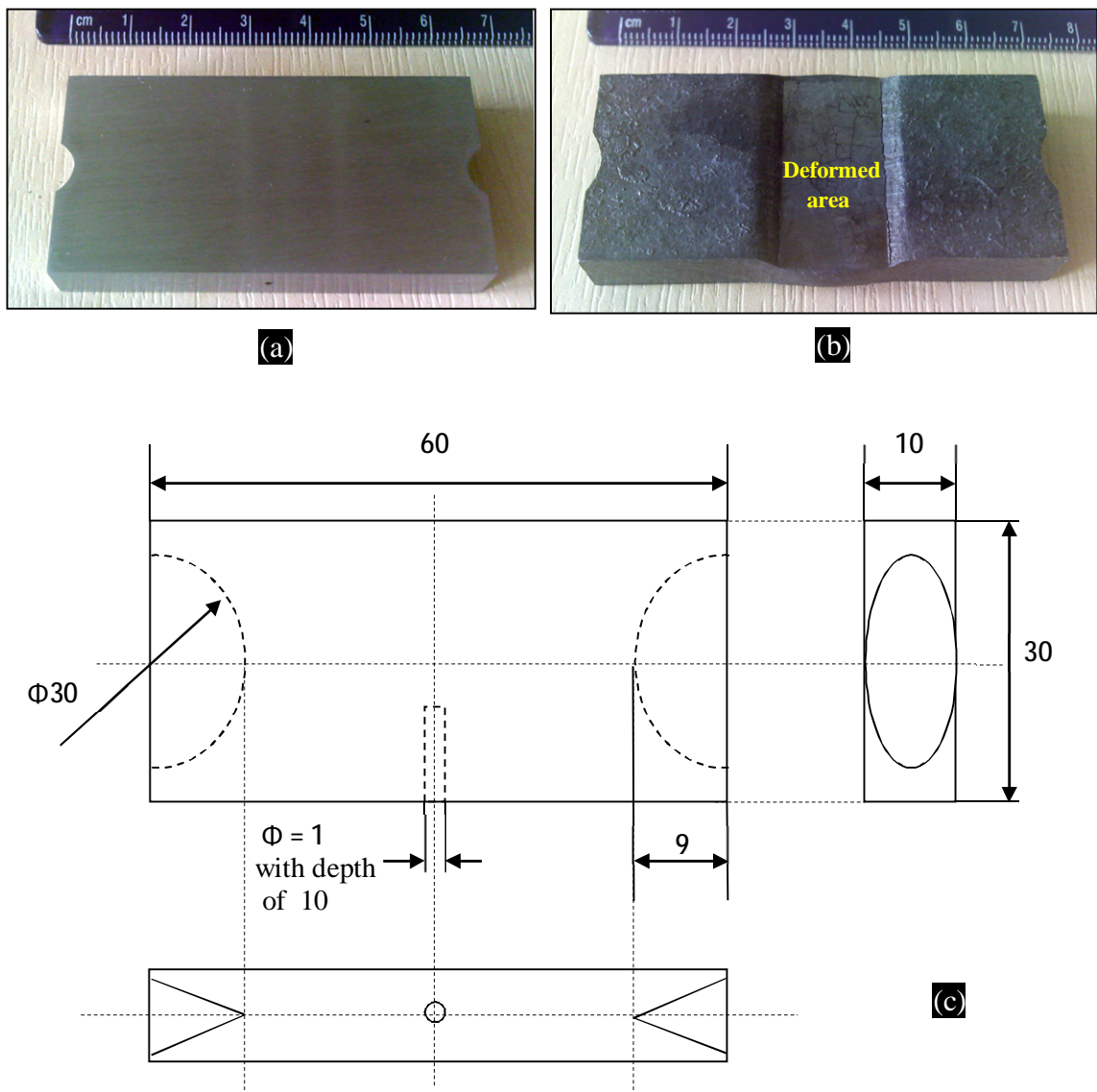


Fig. 3.9, Typical PSC standard specimen, (a) and (b) Pre and post deformation, respectively, (c) Sketch of PSC standard specimen with relevant dimensions (mm).

The specimen was transferred inside the FTTU and deformation unit by the robot arm as part of the TMC machine. Before the robot arm moved forward into the deformation furnace, the heat treatment was conducted in the FTTU. At certain predefined temperatures the robot arm moved the specimen inside the deformation unit automatically according to the heat treatment programme and then it was immediately returned to the FTTU for controlling the heat treatment.

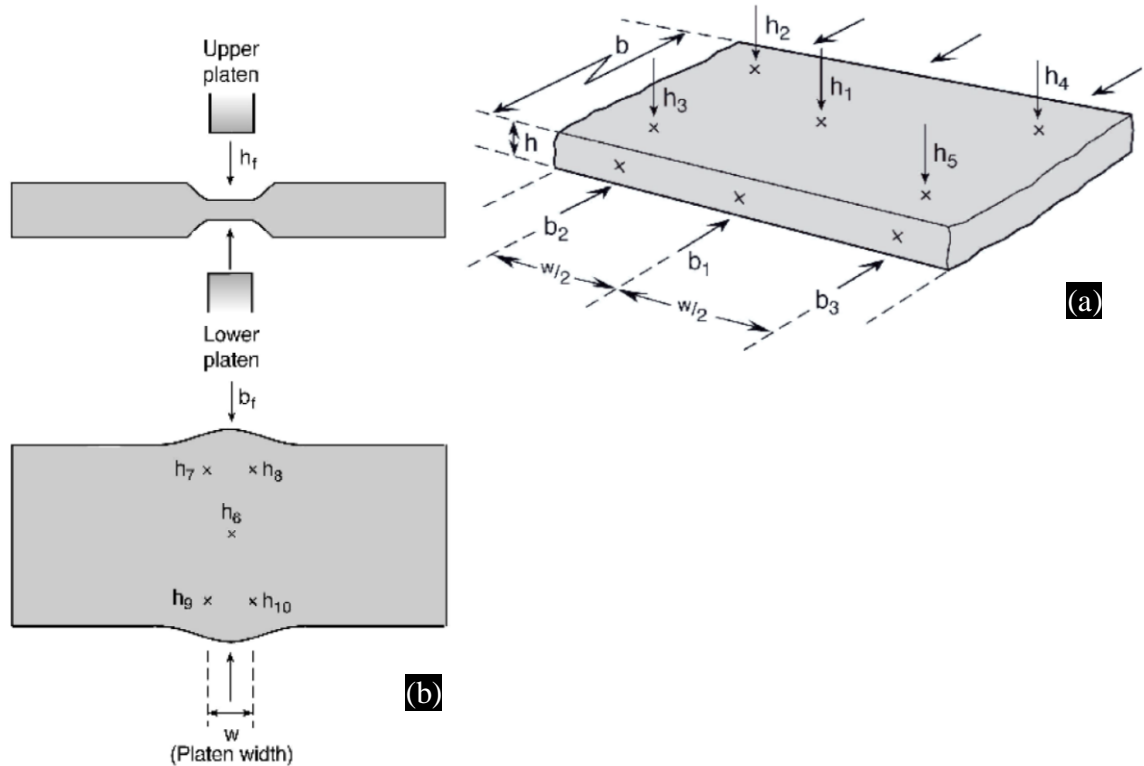


Fig. 3.10, Schematic illustration of critical dimensional points for measurement in PSC specimen, (a) Before deformation, (b) After plane strain compression test [118].

Initial trials showed that during the first pass the lubrication was lost. Clearly, loss of the lubricant changes the frictional conditions between tools and specimen. In order to avoid changes in friction and therefore interpretation of the flow stress, it was therefore decided to use the specimens without lubricant.

### 3.2.3.2. The Analysis and Correction of the PSC Data

To analyze the deformation behaviour, the obtained data was recorded and transferred into a MUS file. Five groups of data were recorded automatically by the computer connected to the TMC machine at a frequency on the intermediate speed logger of 10 kHz, including time (s), ram displacement from the zero point between the tools (mm), the load applied by the load cell (kN), the command displacement signal as velocity of the top tool (mm/s) and the specimen temperature (°C).

To plot the stress-strain curves from the hot plane strain compression test, it is necessary to take into consideration the instrumental and thermal conditions as well as sample properties. The data obtained from the machine and dimensional measurements were transferred to the spreadsheet. In this case, the corrections and analysis were carried out based on suggested methodology in the “Measurement Good Practice Guide No.27”, as described in Appendix A [118].

### 3.3. Characterization Techniques

The microstructure of the prepared samples was characterized by means of X-Ray diffraction (XRD), optical and electron microscopy and mechanical testing. The cold and hot rolled specimens were cut in either longitudinal or transverse direction using Buehler ISOMET5000, where the deformed PSC specimen was sectioned from the longitudinal direction, as shown in Fig. 3.11. The post preparation was carried out in terms of testing technique used, as describe in the following sections.

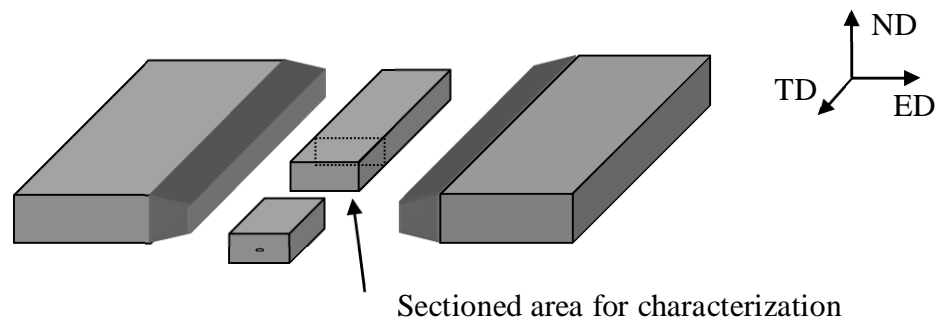


Fig 3.11, Illustration of sectioned area from the deformed PSC sample for characterization.

#### 3.3.1. X-Ray Diffraction Analysis (XRD)

The quantitative identification of phases and the volume fraction of phases after thermomechanical treatment were determined by XRD using a D5000 Siemens with Co  $K\alpha$  radiation without primary beam monochromator. The observed diffraction peaks were corrected by splitting the peaks diffracted by Co  $k\alpha$  1 ( $\lambda=1.78897$  Å) and Co  $k\alpha$  2 ( $\lambda=1.79285$  Å) radiation and the tube operating conditions of 40 kV and 30 mA. Table 3.8 gives some more details about the parameters of the XRD machine used. In order to

minimise the random characters which mostly result from preferential crystal orientations and the presence of carbides the Miller's method was applied [120]. The sample was rotated at 15 rpm and tilted from 40 to 130 degree with a scanning rate 0.1 ( $^{\circ}/\text{min}$ ) and step size 0.02  $^{\circ}$  for all samples. After polishing the sample was etched and subsequently polished again in order to minimize the effect of residual stresses on the surface, resulting from preparation by grinding.

Table 3.8, Specifications of the XRD machine; D5000 Siemens.

Filter	None
Divergence slit	1.0 $^{\circ}$
Anti-Scatter slit	1.0 $^{\circ}$
Receiving slit	0.2 $^{\circ}$
Soller slits	On secondary beam side only
Monochromators	Secondary to reduce fluorescence and background noise

The pattern was calibrated using a diffraction pattern of silicon standard sample (Aldrich, Si powder -325 mesh, 99%). Then using the Rietveld method pattern refinement was carried out by the Topas Academic package software V4.1 based on the least-square method in order to minimize the difference between experimental and simulated profile [121]. This approach was obtained considering a series of influential parameters which are attributed to the instrumental parameters and the sample.

The X-ray diffraction patterns for samples before and after heat treatments were indexed by Joint Committee on Powder Diffraction Standard (JCPDS) cards relevant to IM3-M and FM-3M space groups of ferrite and austenite respectively [122]. The volume fraction of retained austenite was determined via XRD according to the ASTM E 975-84 method. All the diffraction lines took into account for Rietveld refinement in order to minimize the effect of biasing in the results due to any instrumental parameters, preferential orientation and overlapping of peaks in (111) austenite and (110) ferrite. The volume fraction of retained austenite based on each combination of peaks was calculated by software using the following equations [123].



$$V_{\gamma} = \frac{\frac{1}{q} \sum_{j=1}^q I_{\gamma j} / R_{\gamma j}}{\frac{1}{p} \sum_{i=1}^p I_{\alpha i} / R_{\alpha i} + \frac{1}{q} \sum_{j=1}^q I_{\gamma j} / R_{\gamma j}} \quad (3.1)$$

where  $I$  is the integrated intensity and  $R$  is the calculated theoretical intensity for the ferrite and austenite peaks.

The diffraction pattern was simulated by applying a series of parameters, including unit cell, peak shape function, background correction, zero shift and profile parameters ( $U$ ,  $V$  and  $W$ ). The quality and accuracy of the simulation in terms of the quantitative outputs e.g. lattice parameter, volume fraction of phases were monitored using the numerical value of goodness of fit (GOF) which is obtained from the weighted residual error ( $R_{wp}$ ) and expected error ( $R_{exp}$ ). Preferred orientation due to microstructural evolution during thermomechanical processing was corrected based on both spherical harmonics according to the Jarvinen and March technique for each peak selectively. The retained austenite lattice parameter was calculated from the extrapolation method of Nelson and Riley [124].

### 3.3.2. Optical Microscopy and Quantitative Metallography

The specimens after each step, including hot/cold rolling scenarios and heat treatment were ground and polished according to the standard techniques. The etching procedure proposed by [125] was applied to the specimens for light optical and scanning electron microscopes. The etching was a two-step procedure that consisted of etching and drying. The etching in a solution of 2% Nital was carried out with variable holding times which is a function of chemical composition and microstructure (approximately between 5 to 20 seconds).

To observe the prior austenite grain boundaries in fully martensite microstructure the polished samples were etched with saturated aqueous picric acid at 65-75°C for 2min holding time. After etching, the samples were swabbed using isopropanol alcohol and then dried immediately [78, 125].

In order to have a better understanding about the effect of grain size in three-dimensional scale, the optical microscopy and SEM observations were performed in normal and rolling directions. The grain size of ferrite and austenite as the main characteristic phase measured by the intercept method according to ASTM E112 at different working magnifications using Buehler OmniMet 9.5 software.

### **3.3.3. Scanning Electron Microscopy (SEM)**

After optical microscopy, the small features were observed by the secondary electron imaging that was examined using a field emission gun (Inspect F, FEI Company) scanning electron microscope (SEM) operating at 20 and 10 kV. The possible electron charging on the sample was reduced as much as possible using carbon conductive tabs besides conductive paints. The energy dispersive X-ray spectroscopy (EDS) was also applied to micro-analyze the small features similar to precipitates.

### **3.3.4. Transmission Electron Microscopy (TEM)**

Observation of small features with higher resolution was undertaken by transmission electron microscopy (TEM) on a variety of microscopes including Philips EM420 at 120kV, FEI TECNAI 20 at 200kV and Jeol 2010F field emission gun at 200kV. Both extraction carbon replica and thin foil samples were examined with spot size 6 or 7 by EDS detector for microanalysis. X-ray spectra were recorded at a specimen tilt of certain angle with counting times in excess of 100s. The EDS spectrum was collected and indexed using “TEM Quant Materials” software version 3.34. Further identification of very small features or distinction among phases and other features was performed using dark field imaging, which was supported by selected area electron diffraction pattern (SAED) and EDS techniques.

Indexing the SAED was carried out using the standard JCPDS cards relevant to each space group by the package of “CrystalMaker” softwares [126]. The measurements of precipitate radius and SAED indexing were carried out after calibrating the microscope using the standard samples.

### 3.3.4.1. Carbon Extraction Replica

Precipitation behavior was studied using carbon extraction replication. Initially samples were hot mounted in standard bakelite. After standard polishing and etching by 2% Nital etchant, the mounted samples were coated by carbon using a Speedivac coating unit (Model 12E6/1598). Around the edge of sample, between the bakelite and some over parts of the sample that the carbon coating does not need to be removed was varnished by brush Lacomit. Then, the carbon coated samples were scored into 2 square grids manually. To remove the carbon extraction replicas, the sample was dipped into 10% nital until the bubble started to form under the square grids. Afterwards samples were removed carefully from the solution by tongs and immediately immersed in the methanol. Copper grids (400 mesh) were used to support the carbon replicas (Fig. 3.12) [127].

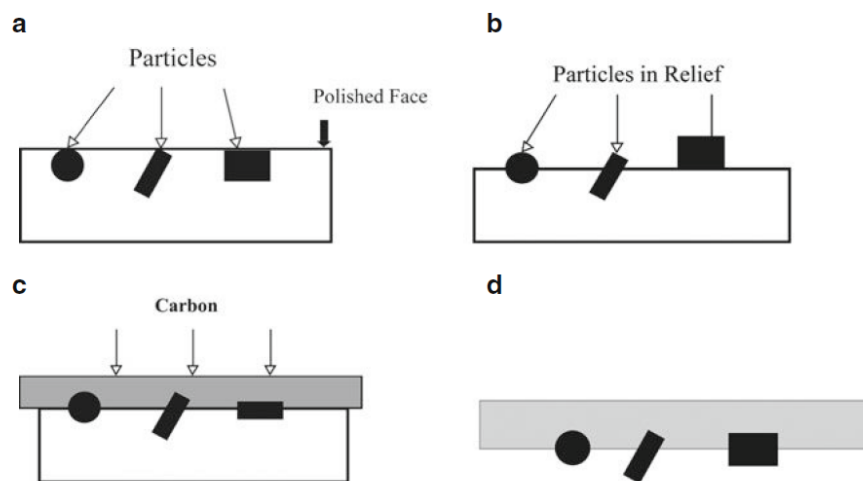


Fig. 3.12, Carbon extraction replication, (a) particles embedded in the microstructure, (b) revealing the particles in the microstructure by etching, (c) coating the surface by a thin amorphous carbon film, (d) extracting the particles adhering to the carbon film [127].

Despite the limitations of the carbon extraction replica technique, it is widely used to investigate the statistical analysis on volume fractions and distribution frequency of microalloying precipitates [128]. However, to increase the accuracy of results the carbon extraction replication was repeated two times for each sample.

#### **3.3.4.2. Thin Foil Sample**

Disk specimens of 3mm diameter were thinned to around 70  $\mu\text{m}$  by an extremely low speed grinding method on 1200-grade silicon carbide paper. The disks were then thinned to perforation using electrochemical jet-polishing in a Metalthin jet electropolisher, by an electrolyte of 5 vol% perchloric, 35 vol% butoxyethanol and 60 vol% methanol solution acid. The optimum conditions for polishing with regard to the age of solution and the type of sample were achieved at about - 40°C and 30V. The foils after perforation were immediately cleaned and stored in methanol.

#### **3.3.4.3. Electron Energy Loss Spectroscopy (EELS)**

The presence of nitrogen and carbon in identified precipitates was determined by the electron energy loss spectroscopy (EELS) measurements. The EELS was performed by a JEOL 2010F field emission gun transmission electron microscope operating at 200kV equipped with a Gatan GIF. EELS spectra were acquired on the carbon extraction replicas, which had been previously examined by the conventional TEM work using an FEI Tecnai 20. The precipitates in terms of their size and morphology were randomly selected for the EELS analysis. Initially, heavy elements such as Fe, Nb and Mo were identified by an EDS fitted to the JEOL2010F. Quantitative determination of the carbon content of a precipitate due to spurious carbon signal from the carbon replica was impossible. Thus, the comparison between nitrogen and carbon ratio was just qualitatively analyzed by studying the selected energy edges using 'DigitalMicrograph' software.

#### **3.3.5. Vickers Hardness and Microhardness Testing**

For a better understanding concerning the kinetics of transformation in the material, the mechanical properties were evaluated by hardness measurements. Depending on the size of features in the microstructure the Vickers hardness and microhardness measurements were carried out according to ASTM E 92-82 and E 384-99 respectively. The Universal hardness and Mitutoyo testers with two different loadings of 10 kg and 10-1000g were used for Vickers hardness and microhardness testing respectively. The imposed loading consisted of one stage with 20s holding time

before unloading. Average hardness/microhardness was determined from at least ten measurements per sample. The size of indentations was measured from the optical microscopy micrograph by ImageJ software. Based on the average size of diagonal length of indentation the hardness was measured according to the following formula:

$$HV = \frac{2000 P \sin(\theta / 2)}{d^2} = \frac{1854.4 P}{d^2} \quad (3.2)$$

where P is the applied load in g,  $\theta$  stands for the face angle of the diamond indenter (i.e. in general  $136^\circ \pm 30 \text{ min}$ ) and d is the mean diagonal of impression in  $\mu\text{m}$ . Some limitations of hardness testing in studying of these steels can be summarized mainly in the effect of heterogeneous distribution of secondary phases and grain size in the microstructure.

### 3.3.6. Tensile Testing

A Zwick/Roell testing machine was used for tensile testing with strain rate of 0.05 mm/mm/min. Elongation was recorded by means of a non-contact, high resolution videoXtens extensometer. The sub-size dog bone samples were prepared according to ASTM E8/E8M and then they were heat treated according to the schedule shown in Fig. 3.2 with three different isothermal bainite holding times, including 5, 40 and 180 seconds. The heat treatment was carried out by the FTTU. With regard to the shape and size of specimens a special holder was made to transfer the sample inside the FTTU furnace, as shown in Fig. 3.13. The test was repeated two times in order to make sure about the repeatability of tensile behaviour.

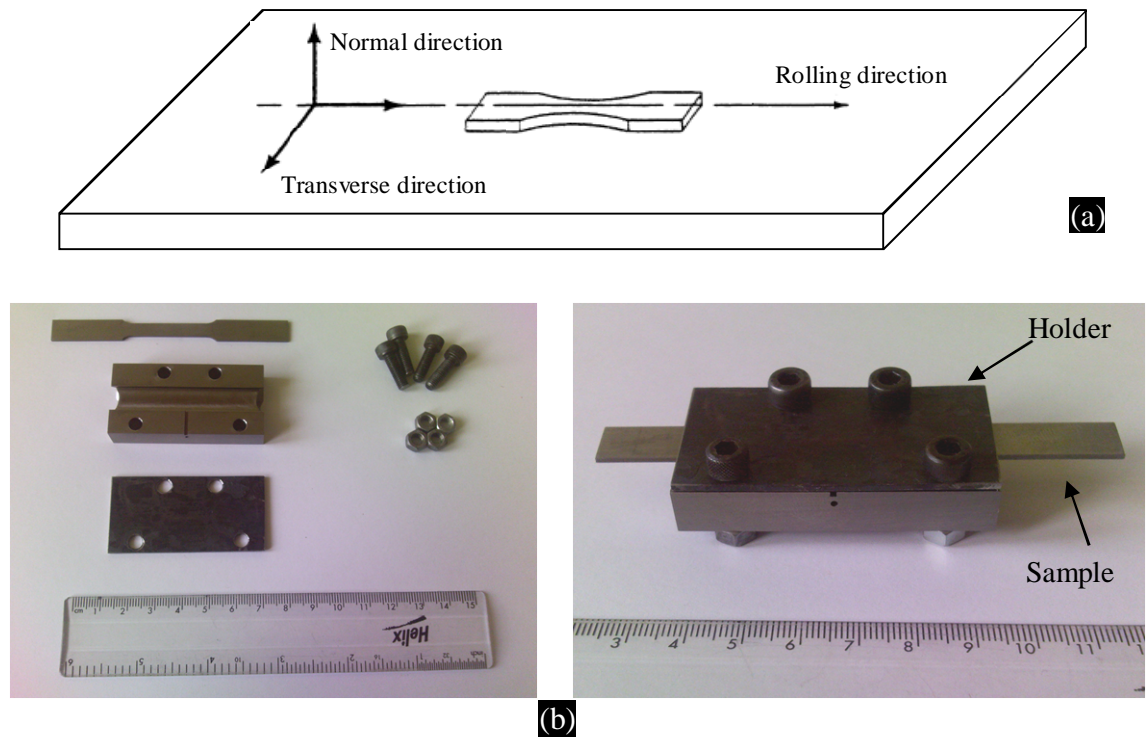


Fig. 3.13, Dog bone shape standard sample for the tensile testing, (a) The selected direction for the sample preparation, (b) Sub size sample dimensions according ASTM E8/E8M and illustration of sample holder used to heat treat the sample by FTTU.

# **Chapter 4. Results and Discussion: Alloy 1; Intercritical Annealing**

## **4.1. Introduction**

The formation of high strength martensite or bainite and precipitation derived from microalloying within a soft and ductile ferritic or austenitic matrix gives high ductility and high strength properties to advanced high strength (AHSS) steels. The presence of retained austenite in AHSS leads to a marked improvement in its mechanical properties.

So far, much research has been reported in the literature to characterize the interaction between phase transformation and precipitation behavior during thermomechanical processing of transformation induced plasticity (TRIP) assisted steels with a polygonal ferrite matrix [40, 41]. The high ductility of these steels is derived from the TRIP effect which is created by the retained austenite. It is well established that the morphology of the retained austenite influences the mechanical properties of these steels. The formation and retention of the austenite with different morphologies is a function of bainite transformation and precipitation behavior. To date, three generations of TRIP assisted steels have been introduced, classified according to their matrix structure as polygonal ferrite, bainitic ferrite and martensite [3].

Within the polygonal ferrite matrix the retained austenite is generally achieved by intercritical annealing after cold rolling, followed by slow cooling to a temperature that allows isothermal bainite transformation. Industrially, this slow cooling usually coincides with the hot dip galvanising treatment, but it is also easily simulated in the laboratory. During the bainite transformation, the retained austenite becomes enriched with carbon.

Precipitation in microalloyed steels is extensive during intercritical annealing [31, 41], but precipitation of microalloyed carbides does not occur during the bainite transformation [85, 109]. Bainite transformation is limited to the blocks of austenite formed along the ferrite grain boundaries. The size, shape and composition of the retained austenite dominate the TRIP effect, and these are strongly influenced by both

isothermal bainite holding time and microalloying elements. Thus, a systematic study was carried out to investigate the interaction between the progress of bainite transformation and the evolution of microstructure.

## **4.2. Results**

### **4.2.1. Microstructural Characterizations**

The evolution of microstructure was characterized using optical and electron microscopy, XRD and mechanical testing. Fig. 4.1 shows the microstructure of the steel before intercritical annealing at different length scales. The microstructure was dominated by the presence of polygonal ferrite and pearlite as the secondary constituent. The microstructure shows a considerable preferential orientation along the rolling direction. The SEM micrograph of the microstructure in the rolling direction plane shows the distribution of pearlite. The TEM micrographs confirmed the classic structure of the pearlite.

After intercritical annealing a considerable difference appeared in the microstructure. Recrystallization of the ferrite had occurred and new phases had formed, particularly at the ferrite grain boundaries (Fig. 4.2). The areas with the brightest contrast and with a smooth surface indicate retained austenite and martensite, whereas the bright comb shape substructure with a sheave and/or block shape indicate bainite.

Fig. 4.3 shows the variation of ferrite grain size as a function of isothermal bainite transformation time. There appears to be no significant variation in the grain size, as expected. The slight variation that was observed results from the heterogeneous distribution of ferrite grains throughout the microstructure.



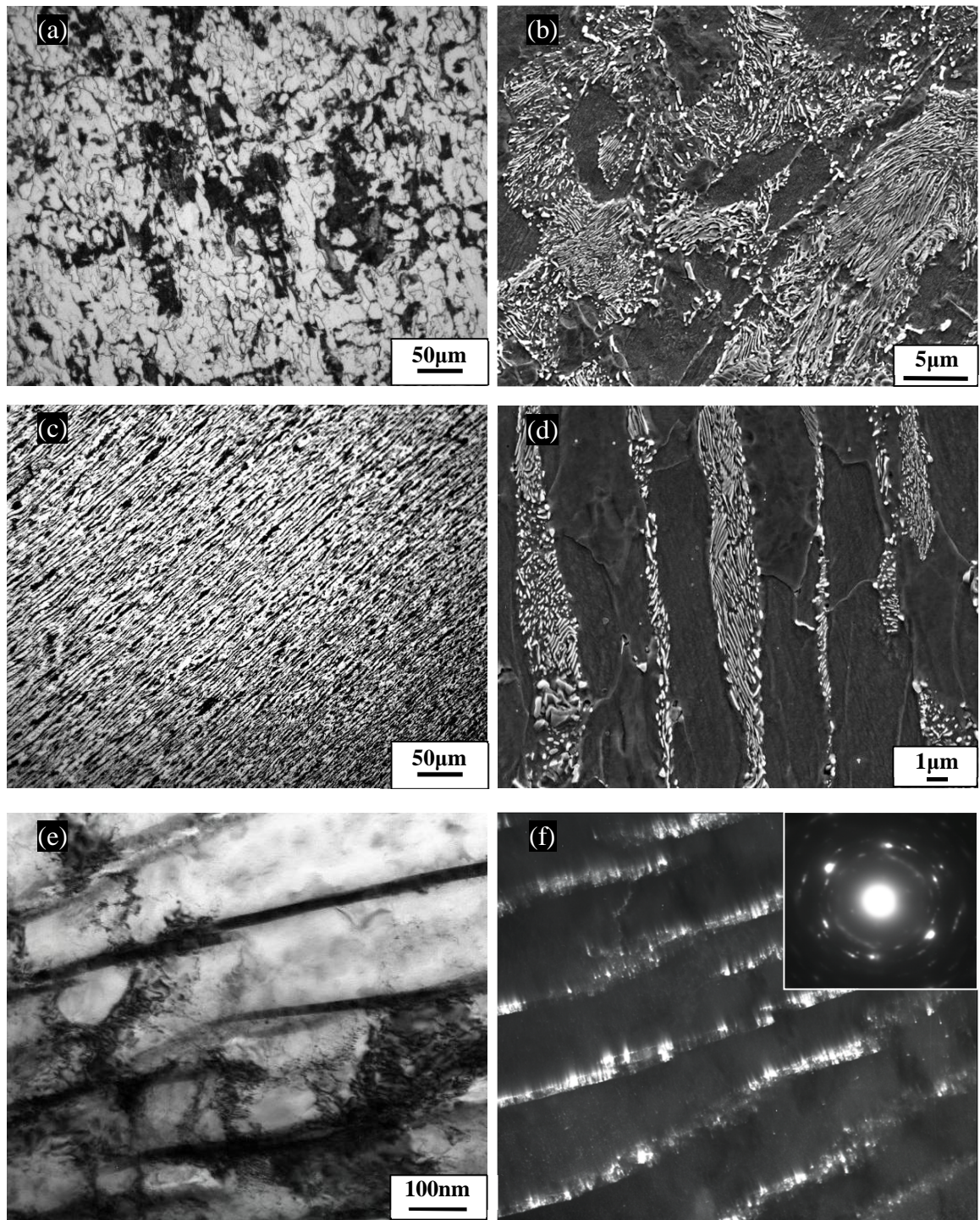


Fig. 4.1, The micrographs of starting microstructure, (a) and (b) Optical micrograph and SEM image, representing the secondary phase inside the ferritic matrix, (c) and (d) Optical and SEM micrographs of structure in rolling direction, (e) and (f) BF/DF, TEM micrographs, showing the pearlite.

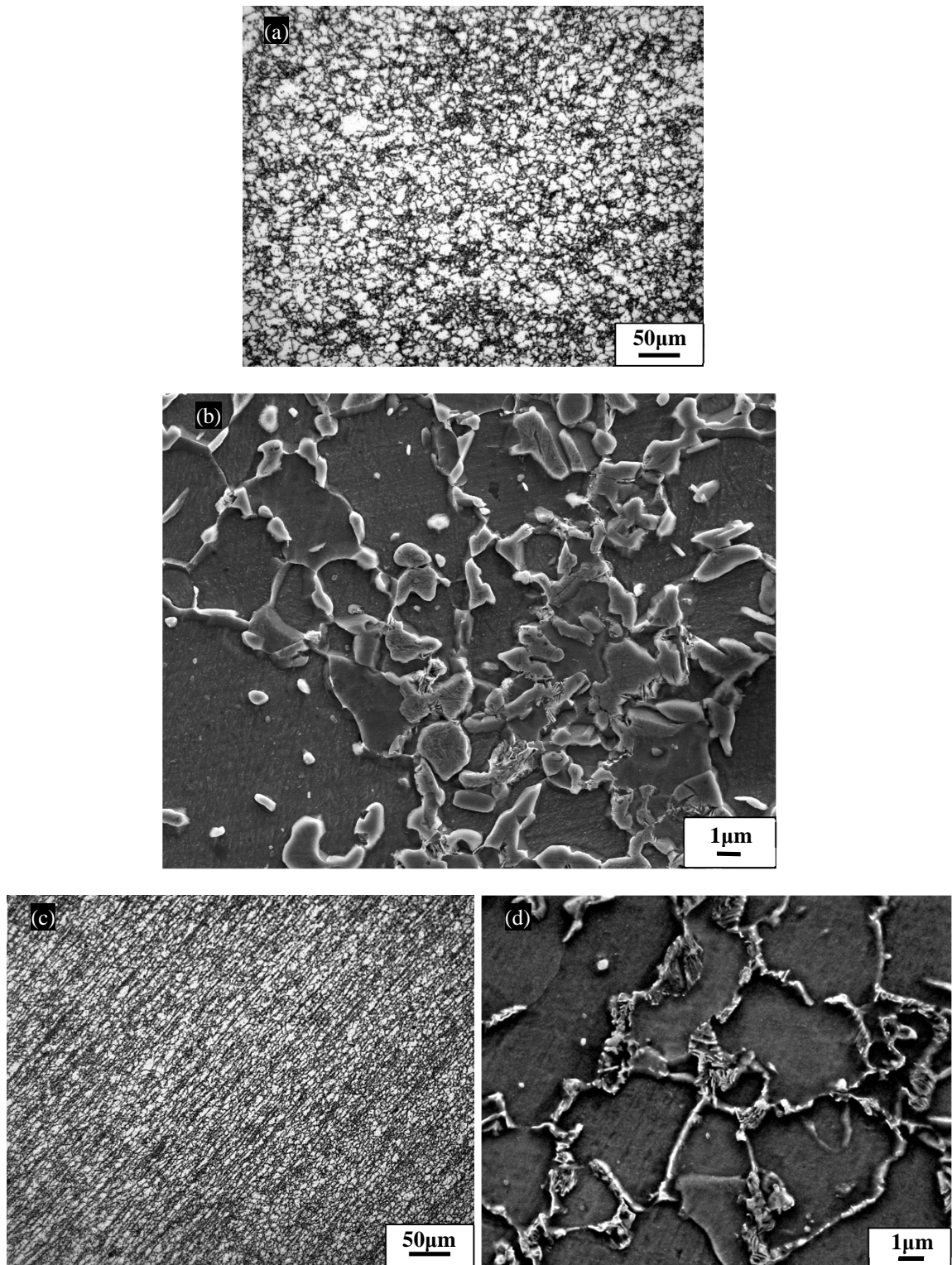


Fig. 4.2, Selected micrographs after the intercritical annealing, (a) and (b) Optical and SEM micrographs corresponding to the normal direction plane, respectively, (c) and (d) Optical and SEM micrographs corresponding to the rolling direction plane, respectively, RA; retained austenite, M; martensite.

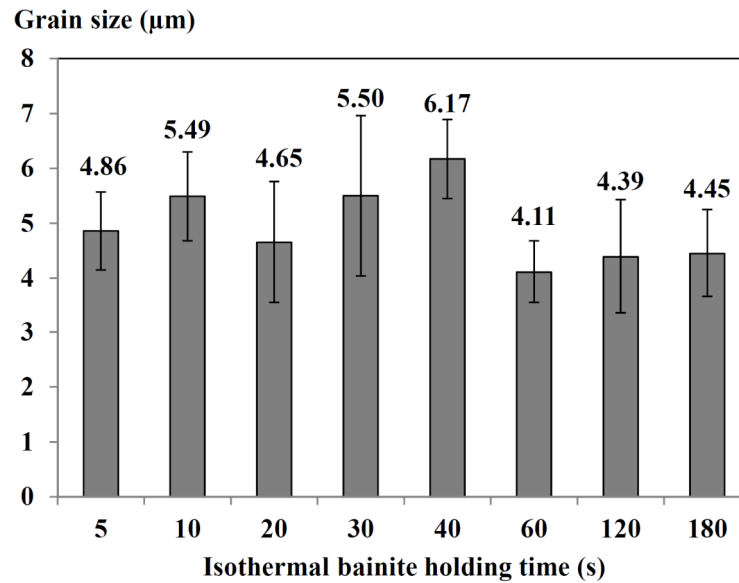


Fig. 4.3, Variation of ferrite grain size versus isothermal bainite holding time, measured by intercept method from the SEM micrographs.

Fig. 4.4 gives SEM micrographs from the sample that was intercritically annealed and then held at the isothermal bainite holding time (IBT) for 5 seconds. The microstructure shows a different structure from the interrupted quench sample, attributed to the bainite transformation in the blocks of austenite. Fig. 4.4 (a) shows the retained austenite located in the microstructure as interlath or intergranular phase and connected to martensite and/or bainite grains.

The micrographs of samples prepared with 5s, 10s and 20s holding times at the isothermal bainite transformation temperature, confirmed the presence of a sheave substructure inside the blocky shape feature, with high intensity in the microstructure (Fig. 4.4). TEM characterization provided evidence that these blocky shape features had already partly transformed to martensite and the remainder contained a high dislocation density and retained austenite (Fig. 4.4). The electron diffraction pattern successfully confirmed the presence of retained austenite inside these features. It is suggested that this may possibly be lower/granular bainite or martensite with a high dislocation density in the adjacent region.

By increasing the holding time over 20s, a rise in the population of secondary phases was observed, with different morphologies compared to that shown in Fig. 4.4 (a) to (c) and 4.5 (a) and (b). As is seen in Fig. 4.5 (a) and (b), a comb shape structure

formed through the blocks of austenite. Fig. 4.6 indicates the bright and dark field TEM micrographs of the thin foil sample after 180s holding time. TEM observations show that these features contained laths of bainitic ferrite with discrete retained austenite/carbide particles regularly distributed throughout (darker contrast). Fig. 4.6 (a) and (b) provide clear evidence of transformation into block austenite. The micrographs suggest the growth of bainitic ferrite in the austenite. Therefore, the remaining laths among bainitic ferrite correspond to film shape retained austenite. No direct evidence of cementite in the bainite was found.

Fig. 4.7 shows three typical TEM micrographs from thin foil samples after 180s holding time at the isothermal bainite transformation temperature, indicating the coexistence of microalloying precipitates and dislocations in the vicinity of interfaces between bainite and ferrite.



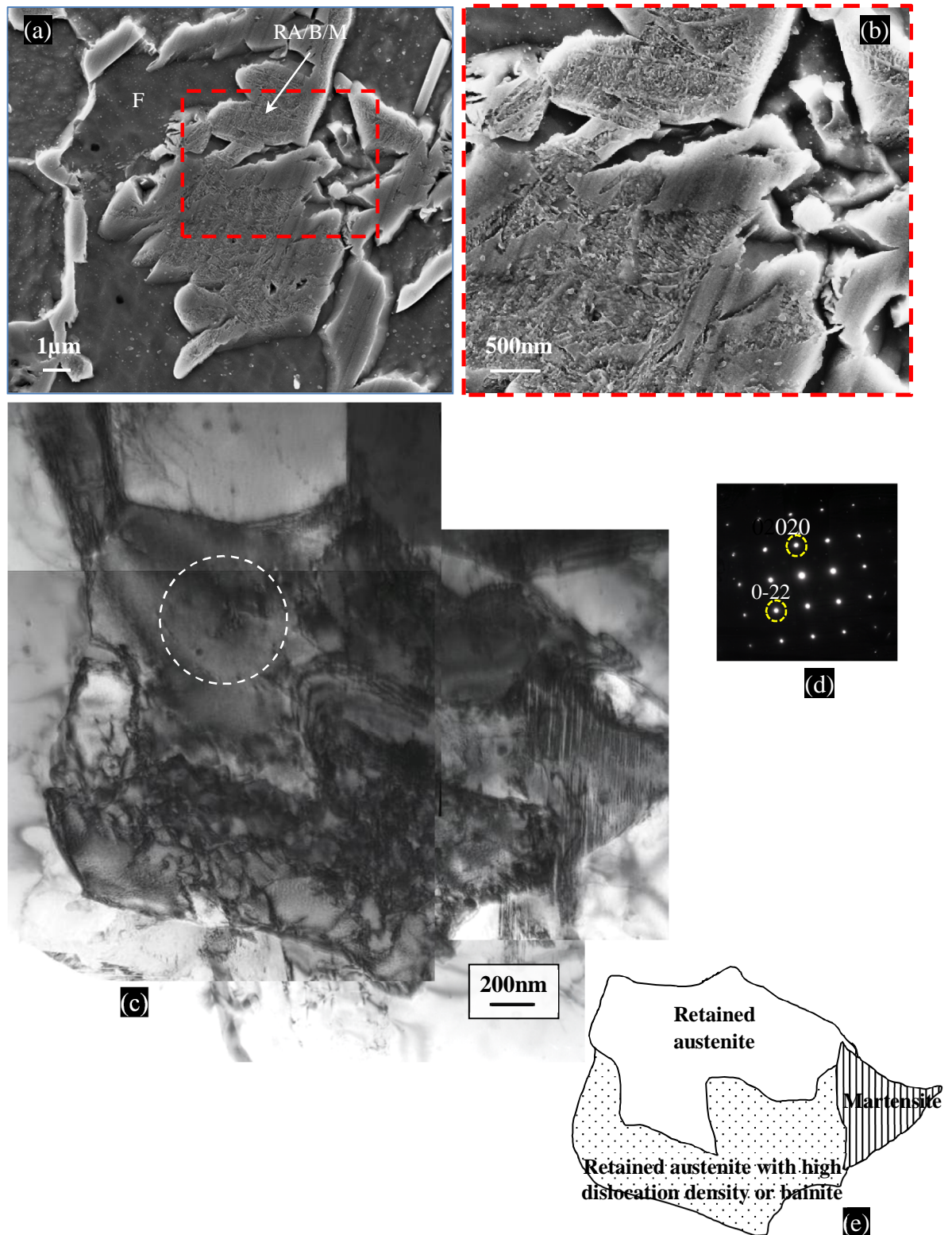


Fig. 4.4, SEM and TEM micrographs of the samples prepared by 5s IBT, (a) and (b) SEM images with two different magnifications, showing a substructure in the block of austenite, (c) and (d) TEM micrograph and corresponding electron diffraction pattern in zone axis [100] of retained austenite, showing different constituents, similar to that shown in (a) and (b), (e) Schematic of observed block shape feature in (c).

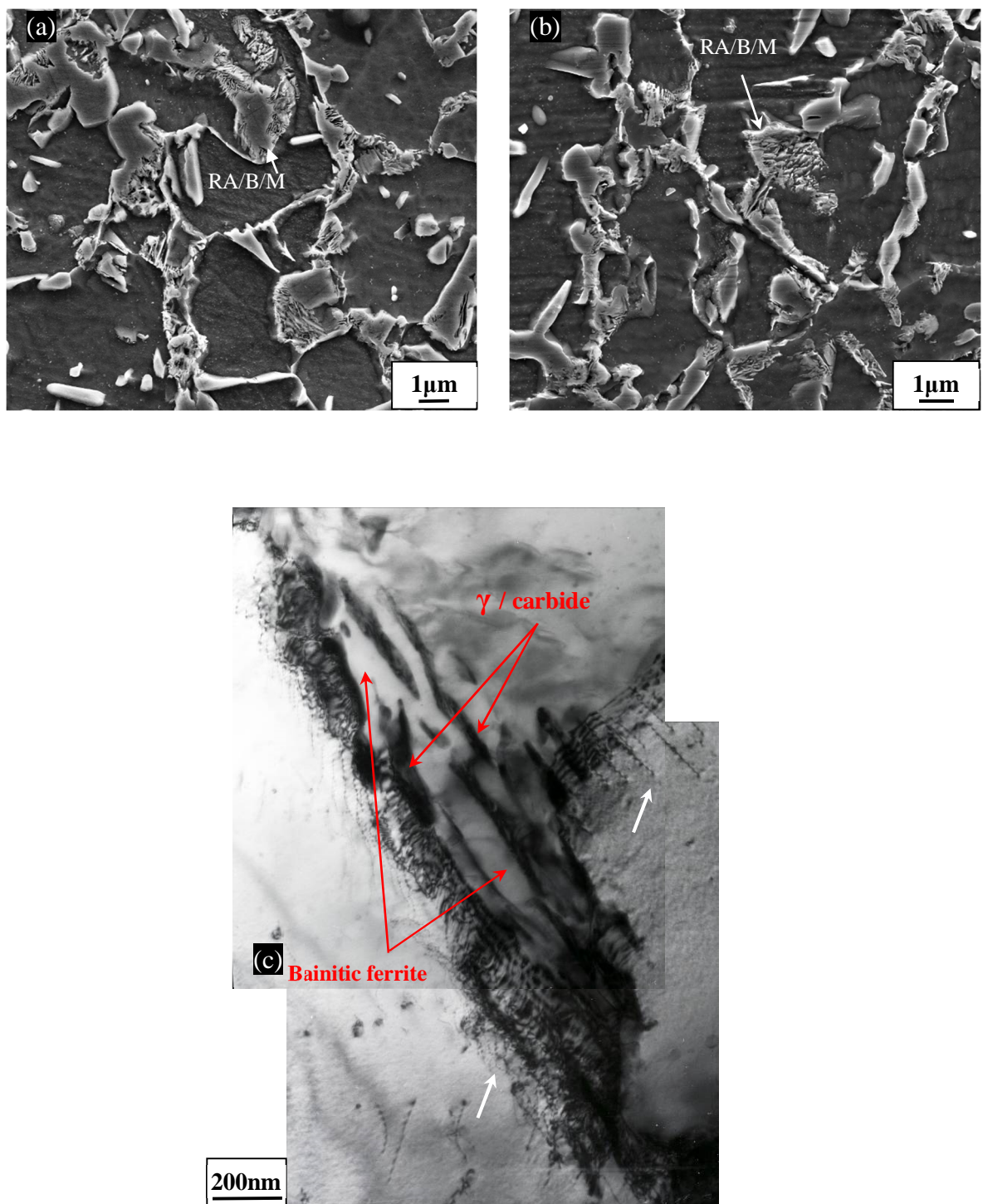


Fig. 4.5, Selected SEM and TEM micrographs of heat treated samples, (a) and (b) SEM micrographs of sample prepared by 30s and 180s holding time at IBT, respectively, (c) Bright field image of a given secondary phase from the sample prepared by 180s holding time.



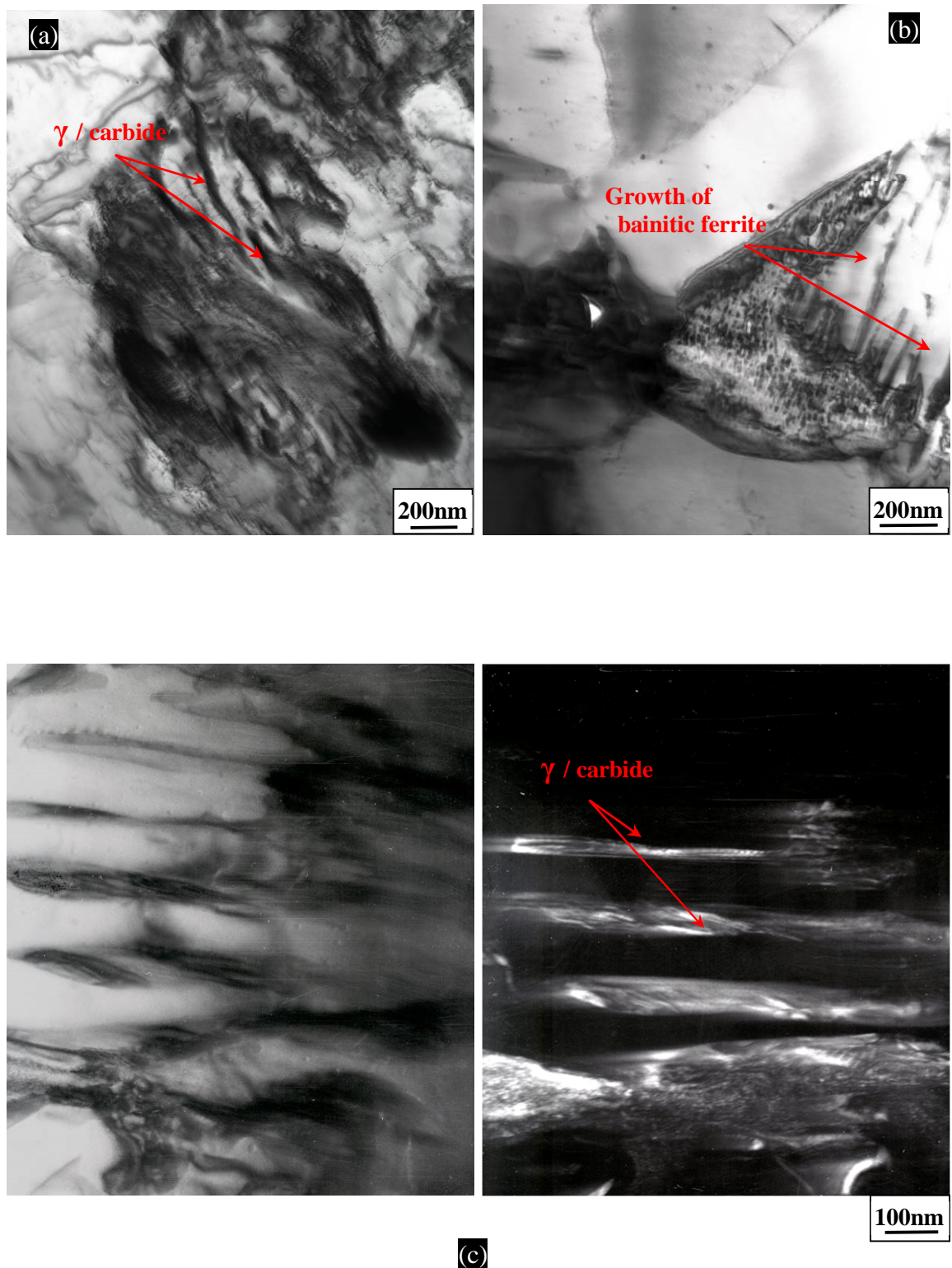


Fig. 4.6, (a) and (b) Thin-foil TEM micrographs of samples prepared by 40s holding at IBT, showing the bainitic ferrite growth into the blocks of austenite, (c) and (d) BF/DF micrographs, illustrating the film shape retained austenite.

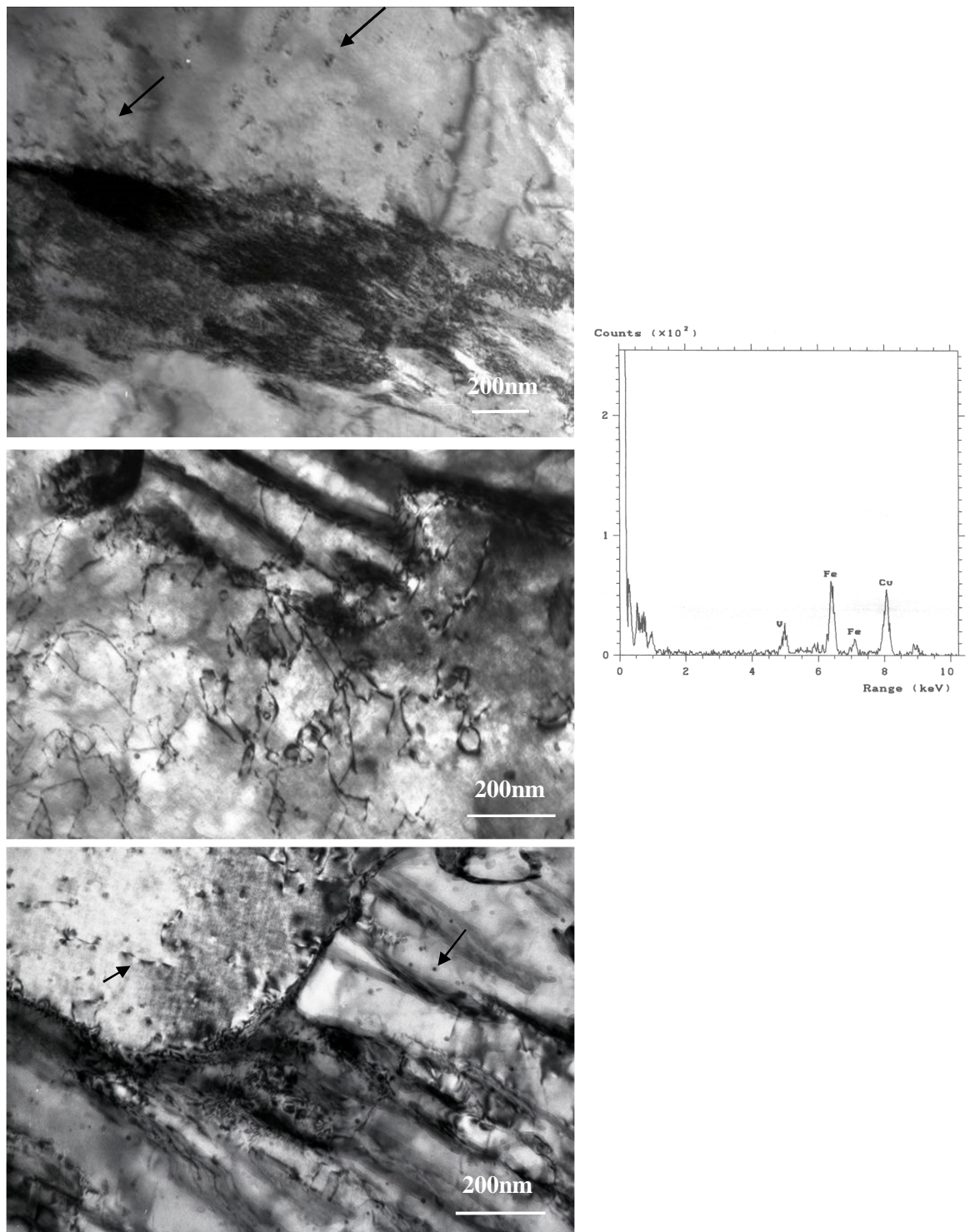


Fig. 4.7, Selected TEM micrographs and corresponding EDS spectrum of thin foil samples prepared by 180s holding, illustrating the presence of dislocations and microalloying precipitates at regions adjacent to the interfaces of retained austenite and bainitic ferrite.



### 4.2.2. Precipitation Behaviour

Investigation of the precipitation behaviour, before and after isothermal bainite holdings, was conducted using the carbon extraction replica samples. Five groups of samples were studied, including cold rolled and heat treated with 5s, 30s, 40s and 180s holding times at the isothermal bainite transformation temperature. Figs. 4.8 to 4.12 show typical TEM micrographs of the precipitates in the carbon extraction replica samples. Different morphologies of precipitates were observed, including spherical, oval, complex and hexagonal.

A combined EDS and dark field technique (DF) was applied to distinguish the precipitates from other unwanted sources of contrast and to chemically analyse the precipitates. Carbon replica successfully extracted the precipitates larger than  $5\pm 1$  nm through bright field and dark field imaging. The EELS was also used to investigate the presence of nitrogen in precipitates (Fig. 4.10 and 4.11). However, as the majority of precipitates appear to have spherical or oval morphology, the EELS could not distinguish carbide and nitride precipitates (Fig. 4.11).

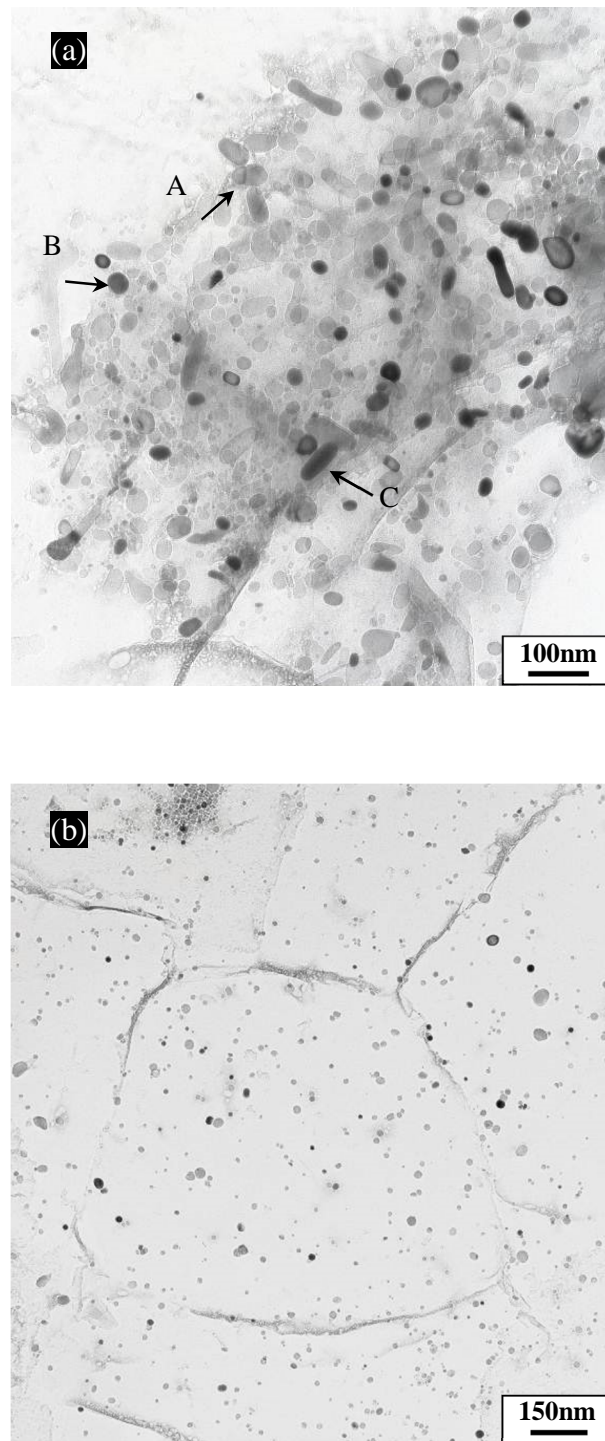


Fig. 4.8, Selected carbon extraction replica micrograph, showing the V/Ti(C,N) precipitates, (a) Different morphologies of precipitates in the microstructure, A, complex; B, spherical; C, oval, (b) Typical distribution of precipitates in the microstructure.

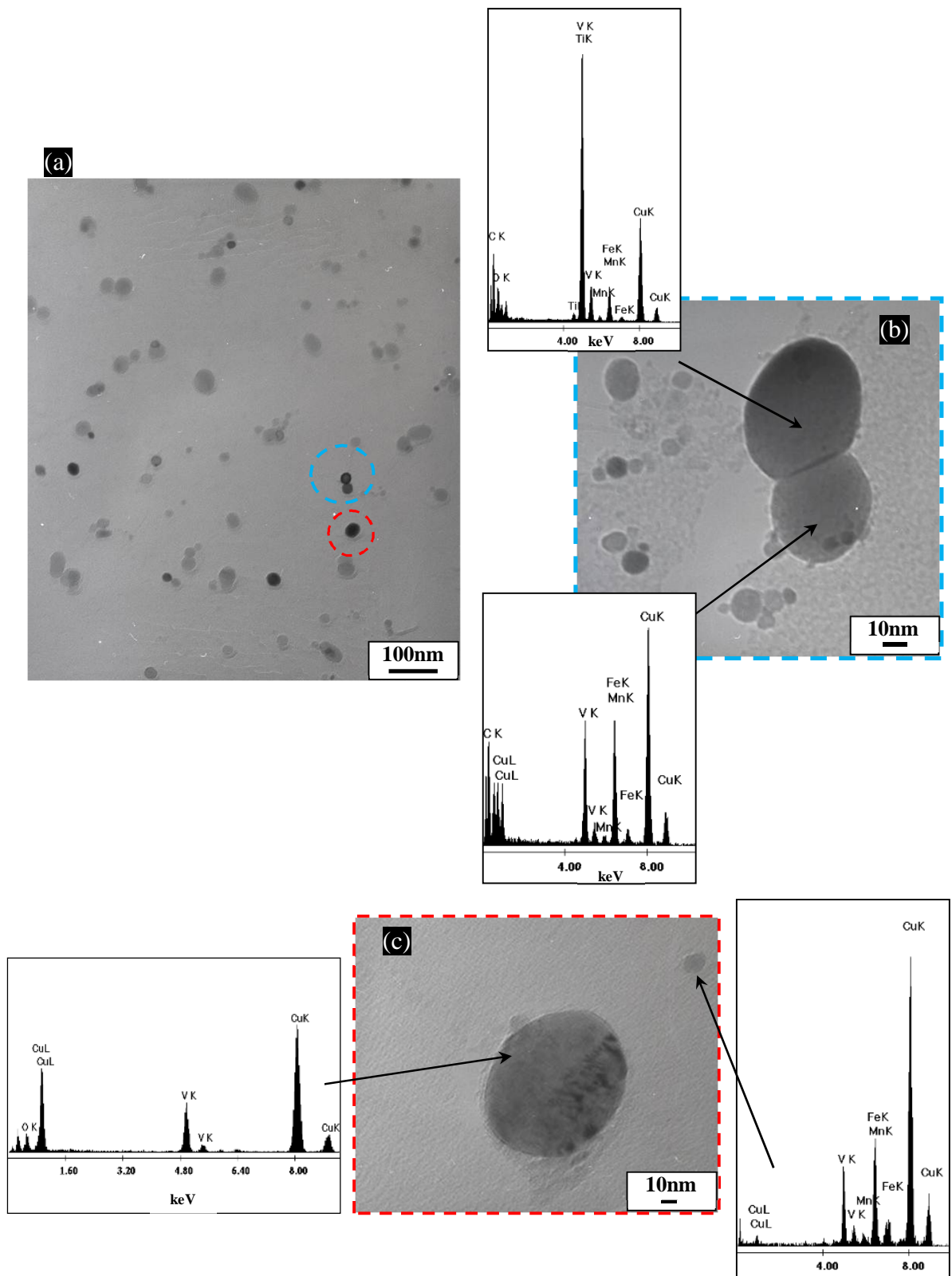


Fig. 4.9, (a) Selected carbon extraction replica micrographs, showing the distribution of precipitates in the microstructure, (b) A typical complex precipitate and corresponding EDS spectra for each cap, (c) Typical spherical precipitates and corresponding EDS spectra.

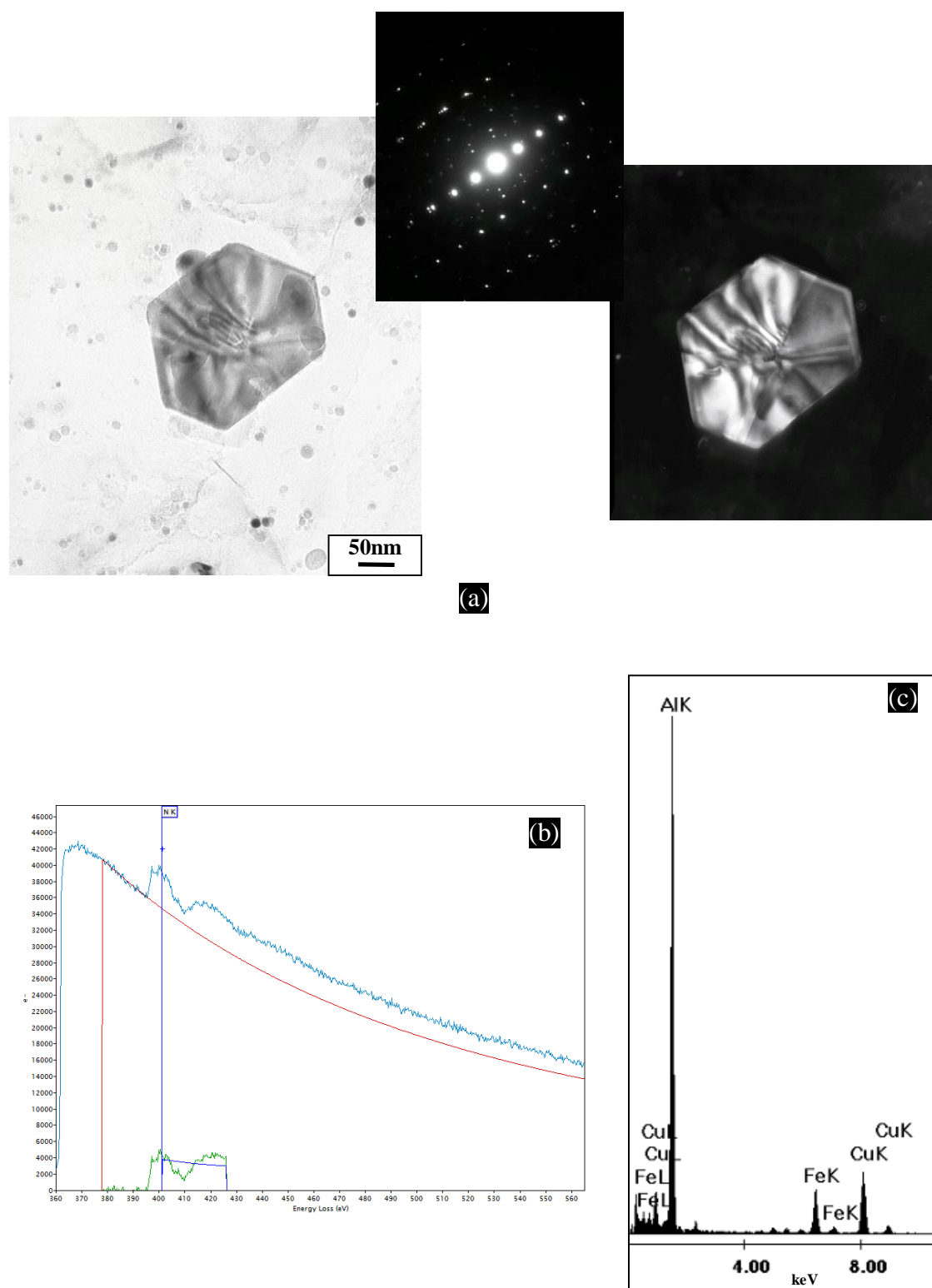


Fig. 4.10, Bright and dark field carbon extraction replica micrographs corresponding to the sample prepared by 30s holding time, (a) An AlN particle in the vicinity of microalloying precipitates, (b) Corresponding EELS spectrum, (c) Corresponding EDS spectrum.

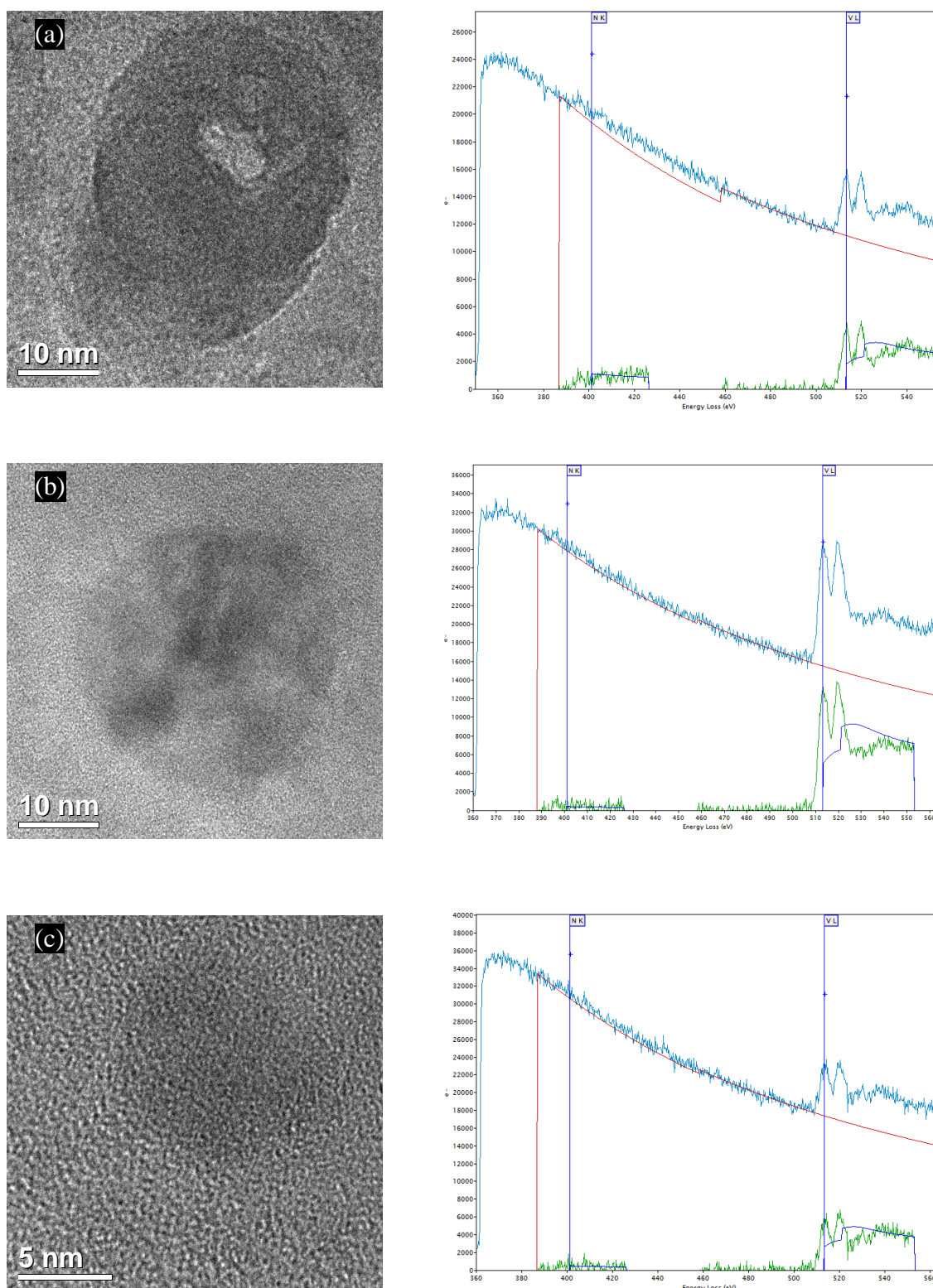


Fig. 4.11, Bright field TEM images of carbon extraction replica and corresponding EELS spectra, showing the existence of nitrogen in precipitates, (a) With N, (b) Without N, (c) Without N.



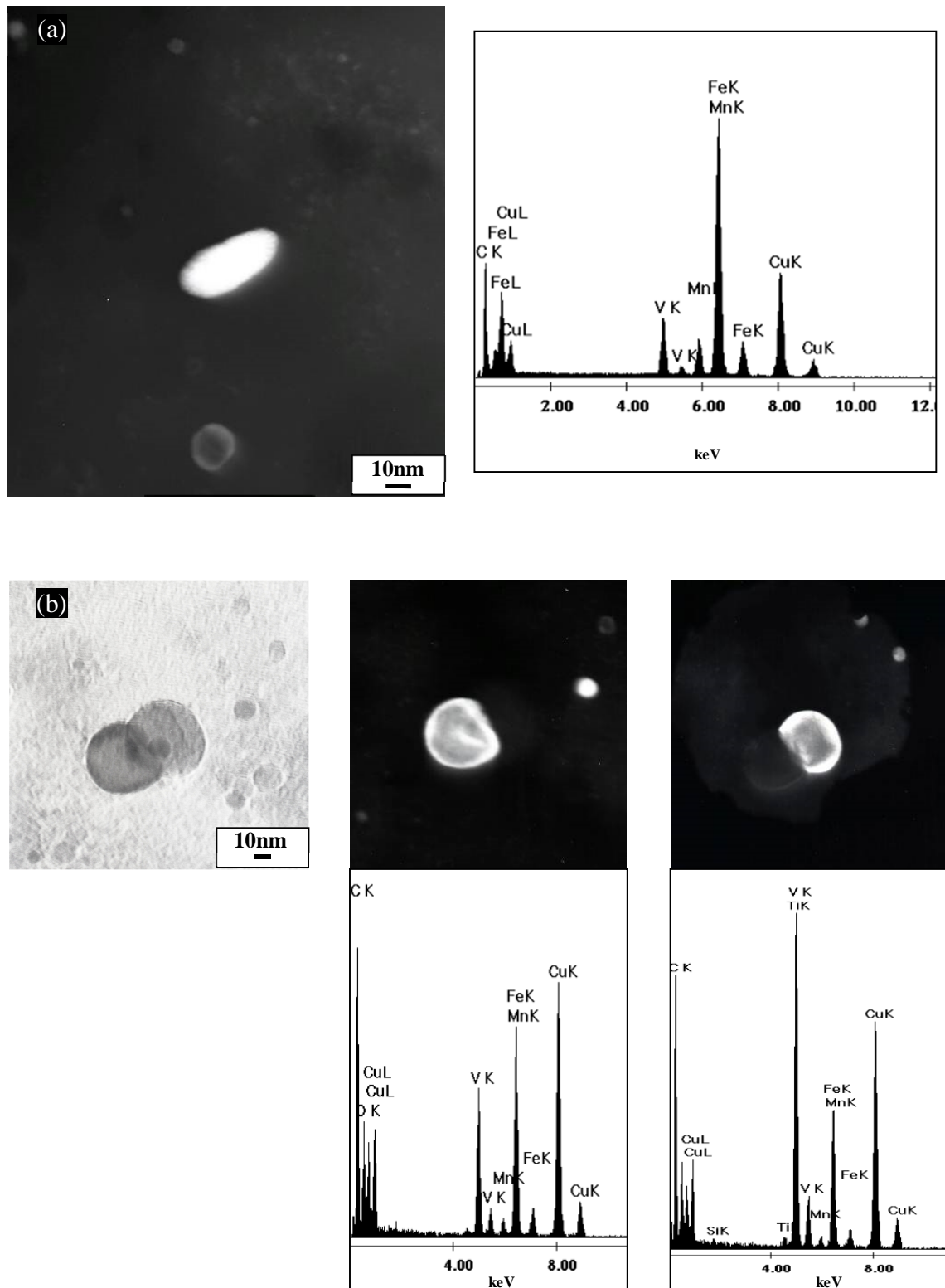


Fig. 4.12, Bright and dark field carbon extraction replica micrographs, showing two typical V precipitates with two different morphologies, (a) An oval shape and corresponding EDS spectrum, (b) A complex shape and corresponding EDS spectra for each cap.

The TEM observations confirmed the presence of V(Ti)C based nano scale precipitation in all the samples. Further qualitative identification of the precipitates by

the EDS showed the presence of V and occasionally Ti in the precipitates, in the form of either individual or complex shapes (Fig. 4.8, 4.9 and 4.12). Considerable quantities of relatively large AlN precipitates were observed as confirmed by Fig. 4.10. It is believed that these particles were formed at high temperatures and were not involved in the intercritical annealing treatment [65].

The density of precipitates was measured using at least ten negatives for each sample. Fig. 4.13 plots precipitate density as a function of holding time. Similarly, the size distribution as a function of holding time was measured using the carbon extraction replica samples indicating no significant change in precipitate size distribution within the tested range (Fig 4.14).

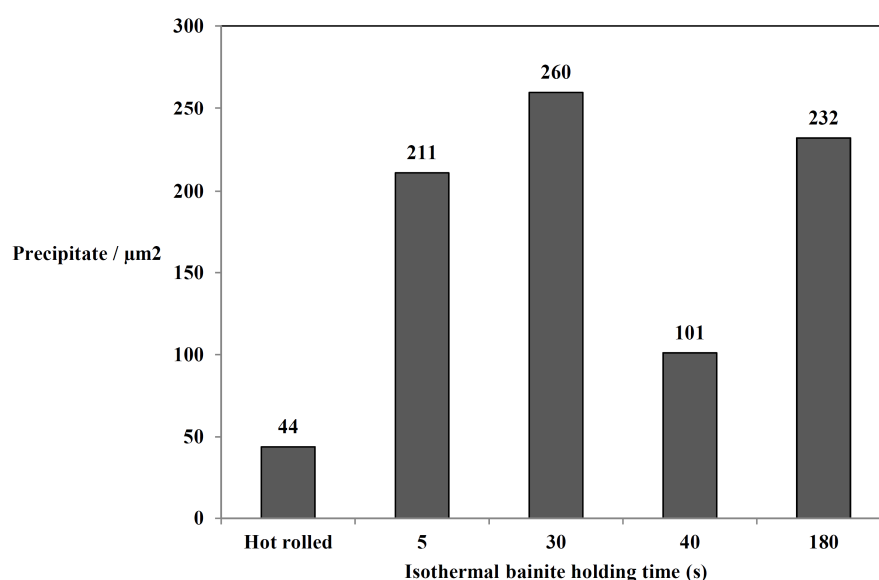


Fig. 4.13, Area density of precipitates versus isothermal bainite transformation holding time, measured from the TEM micrographs of the carbon extraction replica samples.

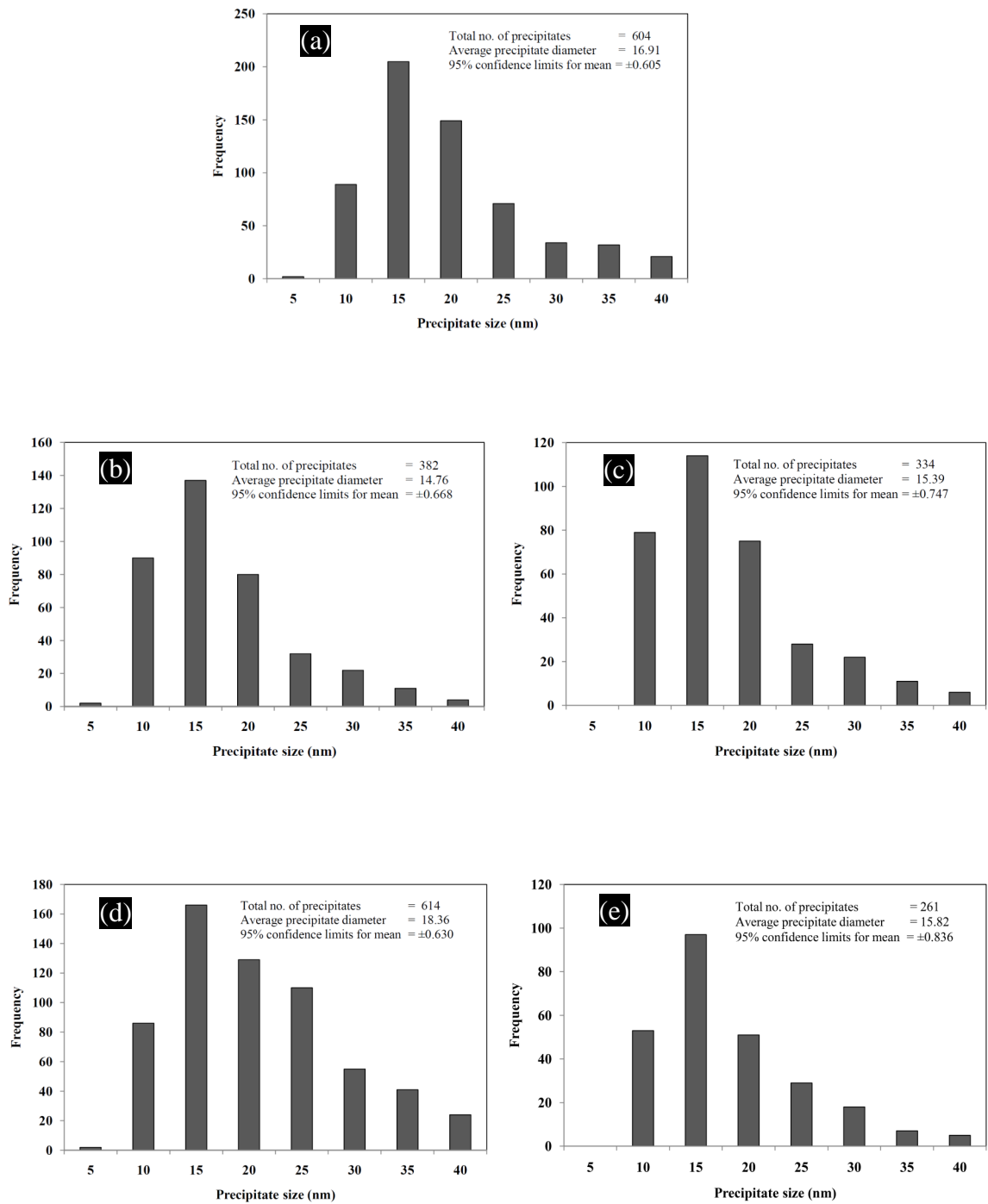


Fig. 4.14, Precipitate size distribution of samples prepared with different holding times at IBT, measured from carbon extraction replica samples, (a) Before intercritical annealing (cold rolled structure), (b) 5s holding time, (c) 30s holding time, (d) 40s holding time, (e) 180s holding time.



### 4.2.3. Retained Austenite Content

Fig. 4.15 gives a typical XRD pattern after intercritical annealing. From the spectrum obtained from 40 to 130 degrees, two main phases were identified - retained austenite and ferrite. Three groups of results are shown in Fig. 4.15, which correspond to experimental patterns acquired, and two other computer generated results, including calculated curve based on Rietveld refinement and characteristic difference profile. The characteristic difference profile indicates the resultant profile obtained from the observed and calculated curves.

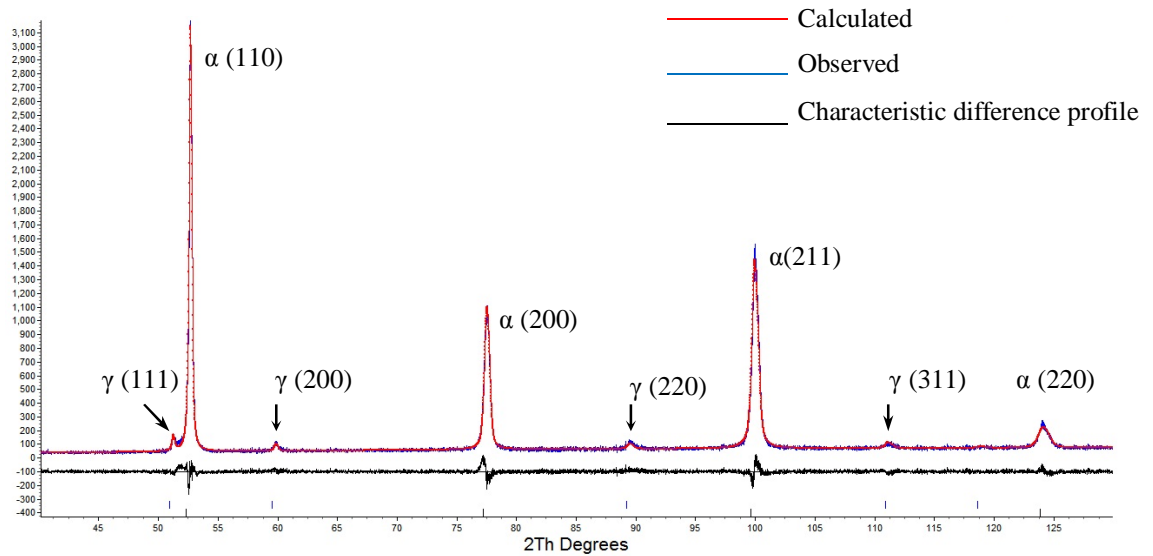


Fig. 4.15, A selected graphical representation of Rietveld analysis for X-ray diffraction pattern of the intercritical annealed sample, followed by the subsequent IBT.

Table 4.1 shows the volume fraction and lattice parameter of retained austenite in terms of holding time. The carbon content was measured according to the lattice parameter of retained austenite using the Nishiyama equation [129]:

$$a_{\gamma} = 0.35467 + 0.00467 \text{ wt\% C} \quad (4.1)$$

Table 4.1, The retained austenite parameters examined by XRD.

Isothermal bainitic holding time (s)	Retained $\gamma$ (%)	$C_{\gamma}$ (%)	$a_{\gamma}$ (Å)
5	9.4	1.212	3.60332±0.00038
10	10.7	1.258	3.60546±0.00031
20	11.1	1.265	3.60581±0.00058
30	5.8	1.270	3.60137±0.00051
40	6.4	1.214	3.60344±0.00038
60	8.7	1.279	3.60645±0.00057
120	8.9	1.326	3.60866±0.00050
180	8.9	1.407	3.61242±0.00063

Fig. 4.16 shows the variation in the volume fraction of retained austenite as a function of isothermal bainitic holding time. As can be seen, the fraction of retained austenite increased with holding time up to 20 seconds, then showed an abrupt decrease at 30s and 40s. The longer holding time over 60s showed no significant variation in the fraction of retained austenite. This result was repeatedly checked on separate samples and repeat heat treatments. The results confirmed a range tolerance approximately 1 to 3vol% in the fraction of retained austenite. Interestingly, the trend here shows a fluctuation during 30s and 40s, but after that the fraction of retained austenite seems relatively stable.

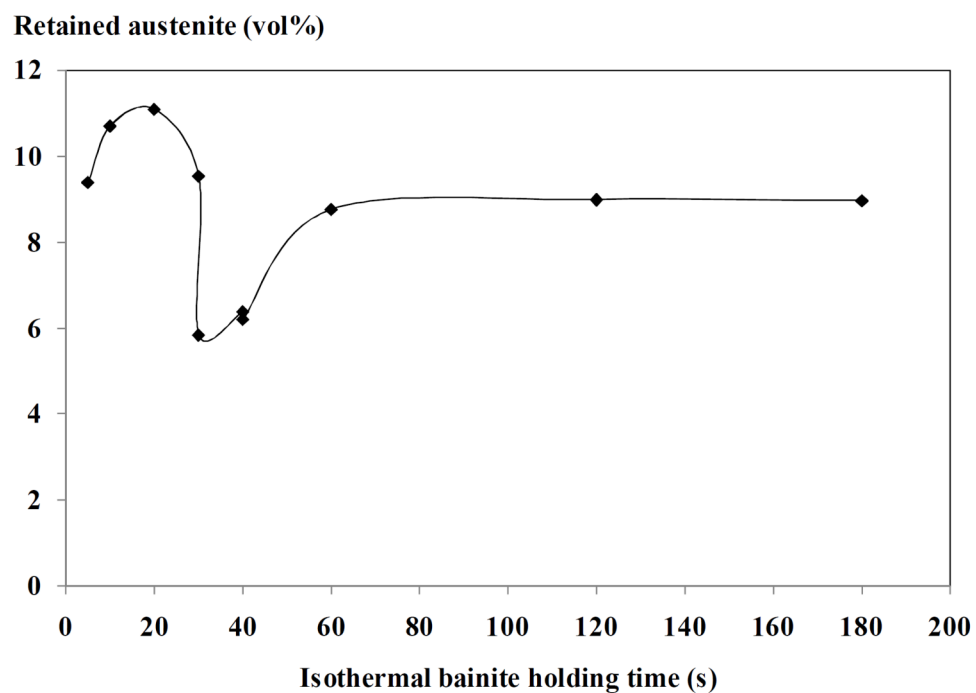
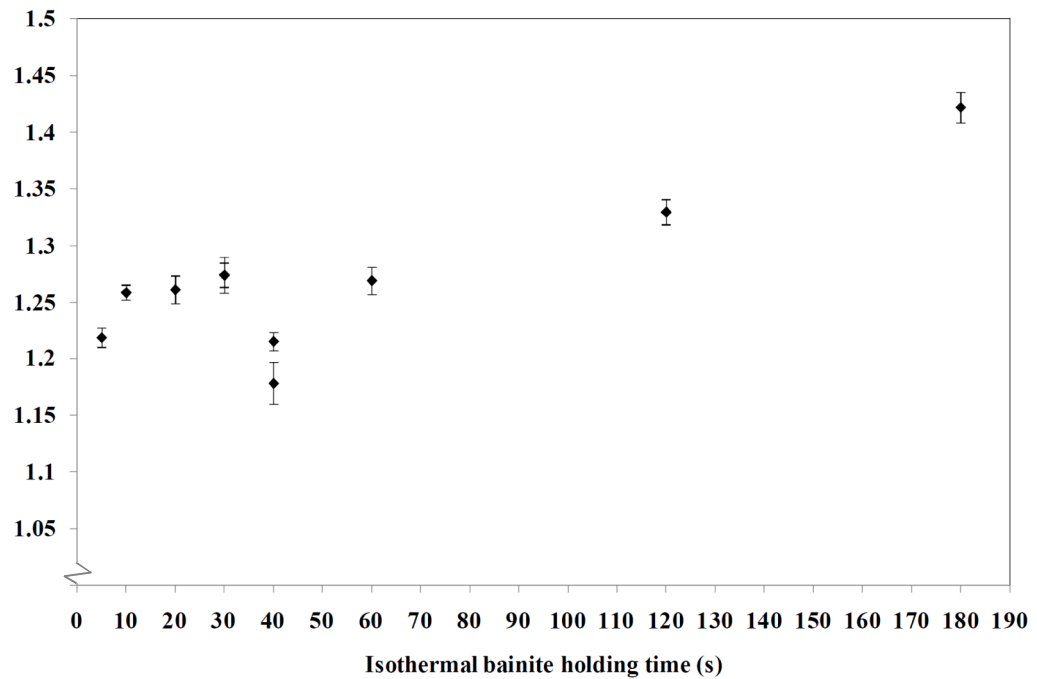


Fig. 4.16, Evolution of the volume fraction of retained austenite in terms of IBT holding time in the studied steels measured by XRD method.

The carbon content of retained austenite was calculated according to the lattice parameter using the Nishiyama equation (Table 4.1). It can be seen from Table 4.1 and Fig. 4.17 that the progress of isothermal bainite holding time is associated with an increase in the lattice parameter of retained austenite. This is attributed to the higher carbon content.

Carbon content of retained austenite (wt%)



Carbon content of retained austenite (wt%)

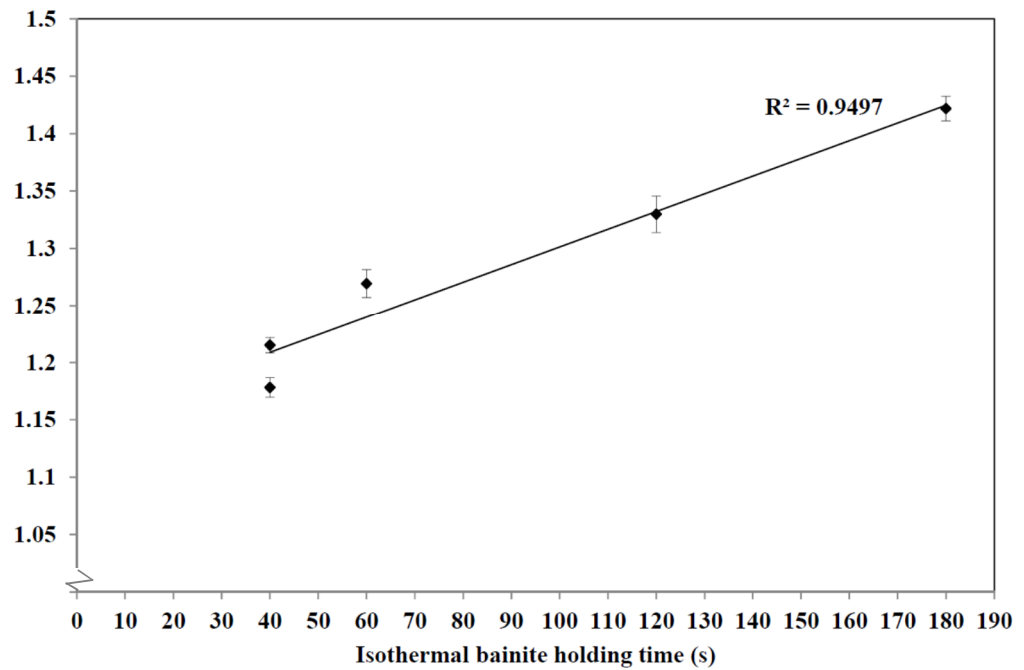


Fig. 4.17, (a) Carbon content of retained austenite after different IBT holding times, measured from the lattice parameter (b) The best fit line, showing the linear trend of variation for the longer holding time  $\geq 40$ s in (a).

#### 4.2.4. Hardness Testing

The influence of IBT holding time on the microstructural evolution was also evaluated by comparing mechanical properties at room temperature. The effect of hardness was investigated using Vickers hardness and microhardness analysis. Fig. 4.18 shows typical optical micrographs of indentations in the microstructure of the etched samples.

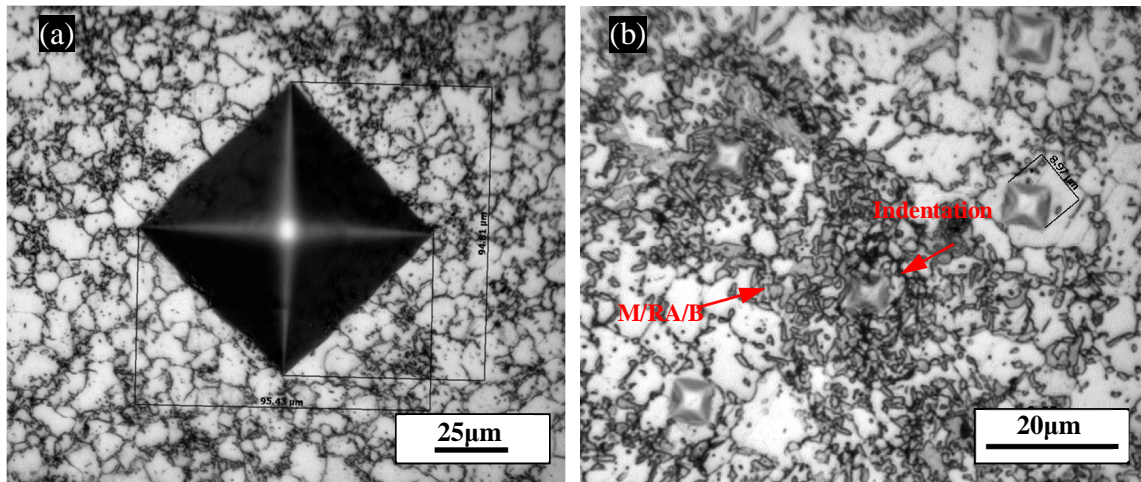


Fig. 4.18, Optical micrographs showing hardness and microhardness indentations, (a) A typical Vickers hardness indentation, (b) Microhardness indentations, M/RA/B; martensite/retained austenite/bainite.

As shown in Fig. 4.19, the hardness after 5 seconds holding time was higher than that for longer holding times. Beyond 10s the hardness shows an almost constant range of hardness (Table 4.2).

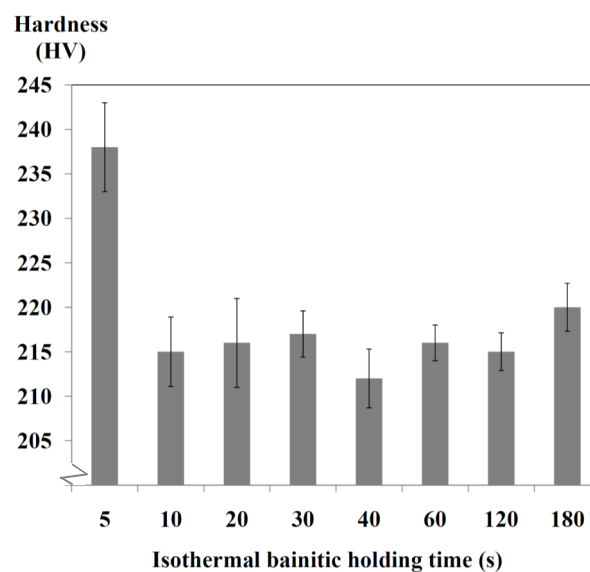


Fig. 4.19, Variation of hardness values as a function of IBT holding time.

Table 4.2, The result of Vickers hardness measurements.

Isothermal bainitic holding time (s)	HV
5	$238 \pm 5$
10	$215 \pm 4$
20	$216 \pm 5$
30	$217 \pm 3$
40	$212 \pm 4$
60	$216 \pm 2$
120	$215 \pm 2$
180	$220 \pm 3$

#### 4.2.5. Tensile Testing

Fig. 4.20 shows the engineering stress-strain curves of the specimens prepared with different IBT holding times, including 5s, 40s and 180s. The tensile curves show a considerable variation in yield strength, ultimate tensile strength (UTS) and elongation as a function of isothermal holding time. The UTS and yield strength of samples are plotted in Fig. 4.20 (b) against the holding time. The details of tensile properties are listed in Table 4.3. Fig. 4.20 suggests that the longer holding time leads to a significant improvement in the mechanical properties of steels as well as a bake hardening effect.

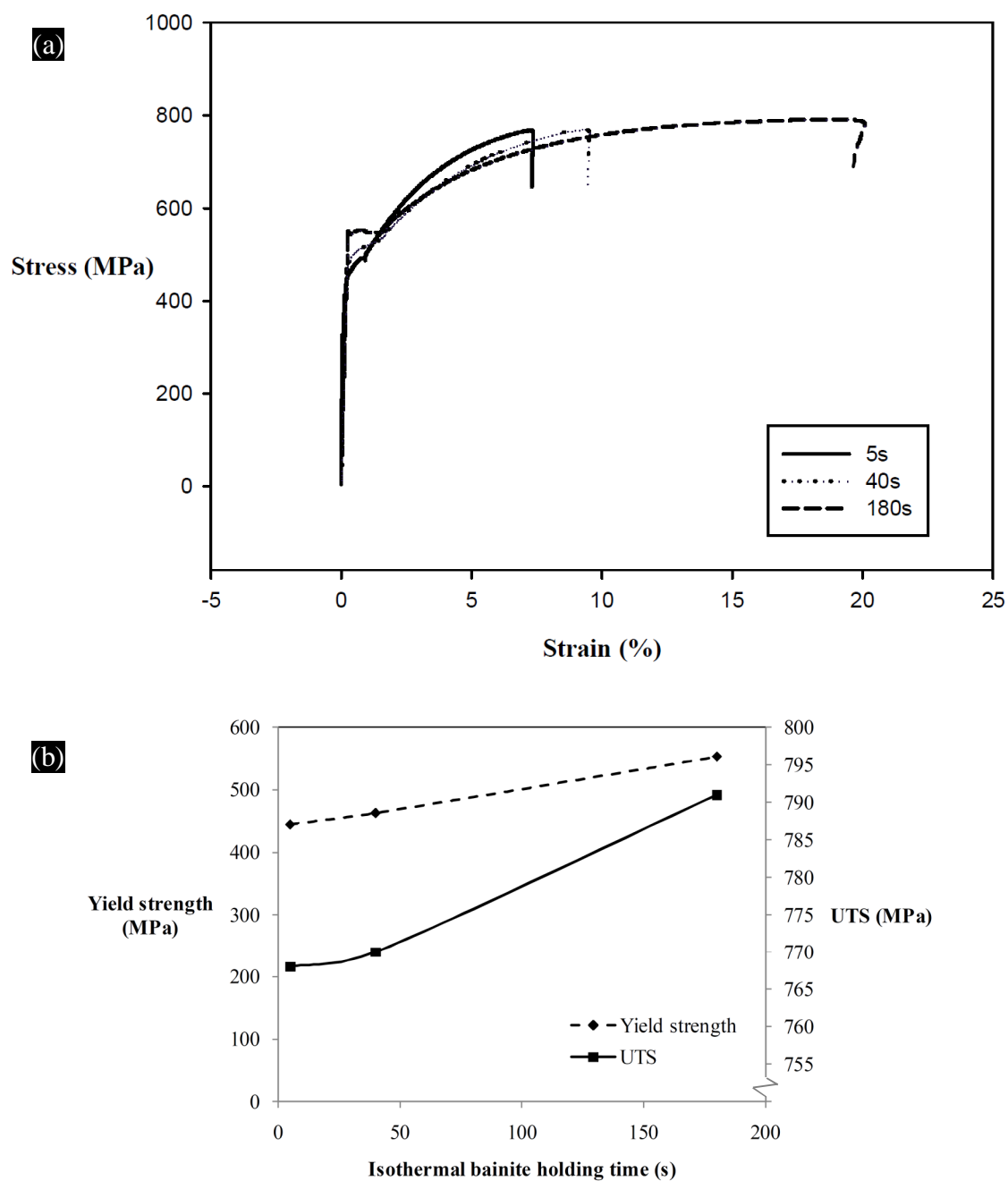


Fig. 4.20, (a) Engineering tensile stress-strain curve of samples in terms of IBT holding time, (b) Trend of yield strength and UTS versus isothermal bainite holding time.

Table 4.3, Tensile properties in terms of isothermal bainite holding time.

IBT holding time (s)	Yield point (MPa)	UTS (MPa)	Strain (%)
5	445	768	6.98
40	463	770	9.40
180	553	791	19.64

## 4.2. Discussion

### 4.2.1. Characterization of Microstructure

The significant impact of the bainite transformation on the morphology of the retained austenite was evidenced by the microstructural observations. Detailed quantitative XRD analyses indicated the complex dependence of austenite volume fraction on isothermal bainite transformation holding time. The volume fraction of retained austenite peaked after 20 seconds holding time, then abruptly fell until 30 seconds, before rising again until 60 seconds, thereafter remaining almost constant (Fig. 4.16). These results are similar to those reported elsewhere (e.g. Tomia et al.), although the maximum point in their studies was generally obtained from much longer holding times (i.e. ~240s) [105]. It has been suggested that the retained austenite initially increases with isothermal bainite transformation time but later decreases as a result of carbide precipitation [60, 105, 130]. The reasons for this complicated behaviour is difficult to determine precisely, but will be considered in detail in the coming sections.

The complex change in retained austenite content with holding time was not believed to be a result of experimental errors. As mentioned earlier, the volume fraction and carbon content of retained austenite were calculated from the integrated intensity and lattice parameter using XRD patterns. Measuring volume fraction and lattice parameter of retained austenite are subject to errors, the most likely possibilities include:

- 1- Variations in carbon concentration of the retained austenite due to localized carbide precipitation or heterogeneous development of bainite and martensite inside the austenite blocks.
- 2- Heterogeneous strain accommodation in austenite due to bainite or martensite transformation and preferential orientation of structure due to cold rolling and sample preparation leading to the displacement of the diffraction peaks.
- 3- Instrumental errors are another potential source, although these were minimised using standard silicon powder pattern calibration and Rietveld method pattern refinement.

Despite all these potential contributors random retesting confirmed that the variation in the amount of retained austenite due to the heterogeneous structure of this steel was in the range 1 to 3 wt%.

Classical models of isothermal bainite transformation predict that austenite blocks with lower stability transform to martensite during final quenching (Fig. 4.4). In general, the lower stability blocks are those which are coarse and less enriched by carbon.

The fluctuation in retained austenite content observed in Fig. 4.16 infers a mechanism which enriches the austenite with carbon. The rejection of carbon at the interface between transforming bainite and austenite results in a higher mean concentration of carbon in these regions [101]. The extended holding time increases diffusion of carbon through the austenite, so that the carbon concentration gradient decreases. This is consistent with the observation that the carbon content in the retained austenite increased from 1.21% to 1.27% after a 20 second hold (Table 4.1).

The morphology of a typical block shaped microstructural feature of retained austenite was common in the microstructure (e.g. Fig 4.4). This evidences the formation of martensite and bainite-like features inside the blocks of austenite after short holding times. The initial increase in the amount of retained austenite is attributed to the promotion of bainite and the partial growth of bainitic ferrite through the blocks of austenite. This would be consistent with the earlier assumption of carbon enrichment in the retained austenite during the shorter holding times (up to 20 seconds). Microscopy observations indicate that bainitic ferrite growth dominates during later holding times.

After 20 seconds hold there was an abrupt fall in the volume fraction of retained austenite, falling from 11.1% at 20s to 5.8% at 30s. This result was repeatedly checked on separate samples and heat treatments. It was found that there is a tolerance in the fraction of retained austenite of around 1 to 3%, while the carbon content of retained austenite shows a similar trend (Figs. 4.16 and 4.17).

TEM observations indicated considerable growth of bainitic ferrite through the austenite blocks after longer holding times of 40s (Fig. 4.6). It is well established that the growth of bainitic ferrite is accompanied by the rejection of carbon through interfaces



from bainitic ferrite to lath austenite, creating higher carbon concentration on the austenite side. However the short holding time i.e. 30s to 40s limited carbon diffusion within the austenite.

Beyond 40s holding time the carbon content in the retained austenite continued to increase but the volume fraction of retained austenite remained constant. This is consistent with the findings of Hell et al., for cold rolled carbide free bainitic steels [131]. They proposed an incubation time for bainite transformation so that the carbon linearly increases in the austenite after 40% transformation of austenite to bainite. In general, it is unlikely substitutional elements are redistributed during the isothermal bainite transformation [132, 133]. It is suggested therefore that the linear increase in the lattice parameter of retained austenite for hold times greater than 40s corresponds to the carbon enrichment of retained austenite only at this temperature (Fig. 4.17 (b)).

Microstructural evolution was used to interpret the observed variations in the XRD results. Figs. 4.5 and 4.6 show the microstructure for holding times in excess of 40s where additional phases can be seen, in particular, the growth of ferrite laths within the austenite blocks, and the formation of martensite islands (Figs. 4.6 (a) and (b)). The distribution of carbon through the austenite led to the formation of film shape austenite among laths of bainitic ferrite with the higher carbon concentration (Fig. 4.5 (c)). These findings support Lawrynowicz's hypothesis that carbon is more effectively trapped in austenite regions between platelets than in blocks when austenite decomposes to bainite [107]. He suggested that the reduction of carbon penetration diffusion distance due to the formation of lath-like austenite facilitates a more homogeneous distribution of carbon with a higher concentration throughout these regions. The higher level of carbon content in the film shape austenite inhibits martensite transformation during final quenching and leads to the retention of austenite with a film shape morphology in the microstructure, such as that seen in Figs. 4.5 (a) and (b).

From the obtained results up to 180s holding time, it is evident that the mechanism of transformation is strongly time dependent. This is consistent with earlier studies [134] and [135] which used synchrotron X-ray to study austenite and bainitic ferrite in a V microalloyed high carbon steel. These studies showed that during the early stages of isothermal bainite transformation at 300°C, the austenite peaks are divided into two,

indicating that the austenite was present with two compositions and therefore two different lattice parameters. This was attributed to the heterogeneous distribution of carbon in the austenite, which resulted from the austenite that had been retained from cooling with no change in structure and the austenite which had partially transformed to bainite, which had therefore become enriched with carbon. However, the resolution limit of X-ray diffraction used in the present work precluded a definitive statement as to whether such a split in austenite carbon content had occurred in the present work. This could be investigated further in future work.

#### 4.2.2. Microalloying Precipitation

The statistical analysis using the carbon extraction replica data clearly showed a considerable V(C,N) precipitation during the intercritical annealing (Figs. 4.8 to 4.12). Further TEM/EDS observations on thin foil samples also provided evidence to indicate the presence of VC precipitates in polygonal ferrite, acicular/bainitic ferrite and martensite, but with a heterogeneous density (e.g. Fig 4.7). Among these, a random distribution of Al(N) precipitates was also detected inside the microstructure (Fig. 4.10). The Al could affect the amount of free nitrogen by building up the AlN precipitates at high temperatures. It is believed that this in turn would have lowered the possibility of some VN precipitation [64, 65].

A comparison was also made of the average density and size distribution of V(C,N) precipitates between samples subjected to different holding times at the isothermal bainite transformation. The size distribution and density of V(C,N) precipitates in samples subjected to 5s, 30s and 180s holding times failed to show a considerable difference (Figs. 4.13 and 4.14). These findings ruled out any significant V(C,N) precipitation and coarsening at this temperature during the bainite transformation. Nevertheless, as the replica samples failed to extract the precipitates with a size of  $\leq 5\text{nm}$ , it is not still clear whether or not the fresh small precipitates formed within 180s and to what extent they contributed to this behaviour. Thus any future work on the precipitation behaviour should consider this influence.

The carbon extraction replica samples showed a considerable increase in the average size and reduction in the density of the sample prepared by 40s holding time

(Figs. 4.13 and 4.14). This behaviour was observed in repeat experiments. The reason for this behaviour has not yet been fully understood. However, it is thought that the interaction between the microalloying elements and perhaps the formation of cementite, other transition carbides or a larger fraction of martensite was responsible for the observed coarsening. Perhaps, the carbon replicas might extract the V(C,N) precipitates with other features from the substrate. This phenomenon needs to be further investigated in future work.

Of particular note was that the V(C,N) clearly appeared in the bainitic ferrite adjacent to the tangle of dislocations after 180s holding time, when a considerable amount of austenite had decomposed to bainitic ferrite (Fig. 4.7). It is thought that these dislocations were mainly generated as a result of bainite and martensite transformations. The question then arises if the observed precipitates are relevant to the newly formed precipitates or are due to the coarsening of pre-existing precipitates during the intercritical annealing. This will be further elucidated later in more detail in the following chapters.

### **4.2.3. Mechanical Testing**

The effect of the change in phase constitution with time on the mechanical properties was also investigated. Hardness and tensile testing were conducted on samples that had been subjected to different holding times. The equation 2.1 was a good fit to the dependence of hardness on microstructure evolution. Hardening may result from work hardening, solid solution strengthening, precipitation hardening, martensitic transformation and grain refinement.

Quantitative metallography confirmed no significant change in the ferrite grain size arising from isothermal bainite transformation in the eight samples tested, as expected. However, it is clear that the slight fluctuation between about 1-2  $\mu\text{m}$  can be attributed to the heterogeneous microstructure of these steels (Fig. 4.3).

The hardness of the sample isothermally transformed for 5 seconds was considerably higher than for any other transformation time (Fig. 4.19). This can be explained based on the formation of bainite and a larger quantity of martensite in the 5 second sample. The lower thermal stability of the austenite due to the lower and

heterogeneous distribution of the carbon content was likely to have been the reason for significant transformation of austenite to martensite after final quenching. TEM observations also confirmed the high frequency of martensite in the microstructure, but due to difficulty in measuring the martensite content, it is impossible to quantitatively suggest the proportion of martensite. An almost constant hardness was observed for all other holding times, despite the significant growth in the amount of bainite and reduction in the volume fraction of martensite. It would appear, therefore, that the increase in bainite content had offset the decrease in martensite hardness through tempering yielding an approximately constant hardness.

The tensile tests indicated a good repeatability with different holding times. It is evident that increasing the holding time led to an increase in the yield strength, UTS and elongation (Fig. 4.20). This was considered to be primarily a result of the amount of retained austenite morphology and the proportion of either blocky or film shape.

The microscopy observations demonstrated an increase in the frequency of austenite with a film morphology in the samples prepared by longer holding times. This is in agreement with the results of Miihkinen et al., who reported that the retained austenite with film morphology led to a steel with a higher tensile yield strength than the blocky austenite [15]. This increases the resistance of austenite to the strain induced transformation. Thus, the austenite grains adjacent to bainite are more difficult to transform to martensite due to volume expansion associated with austenite to martensite transformation. In addition, increasing the population of film shape austenite in the microstructure facilitates either a higher or slower strain-induced transformation, which leads to more elongation.

Fig. 4.21 shows an ideal schematic diagram of polygonal ferrite in addition to the lath structure of retained austenite/bainitic ferrite at the grains junctions/boundaries for the studied alloy. This suggests that the formation of film shape retained austenite adjacent to the bainitic ferrite can ultimately reduce the stress concentrations, in particular, at the junctions of grains.

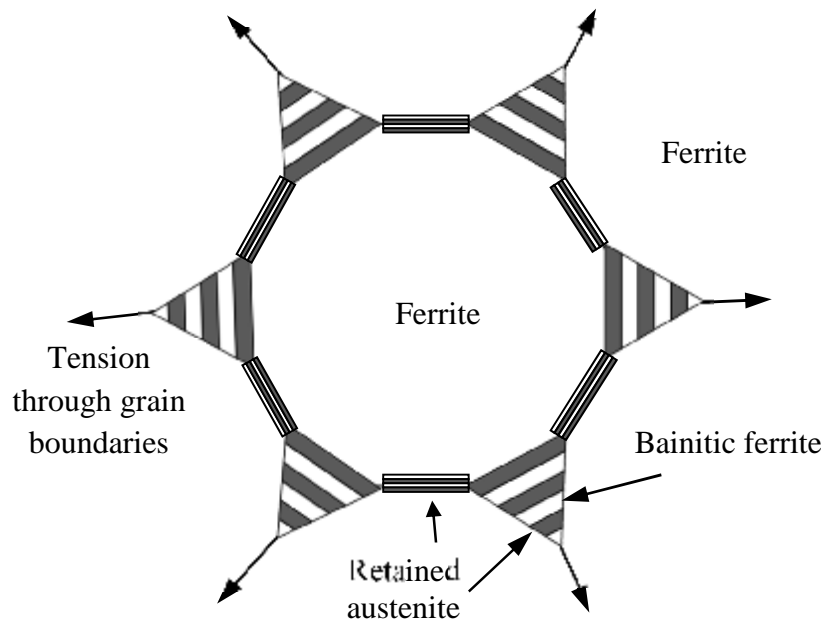


Fig. 4.21, Ideal schematic representation of the polygonal ferrite TRIP assisted steels with the presence of retained austenite and bainitic ferrite at the junctions of grain boundaries.

Holding the sample for longer time i.e. 180s, was found to reveal the effect of bake hardening (discontinuous yielding) on the tensile properties of this steel. Caballero et al. suggested that the dislocations produced during growth of bainite transformation are able to trap a substantial quantity of carbon in the vicinity of the ferrite-austenite interface [136]. This prevents the decarburization of super-saturated ferrite, which provides a condition for carbon Cottrell atmospheres in bainitic ferrite [137]. The findings suggest that the observed upper/lower yield strength of this steel with longer holding time is attributed to the effect of bainite transformation. In addition, the TEM observation elucidated the interaction between dislocations and microalloying precipitates inside the ferritic regions in the vicinity of film shape retained austenite (Fig. 4.7). This confirms the present conclusions, drawn from the XRD results and microscopy observations that the longer holding time led to the growth of bainitic ferrite through the blocks of austenite. However, this was accomplished by the formation of dislocations through the ferrite and trapping the free atom carbons in super-saturated ferrite. Another possible explanation was found in the results of Timokhina et al., who reported that by holding the TRIP steels at the paint coating temperature i.e. 150°C to 200°C, the carbon diffuses from the grain boundaries to the grain interiors, which increases the bake hardening response [138, 139]. This is consistent with the assumption that the longer holding time at isothermal bainite transformation temperature decreases the carbon concentration gradient from the

interfaces of ferrite and austenite. This increases the diffusion of carbon atoms through the grain interiors and high diffusion paths e.g. dislocations, which enhances the bake hardening effect.

With regards to the presence of microalloying precipitates inside the tangle of dislocations, it was assumed that the presence of microalloying elements might intensify the generation or pinning of dislocations. The transformation of bainitic ferrite is accomplished by the plastic relaxation due to displacive shape change during the bainitic ferrite growth. This can be considered as an effective source of dislocation generation. It has been established that this plastic relaxation results from a relatively higher temperature compared to the martensite transformation. Indeed the material is softer at this temperature, which makes it possible to relax the shear transformation inside the microstructure [102]. The presence of dislocation tangles in Fig. 4.7 is good evidence of potential sites for trapping the carbon [136]. However, from the TEM observations and the bake hardening effect (discontinuous yielding) in the stress-strain curves, it can be concluded that the presence of microalloying precipitates were effective in inhibiting the annihilation of dislocations and possible generation of dislocations (Figs. 4.7 and 4.20). This is in line with other reports in the literature concerning the interaction between microalloying precipitates and dislocation recovery during bainite transformation. It is believed that the microalloying precipitates prevent the recovery of the dislocation structure of bainite [47, 48, 49, 64]. However, further investigations as future work could resolve the uncertainties in this influence.

# **Chapter 5. Results and Discussion: Alloys 2 and 3; Intercritical Annealing**

## **5.1. Introduction**

As mentioned earlier, in general, TRIP assisted steels are categorized in three groups in terms of the structure of their matrices, i.e. either polygonal ferrite or bainitic ferrite or annealed martensite. It has been established that in cold rolled TRIP steels, the intercritical annealing process results in the formation of a considerable amount of retained austenite in the microstructure. In these steels, the volume fraction and morphology of retained austenite and microalloying precipitates also contribute significantly to the mechanical properties of the final products [3].

Much research has been reported in the literature about the interaction between the microstructural evolution and microalloying precipitation in these steels [54, 140]. Much less investigation has been focused on the effect of initial structure as a result of thermomechanical processing and the presence of microalloying elements. However, it was of interest to investigate cold rolled TRIP steels with microalloy additions designed to give intense precipitation in addition to the effect of intercritical annealing. Two alloys were investigated from a split cast; one where the principal microalloy addition was V, with a second with otherwise identical composition, but additionally containing Mo and Nb microalloy additions. This is of paramount importance in the context of microalloyed steels, because of the interaction between strong microalloying carbonitride formers and the evolution of microstructure at temperatures up to the range of intercritical annealing.

In this chapter the aim was to investigate the interaction between the evolution of microstructure and precipitation behaviour after intercritical annealing, focusing on the Nb,Mo,V or only V precipitation systems. The results corresponding to each thermomechanical processing stage are initially presented and then their contributions to the microstructure and precipitation behaviour will be discussed.

## **5.2. Results**

### **5.2.1. Microstructural Characterizations**

In this section the results of microstructural examination after each thermomechanical processing step (i.e. rough rolling, cold rolling and intercritical annealing) are presented.

#### **5.2.1.1. Rough Rolled Structure**

Figs. 5.1 (a) and (b), show the microstructure of the as-cast Alloys 2 and 3, containing ferritic matrix and pearlite islands as secondary constituents. The rough rolling was conducted according to the schedule shown in Fig. 3.5. The evolution of microstructure after the roughing process, in the rolling and normal directions is shown in Fig. 5.1.

The micrographs of normal and rolling directions of Alloy 2 and 3 indicate that there was no significant elongation. It is clear that during cooling the allotriomorphic ferrite formed at grain boundaries. The presence of small lath shape constituents is considered as acicular/bainitic ferrite and martensite. In addition, from the optical microscopy observations, it was found that the Widmanstatten ferrite formed in the microstructure of Alloy 3 with a random distribution after the roughing. Fig. 5.2 shows the optical micrograph of Widmanstatten ferrite among other phases, whereas it was no longer seen in Alloy 2. The structure is similar to that shown by Bhadeshia regarding a typical Widmanstatten ferrite [67]. This behaviour is consistent with the results reported by Pereloma et al. about the TRIP assisted steels without Nb. They pointed out that the absence of Nb might encourage the formation of such a feature in the microstructure [40].

As can be seen in Fig. 5.1, the final microstructure due to the presence of NbMo in Alloy 2 was significantly different to that from Alloy 3. The dark regions in Fig. 5.1 were studied in more detail by SEM (Fig. 5.3). The areas with the brightest contrast and a smooth surface are retained austenite and martensite, whereas the bright comb shape substructure with a lath and/or block shape are considered to be bainite. TEM



observations also confirmed that the secondary constituents in as-cast structure are pearlite (Figs. 5.4 (a)).

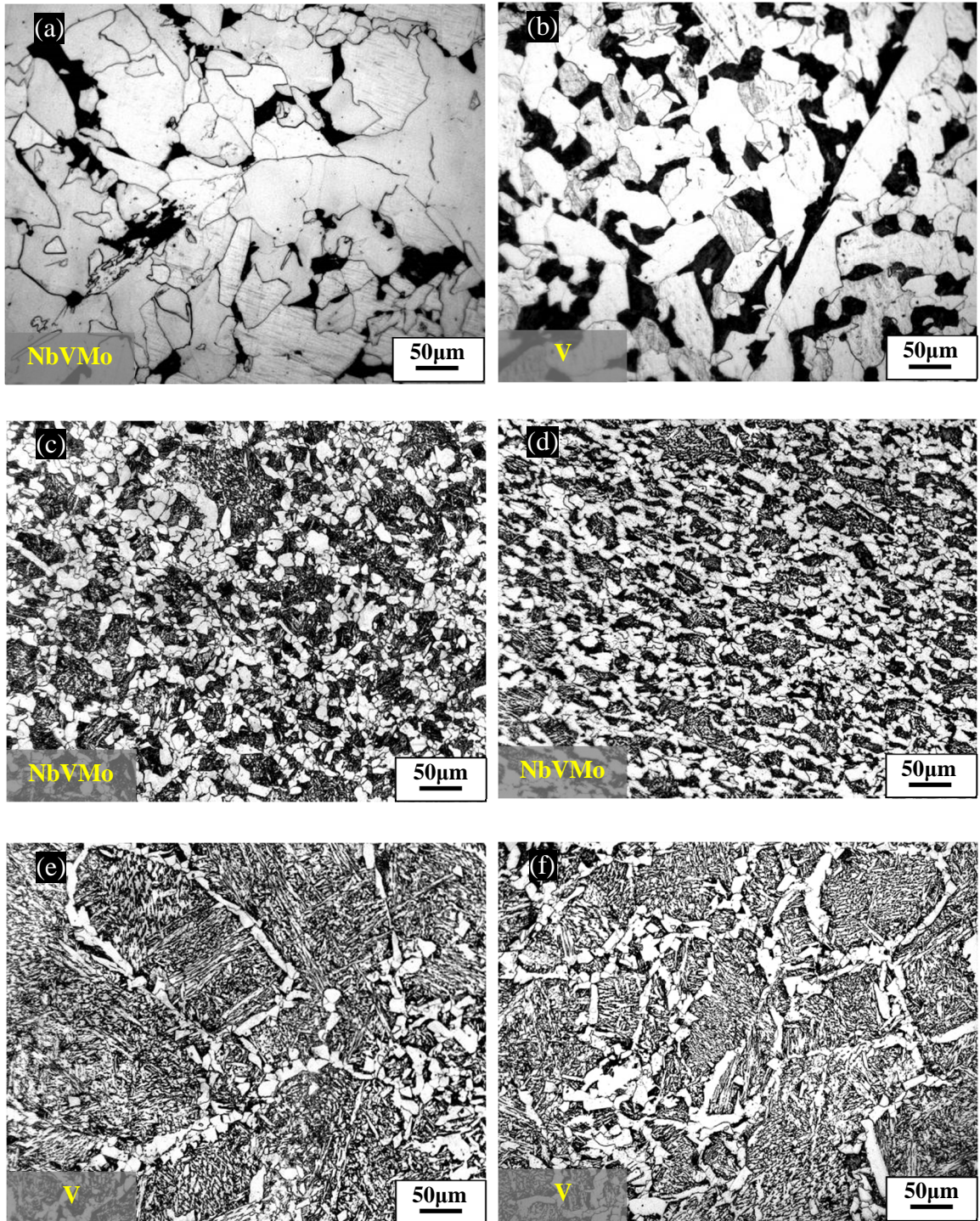


Fig. 5.1, Optical micrographs of as-cast and rough rolled samples, (a) and (b) As cast of Alloys 2 and 3, respectively, (c) and (d) Normal and rolling direction planes of rough rolled Alloy 2, respectively, (e) and (f) Normal and rolling direction planes of rough rolled Alloy 3, respectively.



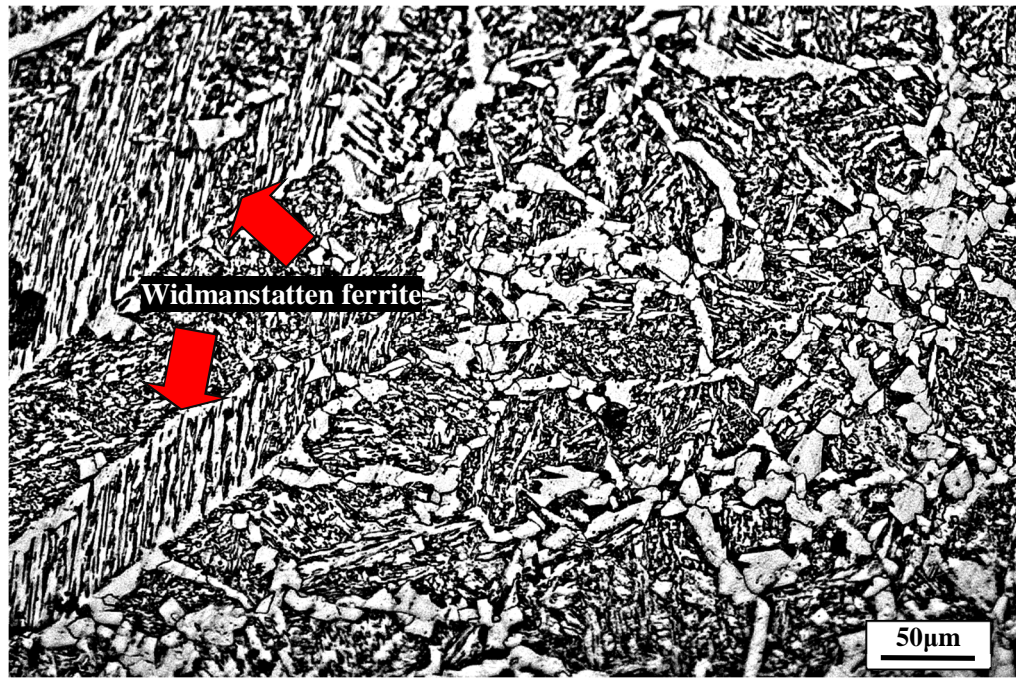


Fig. 5.2, Typical optical micrograph of the rough rolled Alloy 3, showing the presence of widmanstatten ferrite.

Fig. 5.3 compares SEM micrographs of the microstructure of Alloys 2 and 3, before and after the roughing process. The packets of secondary constituents are retained austenite, bainitic ferrite, cementite and randomly distributed martensite (Figs. 5.4 to 5.6). These features are also named by some authors in the literature as “granular bainite” (Fig. 5.3 (c) and (d)) [17, 141]. However, the TEM observations clarified the nature of different constituents in these regions. TEM observations of thin foil samples illustrate the presence of bainite and martensite through these regions (i.e. bright features in SEM micrographs), which are named here as “secondary phases” (Figs. 5.4 and 5.5).

Fig. 5.6 shows a partial decomposition of a blocky shape austenite and the remaining film shape retained austenite among lath ferritic constituents.



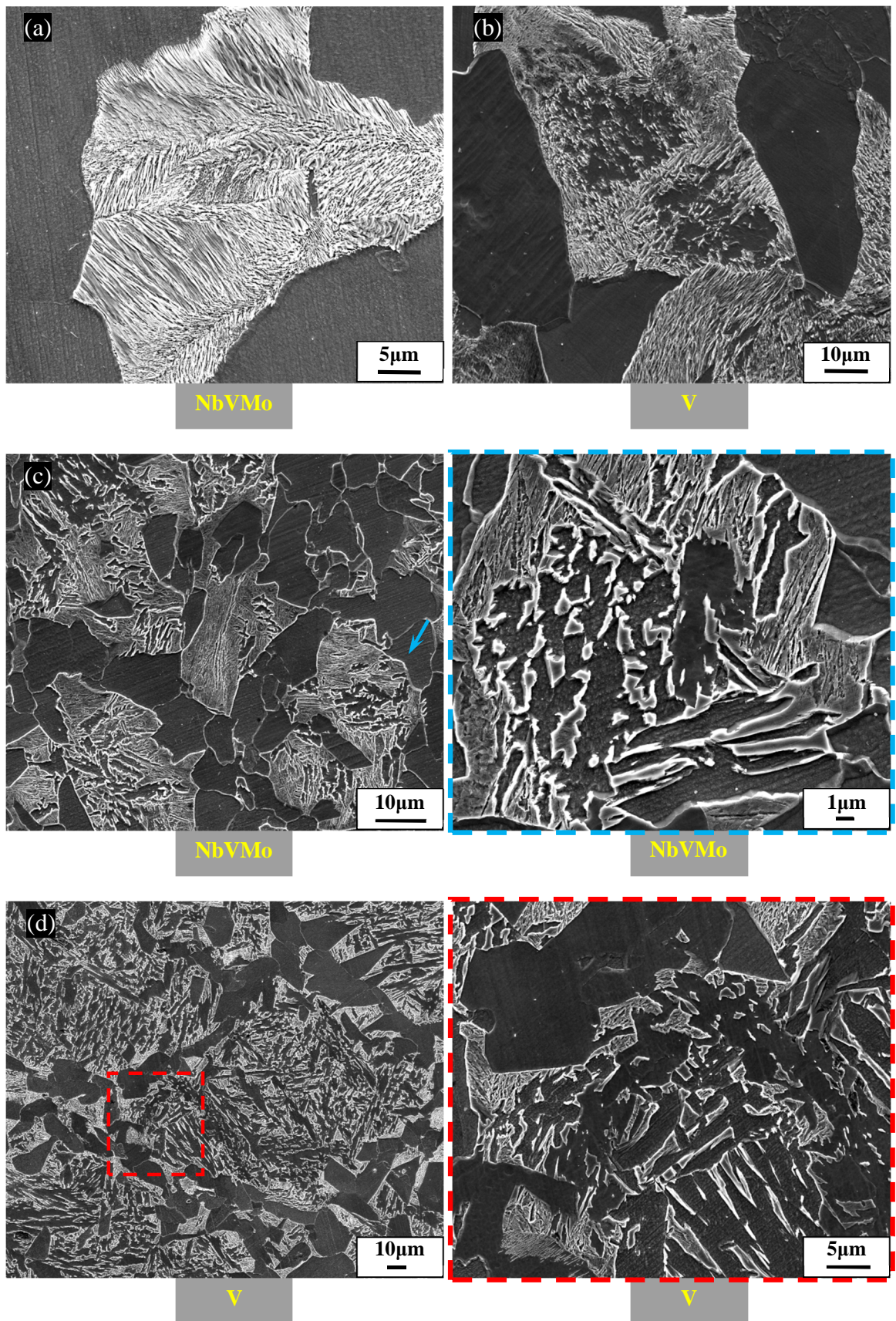


Fig. 5.3, Scanning electron micrographs of as-cast and rough rolled samples, (a) and (b) As-cast of Alloys 2 and 3, respectively, (c) Rough rolled Alloy 2 and a magnified image, (d) Rough rolled Alloy 3 and a magnified image, respectively.



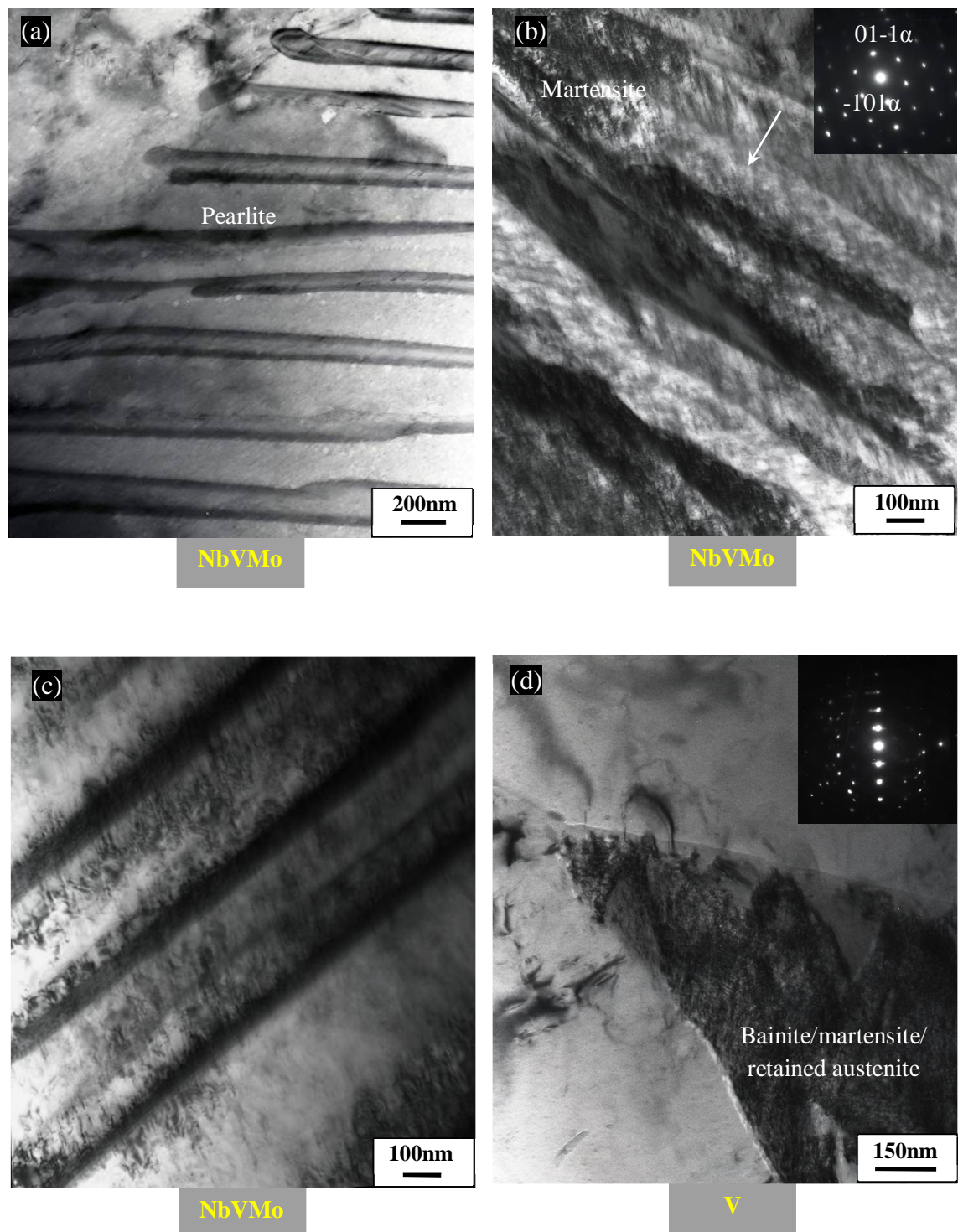


Fig. 5.4, Selected transmission electron micrographs of thin-foil samples of Alloys 2 and 3 before and after the rough rolling, showing different features as secondary phases in the microstructure, (a) As-cast Alloy 2, (b) Rough rolled Alloy 2 and corresponding electron diffraction pattern with bcc structure in zone axis  $[111]$ , (c) Rough rolled Alloy 2, (d) Rough rolled Alloy 3.

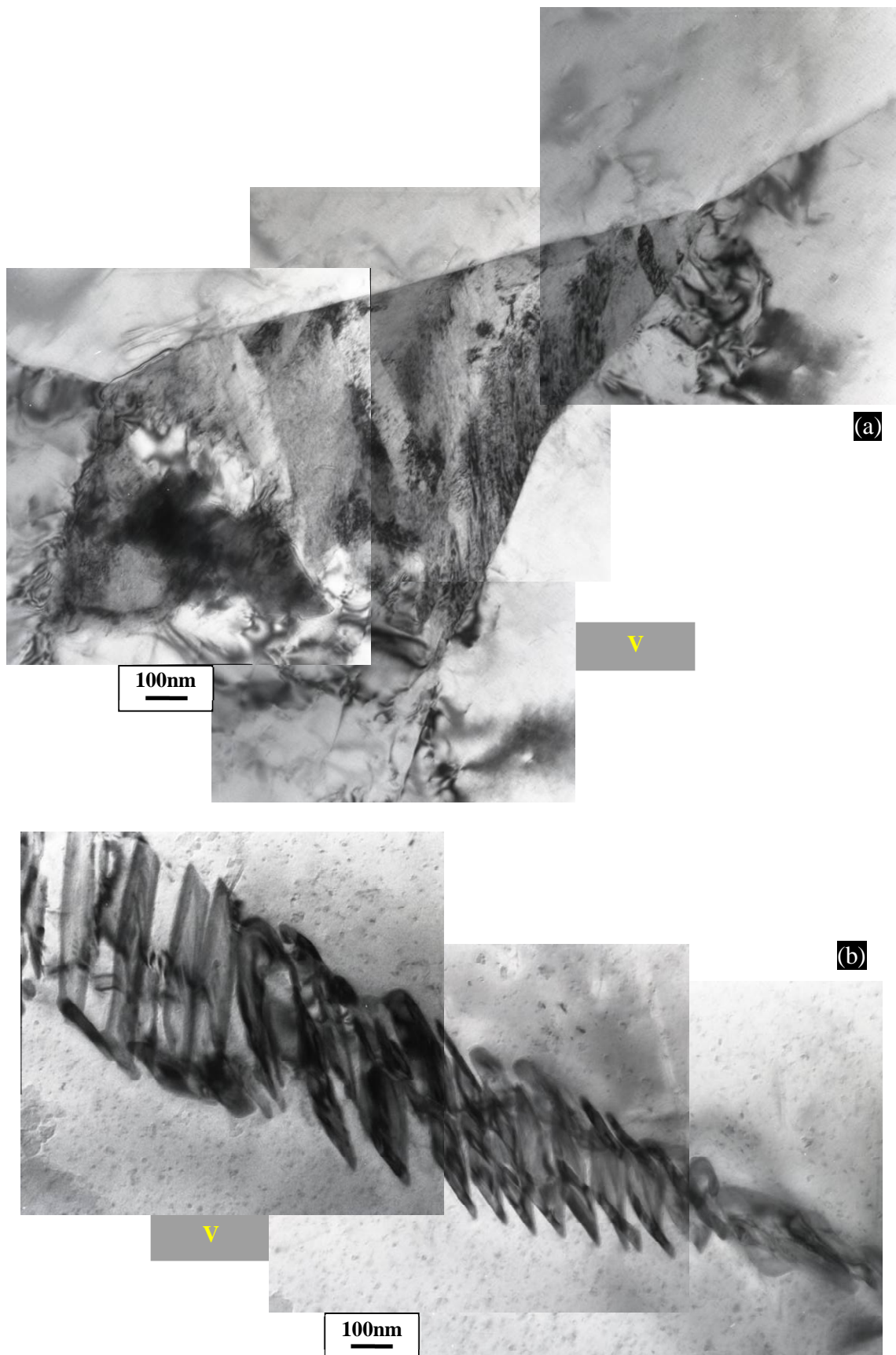


Fig. 5.5, Selected transmission electron micrographs of thin-foil sample of Alloys 3 after rough rolling, (a) Showing a bainitic ferritic feature, (b) Showing a feature similar to pearlite.

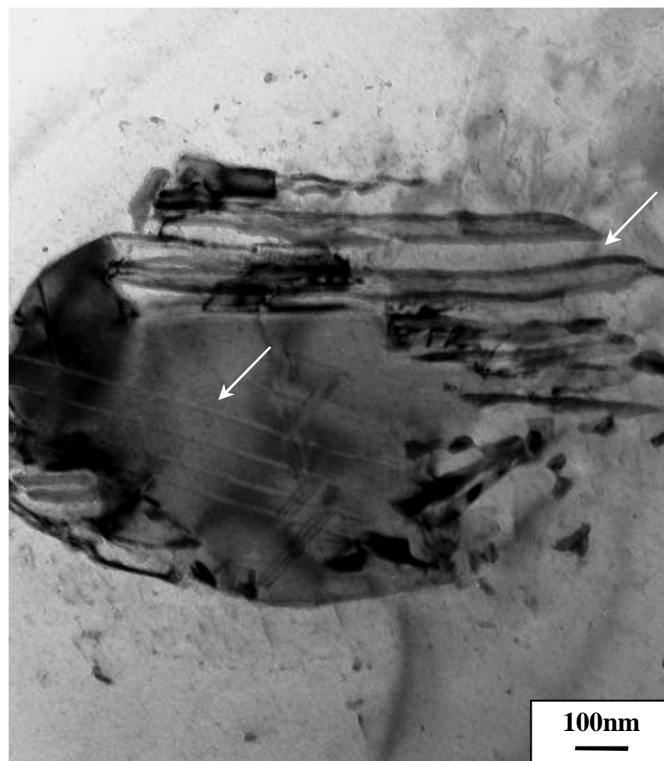


Fig. 5.6, Bright field TEM image of thin foil from the rough rolled Alloy 3, showing the partial decomposition of a block shape retained austenite with features similar to martensite.

#### 5.2.1.2. Cold Rolled and Intercritical Annealed Structure

Fig. 5.7 shows typical optical and SEM micrographs of the cold rolled samples of Alloys 2 and 3, after ~20% rolling reduction. As expected, in both alloys the microstructure shows a preferential orientation along the rolling direction. In addition, the microstructure shows a slight fragmentation of secondary phases throughout the ferritic matrix (Figs. 5.7 (e) and (f)). Interestingly, the Nb,V,Mo containing steel (Alloy 2), after the cold rolling exhibited a significant ferrite grain size reduction, whereas in Nb,Mo free steel (Alloy 3) it was less effective and the microstructure exhibited an equiaxed ferrite structure.

Fig. 5.8 shows the microstructure of the cold rolled samples after the intercritical annealing. A comparison between Figs. 5.7 and 5.8 shows that the intercritical anneal had resulted in recrystallization, as expected. The recrystallization of ferrite did not occur through the dark regions, i.e. lath ferritic and martensite, and it was mainly observed in the allotriomorphic ferrite.

Figs. 5.8 (c) and (d), compare the microstructure of the secondary phases i.e. retained austenite, martensite and bainite, after the intercritical annealing of the cold rolled samples.



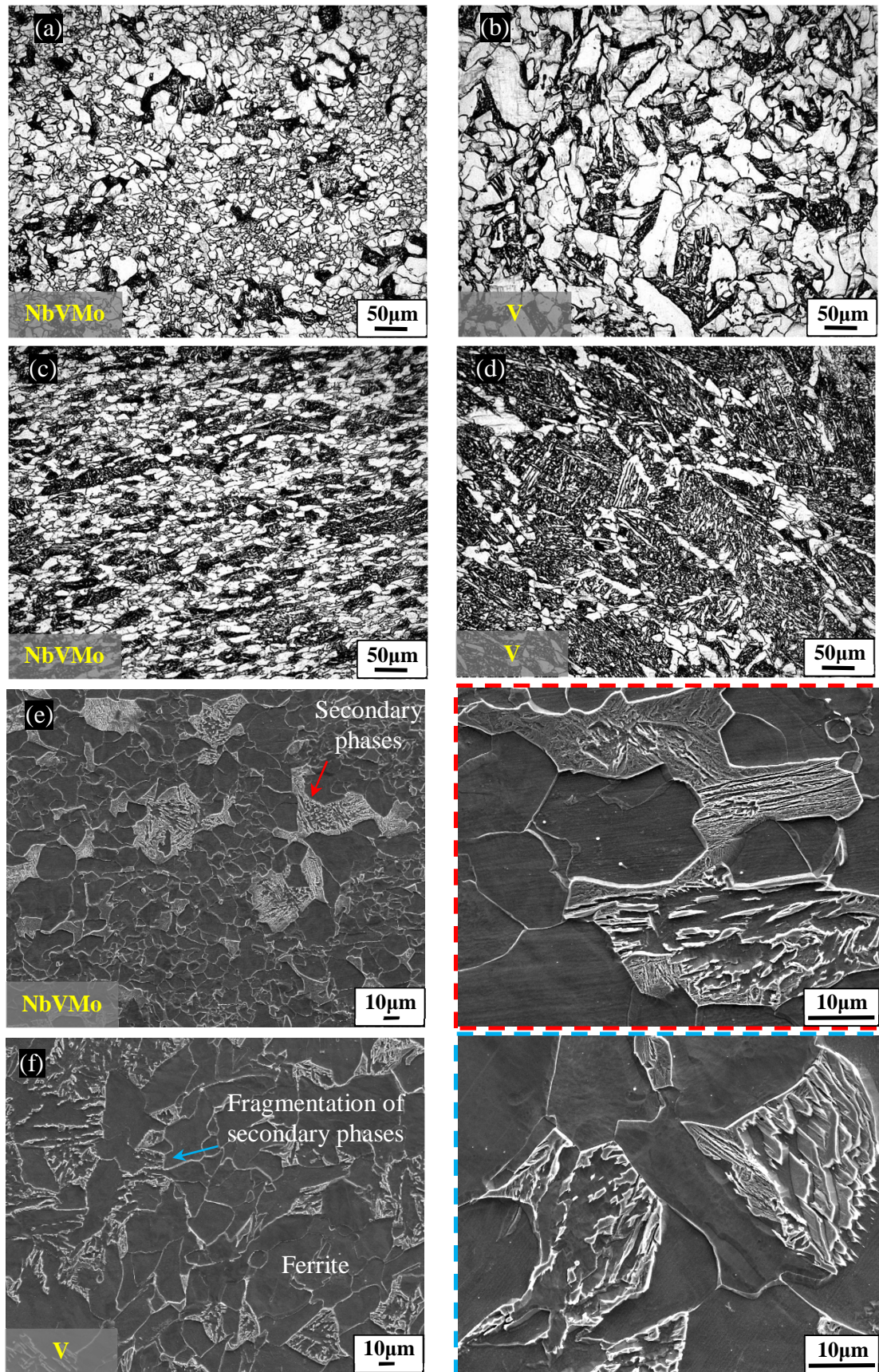


Fig. 5.7, (a) and (b) Optical micrographs of the normal direction plane of cold rolled Alloys 2 and 3, respectively (c) and (d) Optical micrographs of the rolling direction plane of cold rolled Alloys 2 and 3, respectively, (e) and (f) Scanning electron micrographs of cold rolled Alloys 2 and 3 in normal direction with two different magnifications, respectively.



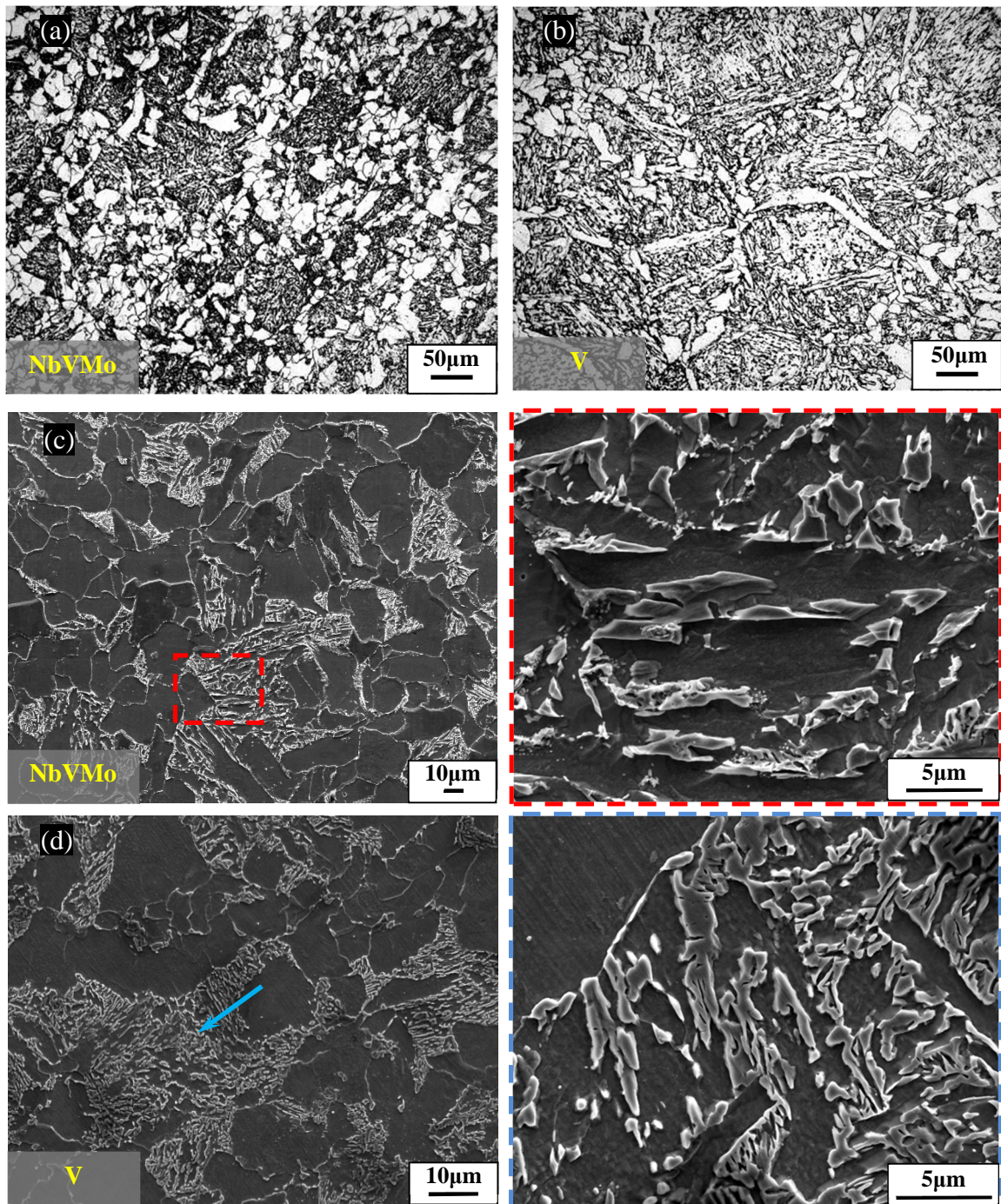


Fig. 5.8, Micrographs corresponding the normal direction plane of the intercritical annealed samples, (a) and (b) Optical micrographs of Alloys 2 and 3, respectively, (c) Scanning electron micrographs of Alloy 2 with two different magnifications, (d) Scanning electron micrographs of Alloy 3 with two different magnifications.

Fig. 5.9 shows the microstructure of the interrupted quench samples at the end of isothermal intercritical annealing stage (stage 3 at 795°C, see Fig .3.5). The bright constituents correspond to the martensite and possible retained austenite. The



microstructures of the interrupted quench samples showed the partial dissolution and coalescence of the secondary phases.

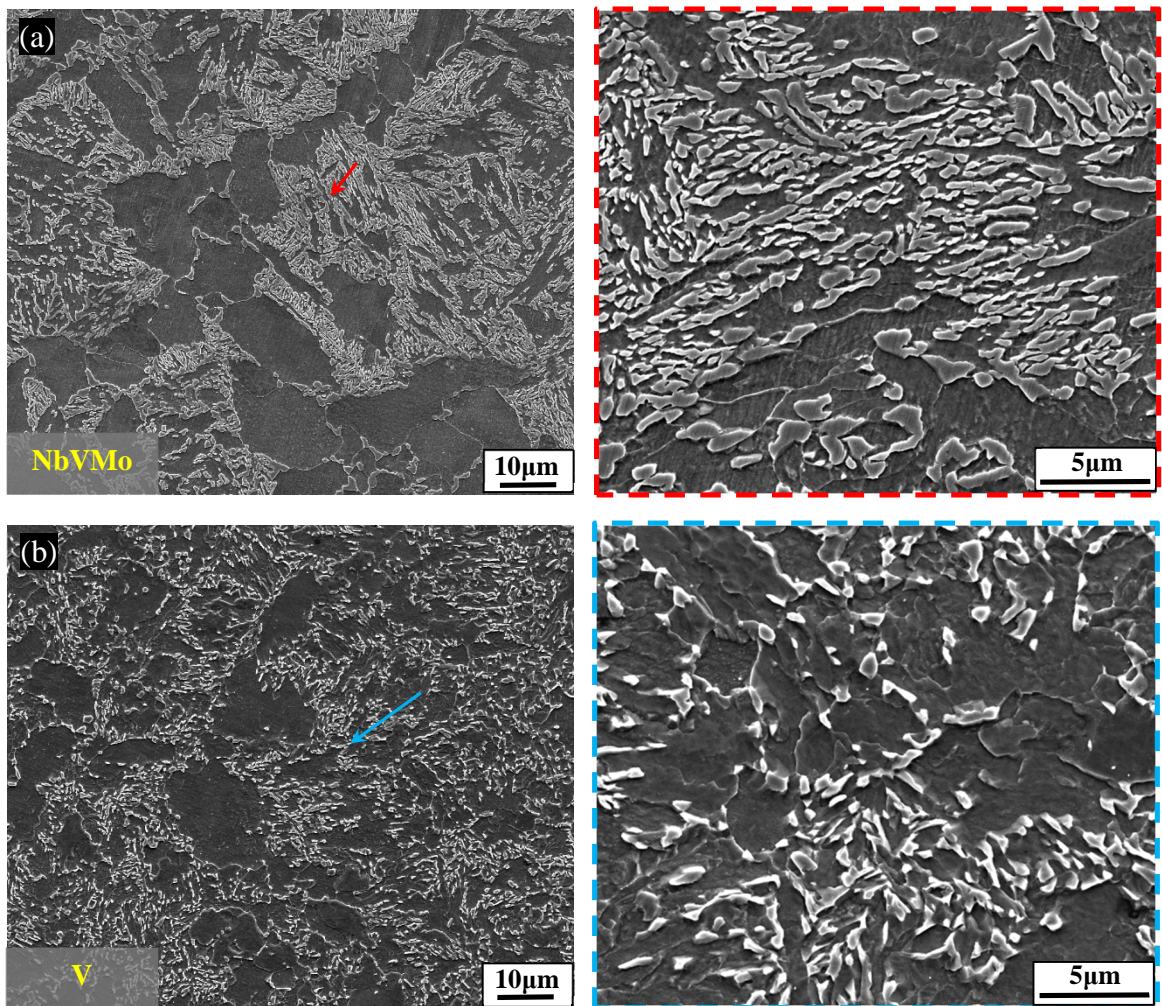
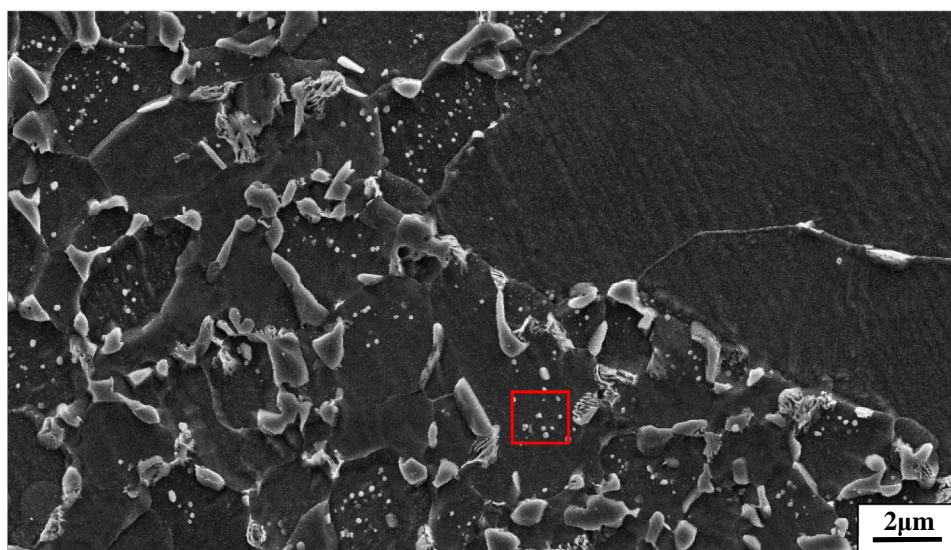
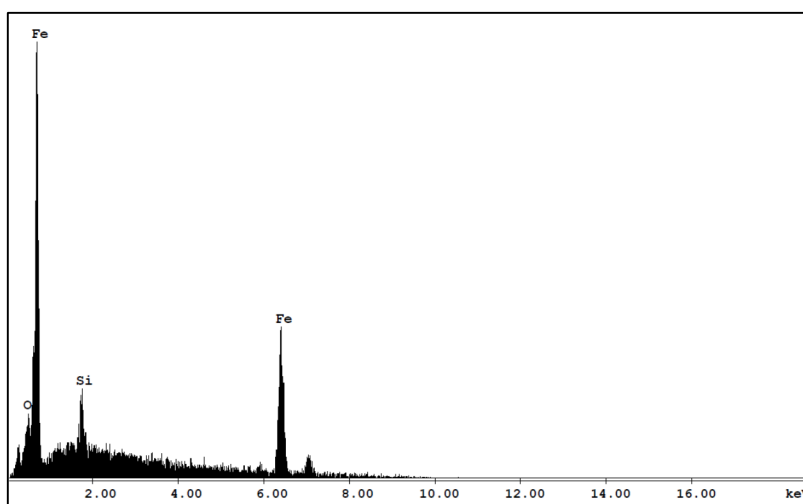
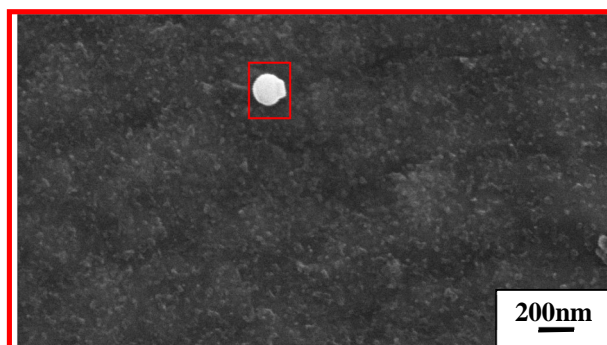


Fig. 5.9, Scanning electron micrographs, showing the microstructure of interrupted quench samples at the end of isothermal intercritical annealing, (a) Alloy 2 with two different magnifications, (b) Alloy 3 with two different magnifications.

In addition, small particles similar to precipitates after the intercritical annealing with an average size between 180 and 200nm were observed in SEM micrographs of both alloys (Figs. 5.10 and 5.11). However, the EDS spectra acquired from SEM microscopy failed to show the peaks corresponding to the microalloying elements in these features. This was probably due to the relative small size of these particles compared with the interaction volume of beam. It is therefore impossible to suggest that whether or not these features contain microalloying elements.



(a)



(b)

Fig. 5.10, (a) Scanning electron micrograph of the cold rolled Alloy 3 after the intercritical annealing, showing features similar to the precipitates, (b) EDS spectrum corresponding to these precipitates.

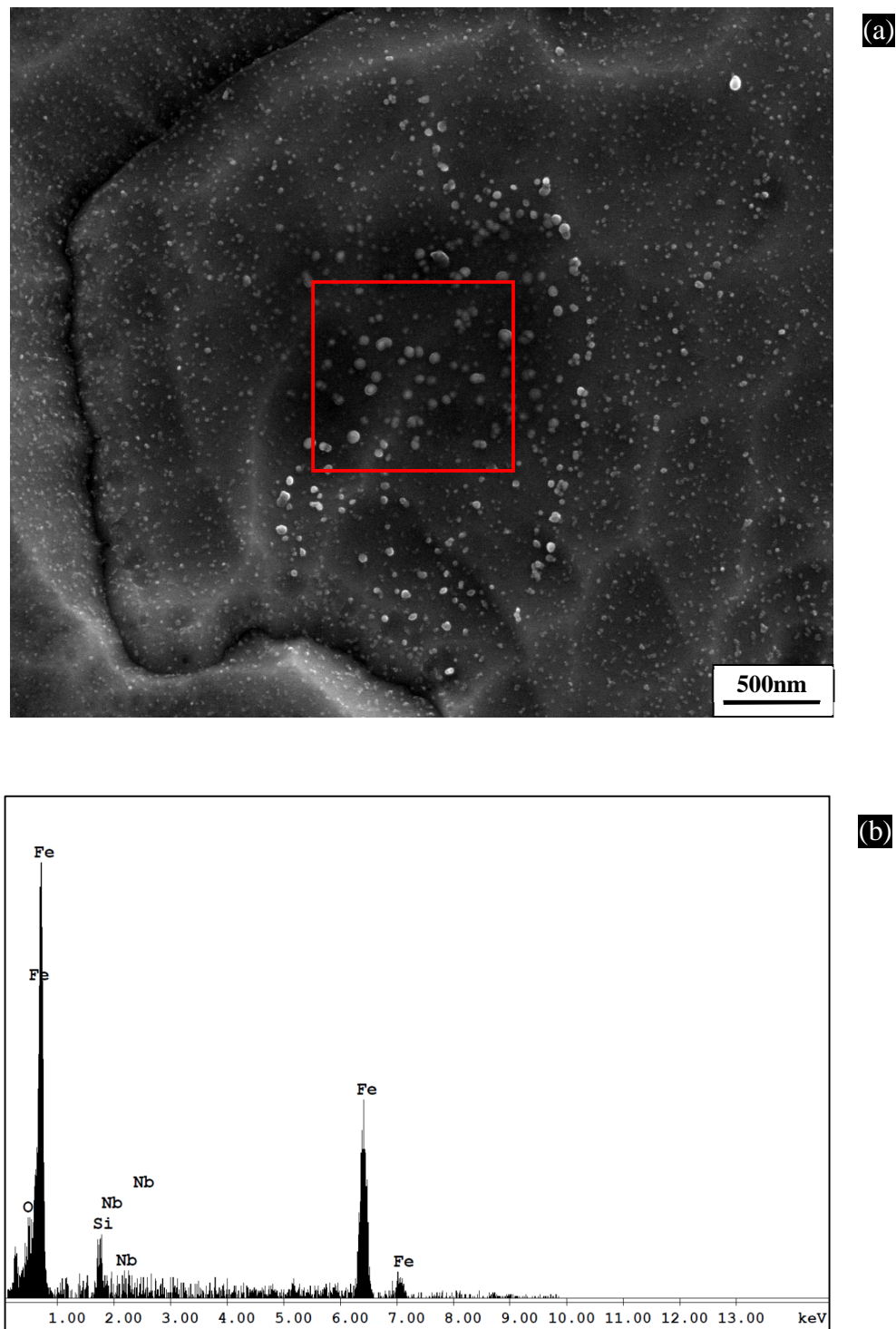


Fig. 5.11, (a) Scanning electron micrograph of the cold rolled Alloy 2 after the intercritical annealing, showing features similar to the precipitates, (b) EDS spectrum corresponding to these precipitates.

The TEM observations revealed the presence of retained austenite, martensite, and bainite after the intercritical annealing of both Alloys 2 and 3 (Figs. 5.12 and 5.13).



Fig. 5.12 shows a typical micrograph of the retained austenite adjacent to the microalloying precipitates of Alloy 3 which was formed during the intercritical annealing.

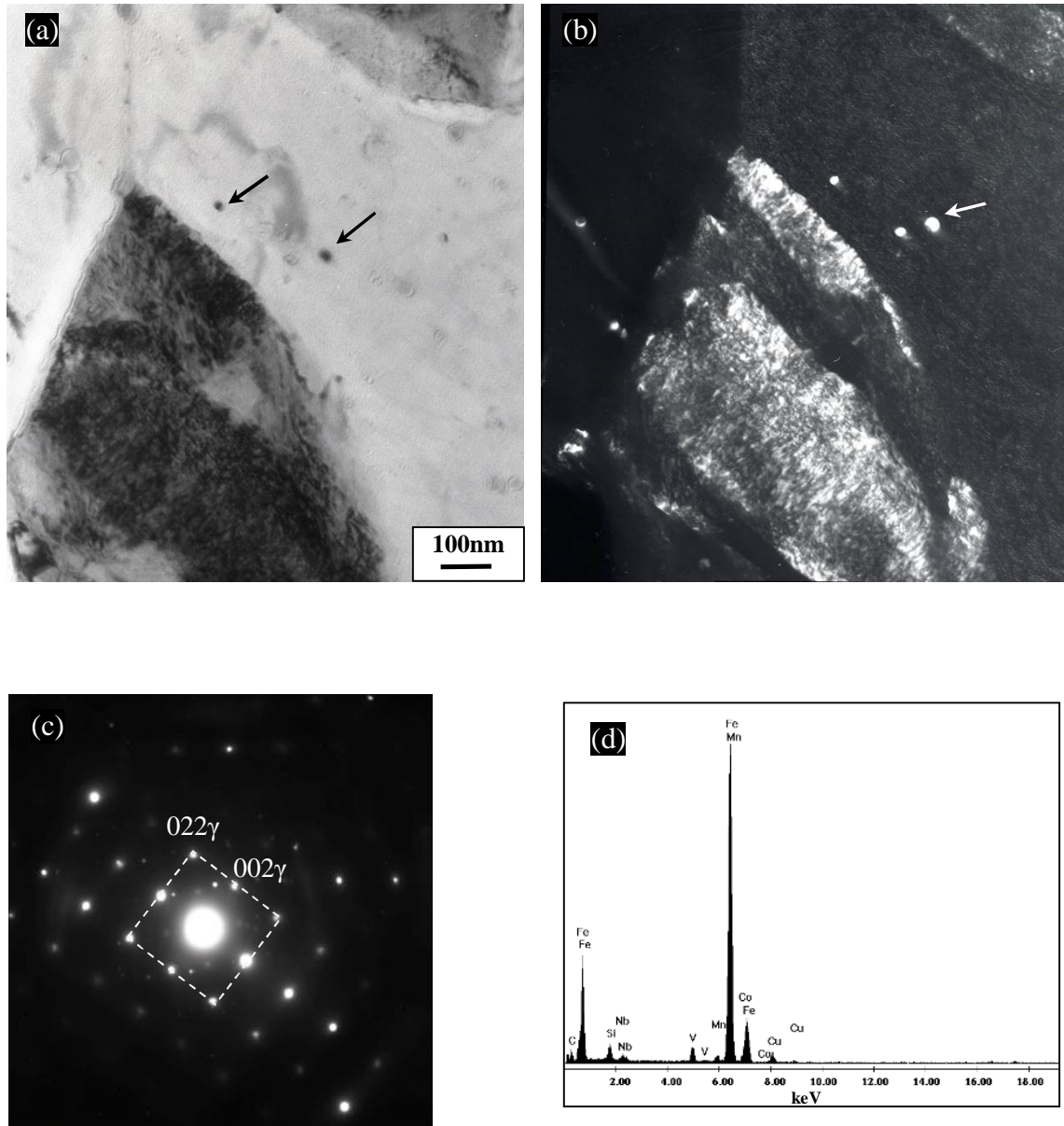


Fig. 5.12, Selected thin-foil transmission electron micrographs of cold rolled Alloy 3 after the intercritical annealing, (a) and (b) Bright and dark field images, showing the presence of precipitates adjacent to retained austenite, respectively, (c) Corresponding SAED pattern ([100] zone axis), (d) A typical EDS spectrum, showing the presence of Nb and V in the observed precipitates in (a).

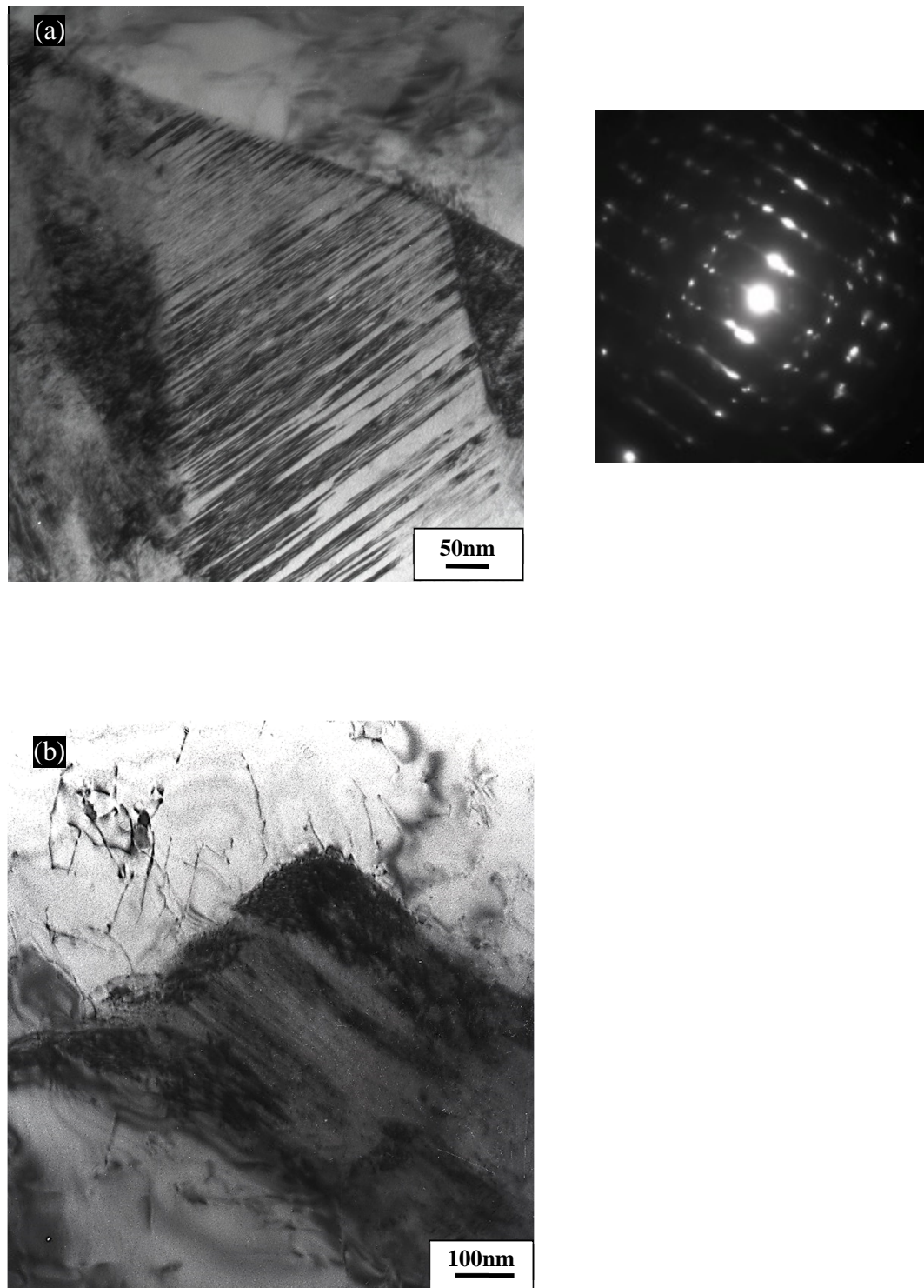


Fig. 5.13, Two selected bright field images of thin-foil transmission electron micrographs of cold rolled Alloy 3 after intercritical annealing, (a) A typical twinning structure and corresponding SAED pattern, showing the presence of martensite, (b) Showing a bainitic feature and the presence of dislocations in the vicinity of interfaces.

### 5.2.2. Grain Size Measurements and Retained Austenite Content

The prior austenite grain size of the rough rolled structure was approximately delineated by the position of allotriomorphic ferrite formed at the prior austenite grain boundaries (Fig. 5.1). Details of grain size measurements are summarized in Table 5.1.

Table 5.1, The grain size of ferrite and prior austenite measured by intercept method.

		As cast	Rough rolled (prior $\gamma$ )	Rough rolled (ferrite ( $\alpha$ ))	Cold rolled (ferrite)	Intercritical annealed
Grain size ( $\mu\text{m}$ )	Alloy 2	38.6 $\pm$ 10.1	53.0 $\pm$ 5.0	13.3 $\pm$ 1.9	9.5 $\pm$ 1.9	13.9 $\pm$ 3.4
	Alloy 3	47.9 $\pm$ 15.4	97.0 $\pm$ 8.0	15.1 $\pm$ 5.5	21.3 $\pm$ 2.8	17.3 $\pm$ 4.9

In addition, the variations of ferrite grain size and prior austenite grains in terms of the thermomechanical processing used for Alloys 2 and 3 are compared in Fig. 5.14.

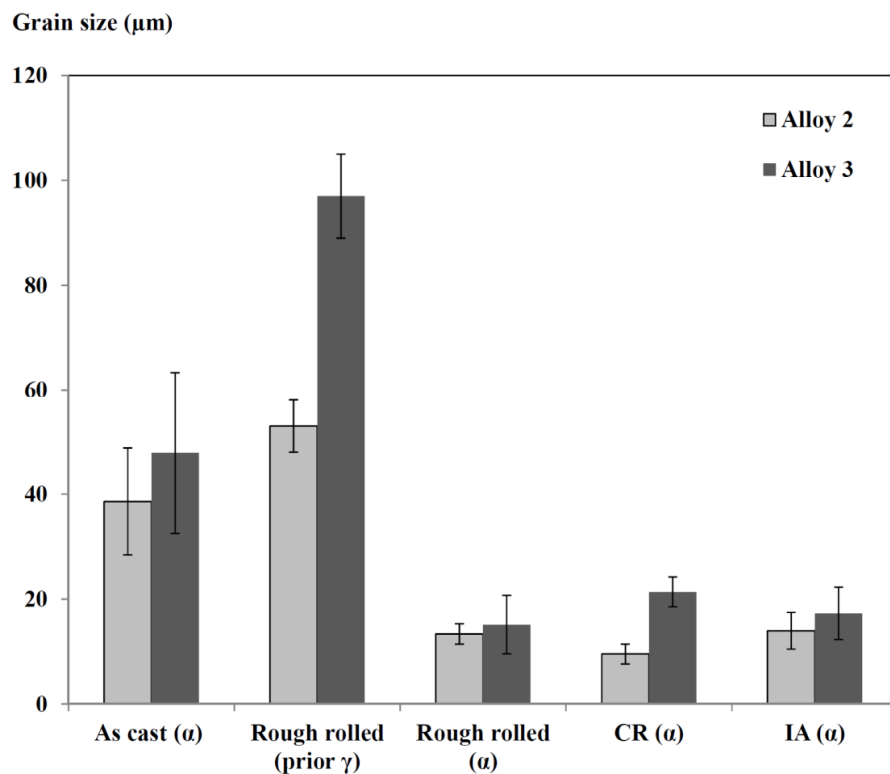


Fig. 5.14, Variation of ferrite grain size versus different thermomechanical processing, measured by intercept method from the SEM micrographs,  $\gamma$ ; austenite,  $\alpha$ ; ferrite, CR; cold rolled, IA; intercritical annealed.

Fig. 5.15 gives typical XRD spectra corresponding to Alloy 2, which is indexed by the standard JCPDS cards [122]. The XRD patterns of intercritical annealed samples showed two main peaks corresponding to ferrite and retained austenite. By contrast, in the rough rolled samples before the intercritical annealing an extra set of peaks was observed, which corresponded to cementite that was found in the XRD pattern of both Alloys 2 and 3.

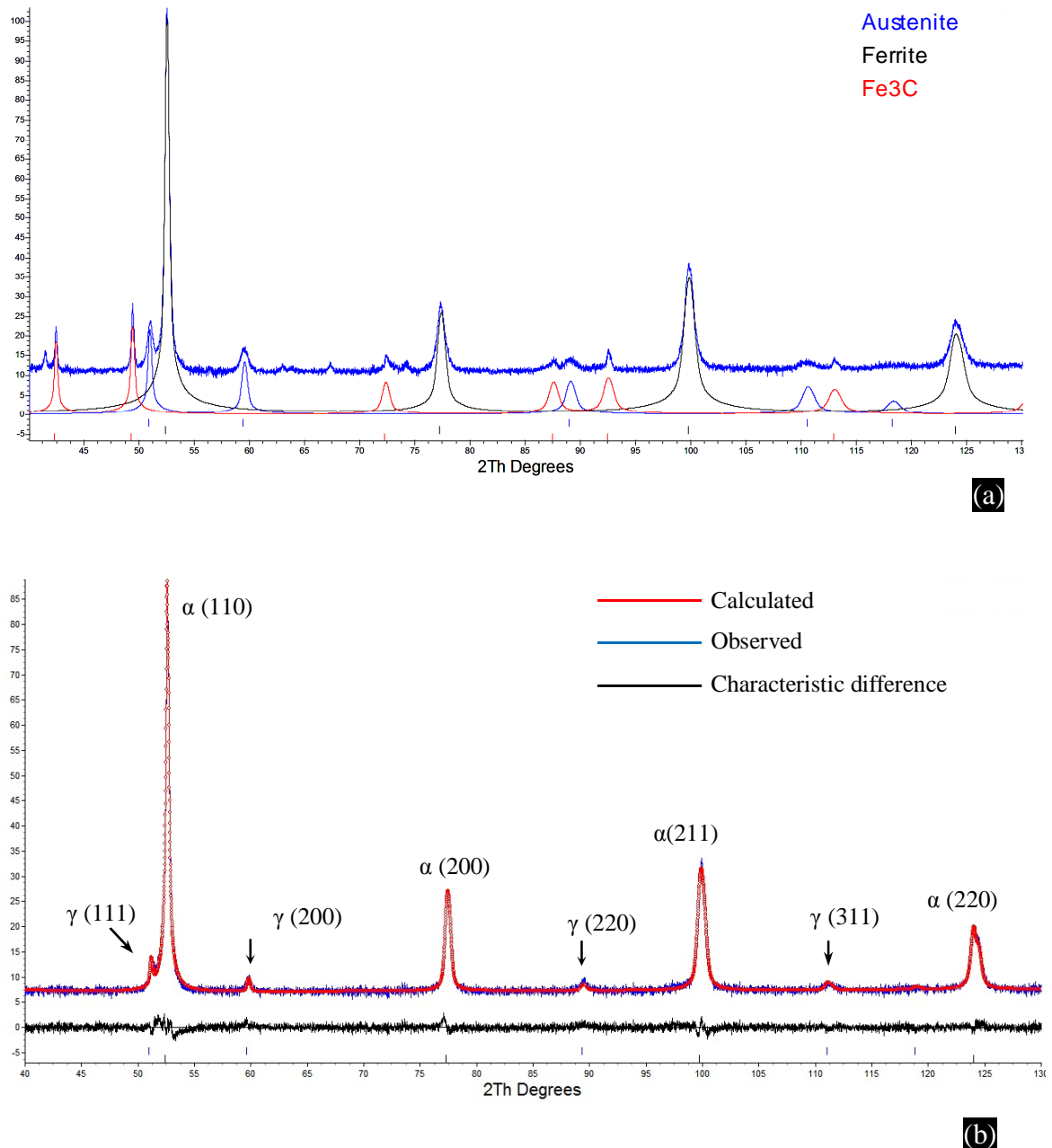


Fig. 5.15, Selected graphical representation of X-ray diffraction pattern of Alloy 2, (a) Showing the peaks corresponding to the ferrite, retained austenite and cementite in the rough rolled sample, (b) A selected graphical representation of Rietveld analysis for X-ray diffraction pattern of the intercritical annealed sample.



The amount of retained austenite was measured from the integrated intensity of XRD patterns. Table 5.2 shows the details of the volume fraction, lattice parameter and carbon content of the retained austenite and the volume fraction of cementite in Alloys 2 and 3.

The carbon content was measured from the lattice parameter of retained austenite using equation 4.1. From the results, it was found that the presence of Nb and Mo in the microstructure did not significantly change the amount of retained austenite after the intercritical annealing. Similarly, the carbon content of retained austenite after the intercritical annealing showed a slightly lower level compared to Alloy 3.

Table 5.2, The retained austenite characteristics and Fe<sub>3</sub>C, examined by XRD.

	Thermomechanical processing	Retained austenite (%)	Carbon content of austenite (%)	Austenite lattice parameter (Å)	Fe <sub>3</sub> C (%)
Alloy 2 (NbMo containing)	Rough rolled	9.7	1.305	3.60767±0.00119	1.4
	Intercritical annealed	7.4	1.164	3.59773±0.00198	Neg.
Alloy 3 (NbMo free)	Rough rolled	2.9	1.248	3.60497±0.00127	1.2
	Intercritical annealed	8.2	1.193	3.60105±0.00095	Neg.
Neg.; negligible, i.e. less than 1.0%					

### 5.2.3. Precipitation Behaviour

#### 5.2.3.1. TEM Thin Foil Analysis

It has been well established that Nb and V are able to precipitate during intercritical annealing [19, 41]. IZA-Mendia's et al. studies on the low temperature transformations i.e. temperatures between 600°C to 750°C, showed the possible NbC precipitation [53]. After the roughing stage and also intercritical annealing the

characterization of precipitates was carried out by thin foil sample and carbon extraction replica techniques.

The TEM observations indicated the presence of precipitates with different morphologies and a wide size distribution. The position of precipitates, the size distribution and their chemical analysis were taken into consideration to interpret the precipitation behaviour in Alloys 2 and 3. The precipitates were present in both Alloys 2 and 3, before and after the intercritical annealing. They were characterized in terms of their size, density, morphology and chemical composition.

The analyses indicated considerable precipitation in both Alloys 2 and 3 at transformation  $\leq 795^{\circ}\text{C}$ . In thin foil samples, two different techniques of EDS microanalysis and dark field (DF) were applied to identify the precipitates from other unwanted sources of contrast such as a periodic contrast of dislocations, thickness fringes and oxides.

Fig. 5.16 shows typical bright and dark field images of the thin foil samples of the rough rolled Alloy 3. The EDS spectra acquired from the small precipitates revealed the presence of vanadium. It is seen clearly that precipitates with different morphologies were formed inside the ferrite grains as well as throughout grain boundaries.

The copper and iron peaks were present in almost all of spectra. The observed copper peaks in EDS spectra are due to the copper grid and TEM holder and the Fe peaks in replica samples arises from the extraction of iron from the substrate.

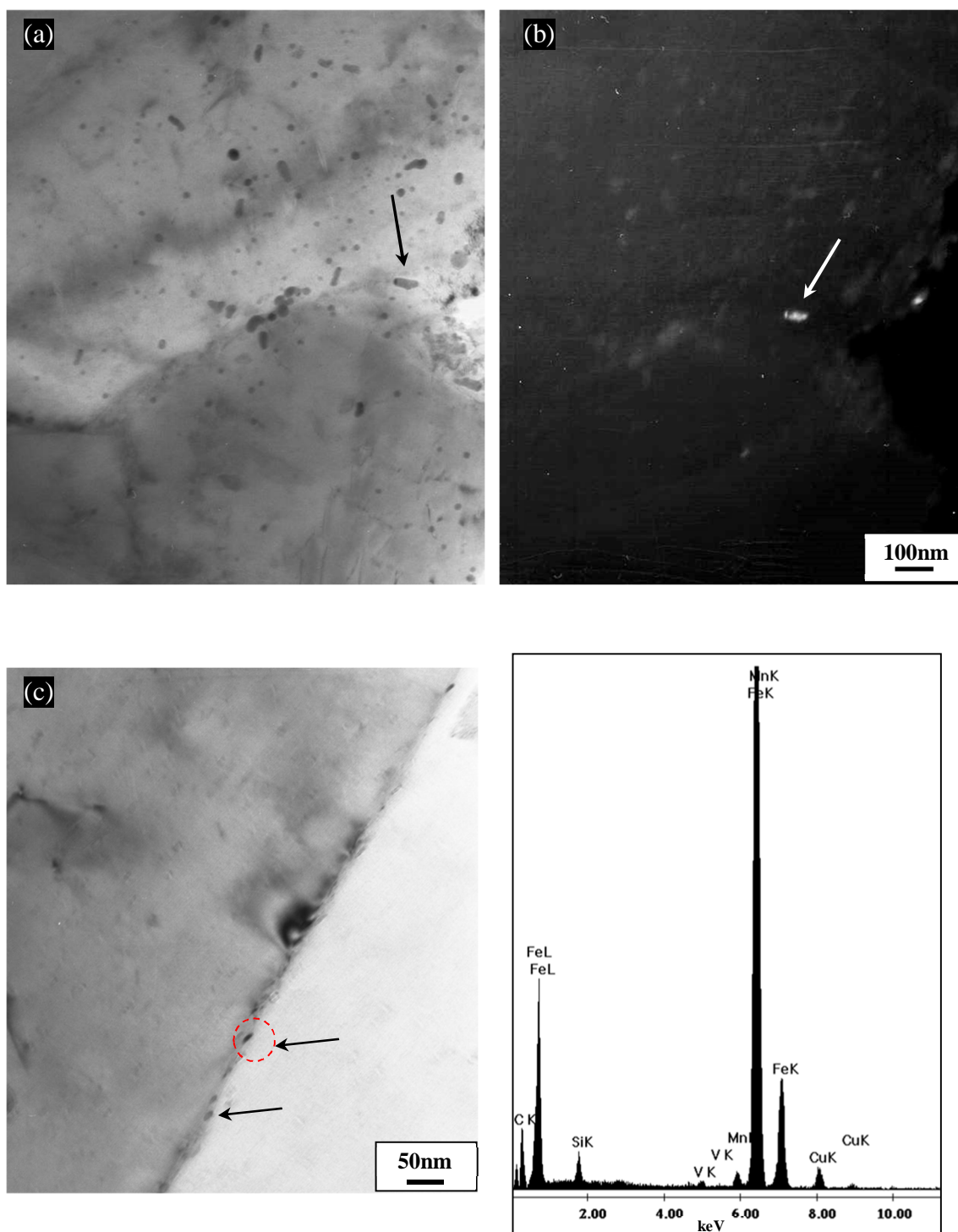


Fig. 5.16, Thin-foil transmission electron micrographs of rough rolled Alloy 3 (a) and (b) Bright and dark field images, showing the presence of precipitates at grain boundary and interior of ferrite, (c) Showing the presence of precipitates along grain boundary and a typical corresponding EDS spectrum.

Fig. 5.17 gives TEM micrographs of ferrite with microalloying containing precipitates in Alloy 3. The EDS microanalysis revealed the presence of V based precipitates among dislocations and inside the grain interior. The dislocation density in both steels was generally low, although accumulations of dislocations at the corner of grain boundaries were occasionally observed (Fig. 5.17 (b)).

It is believed that increasing the temperature up to the intercritical range (i.e. 795°C) might lead to recovery in the microstructure [47, 142]. Interestingly, despite the high possibility of recovery, the presence of precipitates through the regions with a high dislocation density was observed. It can be assumed that the interaction between dislocations and precipitation was due to those dislocations that were formed due to the transformation and being pinned by precipitates. This will be discussed in section 5.3.

Additionally, precipitates were observed inside the martensite and retained austenite for both alloys (Figs. 5.18 and 5.19). It is likely the observed martensite arose from transformation of the austenite formed during the intercritical annealing. This will be discussed in section 5.3.

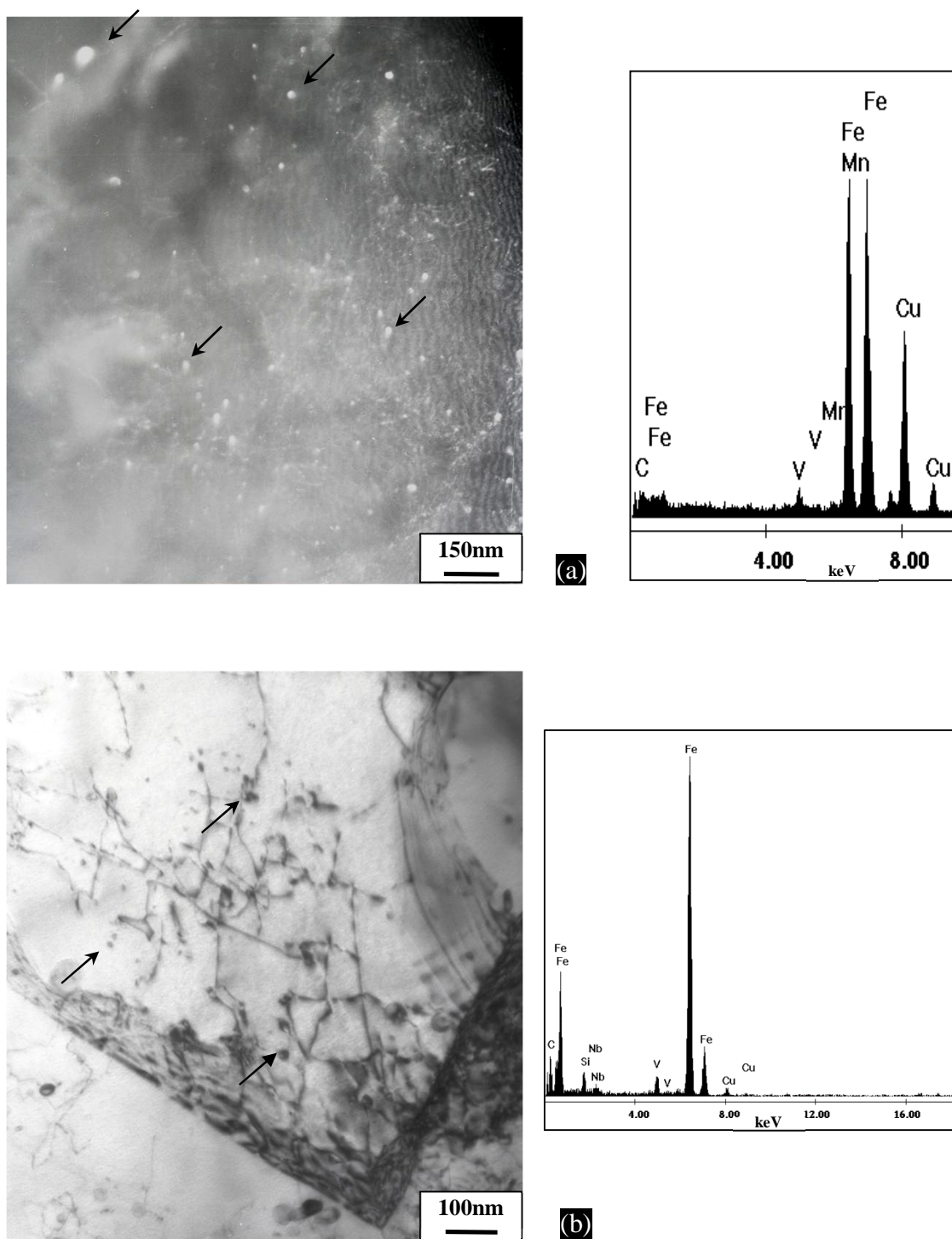


Fig. 5.17, Typical thin-foil transmission electron micrographs of cold rolled sample after the intercritical annealing, (a) Showing the presence of fine precipitates in the ferrite in Alloy 3 and corresponding typical EDS spectrum, (b) Showing the presence of fine precipitates in the vicinity of grain boundary of the ferrite in Alloy 2 and corresponding typical EDS spectrum.

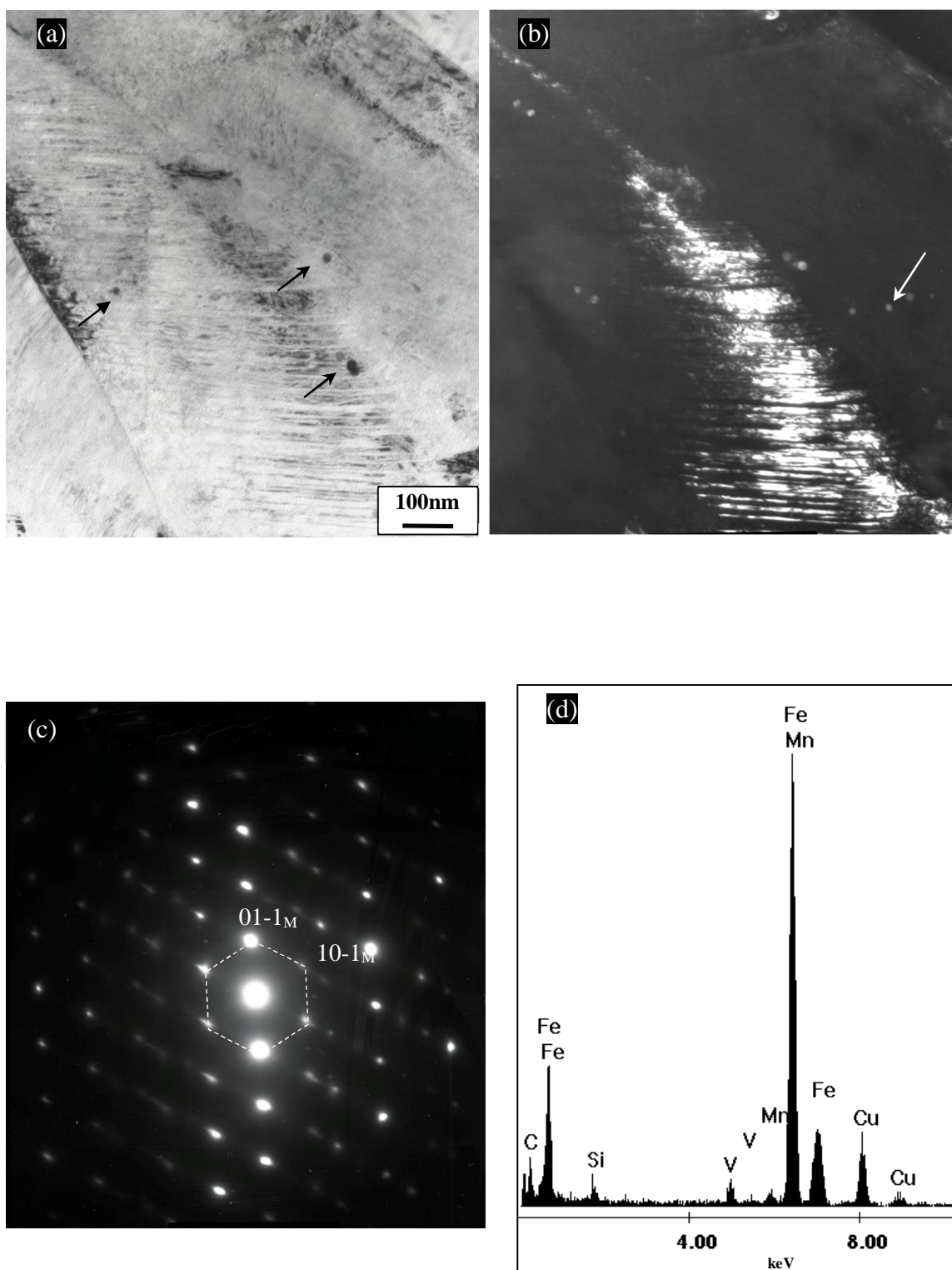


Fig. 5.18, Selected thin-foil transmission electron micrographs of Alloy 3 after the intercritical annealing, (a) and (b) Bright and dark field images, showing the presence of V precipitates inside the martensite, respectively, (c) SAED pattern corresponding martensite region (zone axis  $[111]$ ), (d) Corresponding typical EDS spectrum of precipitates shown by arrows.

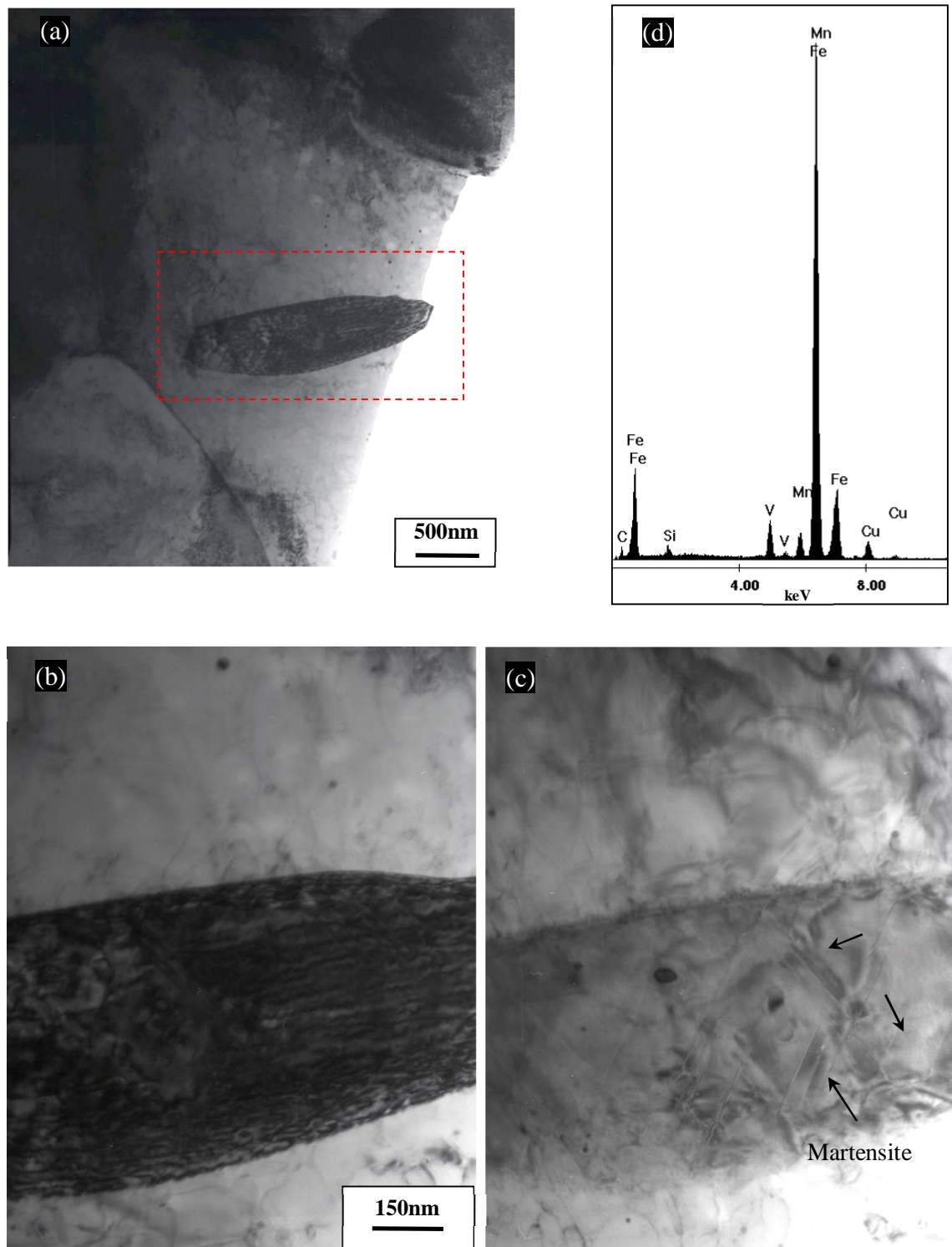


Fig. 5.19, Typical thin-foil transmission electron micrographs of cold rolled Alloy 3 after the intercritical annealing, (a) Showing the presence of a small feature similar to retained austenite, (b) Showing the presence of high density of dislocation inside the feature, (c) Showing the presence of fine precipitates in the vicinity of the intersection of two martensite twins after slight tilting of the sample, (d) Corresponding EDS spectrum from the observed precipitates.



Fig. 5.20 gives a typical micrograph of retained austenite after the intercritical annealing. The observed twin structure inside the blocky retained austenite suggests recrystallization occurred during thermomechanical processing. Micrographs and EDS results confirmed the presence of microalloying precipitates inside and at places close to the edge of retained austenite.

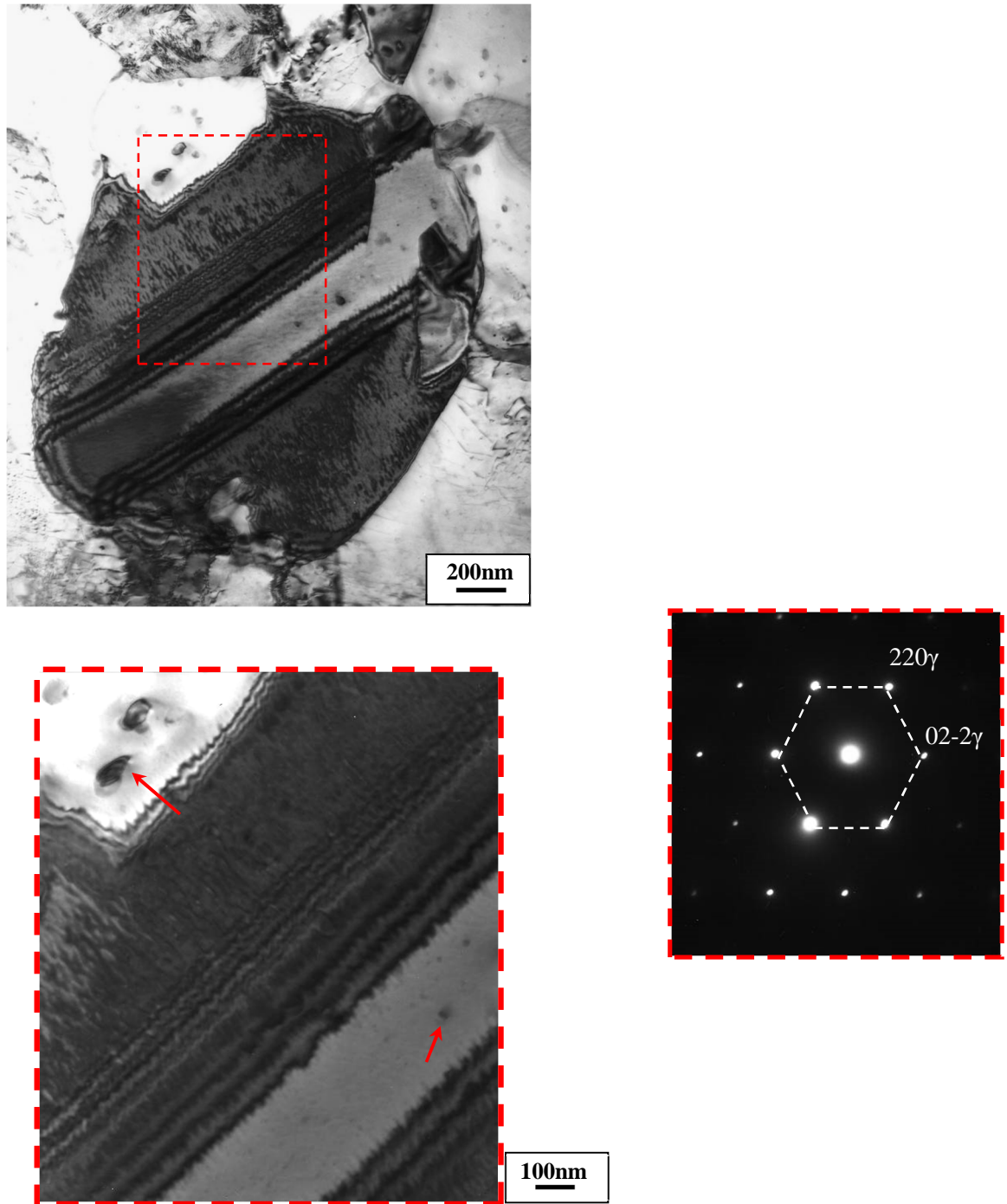


Fig. 5.20, Thin-foil transmission electron micrographs of rough rolled Alloy 2 after the intercritical annealing, showing the block shape retained austenite with annealing twin and corresponding electron diffraction ([111] zone axis).



### 5.2.3.2. TEM Carbon Extraction Replica Analysis

According to the bright/dark field TEM images, the carbon extraction replicas successfully extracted the precipitates larger than  $5\pm 1$  nm (Figs. 5.21 to 5.28). The identification of precipitates was performed by the EDS and selected area electron diffraction (SAED) to give their chemical composition and crystal structure respectively. Dark field was used specifically to reveal the very fine precipitates (e.g. Figs. 5.25 and 5.28). Additionally, using the Fresnel fringes by under/over focusing to some extent was helpful to ensure the features demonstrate a real precipitate rather than an artefact in the carbon film.

Fig. 5.21 gives a typical collage of bright field TEM images from a carbon extraction replica. It can be seen that precipitates were distributed heterogeneously with different morphologies. This behaviour was common among the majority of samples for both alloys.

Figs. 5.21 to 5.23, show the typical complex shape of the precipitates observed. EDS analyses showed that the majority of these precipitates in Alloy 2 contained Nb and V. It has been established that the cap with a higher thermal stability can be formed first in a fully austenitic region and acts as nucleation sites for the subsequent precipitation at lower temperatures [19, 81].

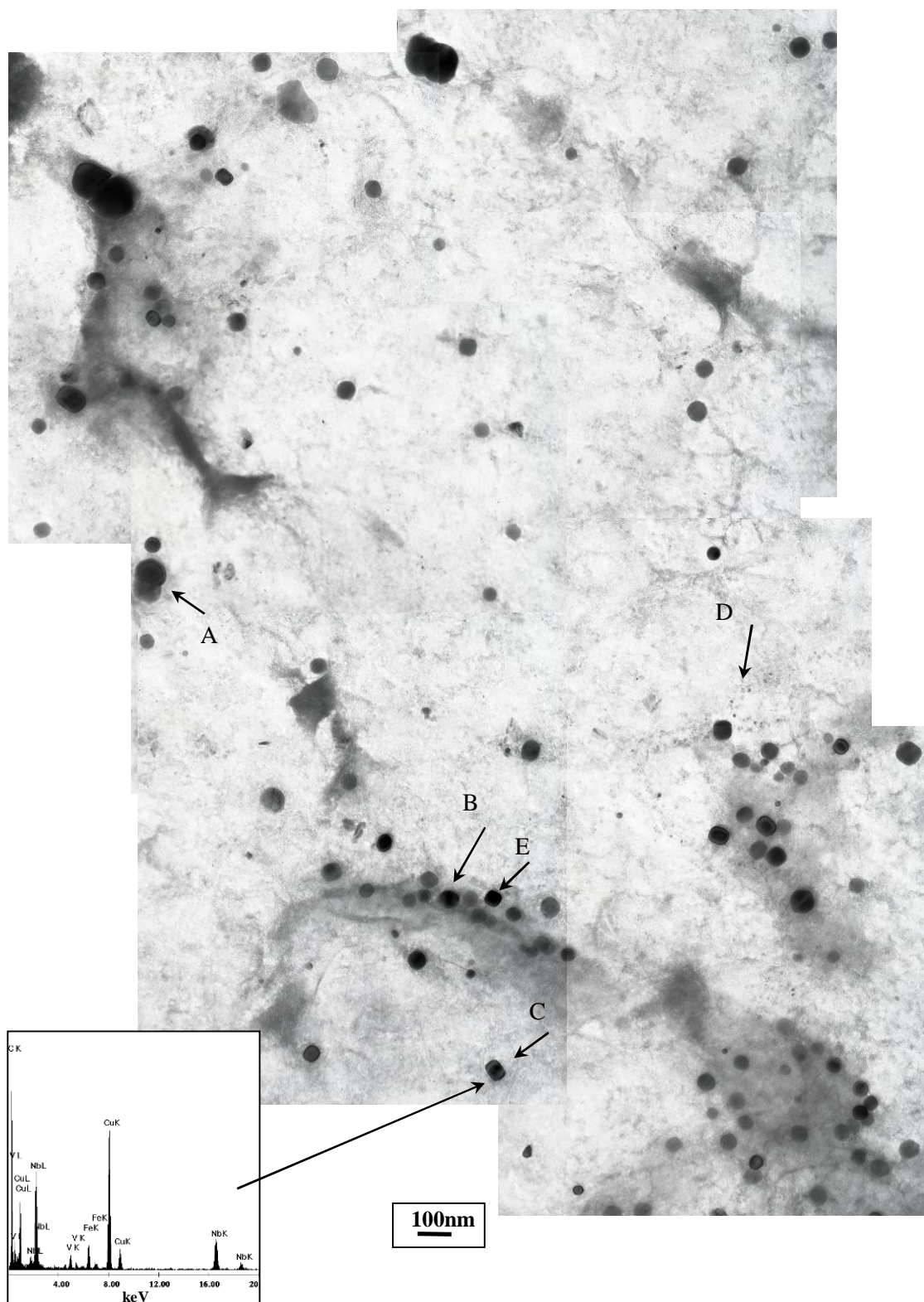


Fig. 5.21, Selected carbon extraction replica micrograph of Alloy 2 after the intercritical annealing, showing different morphologies of the microalloying precipitates and a typical EDS spectrum, A; complex shape, B; round shape, C; square shape; D; small precipitates, E; cuboid.

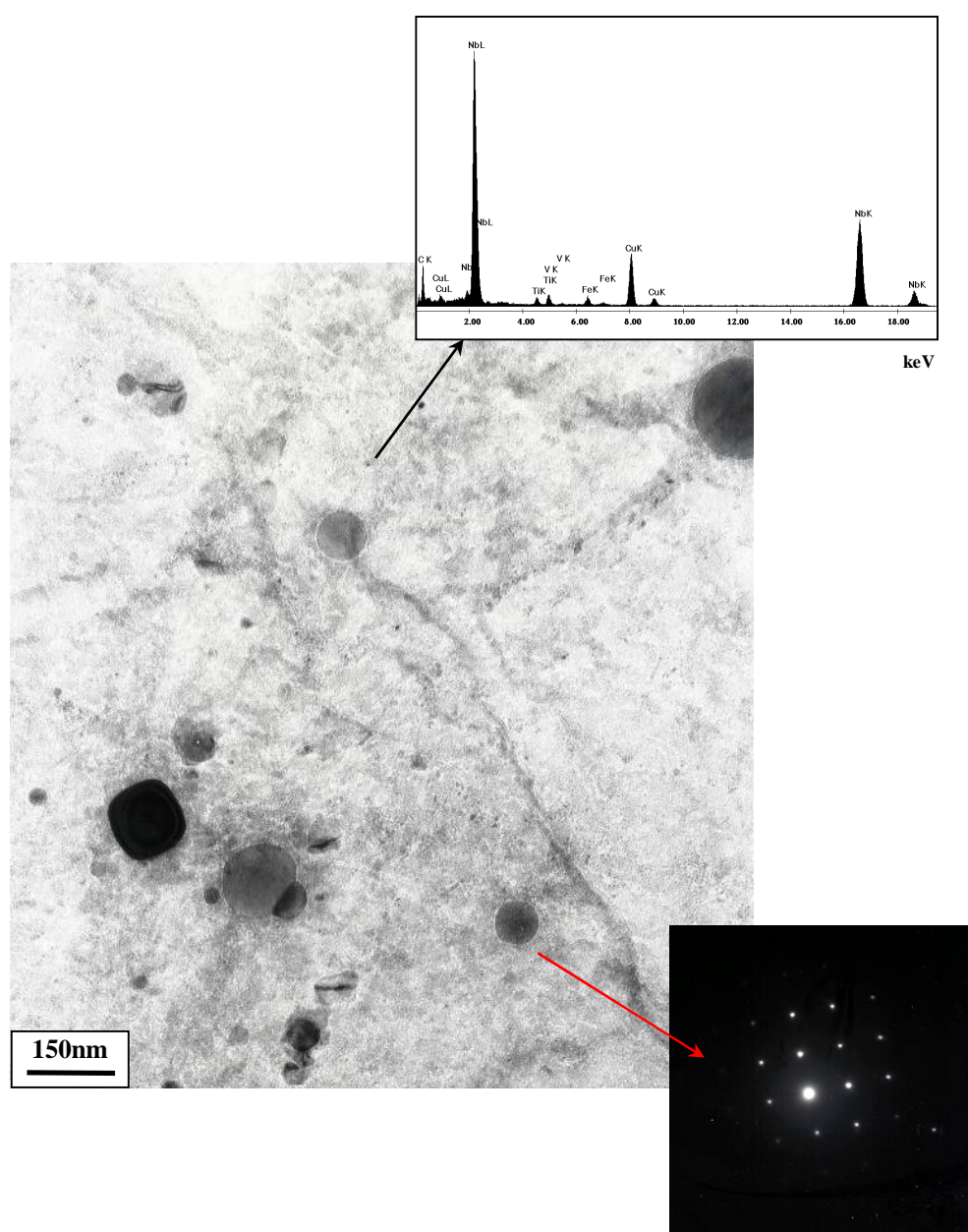


Fig. 5.22, Selected carbon extraction replica micrograph of rough rolled Alloy 2 and a typical EDS spectrum from the fine precipitates and electron diffraction pattern from a selected spherical precipitate in zone axis [100] FCC.

Fig. 5.23 shows TEM micrographs and corresponding EDS spectra of a typical complex precipitate. The dark field images of upper and lower caps are strong evidence showing different crystallographic orientations of duplex precipitates. In this way, the spectra acquired from the upper and lower caps showed that the lower cap is rich in Nb,V,Ti, where upper cap is rich in Nb. The significant difference between the size of upper and lower caps suggests that Nb,V,Ti was formed at a higher temperature.

A wide range of size and shape distribution of precipitates and also chemical compositions was frequently observed (e.g. Fig. 5.24). The EDS spectra from these carbides confirmed the presence of different microalloying elements i.e. Nb/V and Mo in Alloy 2. It is evident that the mechanism of precipitation was affected by those alloying elements with a higher thermal stability that formed at higher temperatures e.g. Nb.

According to the TEM micrographs and the relevant EDS results, it can be suggested that during the roughing and intercritical annealing processes, nano-scale precipitates of Nb/V/Mo/Ti with a cuboid, spherical, needle-like/oval and complex shape were formed (Fig. 5.21 and 5.27). Fig. 5.26 shows a microalloying precipitate with triangular morphology which is rich in vanadium. Further investigations by EELS established the extent of carbide/carbo-nitrides or nitride precipitates, which will be discussed in detail through chapter 6.

It must be emphasised that the TEM micrographs are a 2-dimensional projected image from the 3-dimensional configuration in accordance with the viewing angle. Thus, to avoid producing inaccurate or misleading data the analyses were mainly focused on the size distribution and density of precipitates.

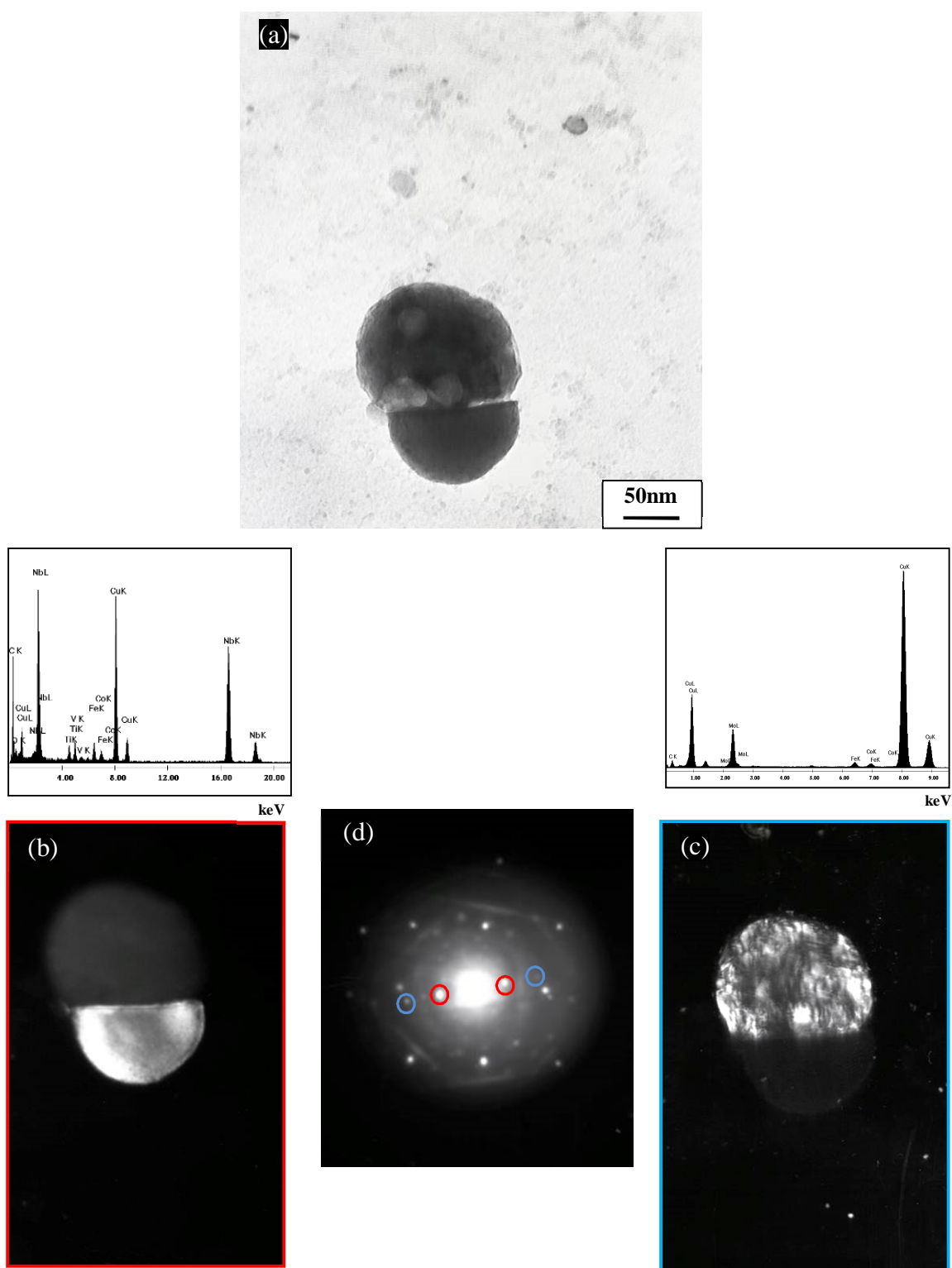


Fig. 5.23, Selected carbon extraction replica micrograph of rough rolled Alloy 2, (a) Bright field image of a complex NbV precipitate, (b) and (c) Showing the dark field images of upper and lower caps and corresponding EDS spectra, respectively, (d) Electron diffraction pattern showing the relevant variants of each cap.



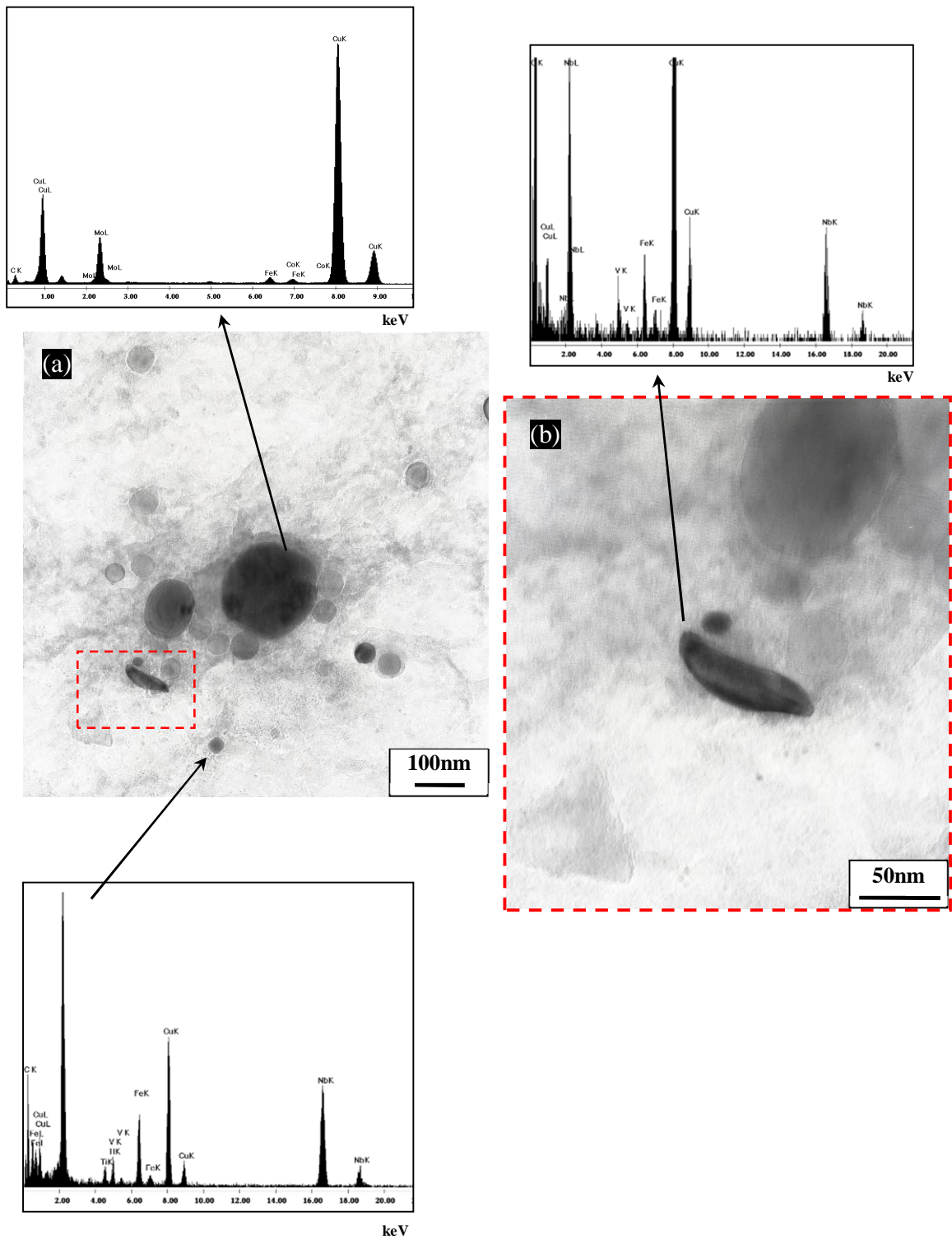


Fig. 5.24, Selected carbon extraction replica micrograph of rough rolled Alloy 2, (a) Showing a wide range of size and shape distribution of precipitates with different chemical compositions and morphologies, (b) A typical oval shape precipitate and corresponding EDS spectrum.

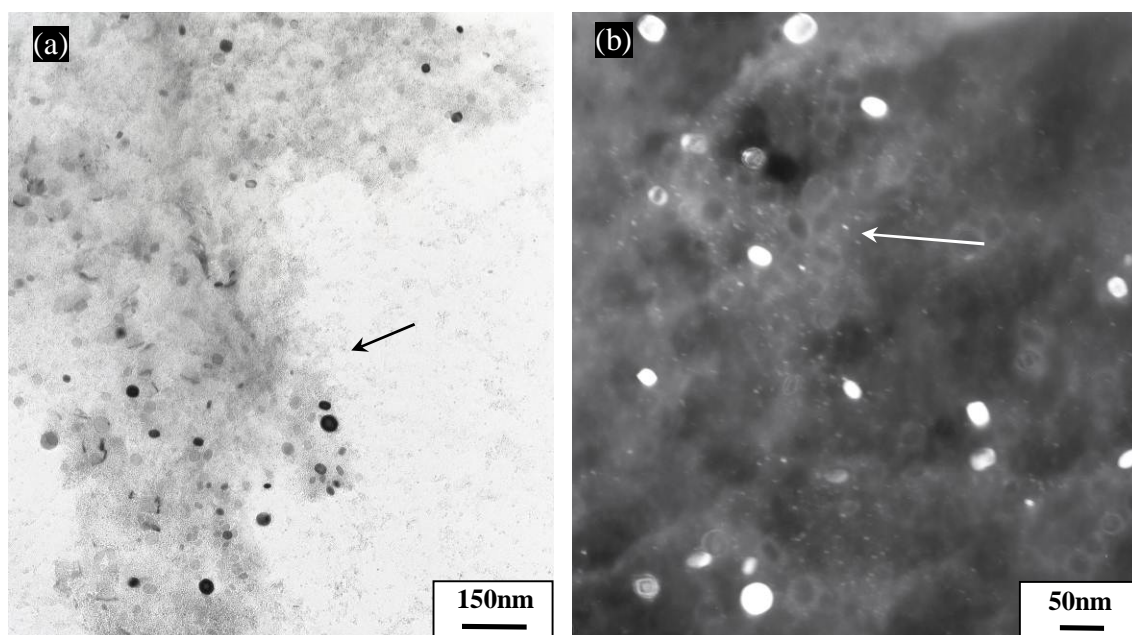


Fig. 5.25, Selected carbon extraction replica micrograph of rough rolled Alloy 2, (a) Bright field image, showing colony of precipitates which can be related to the effect of etching, (b) Dark field image illustrates very fine precipitates through the microstructure.

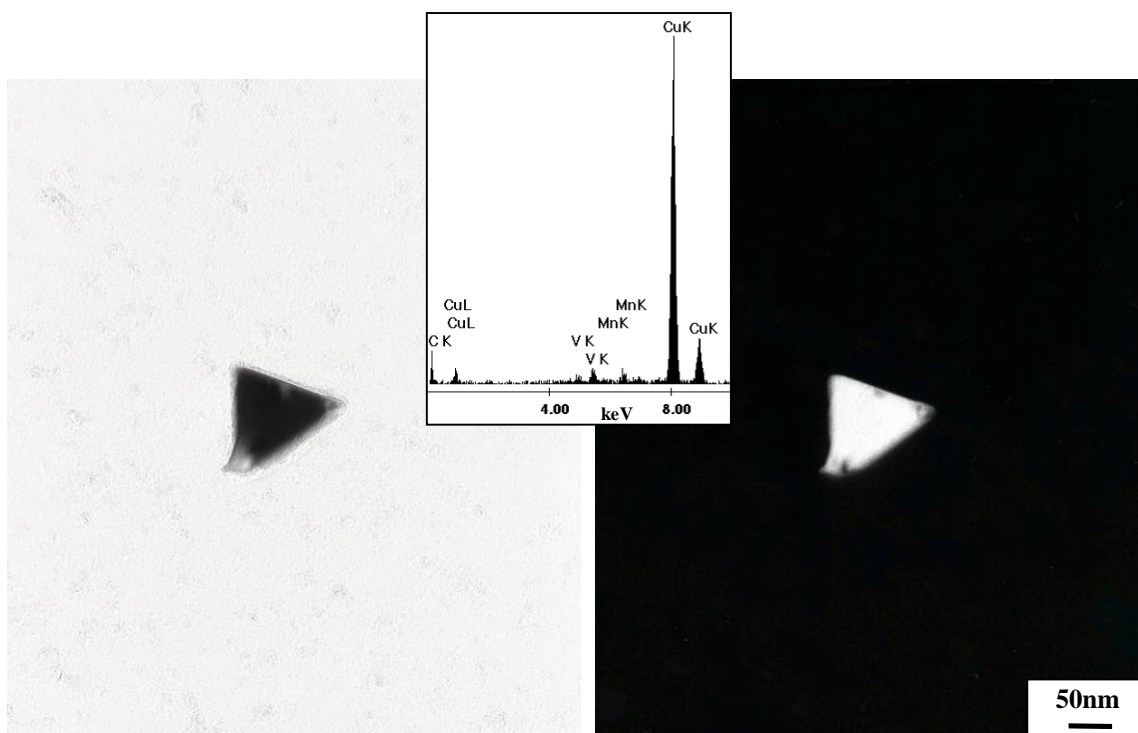


Fig. 5.26, Bright and dark field TEM images of Alloy 3 after the rough rolling and corresponding EDS spectrum, showing a triangle like precipitate.



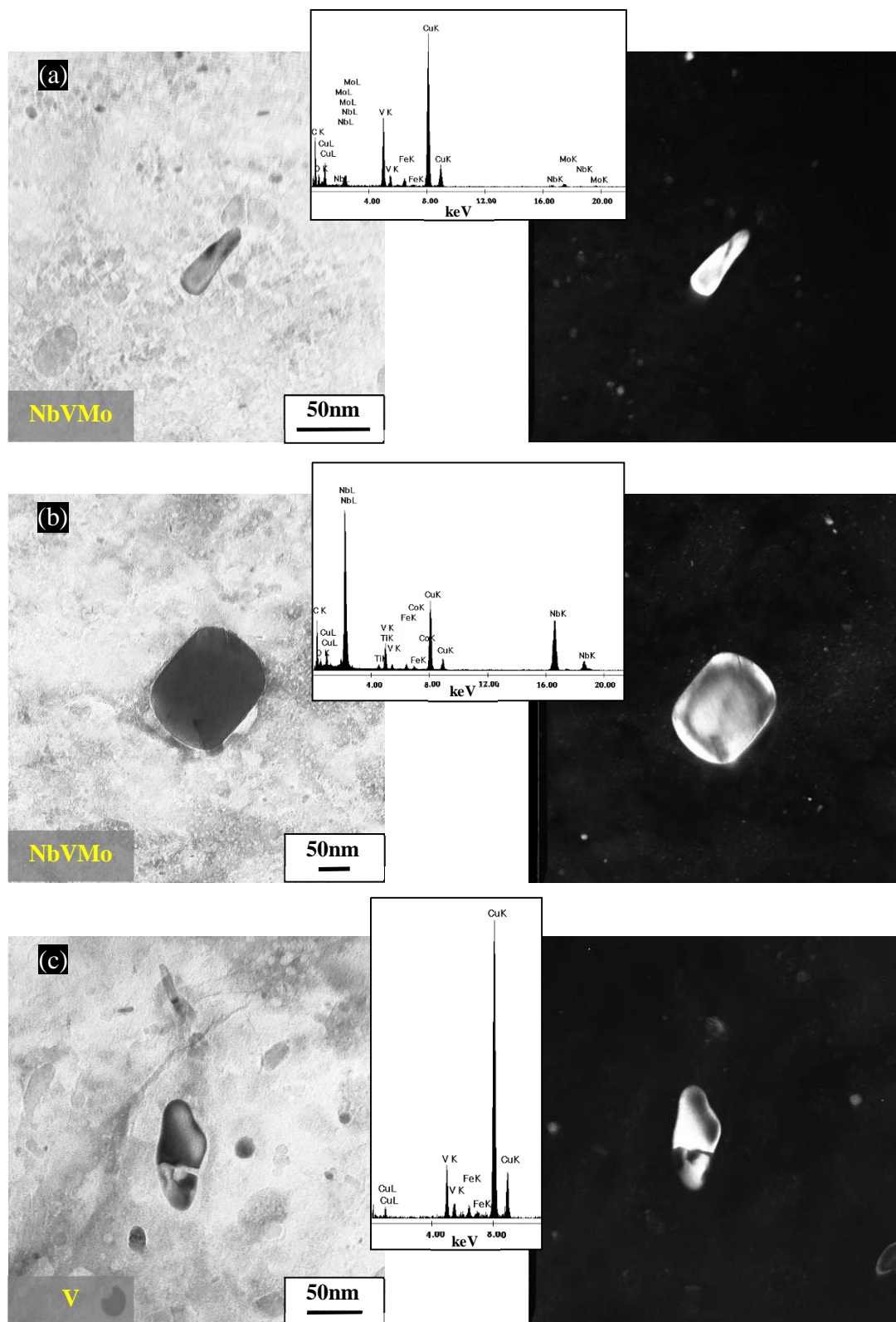


Fig. 5.27, Bright and dark field TEM images and corresponding EDS spectra of the intercritical annealed samples, (a) Showing an oval shape precipitate in Alloy 2, (b) Showing a cuboidal shape precipitate in Alloy 2, (c) Showing an irregular shape precipitate in Alloy 3.

Fig. 5.28 shows a linear (or stringer) distribution of precipitates with a higher density compared to other regions in the carbon extraction replica sample. This was probably a grain boundary or subgrain boundary region.

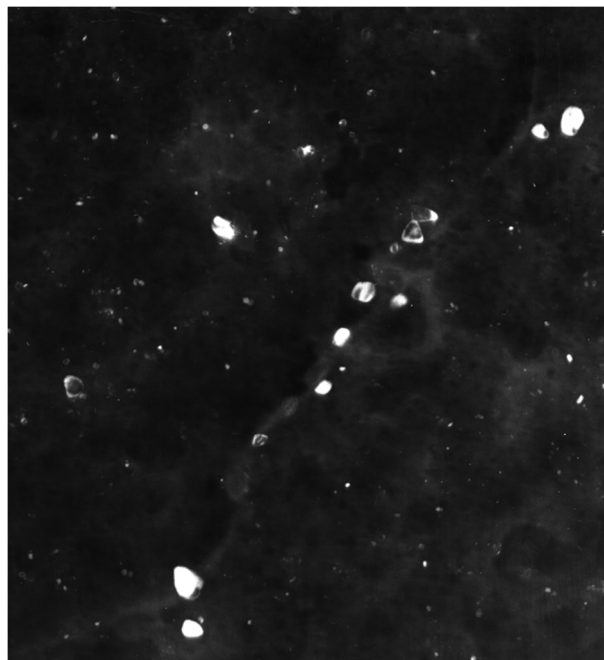
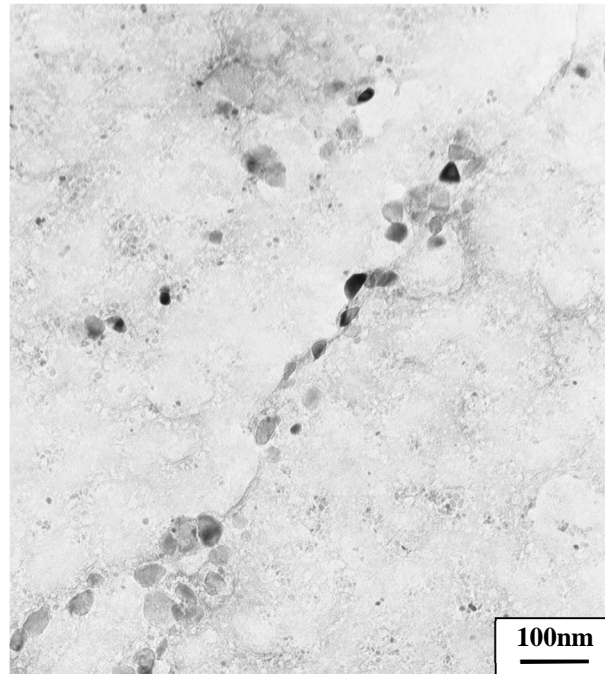


Fig. 5.28, Bright and dark field TEM images of Alloy 2 after the intercritical annealing, showing a distribution of precipitates along a boundary shape feature.

The density of precipitates was measured by counting the number of precipitates through the micrographs, obtained from at least ten negatives for each sample. To minimize the possible errors in counting the precipitates from artefacts in the carbon replica that could provide contrast similar to the precipitates, it was decided that the precipitates were counted based on their morphology, (i.e. cuboid, spherical, needle-like/oval and complex shape). Fig. 5.29 compares the density of precipitates (i.e. number of precipitates per unit area), before and after the intercritical annealing. It can be seen that the intercritical annealing significantly increased the density of precipitates in both alloys.

Fig. 5.30 gives the size distribution of precipitates in Alloys 2 and 3. The comparative histogram shown in Fig. 5.30 (c) indicates the formation of a considerable fraction of fine precipitates (i.e.  $\leq 15$  nm) in Alloy 2. On the other hand, in Alloy 3 the histogram exhibits that precipitates became marginally larger than those before intercritical annealing (Fig. 5.30 (f)).

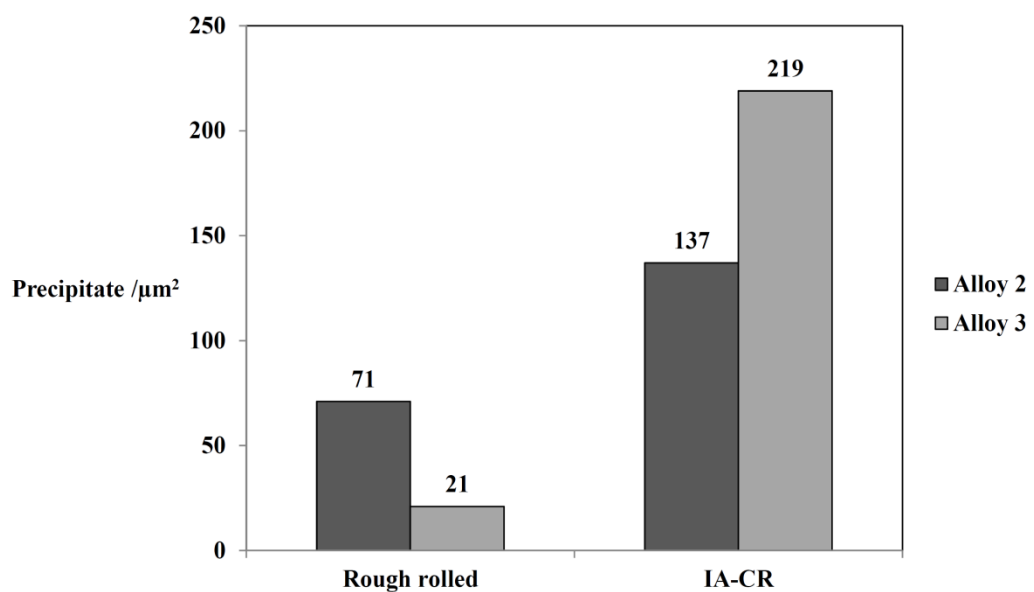


Fig. 5.29, Area density of precipitates versus thermomechanical processing, measured from the carbon extraction replica samples of Alloys 2 and 3.

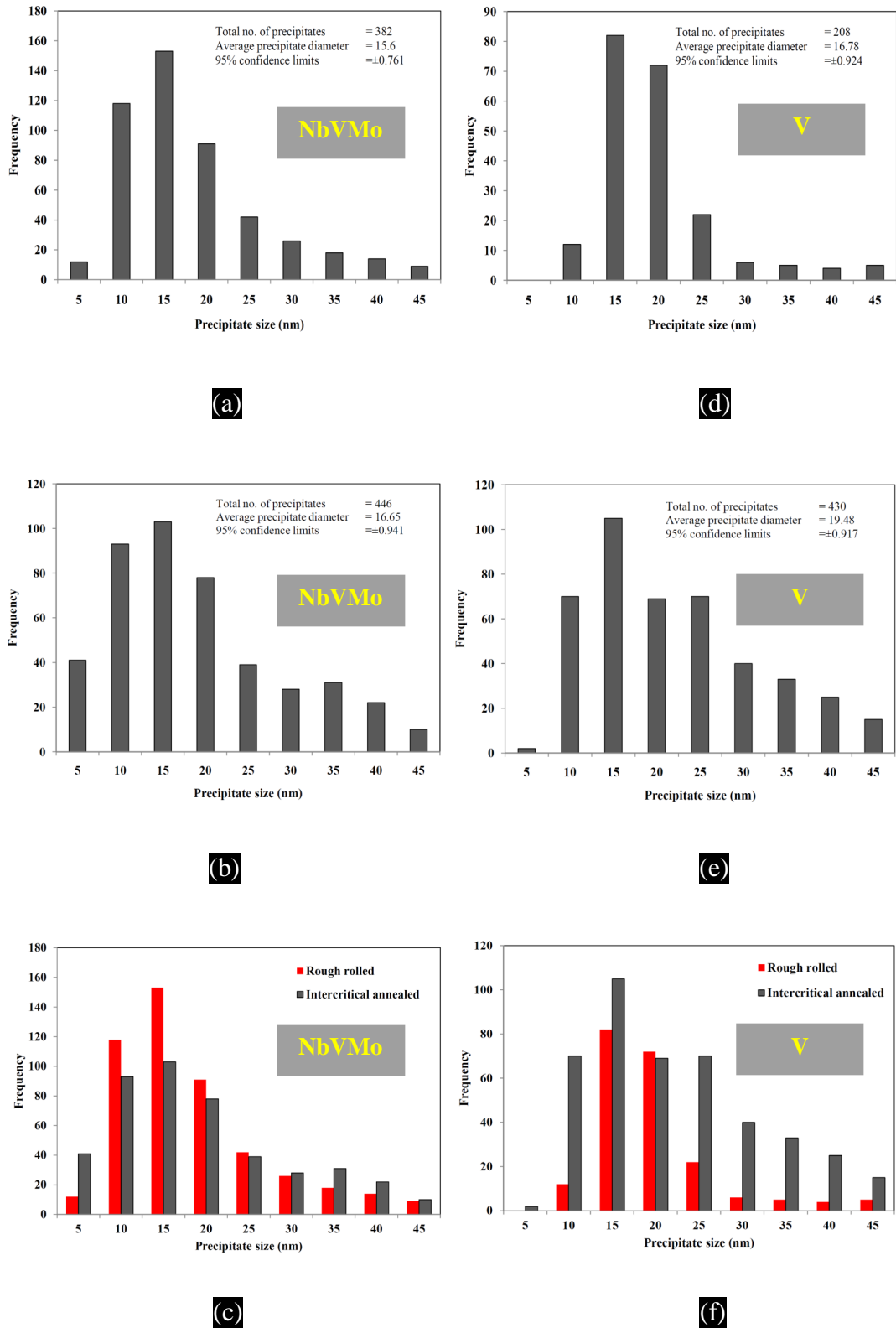


Fig. 5.30, Precipitate size distribution of rough rolled, intercritical annealed samples of Alloys 2 and 3, measured from carbon extraction, (a) Rough rolled Alloy 2, (b) Intercritical annealed Alloy 2, (c) Combined rough rolled and intercritical annealed Alloy 2, (d) Rough rolled Alloy 3, (e) Intercritical annealed Alloy 3, (f) Combined rough rolled and intercritical annealed Alloy 3.

#### 5.2.4. Hardness Testing

The effect of microstructure evolution and precipitation behaviour was also investigated using Vickers hardness measurements, the results of which are summarized in Table 5.3.

Table 5.3, The result of Vickers hardness measurements.

Thermomechanical processing	Alloy 2 (HV)	Alloy 3 (HV)
Rough rolled	256±5	234±5
Cold rolled	275±11	249±8
Intercritical annealed	314±12	251±6

Fig. 5.31 shows the trend of variation in the Vickers hardness as a function of thermomechanical condition. In Nb,V,Mo containing steel (Alloy 2) the hardness in all specimens is higher than Nb,Mo free steel (Alloy 3). The intercritical annealing resulted in an increase in the hardness, while the rate of hardening is different between Alloy 2 and Alloy 3.

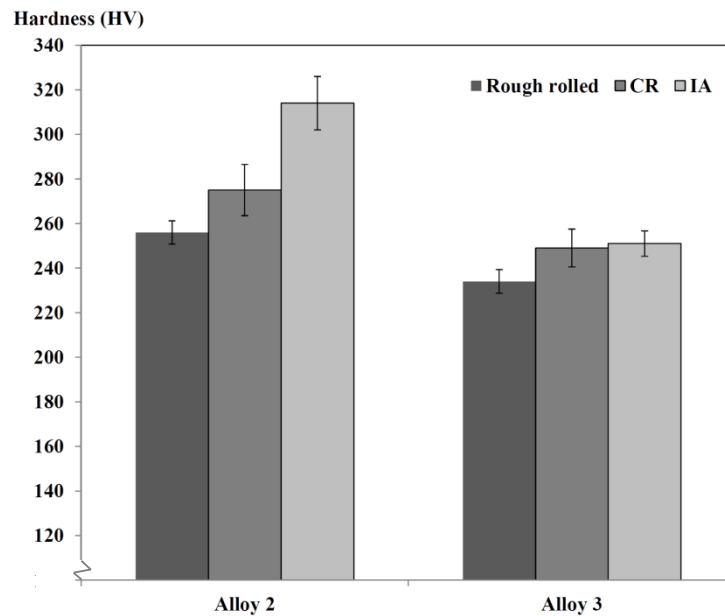


Fig. 5.31, Vickers hardness versus the thermomechanical processing used for Alloys 2 and 3, CR; cold rolled, IA; intercritical annealed.

### 5.3. Discussion

#### 5.3.1. Evolution of Microstructure during Rough Rolling (Rolling Mill)

The optical micrographs of samples, before and after the rough rolling process are compared in Fig. 5.1. It was found that the roughing favoured the formation of allotriomorphic ferrite and lath-shape ferritic constituents.

In the NbVMo containing steel (Alloy 2) the allotriomorphic ferrite showed a cumulative structure around the prior austenite grain boundaries (Figs. 5.1 (c) and (d)). This was also observed in the microstructure of Alloy 3 though the volume fraction of allotriomorphic ferrite was lower than Alloy 2 (Figs. 5.1 (e) and (f)). These micrographs were similar to the microstructures shown by [143, 144] for a given Nb microalloyed air-cooled bainitic steel. This is consistent with the results of Farrar et al., who also found that the allotriomorphic ferrite is mainly formed at grain boundaries [145]. This suggests that the nucleation of equiaxed ferrite was dependent upon prior austenite grain size although the kinetics of growth might be controlled by other mechanisms. Thus, it was clear from the microstructure in Figs. 5.1 that prior austenite grain boundaries had an influential role in the nucleation of ferrite, as expected.

In Alloy 3, the intragranular ferrite was present in the form of acicular/bainitic ferrite and a random distribution of Widmanstatten ferrite morphologies (Figs. 5.1 and 5.2). In Alloy 2, the acicular/bainitic ferrite was finer and no Widmanstatten ferrite was observed. A detailed review of acicular ferrite in carbon-manganese weld metals was undertaken by Farrar and Harrison, and provided a valuable source of knowledge in this area, up to the late 1990s [146]. It deals with the role of chemical composition, cooling rate and nucleation sites in the development of acicular ferrite. They pointed out the exact levels of C, Si, Mn, Nb and Mo required to develop acicular ferrite. Also, they showed that the transformation is dependent upon the initial structure and cooling rate. The same authors in other work [145] reported the effect of prior austenite grain size on the formation of acicular and polygonal ferrite in 0.048C 0.782Mn 0.66Si 0.008S 0.015P 5.53Ni (wt%) steel. They found that the prior austenite grain size has a profound influence on transformation behaviour. They also showed that in the steel with the larger prior austenite grain size, i.e. 93 $\mu$ m, acicular ferrite forms at a higher temperature, implying lower nucleation and higher growth rates and smaller rejection of carbon by diffusion.

This ultimately results in an acicular ferrite structure with a high aspect ratio. He and Edmonds in 2002, reported that in V microalloyed 0.1C 0.25Si 1.2Mn (0.0-0.5)V (wt%) steels the microstructure is prone to form acicular and Widmanstätten ferrite [147]. It is therefore concluded that the smaller prior austenite grain size (i.e.  $53 \pm 5.0 \mu\text{m}$ ) and the presence of NbMo in Alloy 2 were likely to be the reasons for the observed difference in the morphology of intragranular ferrite (Fig. 5.2). As mentioned above, the effect of cooling rate is also an important factor. This will be further elucidated later in chapter 6.

In general, the regions in between allotriomorphic ferrite exhibited a microstructure similar to that reported in [95, 148] for typical bainitic ferrite steels (Fig. 5.3). It has been established that the microstructure of such steels involves a matrix of bainitic ferrite lath and interlath packets of retained austenite and martensite. In the present study, a combination of SEM/TEM observations and XRD results revealed the presence of lath-ferrite and martensite with a high dislocation density, and retained austenite as well as cementite at these regions (Figs. 5.3 to 6 and 5.15). It is therefore clear that the matrix of Alloys 2 and 3 after the rough rolling mainly comprised acicular/bainitic ferrite and martensite.

### 5.3.2. Evolution of Microstructure during Cold Rolling

In this study cold rolling (nominally 20% reduction) was carried out following hot rolling. It was believed that the applied cold rolling could increase the kinetics of austenite formation on reheating by breaking the heterogeneous starting structure [2, 23, 71, 149]. Also, the dislocations generated by cold rolling could enhance the precipitation during intercritical annealing [44].

As is seen from Fig. 5.7, cold deformation was accompanied by a significant deformation of ferrite, as the softer phase. It showed somewhat flattening and overlapping of ferrite in the normal direction plane of samples. However, micrographs from the rolling direction was inconsistent with the observed structure from the normal direction. The cold rolling did not break and deform the lath shape structure. This indicated a refinement of the structure in the normal direction, whereas the structure through the rolling direction exhibited elongation in the rolling direction.



The ferrite in Alloy 3 was more elongated compared with Alloy 2. The difference between Alloys 2 and 3 after the cold rolling was probably a result of the difference in NbMo content. Alloy 2 would have contained additional strengthening from NbMo in the form of precipitates and/or solute drag. However, studying the effect of cold rolling was out of the scope of this research, further investigations on this effect will be able to resolve open questions in this field.

The presence and volume fraction of retained austenite after cold rolling was analysed using XRD to further quantify the extent of phase transformation in the resulting microstructures. According to the XRD results, it was found that the cold rolling led to extensive transformation of the retained austenite to martensite. It is therefore concluded that the microstructure of both alloys after 20% reduction contained allotriomorphic ferrite in addition to lath ferritic constituents.

### **5.3.3. Evolution of Microstructure during Intercritical Annealing Range**

The XRD spectra showed the peaks corresponding to ferrite and retained austenite after the intercritical annealing in both alloys (Fig. 5.15). Further XRD analysis revealed that the intercritical annealing had led to the formation and retention of a considerable amount of retained austenite in the microstructure of both alloys (i.e. 7.4 and 8.2 wt% in Alloys 2 and 3, respectively).

A comparison between the optical and SEM micrographs from before and after the intercritical annealed structures demonstrated a complex behaviour in the evolution of ferrite (Fig. 5.8). After the intercritical annealing the optical micrographs revealed an allotriomorphic ferrite at prior austenite grain boundaries and a distribution of lath shape ferritic constituents at grain interiors (Figs. 5.8 (a) and (b)). This is similar to that observed in the optical micrographs of initial structure (Fig. 5.1). A closer look by SEM showed that the microstructure, in particular constituents exhibiting bright contrast after the intercritical annealing, exhibited a significantly different morphology compared with the cold/hot rolled structures (Figs. 5.3, 5.7 and 5.8). In general, the micrographs of intercritical annealed samples suggested that the majority of austenite was formed at the grain boundaries of lath ferrite in both alloys with a high aspect ratio (i.e. an average around  $2.5 \pm 0.5$   $\mu\text{m}$  in length and  $0.75 \pm 0.25$   $\mu\text{m}$  in width). Also, TEM observations to

some extent confirmed the presence of retained austenite in a needle-like or block shape morphology in the vicinity of martensite and bainite (Figs. 5.12 and 5.13). To further clarify this behaviour, the interrupted quenched structure at the end of the isothermal intercritical range, i.e. 795°C, was studied (Fig. 5.9). The microscopy observations showed concurrent dissolution of secondary phases and the formation of austenite at the grain boundaries of lath ferritic constituents. This confirmed that the austenite was formed at the expense of secondary phases dissolution in the microstructure.

Of particular note was that the lath shape ferrite did not show any significant recrystallization after intercritical annealing (Fig. 5.8). This is in agreement with the results of Sugimoto et al., who reported no significant nucleation of polygonal ferrite after intercritical annealing of a given (0.1-0.6)C 1.5Si 1.5Mn (wt%) martensitic TRIP steel [12]. Recently, Hamzeh et al., and Hossein Nedjad et al., have published similar results about the effect of cold rolling on the formation of an ultrafine ferrite grain size microstructure in bainitic microstructures after an annealing process at 500-700°C. It was pointed out that heavy cold rolling (i.e.  $\geq 50\%$  reduction) can break bainitic structures and enhance ferrite recrystallization. From the microscopy observations in this study and available data in the literature, it can be thus suggested that the cold rolling reduction of  $\sim 20\%$  reduction was insufficient to drive ferrite recrystallization [150, 151].

A possible explanation about the absence of recrystallization in the lath ferrite is deduced by assuming the effect of interfaces. It is generally accepted that the parallel sides of lath shape ferritic constituents are low-energy, coherent or semicoherent boundaries and therefore immobile [67, 152, 153]. It is evident that the existence of such a structure necessitates a higher level of energy for the recrystallization. This is consistent with the results of Ueji et al. in 2002 who discovered that  $\sim 50\%$  plastic strain in a martensitic microstructure leads to subdivision of martensite laths. They showed that introduced heterogeneous subdivisions provide ideal potential sites for the formation of new grains [154].

Nevertheless, the optical micrographs of Alloy 3 revealed a slight coarsening of lath ferritic constituents compared with Alloy 2 (Figs. 5.8 (a) and (b)). This behaviour could be attributed to the effect of NbMo addition in retarding the ferrite growth by pinning the grain boundaries as precipitate or solute drag effect.

From the XRD results, it was found that the average carbon content of retained austenite in Alloy 2 was lower than Alloy 3 after the intercritical annealing (Table 5.2). Sugimoto et al., reported a similar behaviour for a given Nb added bainitic ferrite and/or martensite TRIP steels [63]. They found that Nb considerably decreases the carbon content of retained austenite after a typical annealing treatment. Recent studies by Kobayashi et al., have also shown that the retained austenite in Mo bearing bainitic ferrite TRIP assisted steels lowers the carbon concentration, while its stability against straining is sufficiently high [155]. From the available data, it is not possible to directly link the effect of NbMo addition on the carbon content of austenite. Moreover, the microstructure was not optimized to obtain a reasonable amount of retained austenite. However, as it was outside the scope of this research, further investigations are suggested to clarify these phenomena more accurately.

#### **5.3.4. TEM Thin Foil Analysis of Precipitate**

Much work has been reported on V microalloyed steels. A valuable and detailed review of the literature on V microalloyed steels is provided by Baker [156] in which the interactions between microalloying precipitates and other microstructural constituents is discussed. However, to our knowledge, no report has been made on the precipitation behaviour in acicular/bainitic ferrite TRIP assisted steels during intercritical annealing. In this field, the key findings corresponding to TEM thin foil samples are discussed next.

A comparison between the TEM observations of the rough rolled and intercritical annealing showed that the initial structure as well as final structure contained a larger density of precipitates (e.g. Figs. 5.4 and 5.5 and 5.13 and 5.19). This was good evidence to show that the precipitation and coarsening would be significantly influenced by dislocations during intercritical annealing. This effect will be further discussed in the following section.

Fig. 5.16 shows typical TEM micrographs of microalloying precipitates in the rough rolled structure. From the thin foil samples, it was found that the roughing process led to the formation of a considerable amount of precipitates in a random manner with different morphologies in both alloys. In addition, a high frequency of VC and Nb(V,Mo)C precipitates were observed in the tangle of dislocations and also in the grain

boundaries of ferritic constituents after the intercritical annealing (Fig. 5.17 (b)). Note that in many cases the observations were assisted by EDS analysis to distinguish the precipitates from other sources of contrast such as dislocations. The available results suggested that the dislocations/grain boundaries as short circuit diffusional paths would accelerate the formation and coarsening of precipitates during intercritical annealing. It was also possible that many of the precipitates initially formed in the supersaturated ferrite and then dislocations were generated as result of transformation. On the other hand, a possibility exists that precipitates might enhance the generation of dislocations [20]. However, these results point to the fact that the precipitates increase the strength of steel by precipitation strengthening. These effects will be further clarified through the following sections.

Twinned martensite adjacent to V(C,N) and other Nb(V,Mo)(C,N) precipitates was occasionally observed (Figs. 5.6 and 5.18 and 5.19 and 5.20). These results were important, as they showed the possibility of precipitation in austenite at temperatures up to intercritical annealing range. Therefore, it was likely that precipitates locally had depleted the carbon and consequently reduced the stability of retained austenite against martensite transformation. Nevertheless, if the twinned martensite and other planar defects were not formed during intercritical annealing they could accelerate the coarsening of pre-existing precipitates.

As a general conclusion, precipitates formed in the matrix, on dislocations and at the grain boundaries of polygonal/lath ferrite. The location of precipitates provided good evidence to show the preferential potential sites for the formation and coarsening of precipitates. Moreover, these characterizations suggested that the statistical studies on the density of precipitates cannot be considered for a homogeneous distribution of precipitates in these microstructures. However, the following discussions will be made based on the average of densities of precipitates from different micrographs.

### 5.3.5. TEM Carbon Extraction Replica Analysis of Precipitates

Figs. 5.21 to 5.28 show typical precipitate distributions in the rough rolled and intercritical annealed samples. It is clear that during these processes, precipitates with different sizes and morphologies (i.e. namely spheroid, cuboid, oval, triangle and irregular/complex shape) were formed. It has been established in the literature that differences in the size and morphology of precipitates is generally attributed to the composition, the nucleation temperature, the mechanism of growth and subsequent coarsening [156, 157]. The mechanism of growth and coarsening are mainly influenced by volume and pipe diffusion. On the other hand, the level of coherency can greatly affect the morphology of precipitates [158]. In the present study, no evidence was found to link the precipitate morphology and precipitate size. Also, the micrographs are of course a 2D projected image from the 3D configuration. Therefore, the precipitation behaviour is discussed statistically based upon the feret diameter of precipitates.

A few precipitates with a size of between ~50 to 200nm were observed in replica samples, in particular in Alloy 2 with a chemical composition of Nb(V,Mo)C (e.g. Figs. 5.21 to 5.28). It is believed that these precipitates either did not dissolve during the reheating stage or they formed at high temperatures. This is consistent with the findings of Palmiere et al. who showed that the dissolution temperature of multi-microalloying precipitates is higher than simple Nb carbide [81]. However, at this size, this group of precipitates would not have greatly contributed to precipitation strengthening [156].

Figs 5.30 (c) and (f) showed that ~80% of precipitates in both alloys in the rough rolled and in Alloy 2 in the intercritical annealed condition, were smaller than 20nm. It has been established that the precipitates with a size of less than approximately 15nm are mainly responsible for the strengthening [156]. Therefore, the frequency of precipitates at this range was considered more closely in the following.

The TEM observations and EDS analysis suggested that the majority of precipitates in Alloy 2 comprised NbVC and Nb(VMo)C after hot rolling (e.g. Figs. 5.22 to 5.24 and 5.27). There is no detailed literature about the precipitation behaviour of coprecipitation system of Nb(VMo)(C,N). However, Akben et al.'s studies of austenite recovery and recrystallization in Nb and V microalloyed steels showed that the

recrystallization in Nb containing steels is stopped at higher temperatures compared with V added steels [28]. They suggested that the austenite recrystallization-stop temperature is related to the solute drag effect and carbonitride precipitates. Therefore, it was assumed that a large number of Nb(V,Mo)C precipitates in Alloy 2 would have formed at higher temperatures, (i.e. probably around  $>900^{\circ}\text{C}$ ).

Furthermore, it might be argued that the size of Nb(V,Mo)C precipitates in Alloy 2 should have been larger than VC in Alloy 3, as they could form at higher temperatures and would coarsen during the cooling stage during hot rolling (i.e. probably around  $\leq 900^{\circ}\text{C}$ ). This can be discussed based on two reasons. Firstly, it has been reported in the literature that the presence of Mo in microalloying precipitation systems can significantly reduce the size of precipitates [71, 72, 75, 139]. Another explanation lies in the formation of fresh precipitation during the cooling stage. Presumably, NbMo increased the thermal stability of precipitates, and consequently the increase of austenite recrystallization-stop temperature which could generate, and inhibit the annihilation of dislocations during the subsequent rolling stages. This, in turn, would facilitate a higher degree of heterogeneous nucleation sites for precipitation at lower temperatures. It is still not clear that if the novel chemical composition of NbVMo coprecipitation system in Alloy 2 follows the general rules and whether precipitates mainly formed at temperatures over the intercritical annealing range. Furthermore, to what extent NbMo could control the coarsening of precipitates. However, the validity of these assumptions will be discussed in chapter 6.

The histograms shown in Fig. 5.30 and 5.32 suggest that the precipitates in Alloy 3 were marginally larger than those in Alloy 2 after intercritical annealing, although the difference was not large and not necessarily statistically meaningful. Since most of precipitates in Alloy 2 showed a chemical composition of Nb(V,Mo)C, it is suggested that NbMo addition could control the coarsening of precipitates during the process. Similarly, Balliger and Honeycombe showed that the kinetics of coarsening in V(C,N) interphase precipitates in ferrite at  $740^{\circ}\text{C}$  is rather sluggish over a critical size (i.e.  $\sim 20$  to  $40\text{nm}$ ) [44]. However, these results are important and they gave further insight into the kinetics of V(C,N) precipitation growth and coarsening in random manner in acicular/bainitic ferrite steels. Furthermore, this showed that the majority of precipitates grew to a size of 10 and 15nm whereas they did not tend to coarsen further during the intercritical annealing.

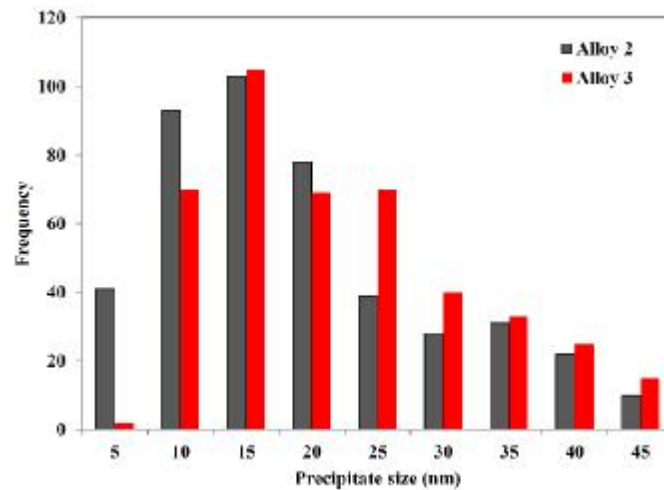


Fig. 5.32, Comparative histograms corresponding to the precipitate size distributions of Alloys 2 and 3 after the intercritical annealing.

Nevertheless, apart from the uncertainty of the efficiency of extraction from the replica technique, it was evident that the average density of precipitates increased after intercritical annealing in both alloys. Similarly, Scott and Perrard have reported on the precipitation of V(C,N) precipitates in TRIP steels after intercritical annealing and above isothermal bainite range [31]. This simply means that during intercritical annealing further precipitation occurred in both alloys.

### 5.3.6. Hardness Testing

The Vickers hardness was also used to compare the effect of microstructural evolution and precipitation behaviour on the strengthening of the material (Fig. 5.31). A comparison between hardness measurements showed the higher hardness in both alloys after the cold rolling, as expected (i.e.  $275 \pm 11$  and  $249 \pm 8$  HV in Alloy 2 and Alloy 3, respectively). An alternative explanation based on the Hall-Petch relationship (equation 2.1), is attributed to the work hardening and subdivision of grains in allotriomorphic ferrite in the microstructure of cold rolled specimens (Fig. 5.7).

The trend of hardness variation in Fig. 5.31 showed the marked effect of intercritical annealing in increasing the hardness in Alloy 2, whereas Alloy 3 exhibited no significant change (i.e.  $314 \pm 12$  and  $251 \pm 6$  HV in Alloy 2 and Alloy 3, respectively). The increase in hardness in Alloy 2 is believed to be associated with precipitation as well



as bainite/martensite transformation [21, 67]. This is supported by TEM observations, which showed an increase in the number of precipitates and a retention of a high dislocation density in Alloy 2 (Fig. 5.29). By contrast, this behaviour was more complex in Alloy 3, as the hardness did not significantly increase due to possible precipitation of vanadium carbide. Based on the available data, two possible explanations can be offered. Firstly, the possible relaxation and growth of lath ferritic constituents and variations in the volume fraction of bainite/martensite could neutralize the possible precipitation strengthening (Figs. 5.7 (c) and 5.8 (b)). Another explanation lies in the coarsening of very fine precipitates (probably with a size of  $\leq 5\text{nm}$ ). This seems reasonable as the average density of precipitates (with diameter of  $\geq 5\text{nm}$ ) increased, whereas no significant variation was observed in the hardness and size distribution of precipitates. Also, it can be concluded that the lower rate of coarsening of precipitates in Alloy 2 was due to the effect of NbMo, which resulted in an increased hardness despite the average density of precipitates being lower than in Alloy 3.

# **Chapter 6. Results and Discussion: Alloys 2 and 3; Controlled Rolling**

## **6.1. Introduction**

Through chapters 4 and 5 the evolution of microstructure in two different TRIP assisted steels were studied (i.e. polygonal ferrite and bainitic ferrite steels). Alloy 1 provided valuable data regarding the precipitation behaviour in parallel to the microstructural evolution at the bainite transformation in a polygonal ferrite matrix. Alloys 2 and 3 with a bainitic ferrite matrix were studied in chapter 5. The results between two different co-precipitation systems of Nb,V,Mo and V were compared after the intercritical annealing to understand the substantial effect of V on the microstructural evolution in the bainitic structure. These efforts led to more systematic studies on Alloys 2 and 3, focusing on the precipitation behaviour at each stage of the thermomechanical processing using the PSC machine and subsequent to the chosen finishing temperature of 830°C. The controlled roll step was achieved by introducing a hold at 900°C for 50s during hot rolling (Fig. 3.8). This could help to understand the interaction between prior austenite structure, precipitation behaviour and bainite transformation as well as the retained austenite.

## 6.2. Results

### 6.2.1. PSC Stress-Strain Curves

Fig. 6.1 shows the stress-strain curves corresponding to the two different thermomechanical processing cycles used for Alloys 2 and 3 (see Table 3.7). The recorded TMC load-displacement data were analysed according to the good practice guide [118]. All flow stresses were corrected in terms of instrumental parameters at each individual stage, as described in Appendix A. It can be seen that by decreasing the temperature the flow stress in both alloys progressively increased. The curves show a slightly lower strain reduction in Alloy 2 compared to Alloy 3.

Five minutes soaking at 1250°C was conducted before PSC testing to obtain a similar initial structure in all samples, aiming at dissolving the precipitates. Moreover, as the quenching stage could not occur inside the deformation furnace, a short delay of approximately one second between the finishing stage and quenching must be taken into account.

To interpret the observed variation of the stress-strain curves, the evolution of microstructure in both alloys was studied by several techniques. The microstructure and precipitates after thermomechanical processing were characterized for each specimen individually.

The initial microstructure of machined PSC specimens was the same as that shown in Fig. 5.1. They contained allotriomorphic ferrite along the prior austenite grain boundaries in addition to acicular/bainitic ferrite, martensite, retained austenite and cementite trapped at the grain interior of prior austenite (see chapter 5).

Fig. 6.2 gives the micrographs of deformed and un-deformed regions of specimens from the longitude/elongation direction (LD/ED) after the hot rolling and controlled rolling. As can be seen in Alloy 3 a larger amount of polygonal ferrite was formed in the microstructure, whereas in Alloy 2 the ferrite was mainly confined to the prior austenite grain boundaries.

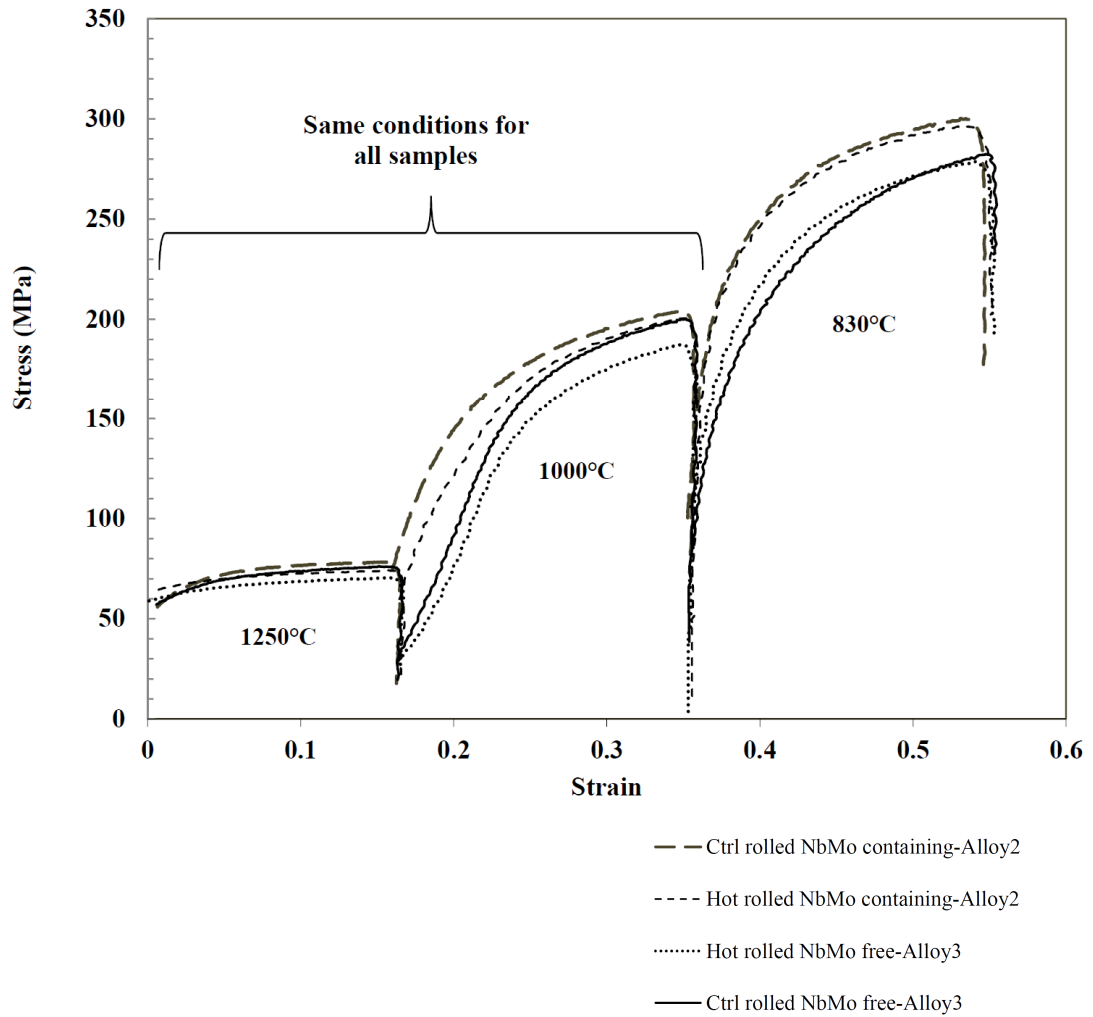


Fig. 6.1, Flow curves corresponding to the hot rolling and controlled rolling simulations using Alloys 2 and 3.

### 6.2.2. Microstructural Characterizations

A comparison between the deformed and un-deformed regions indicated the effect of deformation on the elongation of prior austenite grains, in addition to the acceleration of the kinetics of ferrite formation. Clearly, the prior austenite grain size in Alloy 2 was smaller than Alloy 3, which is attributed to the effect of NbMo on controlling the austenite recrystallization and grain growth (Figs. 6.2 (e) and (f)). Moreover, significant recrystallization was observed throughout the deformation zone of Alloy 3, as shown by the relative large prior austenite grain size compared to the deformed areas. In this context, the contribution of recrystallization and coarsening will be discussed through the following section.

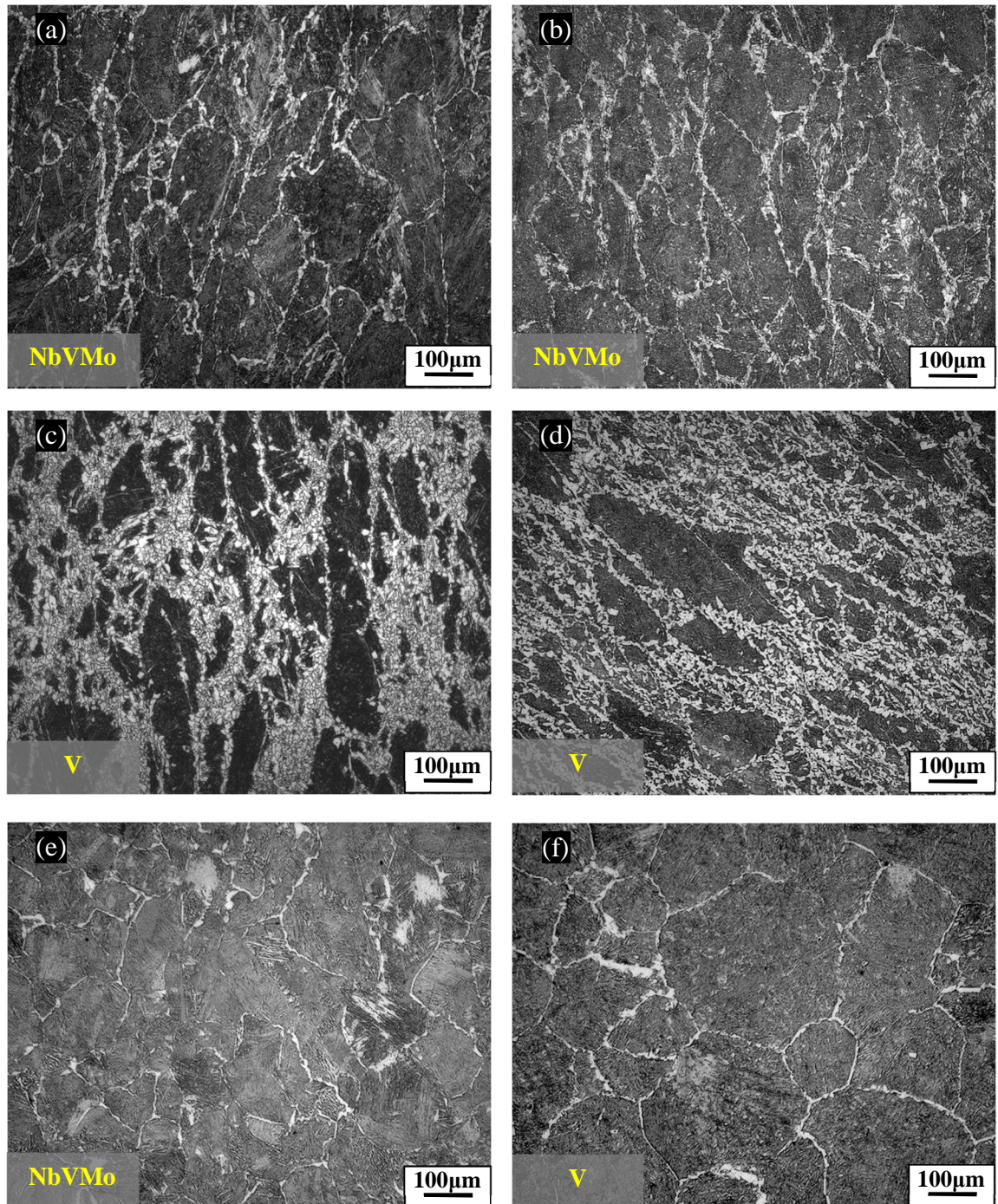


Fig. 6.2, Optical micrographs of hot rolled and controlled rolled samples, (a) and (b). Deformation area of the hot rolled and controlled rolled Alloy 2, respectively, (c) and (d). Deformation area of the hot rolled and controlled rolled Alloy 3, respectively, (e) and (f). Un-deformed area of the hot rolled and controlled rolled Alloys 2 and 3, respectively.



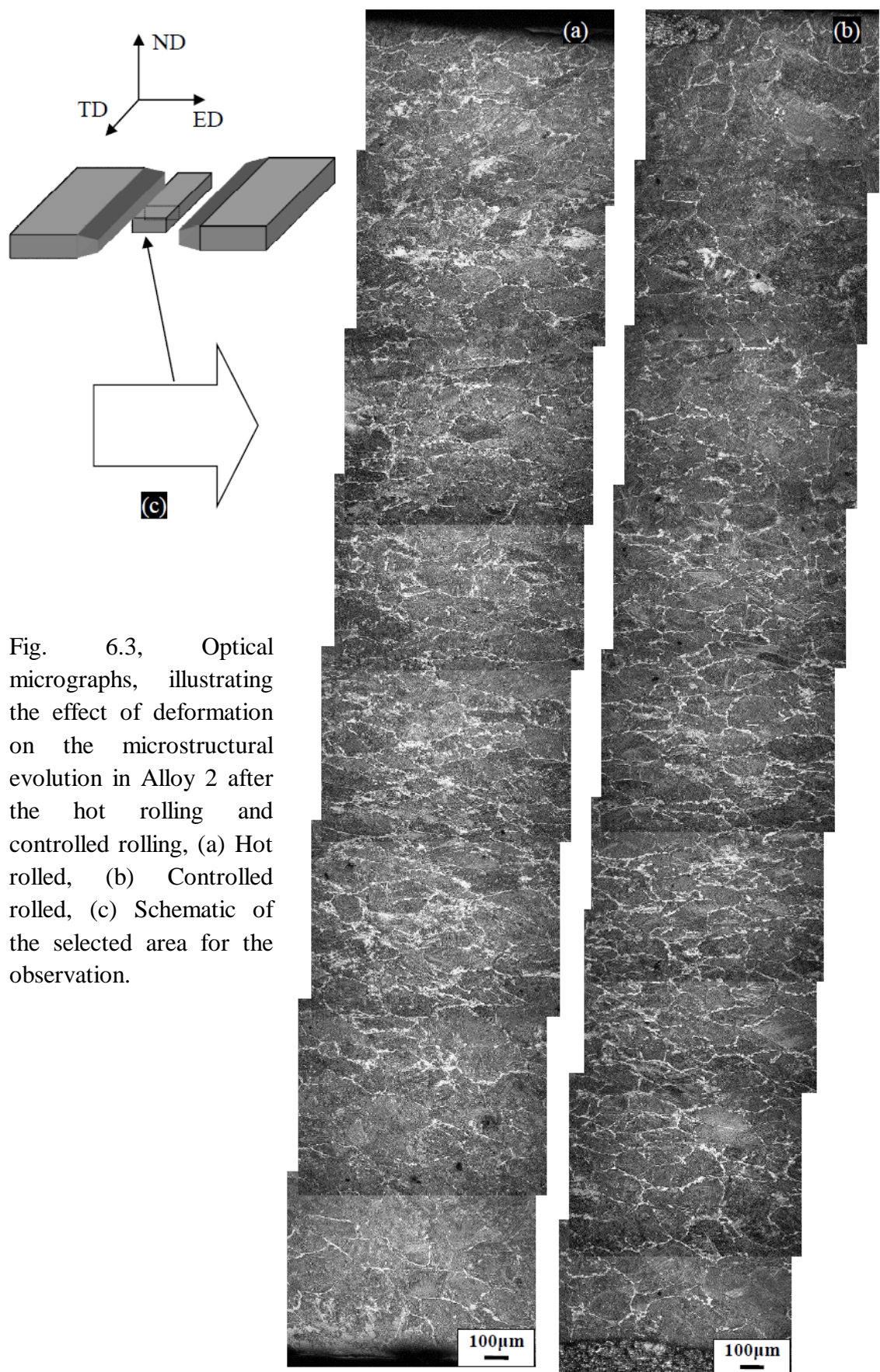


Fig. 6.3, Optical micrographs, illustrating the effect of deformation on the microstructural evolution in Alloy 2 after the hot rolling and controlled rolling, (a) Hot rolled, (b) Controlled rolled, (c) Schematic of the selected area for the observation.



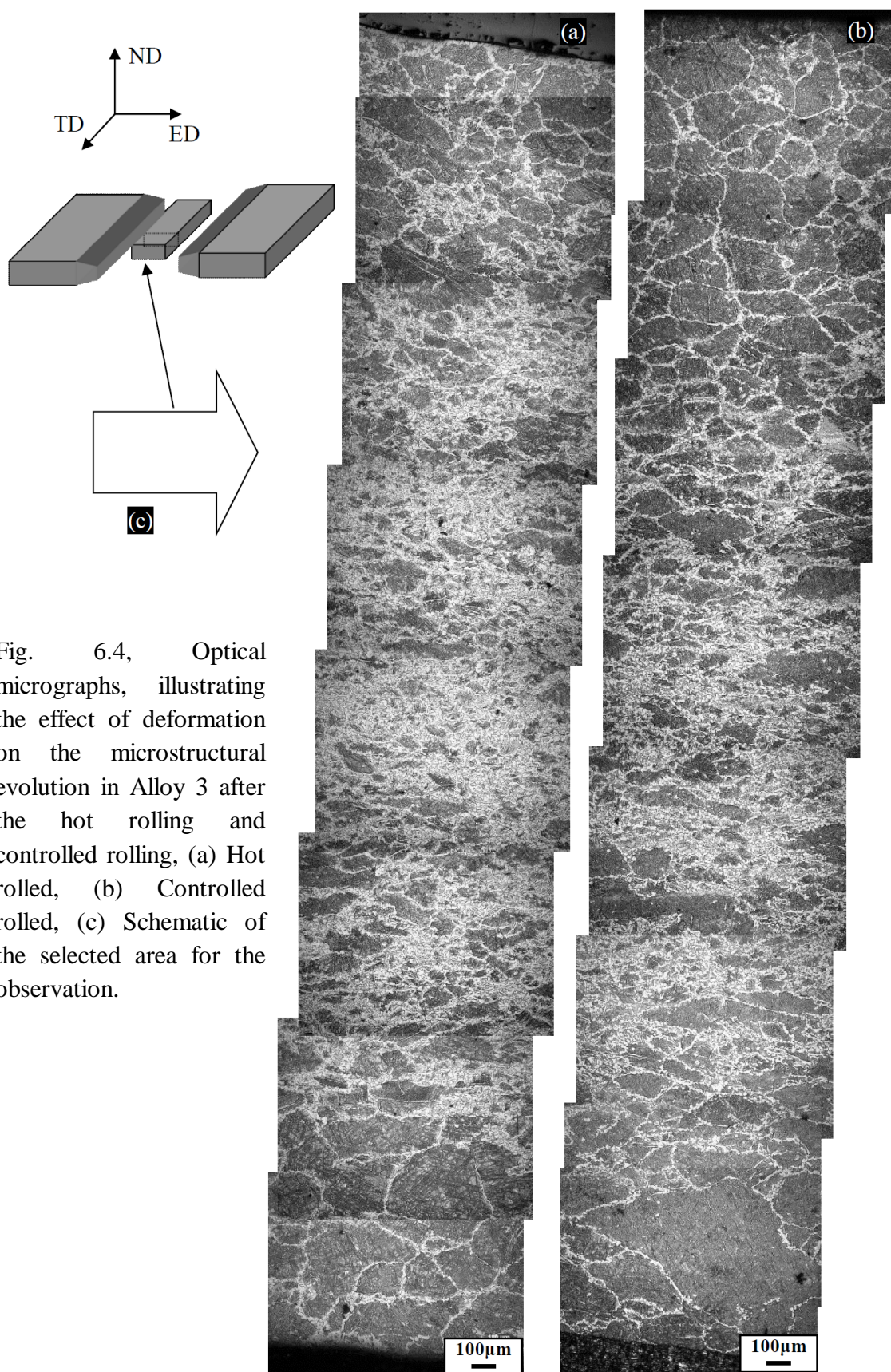


Fig. 6.4, Optical micrographs, illustrating the effect of deformation on the microstructural evolution in Alloy 3 after the hot rolling and controlled rolling, (a) Hot rolled, (b) Controlled rolled, (c) Schematic of the selected area for the observation.

The volume fraction of ferrite was measured using ImageJ software from the optical micrographs. Details of the ferrite volume fraction of Alloys 2 and 3 are summarized in Table 6.1. Fig. 6.5 shows the trend of the volume fraction of ferrite as a function of thermomechanical processing condition. The measurements indicated two different proportions of ferrite for the hot rolled and controlled rolled specimens in both Alloys 2 and 3. Compared to the micrographs shown in Figs. 6.3 and 6.4, a major difference is seen. The volume fraction of ferrite in Alloy 3 shows a reduction after controlled rolling, whereas this led to a slight increase in Alloy 2.

Table 6.1, Volume fraction of allotriomorphic ferrite.

	Hot rolled		Controlled rolled	
	Alloy 2	Alloy 3	Alloy 2	Alloy 3
Ferrite (vol%)	12.5±2.4	36.6±5.7	15.6±5.0	26.2±9.0

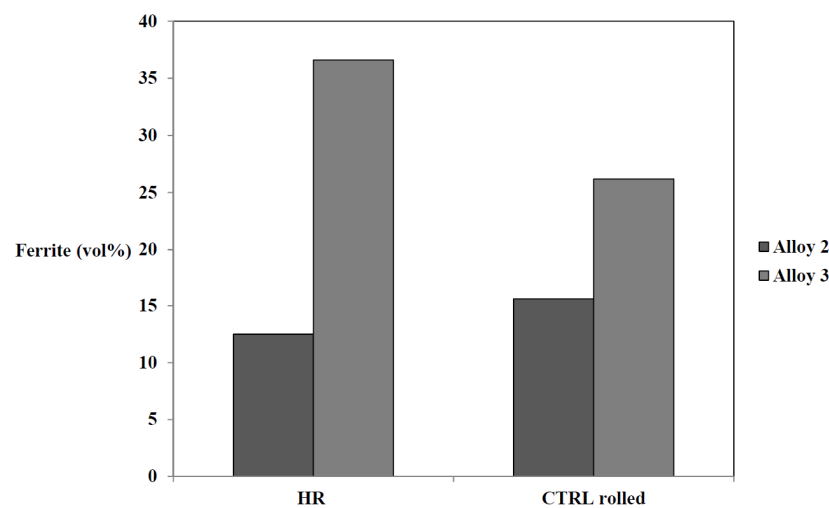


Fig. 6.5, Volume fraction of allotriomorphic ferrite versus the thermomechanical processing condition.

The effect of controlled rolling up to the end of the finishing stage on the precipitation behaviour and evolution of austenite was more specifically studied by quenching the specimens straight away after the last deformation at 830°C. Figs. 6.6 and 6.7 show optical micrographs of the interrupted quench specimens in which the prior austenite grain boundaries can be seen. The images show considerable recrystallization of austenite at regions close to the deformation zone in Alloy 3. In contrast, minimal recrystallization was observed in Alloy 2 (Figs. 6.6 and 6.7 (b)).



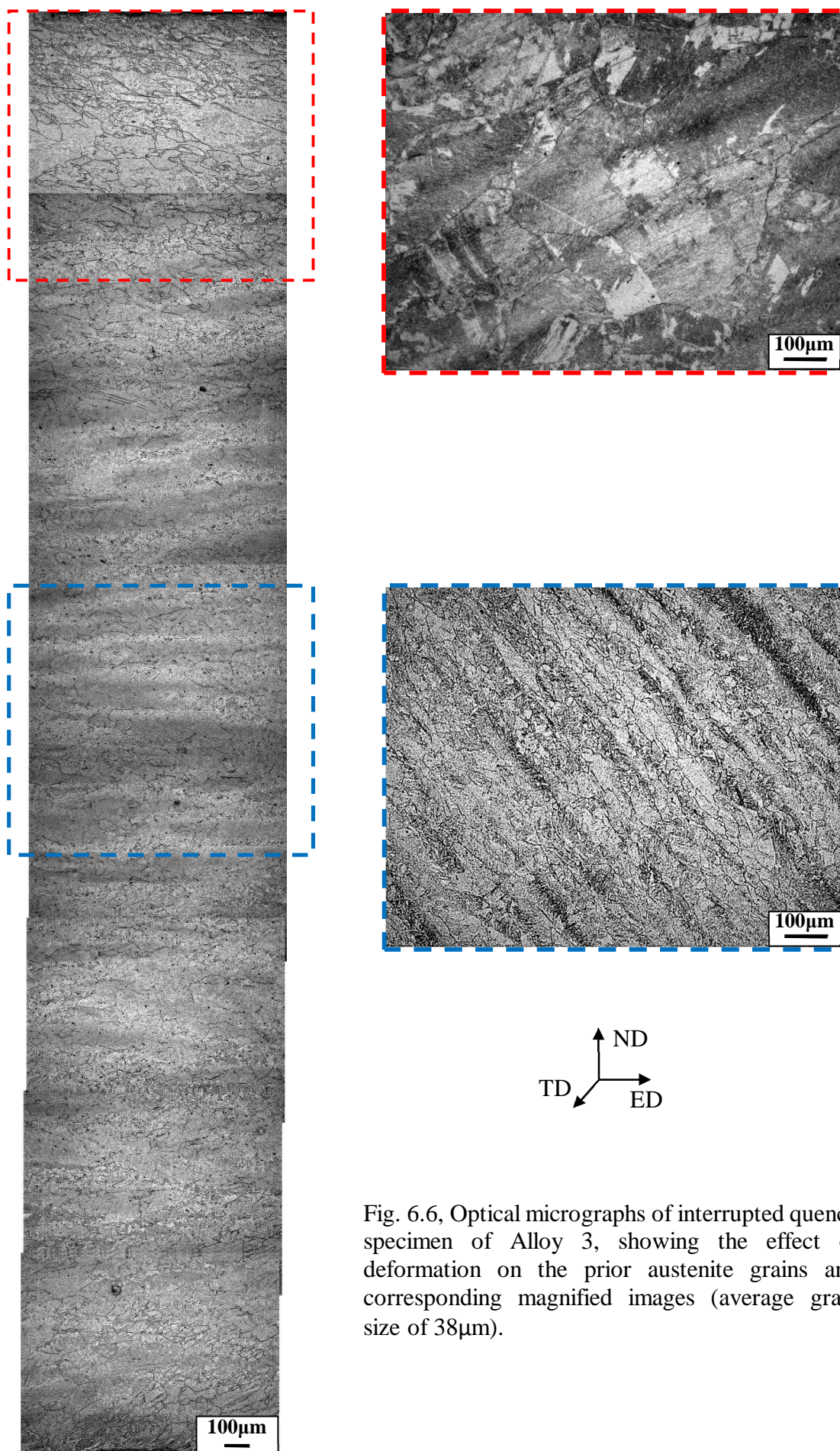
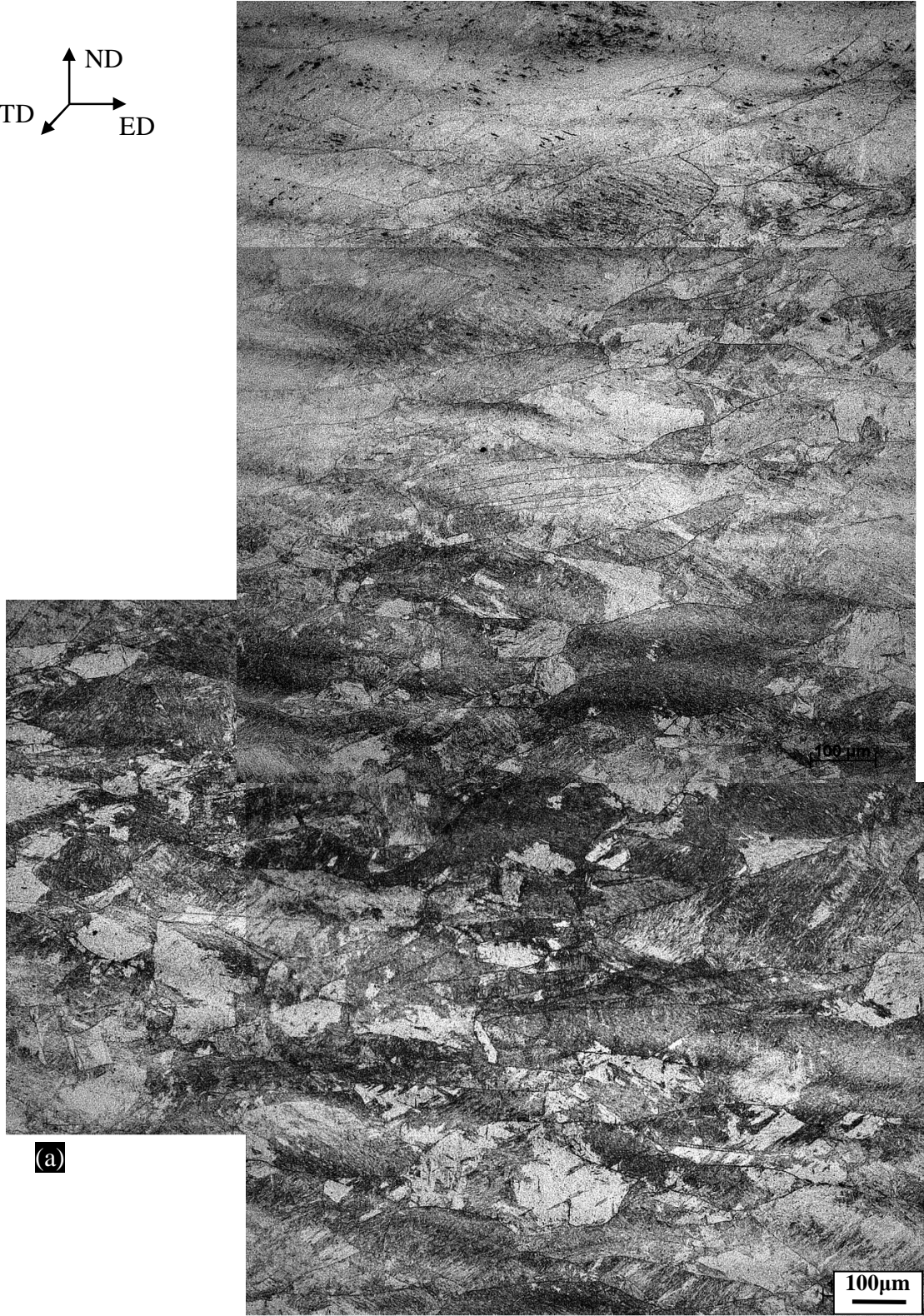


Fig. 6.6, Optical micrographs of interrupted quench specimen of Alloy 3, showing the effect of deformation on the prior austenite grains and corresponding magnified images (average grain size of 38μm).





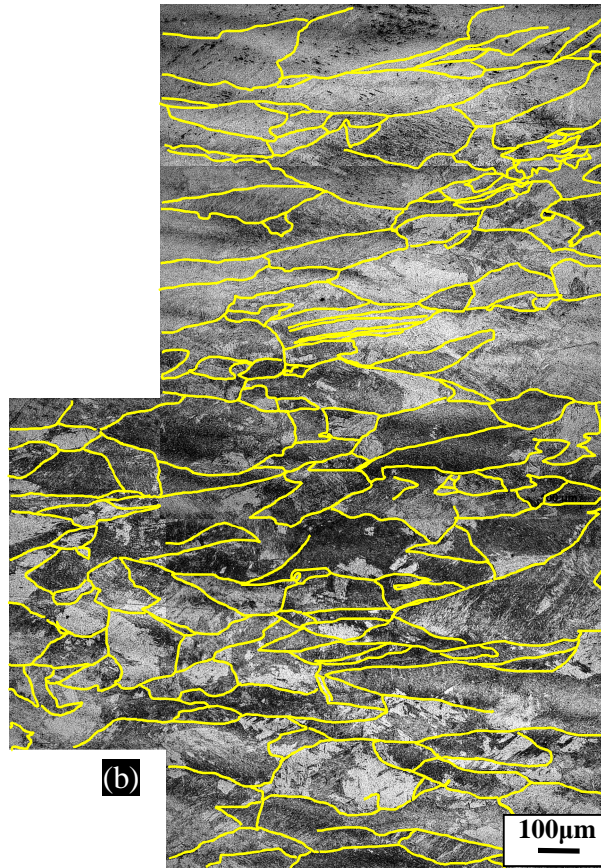


Fig. 6.7, (a) Optical micrograph illustrating the effect of deformation on the prior austenite grains in Alloy 3 after the controlled rolling, (b) The highlighted grain boundaries of micrograph in (a) with average grain size of 121 $\mu\text{m}$ .

Although the recrystallization-stop temperature was not investigated for Alloy 2, the present micrographs clearly show that the deformation at 1000°C and 830°C did not cause recrystallization, Figs. 6.6 and 6.7, resulting in elongated prior austenite grains. This shows that the Nb addition in Alloy 2 was effective in preventing recrystallization for the conditions used here. In contrast, in Alloy 3 the micrographs indicate the concurrent recrystallization and elongation of austenite grains at the deformation zones. It seems that a heterogeneous necklace structure was formed in Alloy 3 that needs to be taken into consideration in interpreting the deformation behaviour and microstructural evolution.

Characterization of the dark regions in the optical micrographs in Figs. 6.2 to 6.4, was carried out by the electron microscopy. Figs. 6.8 (a) to (d) compares SEM micrographs of small bright features surrounded by polygonal ferrite in Alloys 2 and 3 after the hot rolling and controlled rolling. The microstructure mainly involves secondary features in packet shape in the vicinity of fragmented secondary phases along the lath shape ferritic constituents. Similar, structures have been reported in the literature for bainitic ferrite steels [95]. The microstructure of hot rolled and controlled rolled specimens suggest that the secondary phases are retained austenite, bainite, martensite and possibly cementite.

The phases formed in the austenite after the interrupted quenching was also studied by SEM (Figs. 6.8 (e) and (f)). The micrographs are believed to show martensite and bainite. On the other hand, the XRD results confirmed the presence of retained austenite through these regions. It is therefore clear that the microstructures contain lath shape structure which can be ascribed to bainitic ferrite and martensite. In this case, the sheave lath features containing small particles were considered to be bainite.



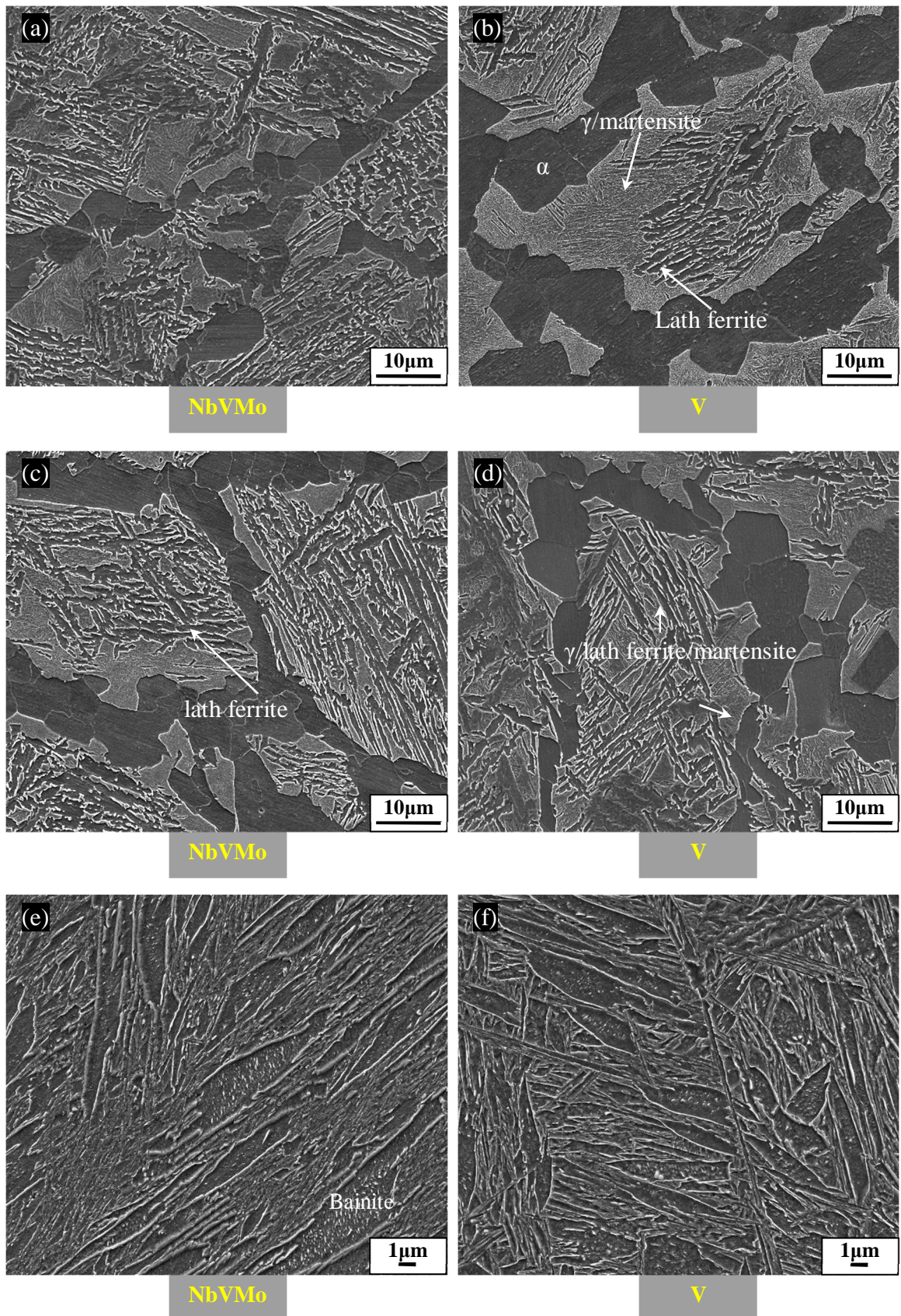


Fig. 6.8, Selected scanning electron microscopy micrographs from Alloys 2 and 3, (a) and (b) After the hot rolling of Alloys 2 and 3, respectively, (c) and (d) After the controlled rolling of Alloys 2 and 3, respectively, (e) and (f) Interrupted quench samples of Alloys 2 and 3, respectively.

### 6.2.3. Retained Austenite Content

Fig. 6.9 (a) gives a typical XRD spectrum which is indexed by the standard JCPDS cards [122]. The presence of three phases was detected in both alloys after the hot rolling, controlled rolling and interrupted quenching, including ferrite, retained austenite and cementite. Fig. 6.9 (b) indicates a typical XRD spectrum and the simulated profile based on Rietveld refinement technique.

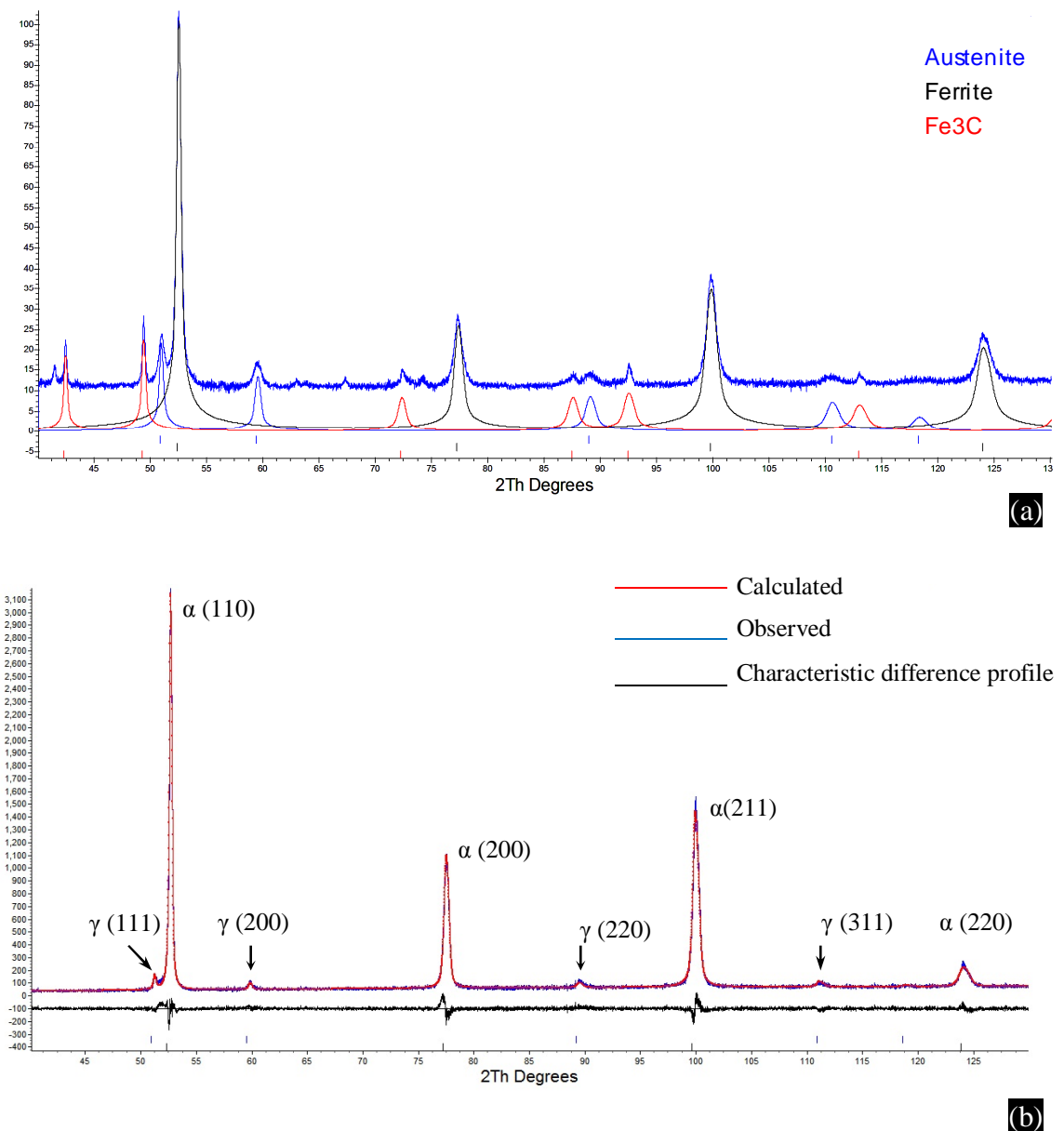


Fig. 6.9, Selected graphical representation of X-ray diffraction pattern of the hot rolled Alloy 2, (a) Showing the peaks corresponding to the ferrite, retained austenite and cementite, (b) A selected graphical representation of Rietveld analysis for X-ray diffraction pattern.

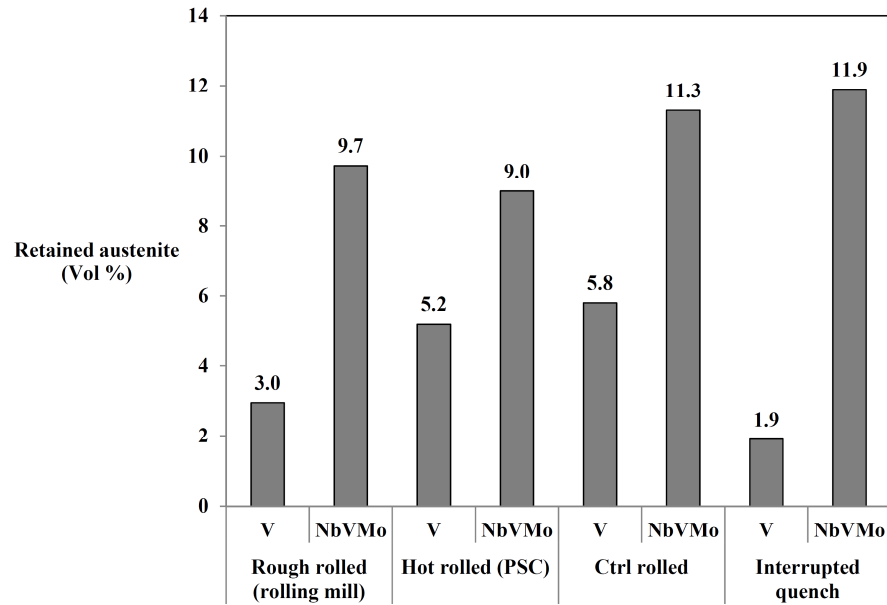
According to the XRD results, a considerable amount of retained austenite was formed in the microstructure after the hot rolling and controlled rolling (Table 6.2). The volume fraction of cementite was measured using the relevant integrated intensity of peaks. Table 6.2 compares the carbon content of retained austenite and the volume fraction of cementite in terms of the thermomechanical processing used. The carbon content was measured according to the lattice parameter of retained austenite using the Nishiyama equation (see equation 4.1).

Table 6.2, The retained austenite parameters and cementite examined by XRD.

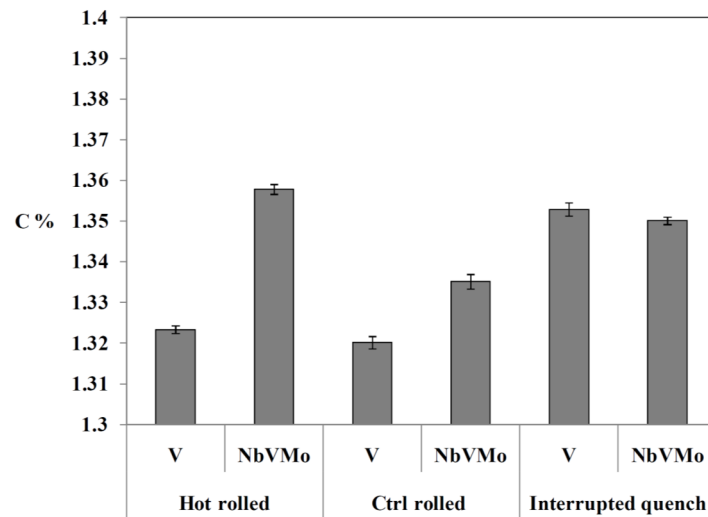
		Retained $\gamma$ (vol%)	$C_\gamma$ (wt%)	$a_\gamma$ (Å)	$Fe_3C$ (vol%)
Nb free	Rough rolled	2.9	1.247	$3.60497 \pm 0.00127$	1.3
	Hot rolled	5.2	1.323	$3.60850 \pm 0.00097$	1.9
	Controlled rolled	5.8	1.320	$3.60835 \pm 0.00153$	0.3
	Interrupted quench	1.9	1.352	$3.60988 \pm 0.00159$	0.7
Nb containing	Rough rolled	9.7	1.305	$3.60767 \pm 0.00119$	1.4
	Hot rolled	9.0	1.357	$3.61011 \pm 0.00120$	5.5
	Controlled rolled	11.3	1.335	$3.60905 \pm 0.00179$	1.1
	Interrupted quench	11.9	1.350	$3.60975 \pm 0.00092$	0.2

The trend in the volume fraction of retained austenite is shown graphically in Fig. 6.10. It was found that the volume fraction of retained austenite in all conditions shows a similar behaviour between Alloys 2 and 3. It appears that the amount of retained austenite in Alloy 2 is higher than Alloy 3, presumably due to the presence of Nb,Mo in Alloy 2. The possible influence of Nb,Mo on the microstructure evolution is discussed based on available data from the precipitation behaviour through the following section.





(a)



(b)

Fig. 6.10, (a) Volume fraction of retained austenite in terms of thermomechanical processing for Alloys 2 and 3, measured by XRD method, (b) Carbon content of retained austenite, measured from the lattice parameter.

The carbon content of the retained austenite after hot rolling and controlled rolling Alloy 2 was higher compared to Alloy 3, while there was little difference between the two alloys after the interrupted quenching at 830°C.

#### 6.2.4. TEM Thin Foil Analysis

More detailed studies on the secondary features were performed using TEM observations. The characterization was repeated at least for two separate thin foil samples for each condition. TEM observations of thin foil samples confirmed the presence of retained austenite, bainitic ferrite and martensite as well as microalloy precipitates in the microstructure. Fig. 6.11 gives typical micrographs, showing the interaction between dislocations and precipitates in the ferrite phase for the hot rolled and controlled rolled Alloy 3. The EDS spectra strongly suggest the presence of precipitates, although the precipitate contrast is obscured by the locally high density of tangled dislocations.

A few large precipitates ( $\geq 50\text{nm}$ ) in Alloys 2 and 3 were observed in the thin foil and extraction replica samples (typically Fig. 6.11 (b)). These precipitates were observed in all samples regardless of the effect of thermomechanical processing.

Fig. 6.12 shows the lamellar structure of ferrite and retained austenite in Alloy 3. The microstructure and SAED patterns confirmed the structure consisting of lath ferrite adjacent to the retained austenite and possible martensite. Similar behaviour was observed in Alloy 2. The illumination of laths from the same diffraction spot demonstrates the same orientation.

It can be clearly seen from Fig. 6.13 that a considerable number of dislocations were piled up throughout the lath ferrite. These features are similar to Misra's et al. report concerning dual phase steels, although they suggested such structure as martensite and retained austenite [159]. However, observing such lath ferrite with the tangle of dislocations was interpreted as acicular/bainitic ferrite in the present study. It can be suggested that the dislocations might be generated due to the relaxation of plastic deformation during bainite transformation. It is consistent with the report of Furuhashi et al., who suggested the possibility of martensite and retained austenite and bainitic ferrite as a lath structure in the vicinity of each other [95]. Fig. 6.13 (d) shows a given structure consisting of dislocation tangles through these particular regions. The EDS confirmed the presence of microalloying elements at precipitates on the dislocations.



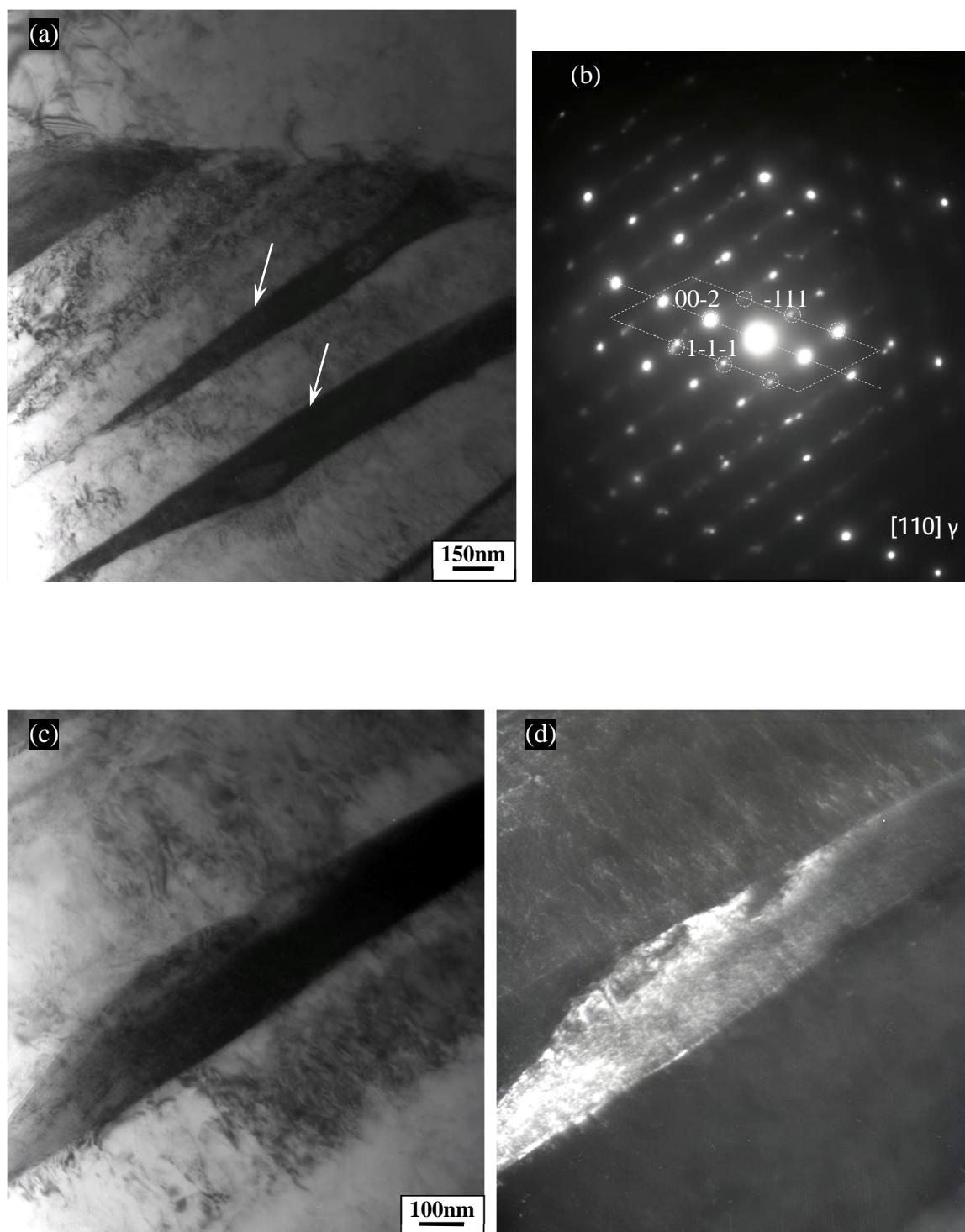


Fig. 6.12, Selected transmission electron micrographs of a thin-foil sample of Alloy 3 after the hot rolling, (a) Bainitic ferrite lath adjacent to retained austenite, (b) SAED pattern of the selected area, (c) and (d) Bright and dark field images of a given retained austenite lath, respectively.

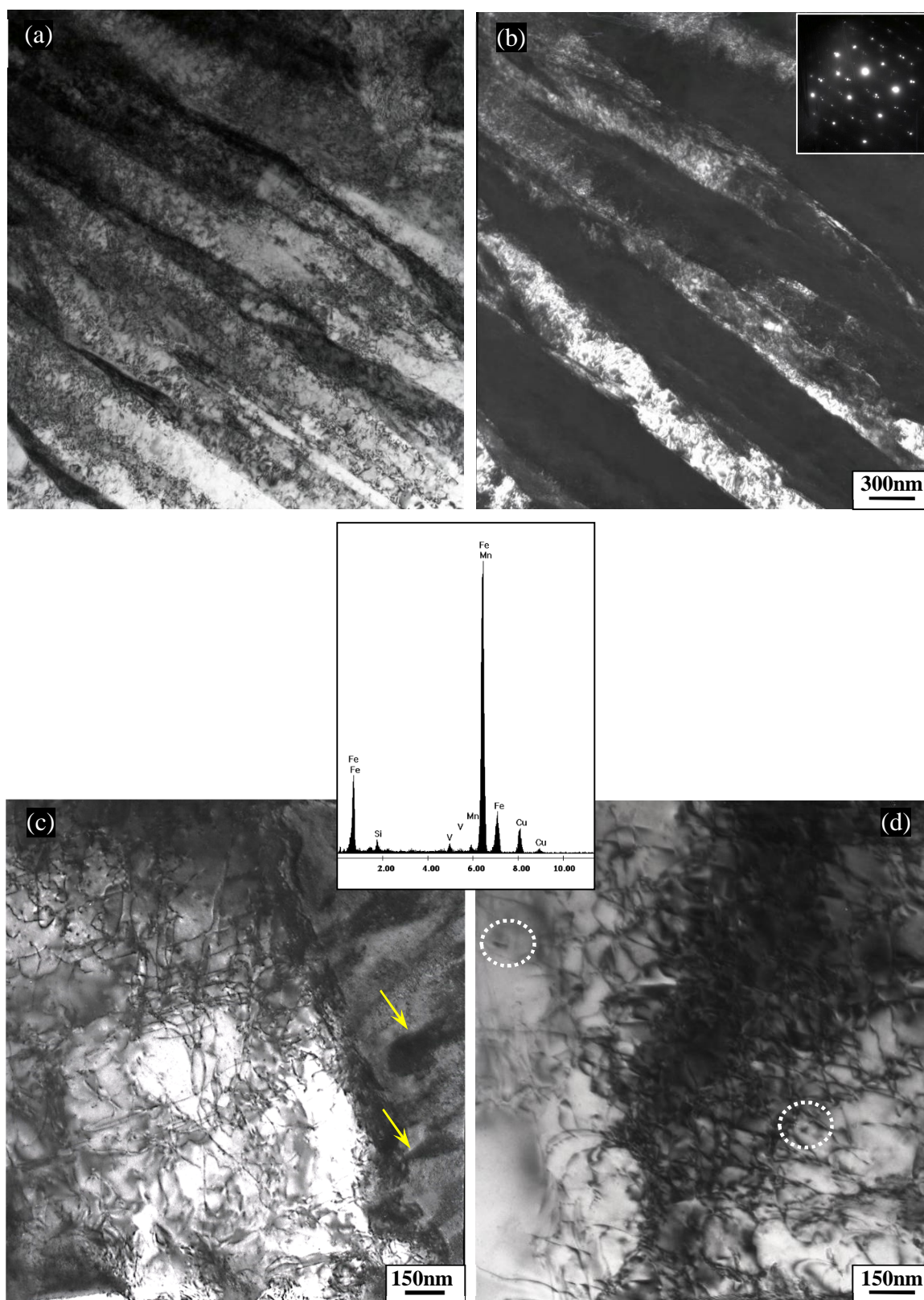


Fig. 6.13, Selected transmission electron micrographs of a thin-foil sample of Alloy 3 after the hot rolling, showing the presence of microalloying precipitates in the vicinity of dislocations, (a) and (b) Bright and dark field images of lath ferrite and corresponding SAED pattern, (c) and (d) Tangle of dislocation in lath ferrite and typical EDS from the microalloying precipitates in these area, arrows indicating features similar to cementite.



Fig. 6.14 shows the retained austenite adjacent to bainite which contained a fine distribution of carbide (arrowed).

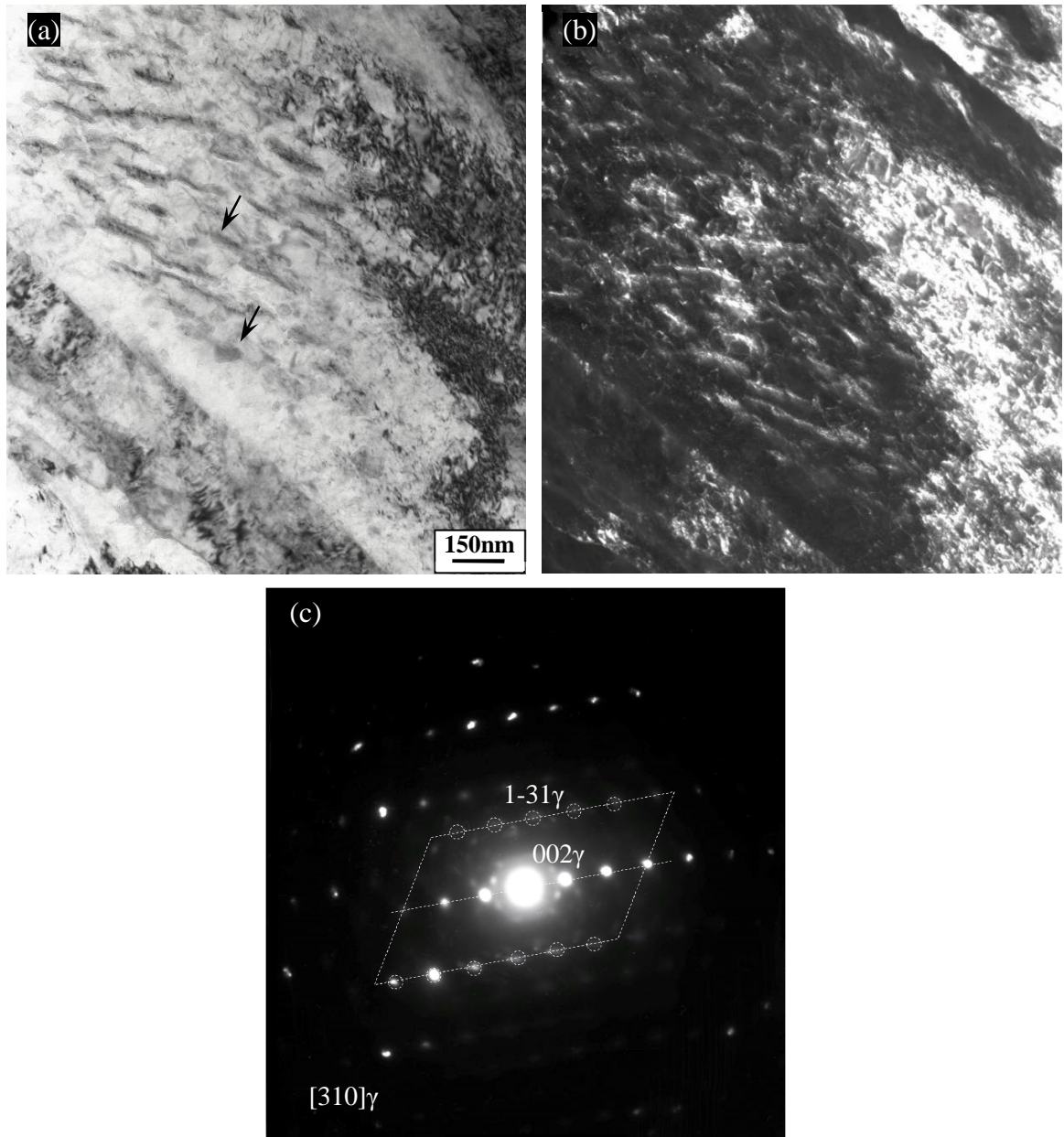


Fig. 6.14, Selected transmission electron micrographs of a thin-foil sample of Alloy 3 after the controlled rolling, (a) and (b) Bright and dark field images of bainite adjacent to retained austenite, respectively, (arrows indicating particle similar to cementite), (c) Corresponding SAED pattern.

Fig. 6.15 gives micrographs of precipitates along a ferrite grain boundary. DF image and EDS confirmed the presence of precipitates through the grain boundaries of Alloy 3. By contrast, no significant amounts of microalloying precipitates were detected in Alloy 2.

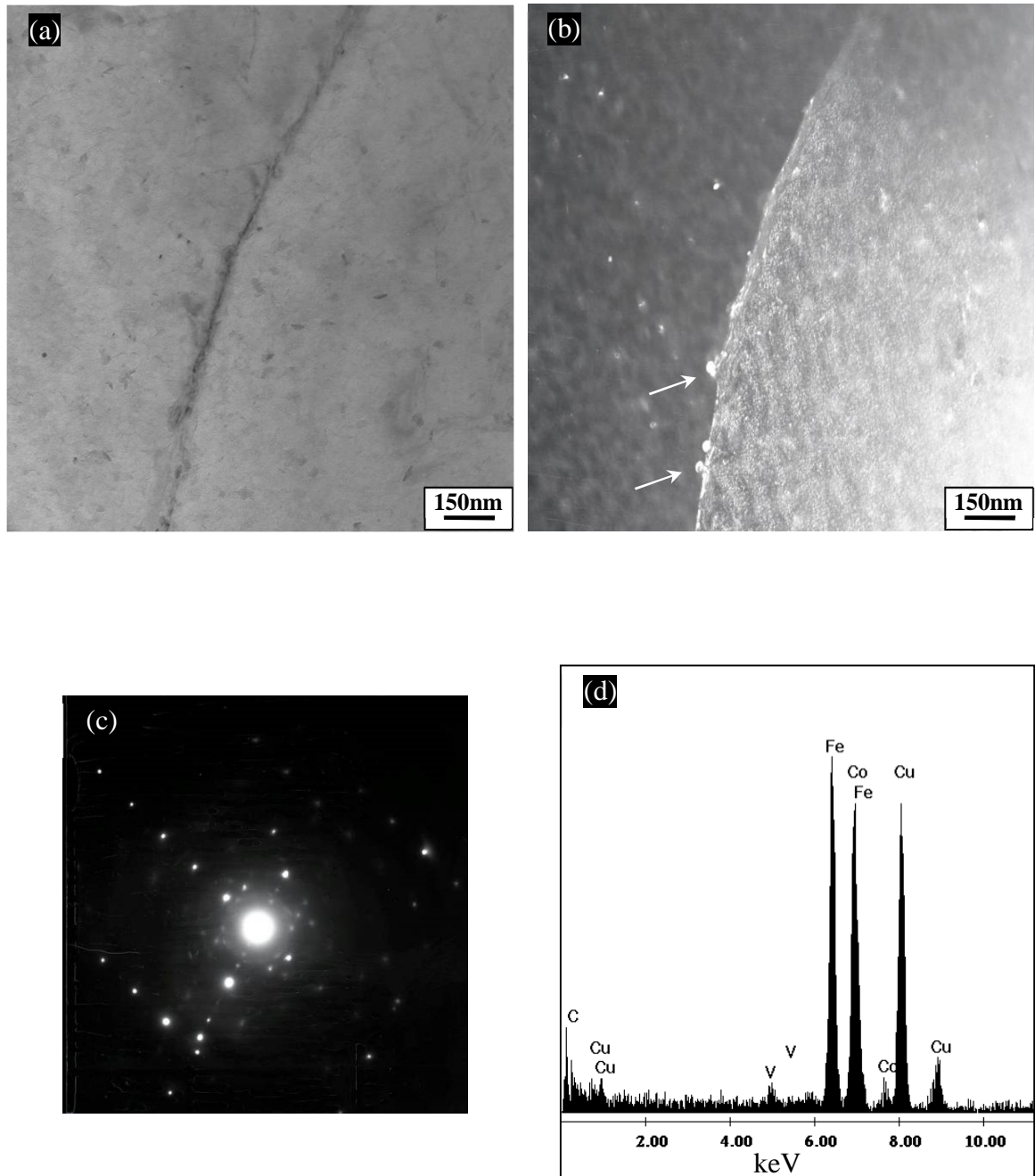


Fig. 6.15, Selected thin-foil transmission electron micrographs of Alloy 3 after the controlled rolling, (a) and (b) Bright and dark field images of ferrite with the presence of V precipitates at grain boundaries, respectively, (c) SAED pattern corresponding precipitates, (d) A typical EDS spectrum of precipitates located at grain boundary.



Similar structure to that shown in Figs. 6.12 and 6.13 was observed in the Alloys 2 and 3 with laths of bainitic ferrite and retained austenite in the controlled rolled samples (Fig. 6.16). TEM observations suggest the interaction between the forest dislocations in lath ferritic regions and microalloying precipitates in both alloys. The presence of dislocations on one side of lamellar interfaces is related to either the shear transformation process or due to the dislocation pile-ups at the regions close to grain boundaries as a result of deformation during the thermomechanical processing.

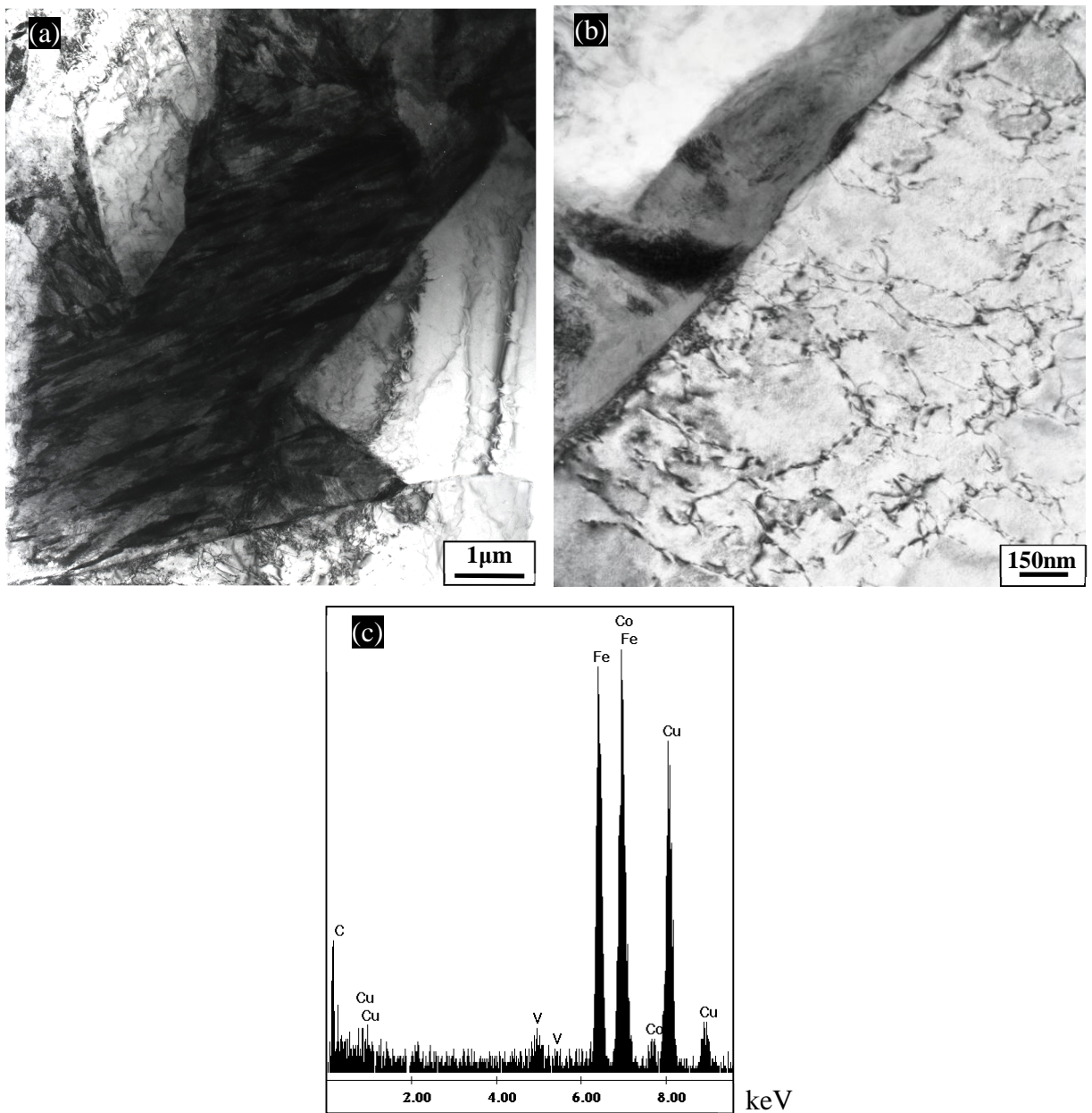


Fig. 6.16, Bright field TEM image of a thin foil from a sample of Alloy 3 after the controlled rolling, (a) Illustrating a very fine scale bainite, (b) Showing the presence of dislocations in bainitic ferrite adjacent to retained austenite, (c) A typical EDS spectrum of precipitates located in bainitic ferrite in (b).

Fig. 6.17 shows a fine ferrite grain in the microstructure of controlled rolled Alloy 3, which could be formed due to a reconstructive transformation. The EDS spectra reveal the presence of microalloying precipitates in this grain whereas no significant numbers of precipitates were detected around the grain in the matrix (Fig. 6.17 (d)).

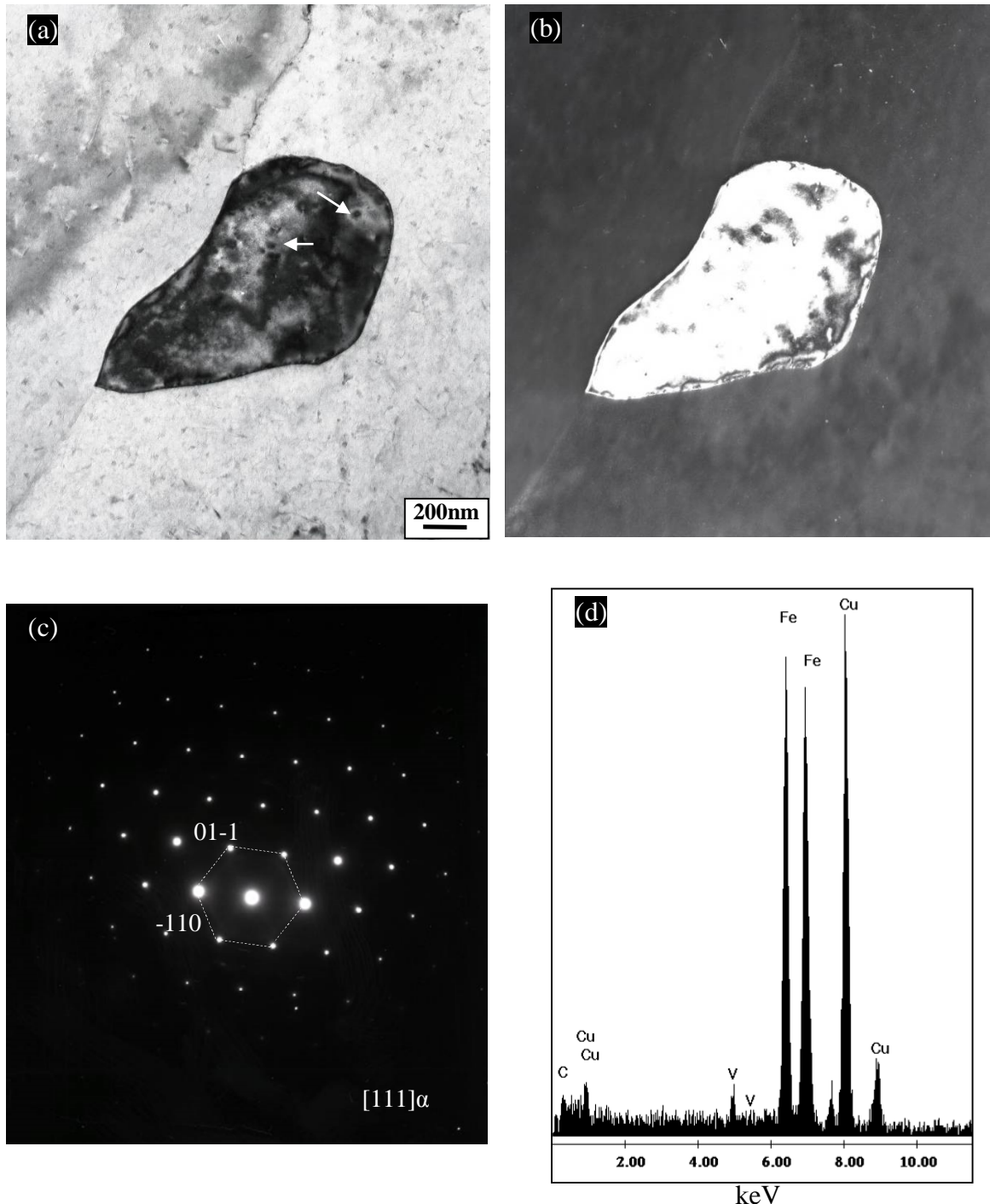


Fig. 6.17, Selected thin-foil transmission electron micrographs of Alloy 3 after the controlled rolling, (a) and (b) Bright and dark field images of a ferrite grain and the presence of V precipitates, respectively, (c) SAED pattern corresponding to the observed ferrite, (d) Corresponding EDS spectrum of the shown precipitates by arrows in (a).

The position of precipitates in the interrupted quench structure was studied by thin foil samples. This shows a martensitic structure in addition to lath ferrite with a high dislocation density and lath shaped constituents (Fig. 6.18). The lath shaped features are interpreted as very fine bainite (arrow). Fig. 6.19 gives typical TEM micrographs, showing the position of precipitates in Alloy 2 after the interrupted quenching.

From the TEM observations, it was found that the precipitates were widely located inside the lath ferrite and adjacent to the tangle of dislocations through these regions (Fig. 6.19). In contrast, the thin foil samples of Alloy 3 did not exhibit any precipitates.

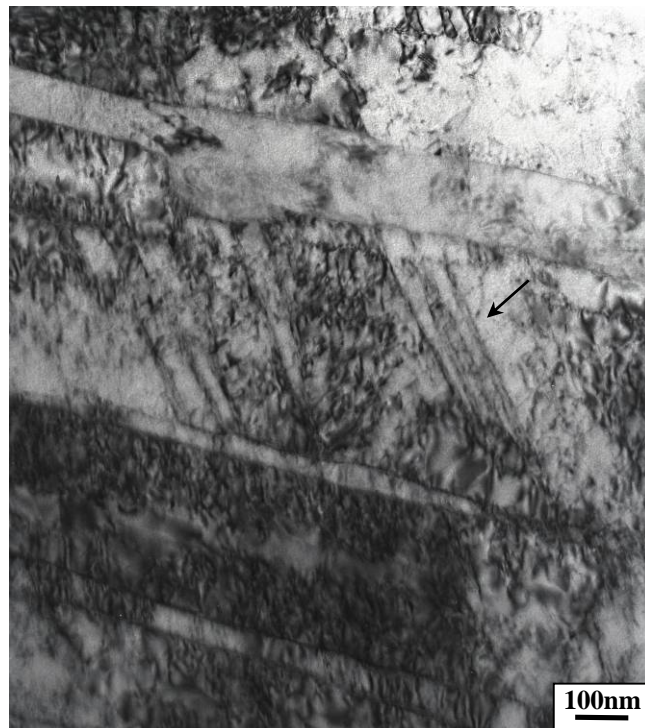


Fig. 6.18, Bright field TEM image of a thin foil sample of the interrupted quench Alloy 2, indicating the lath ferritic constituents with a high density of dislocations.

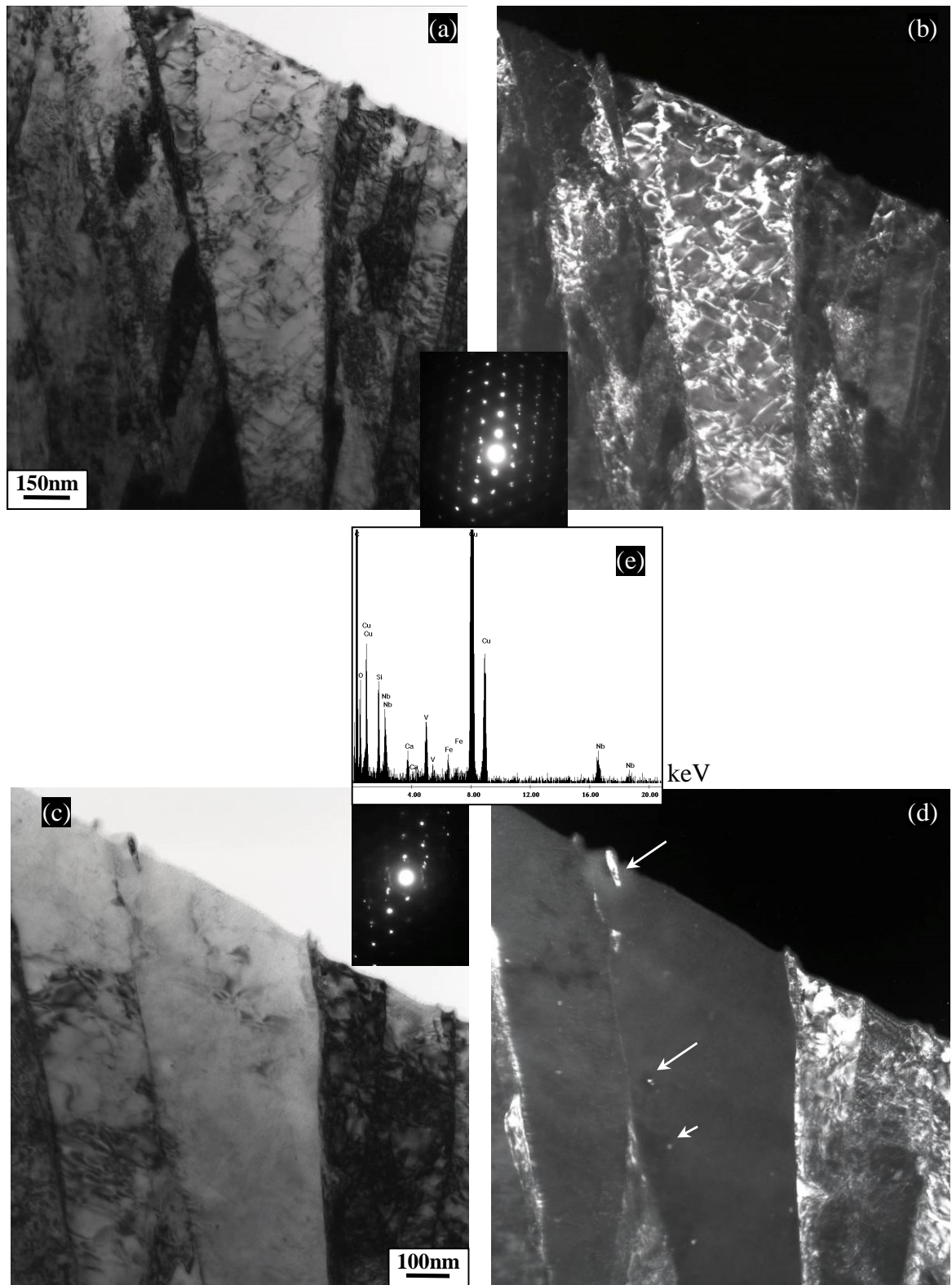


Fig. 6.19, (a) and (b) Bright and dark field TEM images of a thin foil and SAED pattern from a sample of interrupted quench Alloy 2, showing the presence of dislocations in lath ferrite structure, (c) and (d) Bright and dark field TEM images of a thin foil and SAED pattern from a sample of interrupted quench Alloy 2, showing the precipitates in regions close to grain boundaries of lath ferrite, (e) Corresponding EDS of precipitates located in the lath ferrite.



### 6.2.5. TEM Carbon Extraction Replica Analysis

As pointed out earlier, precipitates are ideally categorized in five groups in terms of their morphology, including cuboid, spherical, oval, rectangle and irregular/complex. The precipitates were randomly analysed by combined EELS, EDS and electron diffraction to study the presence of microalloying elements, carbon and nitrogen in them. Figs. 6.20 to 6.22 give typical micrographs and EDS/ EELS spectra from the different morphologies of precipitates in Alloys 2 and 3 after the hot and controlled rolling.

The presence of heavier elements such as Nb, V, Ti and Mo was initially checked by EDS, whereas EELS spectra were used to detect the lighter elements such as N, C and S. In many EELS spectra, a broad hump with low intensity was observed in the range of nitrogen edge which is related to the small amount of nitrogen. The true shape of the ionisation edge was determined by subtracting the background from the edge. Moreover, the observed fine structure after the edge, i.e. the electron energy-loss near edge structure (ELNES), is particularly useful in determining the local bonding environment [160].

Fig. 6.22 shows a typical complex precipitate in the controlled rolled Alloy 2. An inverse fast Fourier transform (IFFT) shows the lattice fringes of the larger precipitate in zone axis of [110] FCC (Figs. 6.22 (d)). The lattice parameter of the larger NbVMo(C,N) precipitate is about 4.82 Å. This shows good agreement with the reported values in the literature for the NbV(C,N), NbTi(C,N) precipitates [20, 161]. However, due to the presence of different elements in the precipitate and possible mutual solubility effect, it is difficult to generalize this to all precipitates [156].

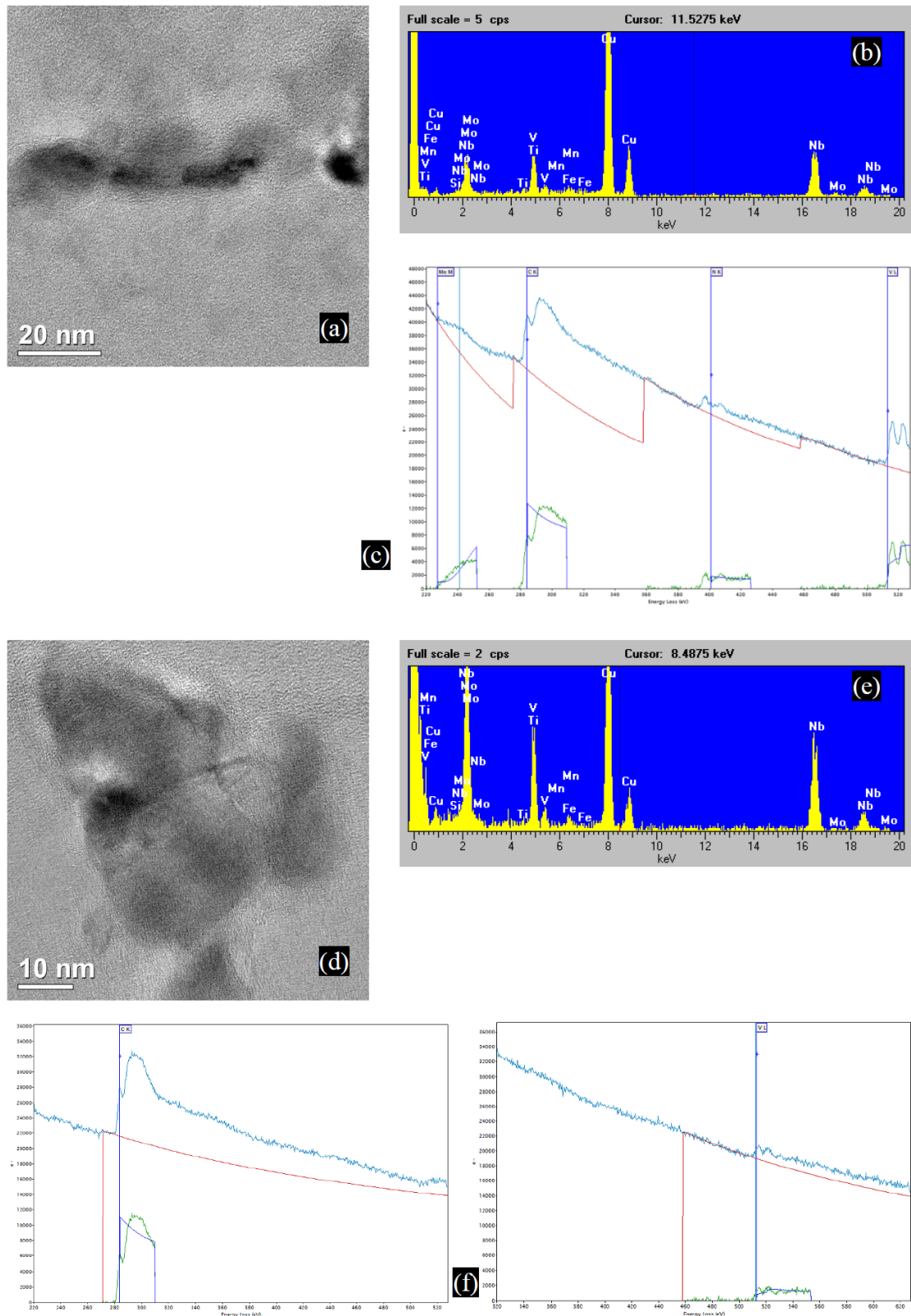


Fig. 6.20, (a) Bright field TEM image of a carbon extraction replica from a sample of Alloy 2 after the hot rolling, showing a typical needle like precipitate, (b) and (c) Corresponding EDS and EELS spectra, respectively, (d) Bright field TEM image of a carbon extraction replica from a sample of Alloy 2 after the hot rolling, showing a typical triangle precipitate, (e) and (f) Corresponding EDS and EELS spectra, respectively.

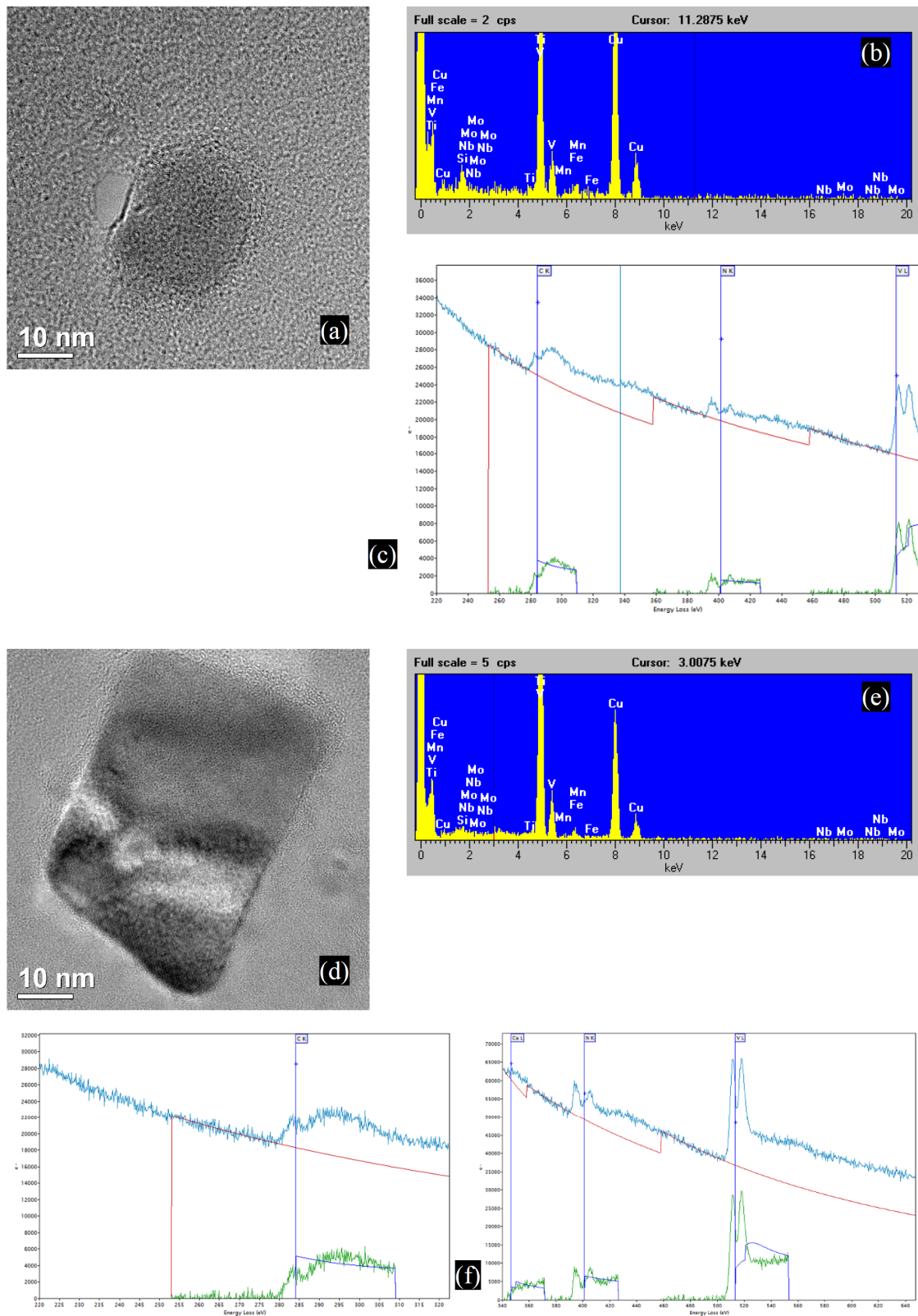


Fig. 6.21, (a) Bright field TEM image of a carbon extraction replica from a sample of Alloy 3 after the hot rolling, showing a typical spherical precipitate, (b) and (c) Corresponding EDS and EELS spectra, respectively, (d) Bright field TEM image of a carbon extraction replica from a sample of Alloy 2 after the hot rolling, showing a typical rectangle precipitate, (e) and (f) Corresponding EDS and EELS spectra, respectively.



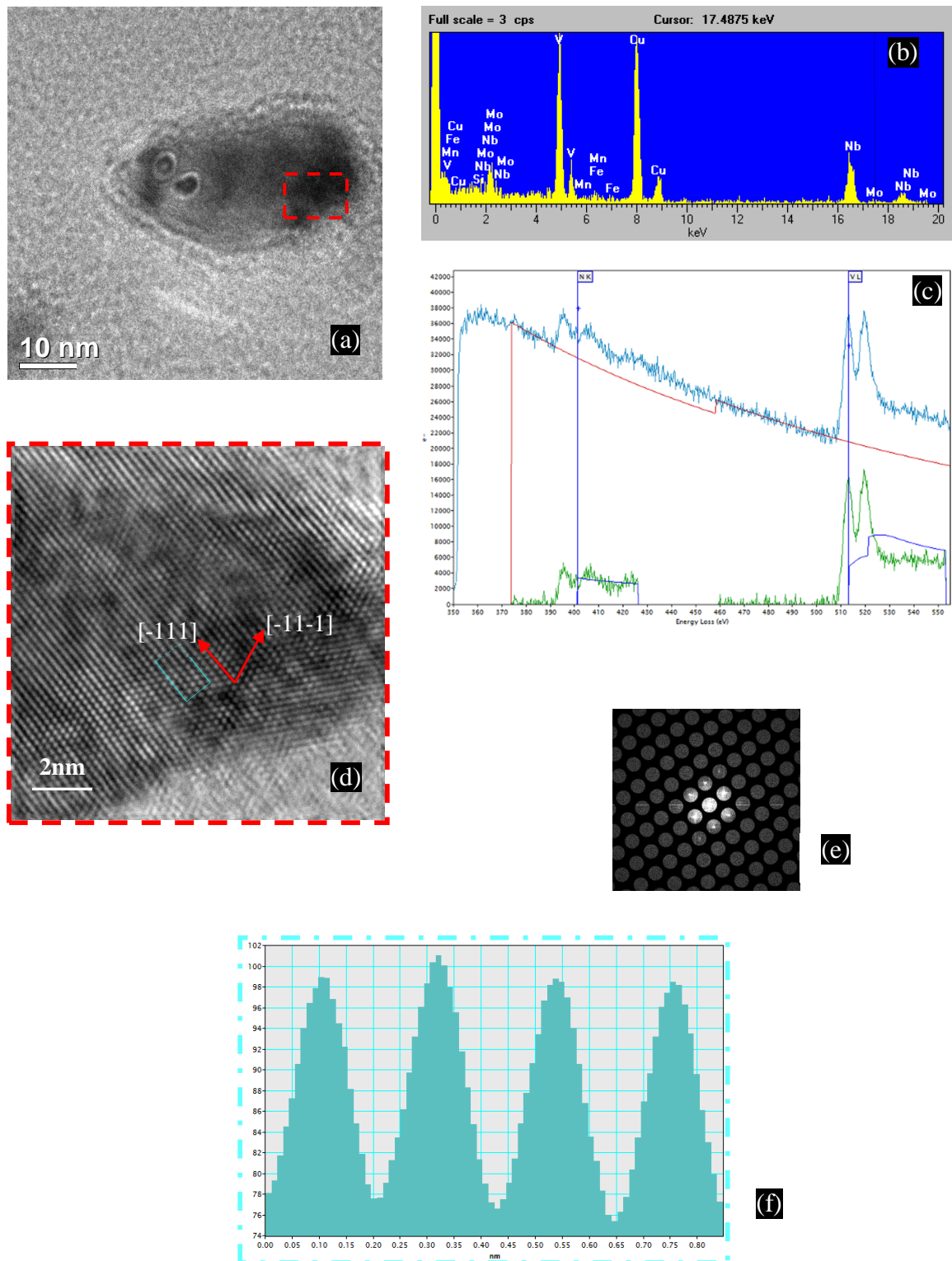


Fig. 6.22, (a) Bright field TEM image of a carbon extraction replica from a sample of Alloy 2 after the controlled rolling, showing a typical complex precipitate, (b) and (c) Corresponding EDS and EELS spectra, respectively, (d) Inverse Fourier images from the red dashed line rectangles in (a), (e) Reflections corresponding to the main precipitate i.e. red dash-rectangle in zone axis [110] FCC, (f) Corresponding graphical contrast between lattice fringes in (d), with a lattice parameter of  $\approx 4.82 \text{ \AA}$ .

Figs. 6.23 to 6.25 give typical TEM micrographs from the extraction replicas of the hot rolled samples. The replication successfully extracted the precipitates with different morphologies from Alloys 2 and 3.

Figs. 6.23 (a) and (b), show fine Nb(C,N) precipitates distributed throughout the microstructure in a small region of Alloy 2. By contrast, the extraction replica failed to show similar behaviour in Alloy 3.

Figs. 6.23 (d) and (e), show precipitates with a large variety of morphologies in the microstructure of hot rolled Alloy 2. The EDS spectra from the different types of precipitate reveal the presence of Nb and V in the majority of precipitates. A few precipitates contained Mo in their chemical composition.

It was also found from TEM observations of Alloy 2 that locally the density of precipitates was higher along a linear direction than other places (Fig. 6.24 (a)). These may have been on a grain boundary or from strain induced precipitation. In the micrographs of Alloy 3 these features were also seen (Fig. 6.25 (a)).

The EDS spectra of Alloy 2 confirmed the high level of vanadium in the precipitates through these linear regions (Fig. 6.24(a)).

As mentioned above, the replica samples successfully extracted a few larger precipitates in Alloys 2 and 3. Figs. 6.24 (c) and (d), represent two typical larger precipitates and corresponding EDS spectra with irregular and spherical morphologies.

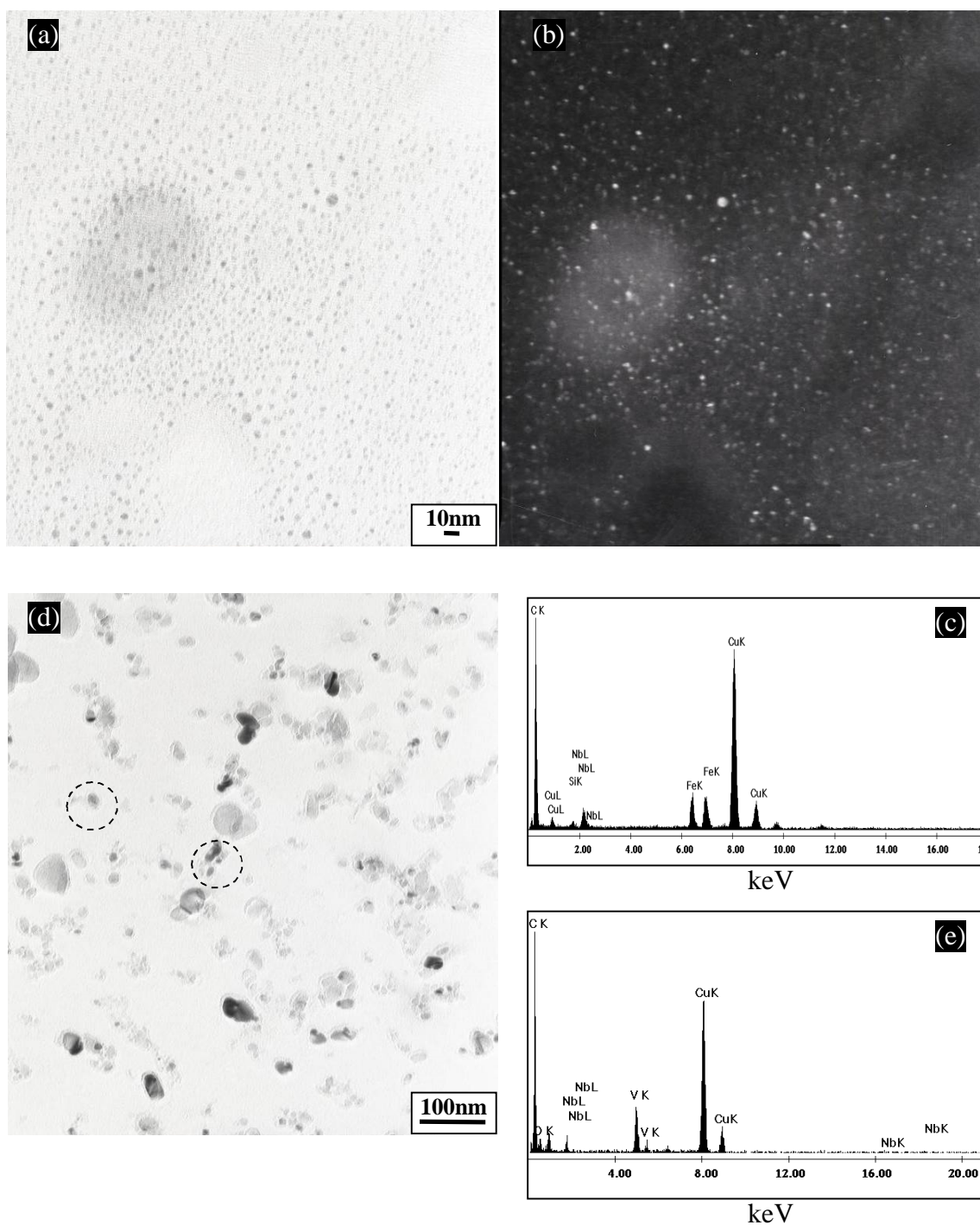


Fig. 6.23, (a) and (b) Bright and dark field TEM micrographs of a carbon extraction replica from a sample of Alloy 2 after the hot rolling, showing typical distribution of fine precipitates, (c) Corresponding EDS in (a), (d) Bright field TEM micrograph of a carbon extraction replica from a sample of Alloy 2 after the hot rolling, showing a typical precipitate distribution, (e) Corresponding a typical EDS spectrum from a given precipitate in (d).

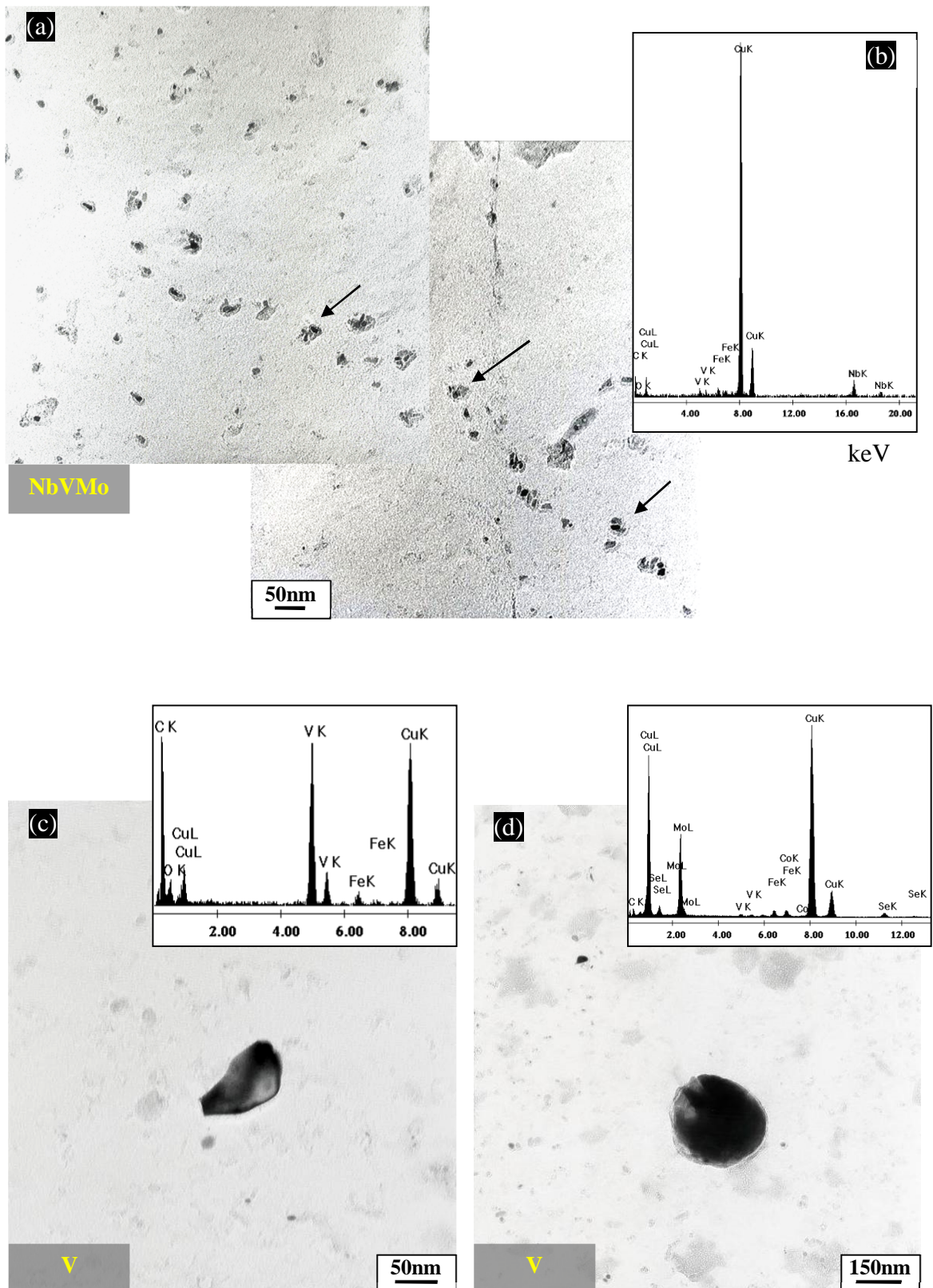


Fig. 6.24, (a) Bright field TEM micrograph of a carbon extraction replica from a sample of Alloy 2 after hot rolling, showing typical distribution of precipitates along a line, (b) Corresponding EDS, (c) TEM micrograph and EDS of hot rolled Alloy 3, showing a typical irregular precipitate, (d) TEM micrograph and EDS of hot rolled Alloy 3, showing a typical spherical precipitate.



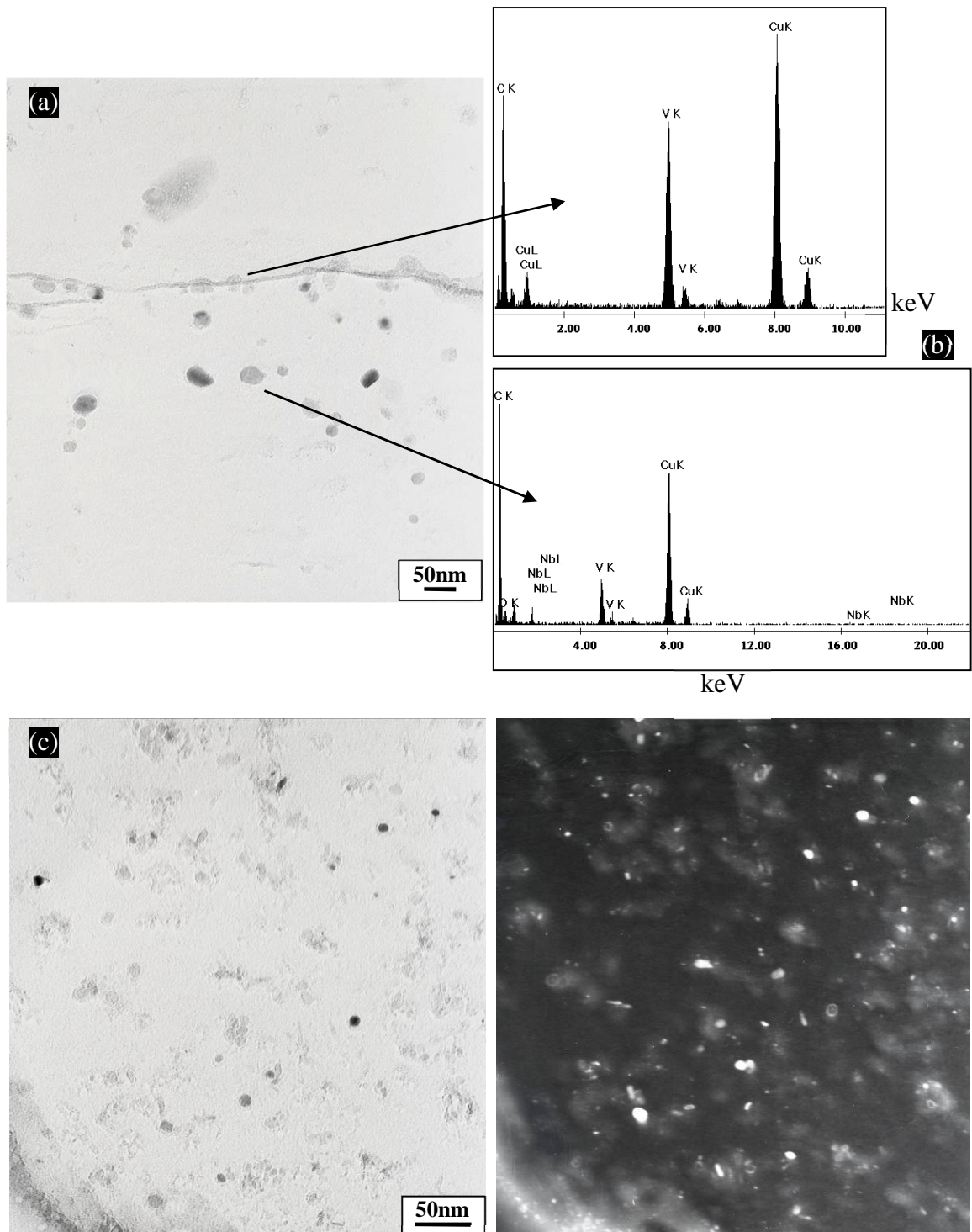


Fig. 6.25, (a) Selected bright field TEM micrograph of a carbon extraction replica from a sample of Alloy 3 after the hot rolling, showing typical distribution of precipitates, (b) Corresponding EDS spectra, showing the high level of V precipitates throughout a grain boundary shape alignment, (c) Bright and dark field TEM micrographs of a carbon extraction replica from a sample of Alloy 3 after the hot rolling, showing typical distribution of fine precipitates.

The precipitation behaviour after the controlled rolling was also investigated using carbon extraction replicas. The precipitates with different morphologies and chemical compositions were detected in the microstructure. Figs. 6.26 and 6.28 show different morphologies and sizes of precipitates from Alloy 3. The EDS spectrum from the complex shape precipitate indicates the presence of V and Ti (Fig. 6.26). As shown in other reports in literature, it is expected that the Ti with higher thermal stability facilitates the potential site for V precipitation that consequently appeared as a complex shape [5].

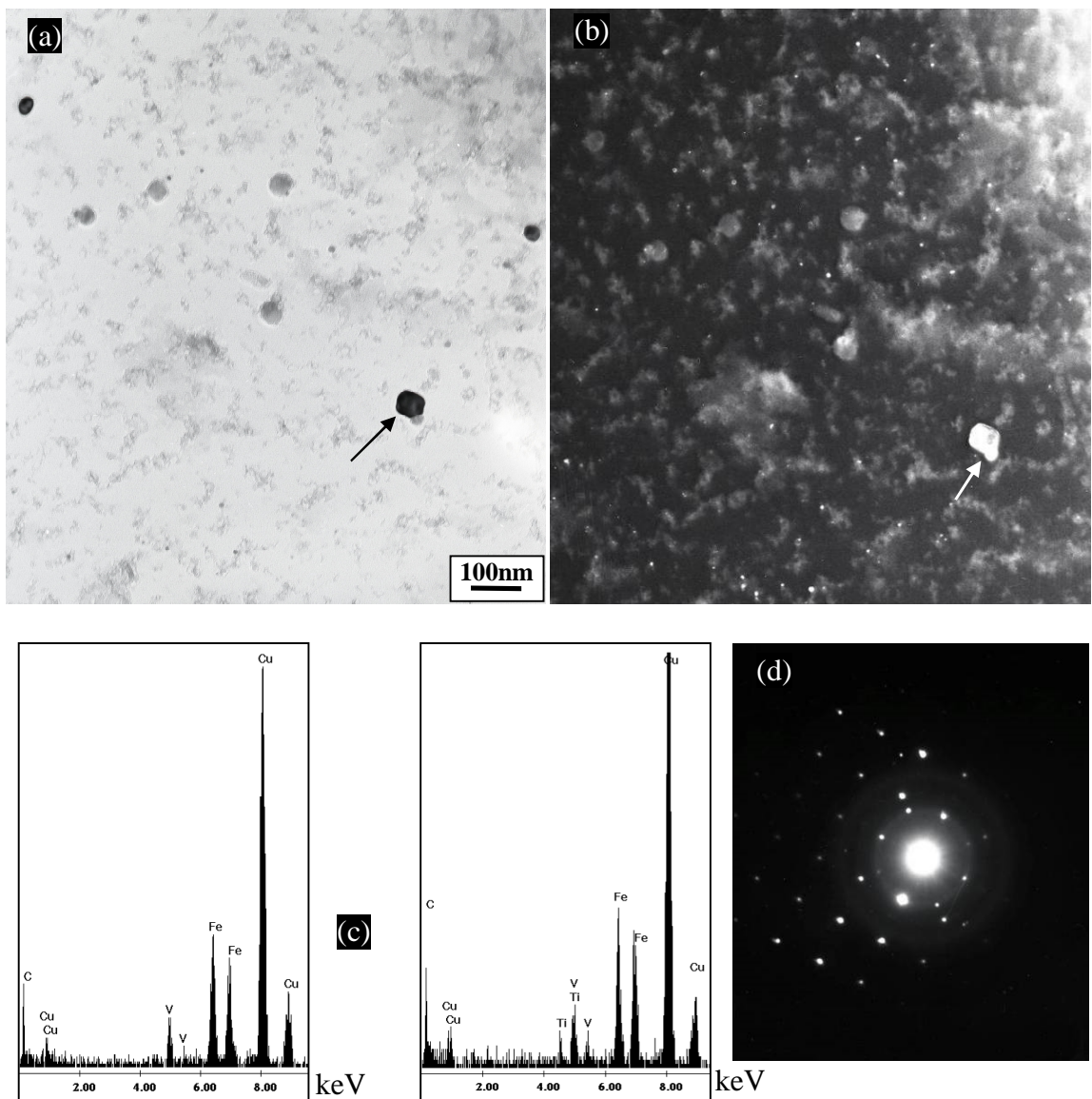


Fig. 6.26, (a) and (b) Bright and dark field TEM images of a carbon extraction replica from a sample of Alloy 3 after the controlled rolling, showing a typical complex shape precipitate, (c) Corresponding EDS spectra from upper and lower caps, (d) Corresponding SAED pattern.

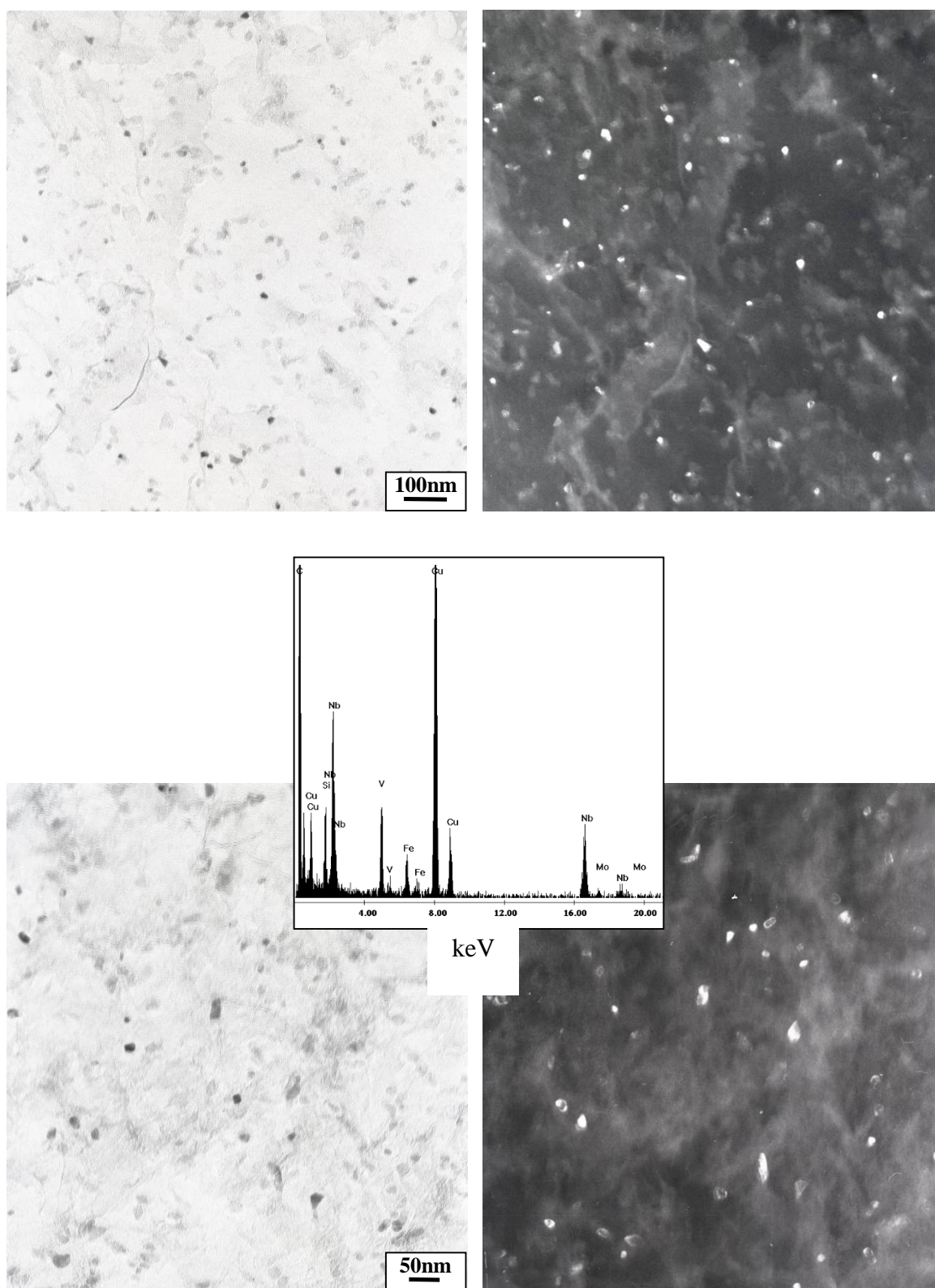


Fig. 6.27, Bright and dark field TEM images of a carbon extraction replica and a typical EDS spectrum from a sample of Alloy 2 after the controlled rolling, showing typical distributions of precipitates.



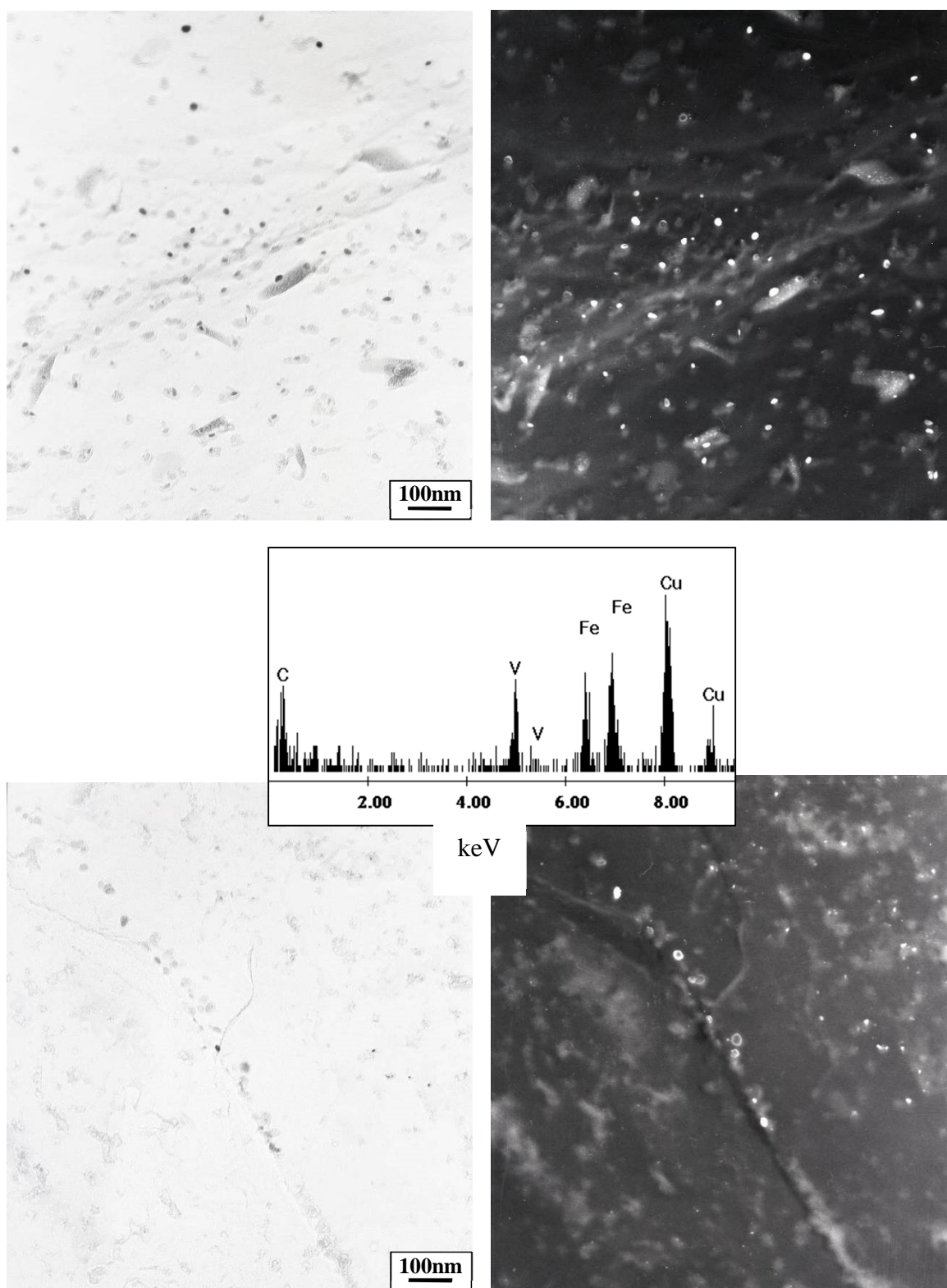


Fig. 6.28, Bright and dark field TEM images of a carbon extraction replica and a typical EDS spectrum from a sample of Alloy 3 after the controlled rolling, showing typical distributions of precipitates.

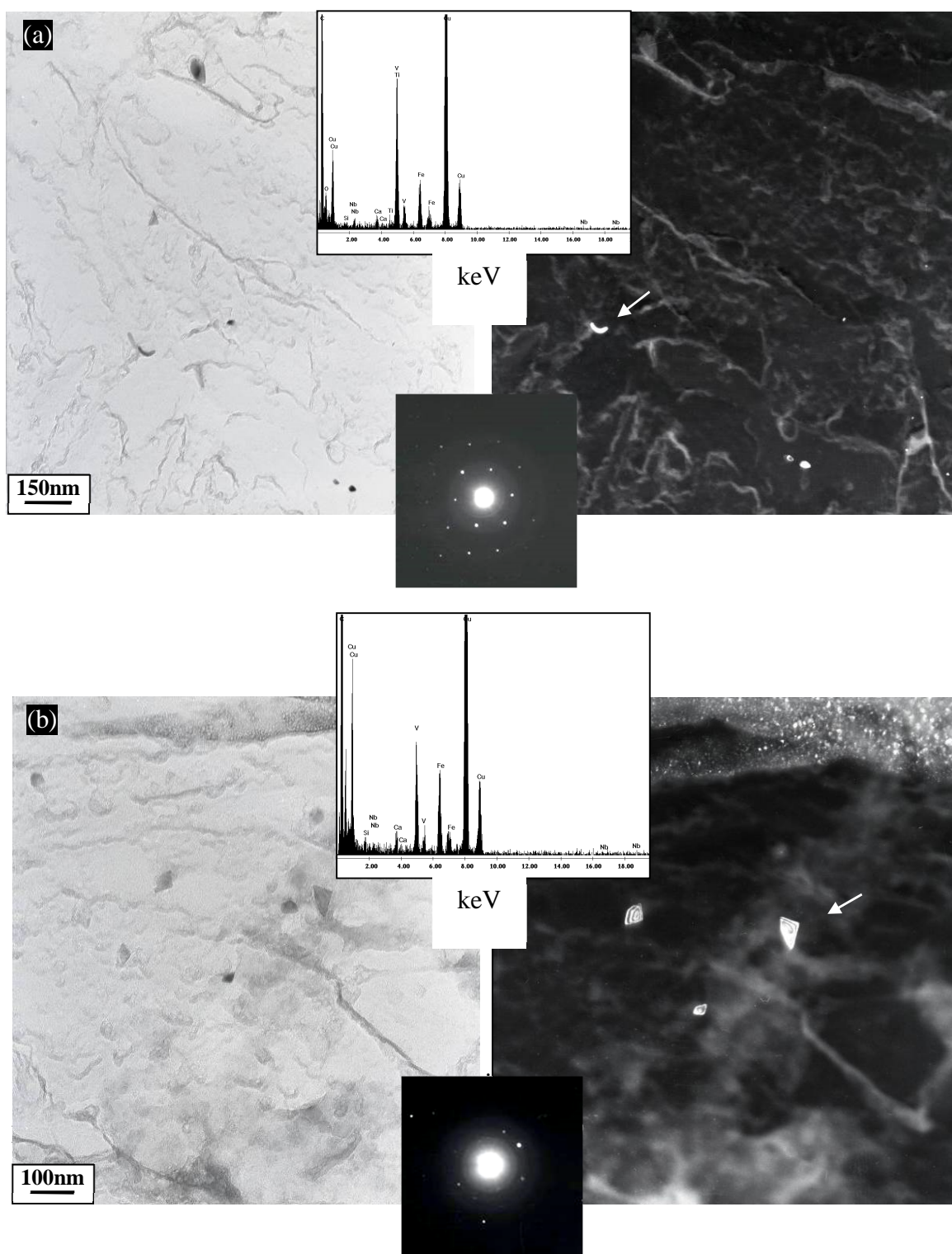


Fig. 6.29, (a) and (b) Bright and dark field TEM images of extraction replica with corresponding SAED pattern and EDS from the interrupted quench sample of Alloy 3, showing very few precipitates.

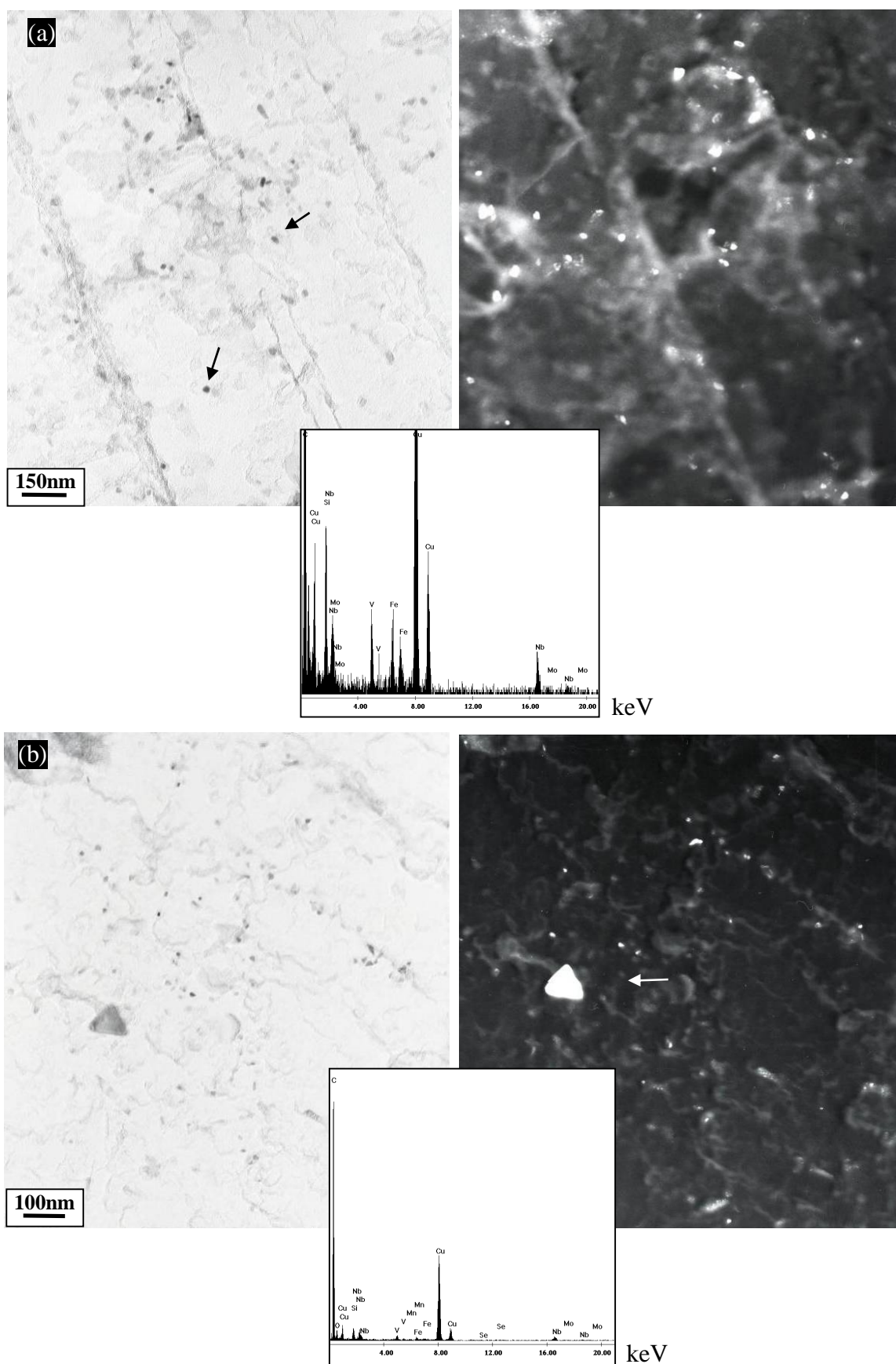


Fig. 6.30, (a) and (b) Bright and dark field TEM images of an extraction replica, corresponding EDS from the interrupted quench sample of Alloy 2.

The precipitates extracted from the interrupted quench specimens at the end of the finishing stage were randomly analysed by EELS and EDS to study the presence of nitrogen in them. Table 6.3 compares the presence of nitrogen in precipitates with different morphologies as a function of thermomechanical processing condition.

In the interrupted quench specimens the size of precipitates was smaller than hot rolled and controlled rolled specimens. In addition to this, the acquired EELS spectra from these precipitates failed to show N peaks which was widely present in the larger precipitates.

Table 6.3, The existence of nitrogen in precipitates as a function of their morphologies and thermomechanical processing.

	Alloy	Spherical	Cuboid	Triangular	Oval	Irregular
Hot rolled	2	C	C	C	N	N
	3	N	N	N	C	C
Controlled rolled	2	C	C	C	N	C
	3	C	C	C	N	C
Interrupted quench	2	C	C	C	C	C
	3	C	C	C	C	C

N; Nitrogen, C; Carbon

According to the TEM observations the presence of cuboid precipitates in Alloys 2 and 3 was confirmed after all the above mentioned thermomechanical processing conditions. It is likely that this morphology of precipitate is a result of the composition and the temperature at which they were formed.

It has been shown that the triangular precipitates are generally rich in Ti and N, and that they are randomly and only occasionally present [5, 162]. From EELS/EDS spectra, it was found that this morphology of precipitates generally contains nitrogen in Alloy 3 and is rich in Ti and V, whereas in Alloy 2 it is rich in Nb and V and the majority of them are free from nitrogen.

In the literature, it has been reported that the spherical shape and needle like or oval shape precipitates generally have a chemical composition of (Ti, Nb)C or (Ti, Nb, V)C and N, where the core is rich in titanium and the shell contains niobium or vanadium [5, 156, 162, 163]. TEM observations suggest the presence of these precipitates preferentially on dislocations and along dislocations in the ferrite. The chemical analyses of oval or needle like precipitates in Alloy 2 indicate that they contain V, Nb, Mo and Ti and also are rich in nitrogen, whereas in Alloy 3 they are rich in V and nitrogen. The precipitates of interrupted quench samples revealed the absence of Mo in Alloy 2 (Table 6.3).

The spherical precipitate showed a variety of chemical compositions. In the hot rolled and controlled rolled Alloy 2 the presence of V, Nb and randomly Mo and nitrogen was observed. In Alloy 3 they mostly showed the presence of V and occasionally nitrogen.

Fig. 6.31 gives the size distribution histogram of microalloying precipitates of Alloys 2 and 3 for each condition, separately. It was found that applying the controlled rolling in Alloy 2 leads to precipitate coarsening, while in Alloy 3 it was not effective in altering the size of precipitates.

The distribution of precipitates in the interrupted quench specimens exhibits a significant precipitation in Alloy 2 and a rare precipitation in Alloy 3, at temperatures over the finishing stage (Figs. 6.31 (d) and (h)).

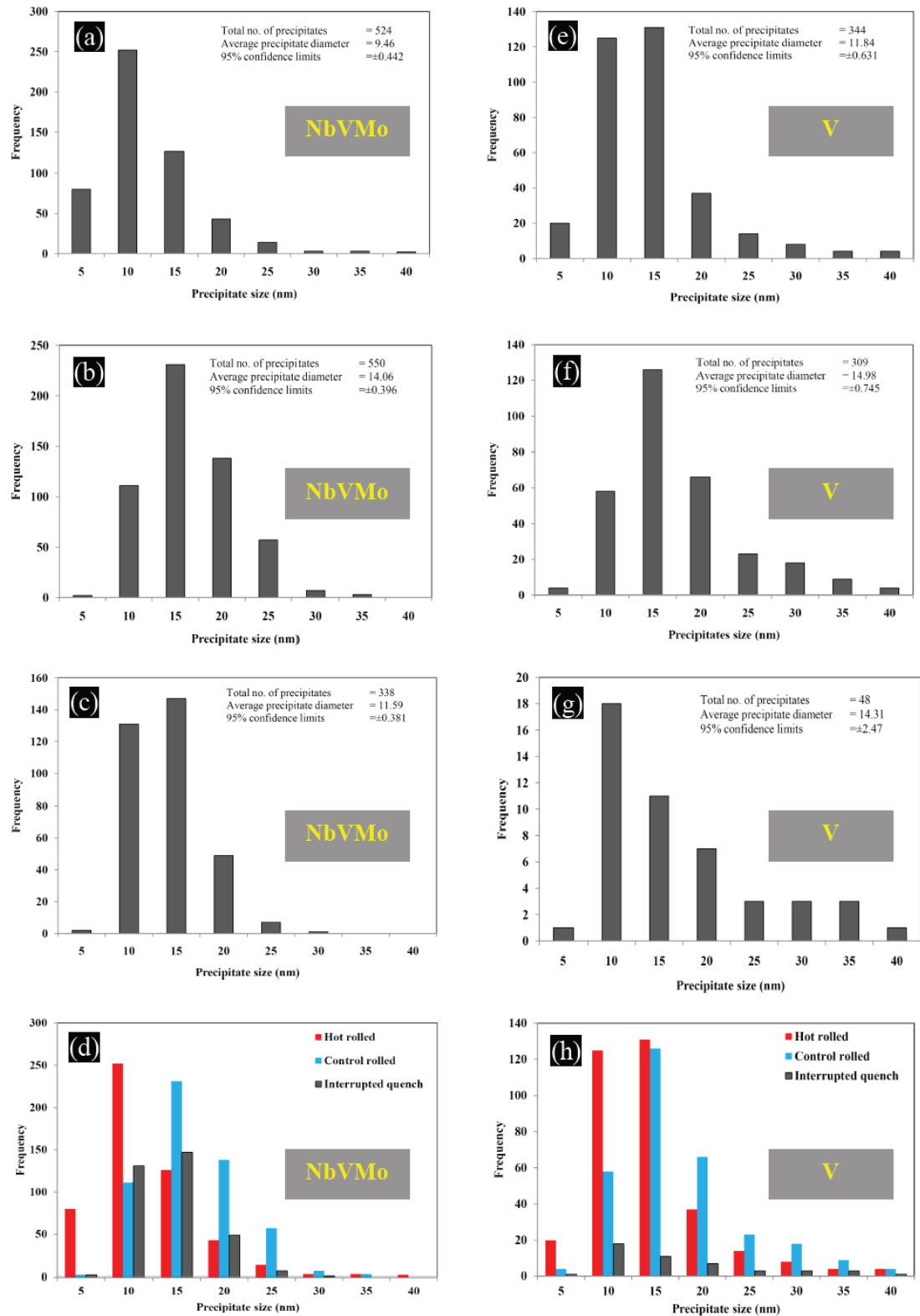


Fig. 6.31, Precipitate size distribution of hot rolled, controlled rolled and interrupted quench samples of Alloys 2 and 3, measured from carbon extraction, (a) Hot rolled Alloy 2, (b) Controlled rolled Alloy 2, (c) Interrupted quench Alloy 2, (d) Combined hot rolled and controlled rolled Alloy 2, (e) Hot rolled Alloy 3, (f) Controlled rolled Alloy 3, (g) Interrupted quench Alloy 3, (h) Combined hot rolled and controlled rolled Alloy 3.



The density of precipitates or the number of precipitate per unit area was measured by counting the number of precipitates throughout the TEM micrographs. Similar to the rough rolled samples, the measurement was conducted using at least ten negatives for each sample. Details of the number of precipitates per unit area are summarized in Table 6.4.

Fig. 6.32 compares the trend of variation in the average density of precipitates in terms of thermomechanical processing. As can be seen the density of precipitates in Alloy 3 is strongly dependent upon the low temperature transformations, whereas in Alloy 2 the precipitation is mainly related to the microstructural evolution at high temperatures.

Table 6.4, Average density of precipitates as a function of thermomechanical processing condition, measured from the carbon extraction replica samples of Alloys 2 and 3.

	Hot rolled		Controlled rolled		Interrupted quench	
	Alloy 2	Alloy 3	Alloy 2	Alloy 3	Alloy 2	Alloy 3
Precipitate / $\mu\text{m}^2$	123	216	111	73	112	16

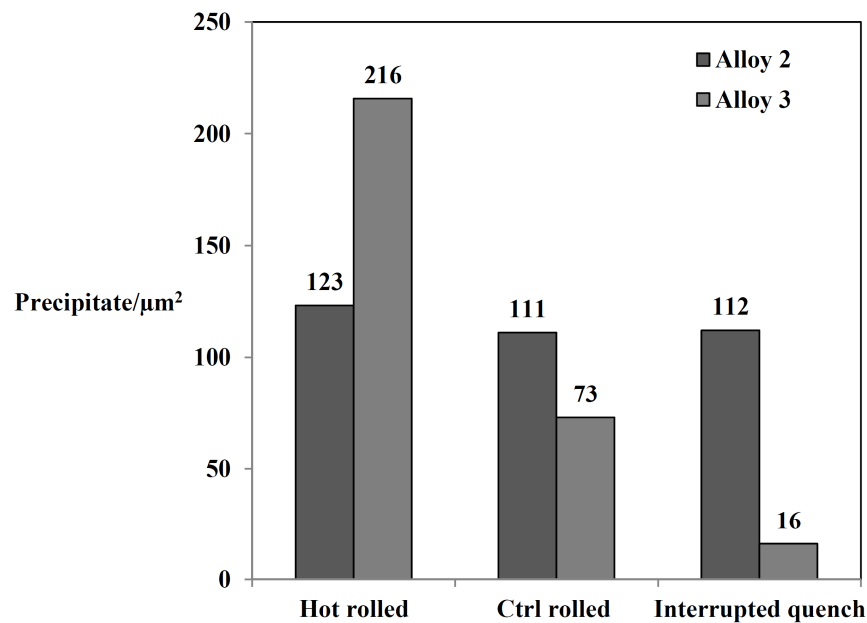


Fig. 6.32, Density of precipitates versus thermomechanical processing, measured from the carbon extraction replica samples of Alloys 2 and 3.

### 6.2.6. Hardness Testing

The influence of thermomechanical processing on the microstructural evolution was also evaluated by the comparison of room temperature Vickers hardness.

As shown in Fig. 6.33, the hardness of interrupted quench specimens had a higher hardness compared to the other specimens. There is a slight variation in the hardness of specimens after the rough rolling, hot rolling and controlled rolling. However, no considerable difference was observed in the hardness between the two alloys after each individual thermomechanical processing condition

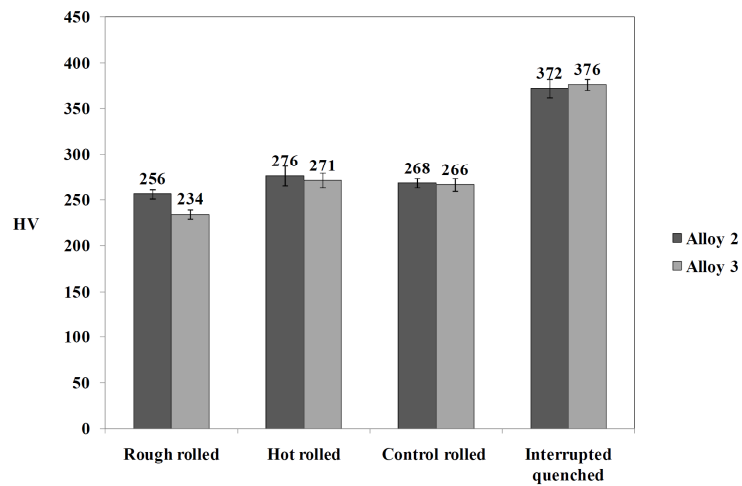


Fig. 6.33, Variation of hardness values as a function of thermomechanical processing condition.

### 6.3. Discussion

#### 6.3.1. Microstructural Characterizations

From the optical/electron microscopy observations and the XRD analysis, it was found that the microstructure after the thermomechanical processing shown in Fig. 3.8 (a) and (b), contained allotriomorphic ferrite, acicular/bainitic ferrite, martensite, retained austenite and carbides. An interesting finding was that in an identical cooling condition the optical morphology and size of lath ferrite constituents at grain interiors in both alloys were similar. As discussed earlier, the presence of these constituents in these steels is an advantage in obtaining a desirable level of formability, work hardening and strength in steels [102].

As can be seen from Figs. 6.2 to 6.4 the evolution of allotriomorphic ferrite in the microstructure of Alloy 2 was different from Alloy 3. Fig. 6.5 showed that the average fraction of allotriomorphic ferrite was clearly higher in Alloy 3 than Alloy 2 (i.e. ~10-20 and ~17-40 vol% in Alloy 2 and Alloy 3, respectively).

In Alloy 3 the recrystallized austenite was found to be operative in increasing the volume fraction of allotriomorphic ferrite compared with the non-recrystallized austenite in Alloy 2 in both hot and controlled rolled specimens (Figs. 6.2 and 6.6 and 6.7). It is clear that the grain boundaries of prior austenite acted as nucleation sites for the formation of allotriomorphic ferrite, and, in the absence of austenite recrystallization served to reduce the fraction of prior austenite grain boundaries in Alloy 2 compared with Alloy 3 (Figs. 6.6 and 6.7). It can be therefore suggested that the lower fraction of prior austenite grain boundaries reduced the volume fraction of allotriomorphic ferrite. However, this cannot be considered as a generalization, since the effect of V and NbMoV additions either as precipitate or solute drag effect could control the kinetics of ferrite formation (see Fig. 2.23) [51, 62].

Inspection of the un-deformed parts of a PSC specimen for Alloy 2 revealed that the allotriomorphic ferrite had hardly formed in the microstructure (Figs. 6.2 (e) and 6.3 (c)). By contrast, in an identical condition the allotriomorphic ferrite was observed in the un-deformed microstructure of Alloy 3 (Fig. 6.2 (f)). This is consistent with the recent findings of Hinton et al. in 2012 who showed that Nb reduces the kinetics of ferrite

formation [52]. Following the analysis of the deformed/un-deformed regions of PSC specimens, it can be suggested that the effect of NbMo on retarding the allotriomorphic ferrite was partly neutralized by mechanical deformation. In this context, Fig. 6.15 also showed the effect of V(C,N) on pinning the grain boundaries of allotriomorphic ferrite in Alloy 3. It can be thus suggested that V and NbVMo coprecipitation systems retarded the growth of allotriomorphic ferrite, but such evidence has not previously been reported.

SEM observations showed that two morphologies of secondary features were present in the prior austenite grain interiors (Fig. 6.8). The distinctive morphologies of these features include a packet shape structure in the vicinity of lath ferrite with a distribution of fine secondary lath bright features. It is clear that there was a lath shape substructure inside the packet shape features. Many authors have interpreted these packet shape features as martensite [95, 164, 165]. A close comparison between these features and interrupted quenched microstructure provided good evidence to confirm that this feature was martensite (Figs. 6.8 (e) and (f)) [166].

Further TEM observations showed that retained austenite with needle-like and block morphologies was present adjacent to acicular/bainitic ferrite and martensite in both alloys, Figs. 6.12 and 6.16, which were observed with various frequencies in all samples. This simply means that the average cooling rate of  $\sim 12^{\circ}\text{C/s}$  after the finishing rolling was rapid enough to retain austenite up to the bainite start temperature during both hot and controlled rolling. Some of the remaining austenite would have transformed to bainite and martensite during the subsequent cooling stage.

The XRD results and TEM observations occasionally revealed the presence of cementite in both alloys (e.g. Figs 6.9 and 6.13 and 6.14). However, the results suggest that the cementite was formed in the microstructure although a high level of Si was present in the chemical composition, which is expected to retard cementite formation. A possible explanation can be found in the report of Kozeschnik and Bhadeshia [167]. They showed that silicon effectively suppresses the cementite precipitation in austenite, while it is less effective in other constituents such as ferrite or martensite. Further investigations into this phenomenon are suggested to shed light on this issue.

### 6.3.2. Retained Austenite

The trend of variation in the austenite volume fraction using the XRD analysis was compared in two alloys. As seen in Fig. 6.10 (a), the amount of retained austenite in Alloy 2 was higher than Alloy 3 for all conditions. This suggests that NbMo greatly contributed to increasing the proportion of retained austenite. This is in agreement with the results of Zarei Hanzaki et al., who also reported about the effect of Nb on the austenite retention in 0.22C 1.55Si 1.55Mn wt% TRIP steel [168]. They pointed out that the solid solution hardening by Nb and work hardening of austenite at temperatures below the recrystallization-stop-temperature increases the stability of austenite against martensite transformation. In the present study the optical micrographs of the interrupted quench structure showed a recrystallized structure in Alloy 3. By contrast, this behaviour was absent in Alloy 2. It is therefore suggested that the strengthening of prior austenite in Alloy 2 might be the reason for the stabilization of austenite [103]. Nevertheless, the effect of NbMo on the other mechanisms such as bainite transformation should be studied as future work.

XRD analyses exhibited the changes in the average carbon content of retained austenite in both alloys in terms of thermomechanical processing (Fig. 6.10 (b)). Apart from the possible uncertainties in XRD analysis, these presumably resulted from the variations in bainite transformation or other mechanisms which altered the carbon content in the retained austenite. It was clear that the amount of average carbon content of retained austenite in Alloy 3 after hot rolling and controlled rolling was lower than Alloy 2. In contrast, in the interrupted quench samples, the carbon content of retained austenite was raised. A possible explanation is that V(C,N) precipitation at temperatures below the finishing rolling stage perhaps reduced the availability of carbon in the remaining austenite. Consequently, this resulted in the lower carbon content of the resultant retained austenite. Due to lack of data, it is impossible to be absolutely sure about the mechanism. However, the following discussions will help elucidate the effect of precipitation on this phenomenon. Also, further investigations into the mechanism of transformation will be helpful to more accurately interpret these results.

### 6.3.3. TEM Thin Foil Analysis of Precipitate

In both alloys, TEM micrographs and EDS spectra revealed random precipitation at grain boundaries and grain interiors of polygonal/lath ferrite, but with different densities (Figs. 6.11, 6.13 and 6.14 to 6.17 and 6.19). This confirms the general rule that V(C,N) precipitates formed in the allotriomorphic ferritic matrix and on dislocations [20]. Finding the precipitates in thin foil samples of bainitic/martensitic steels has been a challenge for many researchers [109]. However, these results presented new evidence to give further insight about the interaction between microalloying precipitates and microstructural evolution in acicular/bainitic ferrite and martensite.

Interestingly, the presence of V(C,N) precipitates was found in the acicular/bainitic ferrite with a random distribution (e.g. Figs. 6.11 and 6.13 and 6.16). As V(C,N) precipitation hardly occurs below the bainite start temperature, it can be suggested that these precipitates formed in austenite [109]. No systematic investigation has been reported on the possibility of V(C,N) precipitation in austenite during intercritical controlled rolling in bainitic steels. Recently, a few works have been reported on Nb precipitation in austenite and bainite [22, 109, 169, 170]. They showed the possibility of Nb(C,N) formation in austenite at different temperatures, in particular on pre-existing boundaries and dislocations. However, the behaviour of microalloying precipitation in austenite during cooling from the intercritical annealing range (i.e. average of  $\sim 12^{\circ}\text{C/s}$ ) after the finishing stage will be further clarified in the next section.

Locally a high dislocation density was observed in different regions of lath ferritic and martensite of both alloys (e.g. Figs. 6.11 to 6.13 and 6.18). The high strain rate (i.e.  $10\text{s}^{-1}$ ) and fast cooling perhaps limited the extent of recovery, which caused the dislocations to pile up at regions close to the boundaries and microalloying precipitates. It was also likely that many of these dislocations were formed by a plastic relaxation as a result of shape deformation during the bainite transformation or due to an elastic strain accommodation in the martensitic lath structure [103]. This indicated that the place of dislocations in prior austenite would be moved away from their original positions.



#### 6.3.4. TEM Carbon Extraction Replica Analysis of Precipitates

PSC testing was used to systematically investigate the precipitation process during hot rolling process at temperatures both above and below the finishing stage. As already discussed in section 6.3.3, it was clear that microalloying precipitation occurred in an austenitic matrix and allotriomorphic ferrite in both alloys. However, it should be noted that the micrographs of carbon replicas are related to the precipitates that were extracted from acicular/bainitic ferrite, allotriomorphic ferrite and martensite. This simply means that the microalloying precipitates extracted from the acicular/bainitic ferrite represented the precipitates that had formed in austenite.

Different precipitate morphologies were observed in both alloys after thermomechanical processing. This is consistent with the observations of precipitates in samples prepared by the rough rolling and intercritical annealing in chapter 5. Similarly, a complex relationship between the morphology and chemical composition was seen in both alloys. In Alloy 2 the TEM/EDS observations revealed that most of the precipitates contained (Nb,V,Mo)C and VC, whereas in Alloy 3 they were mostly VC and a trace amount of (V,Ti)C. The Ti was considered as an impurity. The results showed the availability of different elements in different morphologies of precipitates and this would make an excellent topic for further research.

In Alloy 2, the precipitate size distribution showed that ~90% of precipitates in the hot rolled condition were smaller than 15nm whereas after controlled rolling the size increased to 20nm (Fig. 6.31). As mentioned above, the observed precipitates in Alloy 2 were VC and Nb(V,Mo)C. The histograms of precipitate size did not differentiate between precipitates of different compositions. However, after controlled rolling the peak in the precipitate size distribution increased in size (i.e. from between 5-10nm to 10-15nm). Additionally, the precipitate size distribution in the interrupted quench sample showed similar behaviour to the controlled rolled. This was good evidence to confirm the consistency of results in samples subjected to a holding time of 50s at 900°C with an identical prior thermomechanical processing history. It was therefore clear that the kinetics of growth/coarsening of precipitates in NbVMo containing alloy was mainly influenced by the growth/coarsening of existing precipitates during the holding time before the finishing stage.

Also, as the majority of (Nb,V,Mo)(C,N) precipitates formed at temperatures above the finishing stage, it would have been expected that they would become coarsened during the subsequent cooling stage. However, the results suggested that NbMo effectively retarded the growth/coarsening of existing precipitates during the subsequent cooling stage after the finishing rolling.

As expected, very few V(C,N) precipitates (i.e. 16 precipitate/ $\mu\text{m}^2$ , with the highest frequency at 5 to 10nm) were found in the interrupted quench specimen of Alloy 3 (e.g. Fig. 6.31). This was in agreement with the thin foil analysis, as they also failed to show any precipitates. This demonstrated that the matrix was supersaturated with V, available for V(C,N) precipitation mainly below the finishing stage (i.e. 830°C). Similarly, Balliger and Honeycombe's studies on interphase precipitation showed the possibility of V(C,N) precipitation in austenite during the formation of ferrite [157]. This result is also consistent with the findings of Crooks et al. who reported on the kinetics of V and V-Nb precipitation, and austenite recrystallization at temperatures over 800°C [87]. They showed that the nose of the C-curve for V(C,N) precipitation in deformed austenite in a set of HSLA steels containing 0.1C (0.016-0.026)N (0.1 or 0.2)V wt% is lower than 800°C. Similarly, they observed very few precipitates in specimens held for 60s at 885°C.

Furthermore, a comparison between micrographs of interrupted quench specimen and hot/controlled rolled of Alloy 3 showed that the austenite had recrystallized in both conditions. This is consistent with the findings of Sellars who reported a temperature around 1000°C for the recrystallization stop temperature for a given C-Mn steel (see Fig. 2.20) [62]. In addition, the absence of softening in PSC stress-strain curves was good evidence to further elucidate that recrystallization did not progress during holding time at 900°C. No evidence was found to show that V(C,N) with a size of  $\geq 5\text{nm}$  had precipitated in the microstructure. These results agree with the above conclusions, suggesting that during interpass holding there would not have been a possibility for the formation and coarsening of V(C,N) in the controlled rolled samples.

The observed difference in the precipitate densities of hot and controlled rolled Alloy 3 suggested that there was a factor which reduced the formation of V(C,N) precipitation during controlled rolling (Fig. 6.32). As discussed earlier, TEM thin foil analysis evidenced that it was possible for V(C,N) to precipitate in both austenite and

allotriomorphic ferrite. However, it is highly probable that the cooling rate was too rapid to allow a considerable V(C,N) precipitation. Therefore any future work on these steels should consider this effect.

Table 6.3 summarised the presence of nitrogen in precipitates as a function of their morphology. Nb(V,Mo)CN and VCN precipitates were hardly observed in the interrupted quench specimens, despite the fact that carbonitrides have a higher thermal stability. In general, the available data showed the highest probability of carbonitride precipitation in hot/controlled rolled conditions in both alloys. In other words, it was more likely that carbonitrides formed at temperatures below the finishing stage (i.e. 830°C).

### 6.3.5. PSC Stress-Strain Curves

The PSC stress-strain curves are briefly discussed to further establish the effect of NbMo on the precipitation at temperatures above the finishing stage (Fig. 6.1). As discussed earlier, three deformations under plane strain compression conditions at three different temperatures were undertaken.

Fig. 6.34 shows two typical curves of temperature versus time for the hot/controlled rolled experiments. It is clear that during the whole of the thermomechanical processing there was insignificant overshooting of temperature. However, a slight overshooting in the range of 2-10°C could be attributed to the thermal gradient from the holder to the centre or less likely adiabatic heating due to the high strain rate applied (i.e.  $10\text{s}^{-1}$ ) [118]. These indicated that the observed variations in the mechanical properties of specimens, beyond the instrumental effects, were mainly attributed to the microstructural evolution of specimens.

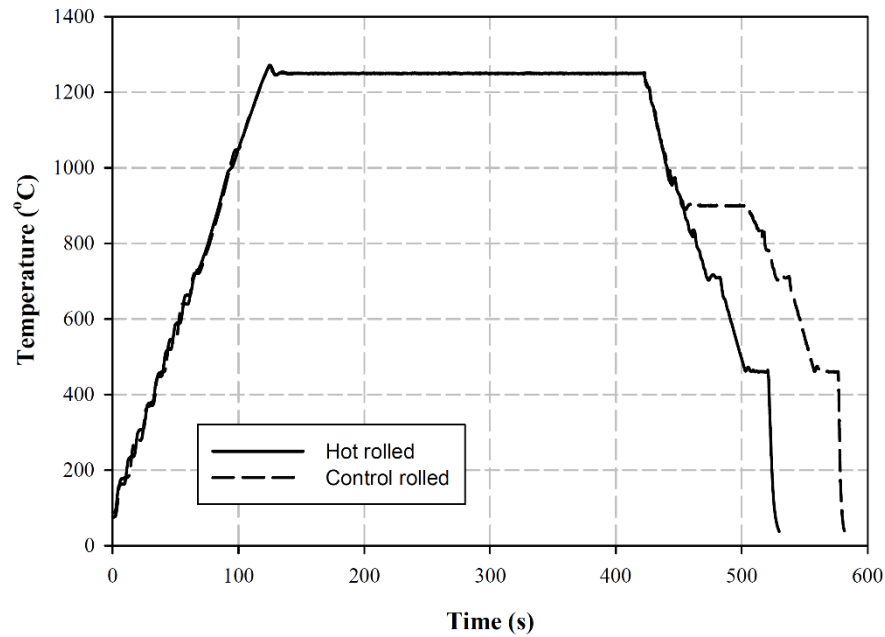


Fig. 6.34, Typical temperature versus time curves, indicating the variation of temperature in the specimens within the hot rolling and control rolling.

The stress-strain curves for the two alloys exhibited similar behaviour at 1250°C, while they showed considerable variations at the lower temperatures i.e. 1000°C and 830°C (Fig. 6.1). The similar behaviour of the two alloys at 1250°C could be ascribed to the insignificant precipitation and the high diffusivity of micro/alloying elements in both alloys. Therefore, this permitted softening to occur by thermally activated mechanisms of recovery, recrystallization and grain growth [23].

In both alloys, by decreasing the deformation temperature the stress-strain curves showed reductions in strain compared to the target strain (i.e. 20% in each pass) and a progressive increase in flow stresses ( $\sigma_f$ ) and peak stress, in the second and the third passes (i.e.  $\sigma_f$  ~150 and 120 MPa and peak stress ~300 and 280MPa in Alloys 2 and 3 in third pass, respectively). This corresponds to the work hardening resulting from the dislocations-dislocations interactions and microalloying elements [171, 172]. However, this effect was different between the two alloys. Indeed, the possible formation of a network of precipitates and solute drag effect in Alloy 2 pinned the advancing boundaries and prevented the softening mechanisms (i.e. recrystallization and recovery).

In Alloy 3, the microstructure of the interrupted quench specimen showed a recrystallized structure with no significant precipitation for temperatures above the

finishing temperature (Fig. 6.6). In contrast, the microstructure of Alloy 2 contained an elongated prior austenite (i.e. pancaked grains) and a large number of precipitates (Figs. 6.7 and 6.31). In addition, the interrupted quench sample did not contain ferrite in the microstructure, which means that there was no ferrite present during intercritical annealing, which would have decreased the hot strength [173]. These results confirmed the above conclusions that, in general, the higher flow stress in Alloy 2 at temperatures lower than 1250°C was a result of solid solution strengthening, precipitation and solute drag effect, resulting from the higher microalloy content of this alloy.

As discussed earlier, it was also found that the flow stresses of Alloy 3 for the hot rolled and controlled rolled were similar at deformation passes of 1000°C and 830°C. Additionally, the peak stress of both alloys did not change significantly at the third pass. These showed that during interpass hold time at 900°C recrystallization did not occur and perhaps it was stopped at temperatures over 900°C.

#### **6.3.6. Hardness Testing**

The effect of precipitation and microstructural evolution on the mechanical properties of the steels were also investigated using the hardness testing (Fig. 6.33). In general, there was no significant difference in the average hardness of two alloys for each thermomechanical processing condition. The hardness of Alloy 3 was not significantly lower than Alloy 2, despite the fact that the higher volume fraction of allotriomorphic ferrite was present in Alloy 3 [174]. The most likely reason for the high hardness of Alloy 3 can be attributed to the martensite/bainite volume fraction and also precipitation strengthening. V(C,N) precipitation in Alloy 3 might offset the softening effect of ferrite. This is inconsistent with the earlier conclusions about the average density of precipitates in section 6.3.4. This suggests that the average precipitate density of V(C,N) was too low to increase the hardness of steel. However, this finding is important since it indicates the similar hardness for V steel and NbVMo steel at room temperature and lower hot strength for V steel. Further investigations are suggested as future work to shed light on this phenomenon.

As expected, the hardness of both alloys increased after interrupted quenching. It is clear that the significant increase in the hardness of interrupted quench specimens was related to the dominant bainite and martensite structure (Figs. 6.6 and 6.7 and 6.8).



## Chapter 7. Conclusions

In the initial part of the project, V(C,N) precipitation and microstructural evolution were studied in a V containing TRIP steel that had been hot and cold rolled (Alloy 1). The focus was on the intercritical annealing stage, in which a microstructure comprising polygonal ferrite matrix, bainite and retained austenite was formed. Particular focus was on the bainite transformation during the isothermal hold following intercritical annealing and how this affected the properties of the retained austenite. Following this, the effect of a further addition of Nb and Mo in addition to V was investigated. This not only changed the precipitation behaviour, but also the initial structure, including the formation of acicular/bainitic ferrite and martensite matrix. These structures provided a clear picture of V(C,N) precipitation during intercritical annealing in TRIP assisted steels. The conclusions here are drawn in terms of the material used and thermomechanical processing practiced.

Alloy 1 (0.2%C, 1.5%Mn, 0.38%Si, 0.31%Al, 0.12%V) was investigated after intercritical annealing followed by an isothermal hold at the bainite transformation temperature of 460°C. Different holding times, from 5s to 180s, were applied to analyse the effect of bainite transformation on the resulting structure in Alloy 1. The findings and conclusions that can be drawn from these investigations are summarized as follows:

- The microstructure showed a large population of retained austenite with block shape morphology before the 40s holding time. For longer isothermal bainite holding times than 40s, there was an increase in the population of film shape retained austenite in the newly formed block intercritical annealed austenite.
- The tensile behaviour of samples showed a strong correlation with the morphology of the austenite. Greater ductility and higher yield/tensile strengths were observed at longer isothermal bainitic holding time (i.e. 180s). This suggested the coupling effect of lath bainitic ferrite in the vicinity of film shape retained austenite improved the tensile behaviour. Also, the presence of V(C,N) on the tangled dislocations indicated the possible interaction between precipitates and dislocations.

- It was found that the V(C,N) precipitates were present in the microstructure after isothermal bainite transformation in ferrite, retained austenite, martensite and bainitic ferrite in a random manner.

After intercritical annealing the density of V(C,N) precipitates slightly increased while their size distribution did not change significantly. It was also found that holding the material at isothermal bainite temperature did not lead to a significant change in the size distribution and average density of V(C,N) precipitates.

- The TEM observations widely showed the presence of V(C,N) precipitates in the martensite. This suggested that V(C,N) precipitates could locally decrease the stability of austenite against martensite transformation.

Alloy 3 had a similar composition to Alloy 1, but with a lower carbon content (0.12% vs 0.2% in Alloy 1 and a higher vanadium content of 0.16% vs 0.12% in Alloy 1). This alloy was used to investigate the effect of the prior processing route. Finally, Alloy 2 was identical to Alloy 3, except it had the addition of 0.08%Mo and 0.04%Nb, which would be expected to promote the additional precipitation of NbC type precipitates during thermomechanical processing. The findings and conclusions that can be drawn from the rough rolled (i.e. using the rolling mill) and intercritical annealed Alloys 2 and 3 are summarized as follows:

- Both alloys showed an acicular/bainitic ferrite matrix surrounded by allotriomorphic ferrite after the rough rolling, ~20% cold rolling and intercritical annealing.
- The intercritical annealing process formed a reasonable amount of retained austenite in both alloys (i.e. 7.4 and 8.2 wt% in Alloys 2 and 3, respectively). The austenite mainly formed at grain boundaries of lath ferritic constituents inside the prior austenite grains. Interestingly, the lath ferritic constituents failed to recrystallize during intercritical annealing in both alloys.

- After intercritical annealing the density of precipitates in Alloy 3 was raised over Alloy 2 (i.e. 137 and 219 precipitate/ $\mu\text{m}^2$  in Alloy 2 and Alloy 3, respectively). This was attributed to the greater kinetics of V(C,N) precipitation than (Nb,V,Mo)(C,N) system at this range of temperature.
- The rate of growth/coarsening of precipitates, in particular with a size of  $\leq 15\text{nm}$ , in Alloy 2 was lower than Alloy 3 after intercritical annealing. This was attributed to the effect of Nb and Mo on retarding the growth/coarsening of precipitates during intercritical annealing range. It was also found that the highest frequency of V(C,N) precipitates was between 10 to 15nm in a random precipitation manner.
- The NbVMo steel (Alloy 2) showed higher hardness after intercritical annealing, whereas the hardness in V steel (Alloy 3) was not significantly changed. This was attributed to the effect of precipitation strengthening of precipitates with a size of  $\leq 15\text{nm}$ .
- Very few microalloying precipitates were observed in the intercritical annealed austenite, adjacent to martensitic regions. This suggested that the carbo-nitrides could locally reduce the stability of austenite against martensite transformation.

The effect of NbMo addition on precipitation behaviour before and after the finishing deformation (i.e.  $830^\circ\text{C}$ ) in parallel to the microstructural evolution was investigated in Alloys 2 and 3. The following concluding remarks can be made:

- After hot/controlled rolling, the resulting microstructure in both NbVMo and V steels was acicular/bainitic ferrite, retained austenite and martensite surrounded by allotriomorphic ferrite.
- Microscopic evidence suggested that both precipitation systems retarded the growth of allotriomorphic ferrite in both alloys.

- No significant precipitation in the interrupted quench specimen of Alloy 3 was observed (16 precipitate/ $\mu\text{m}^2$ ), whereas in Alloy 2 the majority of Nb(V,Mo)(C,N) precipitates had formed up to this stage (i.e. 830°C).
- The controlled rolling led to the growth of microalloying precipitates in Alloy 2 compared with the hot rolled condition. This suggested that the precipitation and growth of Nb(V,Mo)(C,N) precipitates effectively occurred at temperatures above the finishing stage, i.e. 830°C.
- The highest frequency of V(C,N) precipitates were of a size between 10 to 15nm in a random precipitation manner.
- The V(C,N) were observed in both allotriomorphic ferrite and lath ferritic constituents at the prior austenite grain interiors. This suggested that the V(C,N) precipitation occurred in austenite and ferrite below the finishing stage (i.e.  $\leq 830^\circ\text{C}$ ) with an average cooling rate of  $\sim 12^\circ\text{C/s}$ .

As a general conclusion, the high dislocation density in  $\sim 20\%$  cold rolled acicular/bainitic ferrite could lead to the coarsening of V(C,N) precipitates during the intercritical annealing. For the first time, the available data suggested that the NbMo addition extensively controlled the growth/coarsening of Nb(V,Mo)(C,N) precipitates at temperatures over and below the finishing stage.

## **Chapter 8. Future work**

There are a number of unresolved issues and new questions that have arisen from the recent studies. Therefore, for future work, the following list is suggested:

### **Alloy 1**

1. Studying the effect of bainite transformation on the upper/lower yield strength observed in the stress-strain curves.
2. TEM studies of bainitic ferrite and retained austenite structures as a function of holding time.
3. Synchrotron X-ray studies of austenite and bainitic ferrite as a function of isothermal bainite transformation.

### **Alloys 2 and 3**

1. Studying the effect of rough rolling on the refinement of austenite, considering its influence on the microstructural evolution during the air cooling and intercritical annealing.
2. Unfortunately, from the existing data it is not possible to exactly suggest that the formation of precipitates or the effect of microalloying elements in removing the carbon was the reason for the reduction in retained austenite. However, further investigations as future work in examination of this effect are suggested.
3. Studying the effect of controlled rolling on the amount of cementite in the microstructure.
4. Further TEM and HRTEM investigations as future work in characterization of the chemical composition and crystal structure of the microalloying precipitate.

- 
5. Studying the mismatch between lattice parameter of precipitates, ferrite and austenite in two different precipitation systems of NbVMo and V to analyze the mechanism of coarsening. This can be developed by a stereological studying of nanoprecipitates in terms of their chemical composition, in particular, carbon and nitrogen.
  6. Investigation of the tensile properties of these steels to consider the effect of precipitation behaviour and microstructural evolution on the mechanical properties.

## References

- [1] V.F.Zackay, E.R.Parker, D.Fahr and R.Busch, "The Enhancement of Ductility in High-Strength Steels," *Transactions of the ASM*, vol. 60, pp. 252-259, 1967.
- [2] B.C.De.Cooman, "Structure–Properties Relationship in TRIP Steels Containing Carbide-Free Bainite," *Current Opinion in Solid State and Materials Science*, vol. 8, pp. 285-303, 2004.
- [3] K.I.Sugimoto, "Fracture Strength and Toughness of Ultra High Strength TRIP Aided Steels," *Materials Science and Technology*, vol. 25, no. 9, pp. 1108-1117, 2009.
- [4] S.Allain and T.Iung, "Development of Hot Rolled Copper/Nickel Alloyed TRIP Steels with Carbide-Free Bainitic Matrix," *Revue DE Metallurgie-Cahiers D Informations Techniques*, vol. 105, no. 10, pp. 520-530, 2008.
- [5] S.Shanmugam, M.Tanniru, R.D.K.Misra, D.Panda and S.Jansto, "Microalloyed V–Nb–Ti and V Steels, Part 2 – Precipitation Behaviour During Processing of Structural Beams," *Materials Science and Technology*, vol. 21, no. 2, pp. 165-177, 2005.
- [6] A.Halder, S.Suwas and D.Bhattacharjee, "Proceedings of the International Conference on Microstructure and Texture in Steels and Other Materials," Jamshedpur, 2008.
- [7] "Posco Automotive Steels-Internal Report," 2006.
- [8] J.Galan, L.Samek, P.Verbleysen, K.Verbeken and Y.Houbaert, "Advanced High Strength Steels for Automotive Industry," *Revista De Metallurgica*, vol. 48, no. 2, pp. 118-131, 2012.
- [9] H.Mohrbacher, "Niobium Microalloyed Automotive Sheet Steel- A Cost Effective Solution to the Challenges of Modern Body Engineering," in *International Symposium on Niobium Microalloyed Sheet Steel for Automotive Application*, Düsseldorf, 2006.
- [10] B.Mintz, "Hot Dip Galvanising of Transformation Induced Plasticity and other Intercritically Annealed Steels," *International Materials Reviews*, vol. 46, no. 4, pp. 169-197, 2001.
- [11] T.Hojo, K.I.Sugimoto, Y.Mukai and S.Ikeda, "Effects of Aluminum on Delayed Fracture Properties of Ultra High Strength Low Alloy TRIP-aided Steels," *ISIJ International*, vol. 48, no. 6, pp. 824-829, 2008.
- [12] K.I.Sugimoto, A.Kanda, R.Kikuchi, S.I.Hashimoto, T.Kashima and S.Ikeda, "Ductility and Formability of Newly Developed High Strength Low Alloy TRIP-aided Sheet Steels with Annealed Martensite Matrix," *ISIJ International*, vol. 42,



- no. 8, pp. 910-915, 2002.
- [13] F.G.Caballero; M.J.Santofimia; C.Capdevila; C.Garcia-de-Andres; S.Zajac; S.Allain; T.Lung; A.Couturier; J.Drillet; D.Quidort; C.Colin; X.Garat, "Novel High Strength, High Toughness Carbide-Free Bainitic Steels," 2007.
- [14] K.Nishioka and K.Ichikawa, "Progress in Thermomechanical Control of Steel Plates and their Commercialization," *Science and Technology of Advanced Materials*, vol. 13, pp. 1-20, 2012.
- [15] V.T.T.Miihkinen and D.V.Edmonds, "Microstructural Examination of Two Experimental High-Strength Bainitic Low-Alloy Steels Containing Silicon," *Materials Science and Technology*, vol. 3, no. 6, pp. 422-431, 1987.
- [16] A.Saha-Podder, I.Lonardelli, A.Molinari and H.K.D.H.Bhadeshia, "Thermal Stability of Retained Austenite in Bainitic Steel: an in situ study," *Proceedings of the Royal Society A*, vol. 467, pp. 3141-3156, 2011.
- [17] F.G.Caballero, H.Roelofs, St.Hasler, C.Capdevila, J.Chao, J.Cornide and C.Garcia-Mateo, "Influence of Bainite Morphology on Impact Toughness of Continuously Cooled Cementite Free Bainitic Steels," *Materials Science and Technology*, vol. 28, no. 1, pp. 95-102, 2012.
- [18] K.Mills, ASM Handbook, Vol. 12, Fractography, 9th ed., Metals Park, Ohio : American Society for Metals, 1987.
- [19] M.A.Altuna, A.Iza-Mendia and I.Gutierrez, "Precipitation of Nb in Ferrite After Austenite Conditioning. Part II: Strengthening Contribution in High-Strength Low-Alloy (HSLA) Steels," *Metallurgical and Materials Transactions A*, vol. 43A, pp. 4571-4586, 2012.
- [20] T.Gladman, The physical metallurgy of microalloyed steels, Maney Publishing for the Institute of Materials, 2002.
- [21] T.Gladman, "Precipitation Hardening in Metals," *Materials Science and Technology*, vol. 15, pp. 30-36, 1999.
- [22] W.M.Rainforth, M.P.Black, R.L.Higginson, E.J.Palmiere, C.M.Sellars, I.Prabst, P.Warbachler and F.Hofer, "Precipitation of NbC in a Model Austenitic Steel," *Acta Materialia*, vol. 50, pp. 735-747, 2002.
- [23] B.Verlinden, J.Driver, I.Samajdar and R.D.Doherty, Thermo-Mechanical Processing of Metallic Materials, R.W.Cahn, Ed., Elsevier material, 2007.
- [24] W.Bleck and K.Phiu-on, "Effects of Microalloying in Multi Phase Steels for Car Body Manufacture," in *Microstructure and Texture in Steels and Other Materials*, Jamshedpur, India, 2008.
- [25] A.Elsner, "Advanced Hot Rolling Strategies for IF and TRIP Steels," 2005.

- [26] D.P.Dunne, "Review Interaction of Precipitation with Recrystallisation and Phase Transformation in Low Alloy Steels," *Materials Science and Technology*, vol. 26, no. 4, pp. 410-420, 2010.
- [27] M.G.Akben, I.Weiss and J.J.Jonas, "Dynamic Precipitation and Solute Hardening in a V Microalloyed Steel and Two Nb Steels Containing High Levels of Mn," *Acta Metallurgica*, vol. 29, pp. 111-121, 1981.
- [28] M.G.Akben, B.Bacroix and J.J.Jonas, "Effect of Vanadium and Molybdenum Addition on High Temperature Recovery, Recrystallization and Precipitation Behavior of Niobium-Based Microalloyed Steels," *Acta Metallurgica*, vol. 31, pp. 161-174, 1983.
- [29] Q.Yu, Z.Wang, X.Liu and G.Wang, "Effect of Microcontent Nb in Solution on the Strength of Low Carbon Steels," *Materials Science and Engineering A*, vol. 379, pp. 384-390, 2004.
- [30] [Online].Available:[http://www.arcelormittal.com/automotive/saturnus/sheets/catalogue.pl?id\\_sheet=A1&language=EN](http://www.arcelormittal.com/automotive/saturnus/sheets/catalogue.pl?id_sheet=A1&language=EN).
- [31] C.Scott, F.Perrard and P.Barges, "Microalloying with Vanadium for Improved Cold Rolled TRIP Steels," in *International Seminar 2005 on Application Technologies of Vanadium in Flat – Rolled Steels*, Suzhou, China, 2005.
- [32] H.K.D.H.Bhadeshia, *Bainite in Steels, Transformations, Microstructure and Properties*, Second edition ed., Cambridge University, 2001, pp. 277-284.
- [33] D.T.Llewellyn, "Nitrogen in Steels," *Ironmaking and Steel Making*, vol. 20, no. 1, pp. 35-41, 1993.
- [34] L.Samek, E.D.Moor, J.Penning and B.C.D.Cooman, "Influence of Alloying Elements on the Kinetics of Strain-Induced Martensitic Nucleation in Low-Alloy, Multiphase High-Strength Steels," *Metallurgical and Materials Transactions A*, vol. 37A, pp. 109-124, 2006.
- [35] J.Wang and S.V.D.Zwaag, "Stabilization Mechanisms of Retained Austenite in Transformation-Induced Plasticity Steel," *Metallurgical and Materials Transactions A*, vol. 32A, pp. 1527-1539, 2001.
- [36] K.W.Andrews, "Empirical Formulae for The Calculation of Some Transformation Temperatures," *Journal of The Iron and Steel Institute*, pp. 721-727, 1965.
- [37] C.Y.Kung and J.J.Rayment, "An Examination of the Validity of Existing Empirical Formulae for the Calculation of Ms Temperature," *Metallurgical Transactions A*, vol. 13A, pp. 328-331, 1982.
- [38] M.A.Bepari and J.A.Whiteman, "The Effect of Nitrogen on the Precipitation Behaviour of Nb(C,N) in Continuously-Cooled Low-Carbon Structural Steels," *Journal of Materials Processing Technology*, vol. 56, pp. 834-846, 1996.

- [39] J.Lu, J.B.Wiskel, O.Omotoso, H.Henein and D.G.Ivey, "Matrix Dissolution Techniques Applied to Extract and Quantify Precipitates from a Microalloyed Steel," *Metallurgical and Materials Transactions A*, vol. 42A, pp. 1767-1784, 2011.
- [40] E.V.Pereloma, I.B.Timokhina and P.D.Hodgson, "Transformation Behaviour in Thermomechanically Processed C–Mn–Si TRIP Steels with and without Nb," *Materials Science and Engineering A*, Vols. 273-275, pp. 448-452, 1999.
- [41] F.Perrard and C.Scott, "Vanadium Precipitation During Intercritical Annealing in Cold Rolled TRIP Steels," *ISIJ International*, vol. 47, no. 8, p. 1168–1177, 2007.
- [42] S.Yue, "Thermomechanical Processing of Ferrous Alloys," in *ASM Handbook, Vol.14A, Metalworking: Bulk forming*, S.L.Semiatin, Ed., 2005, pp. 286-296.
- [43] A.M.Elwazri, E.Essadiqi and S.Yue, "Kinetics of Metadynamic Recrystallization in Microalloyed Hypereutectoid Steels," *ISIJ International*, vol. 44, no. 4, p. 744–752, 2004.
- [44] N.K.Balliger and R.W.K.Honeycombe, "Coarsening of Vanadium Carbide, Carbonitride, and Nitride in Low-Alloy Steels," *Metal Science*, vol. 14, no. 4, pp. 121-133, 1980.
- [45] D.Jorge-Badiola, A.IZA-Mendia, B.Lopez and J.M.Rodriguez-Ibabe, "Role of Vanadium Microalloying in Austenite Conditioning and Pearlite Microstructure in Thermomechanically Processed Eutectoid Steels," *ISIJ International*, vol. 49, no. 10, p. 1615–1623, 2009.
- [46] H.Adrian and F.B.Pickering, "Effect of Titanium Additions on Austenite Grain Growth Kinetics of Medium Carbon V-Nb Steels Containing 0.008-0.018%N," *Materials Science and Technology*, vol. 7, pp. 176-182, 1991.
- [47] T.Siwecki, J.Eliasson, R.Langneborg and B.Hutchinson, "Vanadium Microalloyed Bainitic Hot Strip Steels," *ISIJ International*, vol. 50, no. 5, p. 760–767, 2010.
- [48] M.Nurbanasari, P.Tsakiropoulos and E.J.Palmiere, "Influence of High Temperature Deformation and Double Tempering on the Microstructure of a H21 Tool Steel," *Materials Science & Engineering A*, vol. 570, p. 92–101, 2013.
- [49] F.Xiao, B.Liao, G.Qiao and Sh.Guan, "Effect of Hot Deformation on Phase Transformation Kinetics of 86CrMoV7 Steel," *Materials Characterization*, vol. 57, pp. 306-313, 2006.
- [50] S.C.Hong, S.H.Lim, H.S.Hong, K.J.Lee, D.H.Shin and K.S.Lee, "Effect of Nb on Grain Growth of Ferrite in C–Mn Steel During Isothermal Holding after Severe Deformation," *Materials Science and Technology*, vol. 20, pp. 207-212, 2004.
- [51] G.I.Rees, J.Perdrix, T.Maurickx and H.K.D.H.Bhadeshia, "The Effect of Niobium in Solid Solution on the Transformation Kinetics of Bainite," *Materials Science*

- and Engineering A*, vol. 194, pp. 179-186, 1995.
- [52] J.S.Hinton, E.J.Palmiere and W.M.Rainforth, "The Effect of High Temperature Grain Refinement on the Isothermal Ferrite Grain Growth Kinetics in Steel S460," *Materials Science Forum*, Vols. 715-716, pp. 907-912, 2012.
- [53] A.Iza-Mendia, M.A.Altuna, B.Pereda and I.Gutierrez, "Precipitation of Nb in Ferrite after Austenite Conditioning. Part I: Microstructural Characterization," *Metallurgical and Materials Transactions A*, vol. 43A, pp. 4553-4570, 2012.
- [54] K.I.Sugimoto, T.Muramatsu, S.I.Hashimoto and Y.Mukai, "Formability of Nb Bearing Ultra High-Strength TRIP-Aided Sheet Steels," *Journal of Materials Processing Technology*, vol. 177, pp. 390-395, 2006.
- [55] A.Zarei-Hanzaki, P.D.Hodgson and S.Yue, "Retained Austenite Characteristics in Thermomechanically Processed Si-Mn Transformation-Induced Plasticity Steels," *Metallurgical and Materials Transactions A*, vol. 28A, pp. 2405-2414, 1997.
- [56] M.Charleux, W.J.Poole, M.Militzer and A.Deschamps, "Precipitation Behavior and Its Effect on Strengthening of an HSLA-Nb/Ti Steel," *Metallurgical and Materials Transactions A*, vol. 32A, pp. 1635-1647, 2001.
- [57] M.Tanniru, S.Shanmugam, R.D.K.Misra, D.Panda and S.Jansto, "Microalloyed V-Nb-Ti and V Steels, Part 1 – Stereological Study of Ferrite-Pearlite Microstructure and Its Relationship to Toughness," *Materials Science and Technology*, vol. 21, no. 2, pp. 159-164, 2005.
- [58] X.D.Wang, B.X.Huang, L.Wang and Y.H.Rong, "Microstructure and Mechanical Properties of Microalloyed High-Strength Transformation-Induced Plasticity Steels," *Metallurgical and Materials Transactions A*, vol. 39A, pp. 1-7, 2008.
- [59] A.Kujanpaa; E.Anelli; P.E.Di-Nunzio; B.Wade, "Ferritic-Bainitic and TRIP Steels for Improved Combinations of Strength and Ductility," 2002.
- [60] P.J.Jacques, E.Girault, A.Mertens, B.Verlinden, J.V.Humbeeck and F.Delannay, "The Developments of Cold-rolled TRIP-assisted Multiphase Steels. Al-alloyed TRIP-assisted Multiphase Steels," *ISIJ international*, vol. 41, no. 9, pp. 1068-1074, 2001.
- [61] G.Frommeyer, U.BruX and P.Neumann, "Supra-Ductile and High-Strength Manganese-TRIP/TWIP Steels for High Energy Absorption Purposes," *ISIJ International*, vol. 42, no. 3, pp. 438-446, 2003.
- [62] C.M.Sellars, "The Physical Metallurgy of Hot Working," in *International conference on hot working and forming processes*, Sheffield, 1979.
- [63] K.I.Sugimoto, M.Murata and S.M.Song, "Formability of Al-Nb Bearing Ultra High-strength TRIP-aided Sheet Steels with Bainitic Ferrite and/or Martensite Matrix," *ISIJ International*, vol. 50, no. 1, pp. 162-168, 2010.

- [64] Y.Li and M.David, "Vanadium in Bainitic Steels: A Review of Recent Developments," in *Advanced Steels-The Recent Scenario in Steel Science and Technology*, H. D. Y. G. Yuqing Weng, Ed., 2011, pp. 303-308.
- [65] A.J.Brown and E.L.DeArdo, "Aluminum Nitride Precipitation in C-Mn-Si and Microalloyed Steels," in *Thermomechanical procesing of microalloyed austenite*, AIME, 1982.
- [66] E.Jimenez-Melero, N. Dijk, L.Zhao, J.Sietsma, S.E.Offerman, J.P.Wright and S.van-der-Zwaag, "The Effect of Aluminium and Phosphorus on the Stability of Individual Austenite Grains in TRIP Steels," *Acta Materialia*, vol. 57, pp. 533-543, 2009.
- [67] H.K.D.H.Bhadeshia and R.Honeycombe, *Steels Microstructure and Properties*, Third ed., Elsevier Ltd., 2003, pp. 25-258.
- [68] N.Cabanas, N.Akdut, J.Penning and B.C.De.Cooman, "High-Temperature Deformation Properties of Austenitic Fe-Mn Alloys," *Metallurgical and Materials Transactions A*, vol. 37A, pp. 3305-3315, 2006.
- [69] E.Gartstein and A.Rabinkin, "On the F.C.C- H.C.P Phase Transformation of High-Manganese-Iron Alloys," *Acta metallurgica*, vol. 27, pp. 1053-1064, 1979.
- [70] J.Cao, Q.Yong, Q.Liu and X.Sun, "Precipitation of MC Phase and Precipitation Strengthening in Hot Rolled Nb-Mo and Nb-Ti Steels," *Journal of Materials Science*, vol. 42, p. 10080-10084, 2007.
- [71] S.Jiao, F.Hassani, R.L.Donaberger, E.Essadiqi and S.Yue, "The Effect of Processing History on a Cold Rolled and Annealed Mo-Nb Microalloyed TRIP Steel," *ISIJ International*, vol. 42, no. 3, pp. 299-303, 2002.
- [72] W.B.Lee, S.G.Hong, C.G.Park and S.H.Park, "Carbide Precipitation and High-Temperature Strength of Hot-rolled High-Strength, Low-Alloy Steels Containing Nb and Mo," *Metallurgical and Materials Transactions A*, vol. 33A, pp. 1689-1698, 2002.
- [73] W.B.Lee, S.G.Hong, C.G.Park, K.H.Kim and S.H.Park, "Influence Of Mo On Precipitation Hardening In Hot Rolled HSLA Steels Containing Nb," *Scripta mater.*, vol. 43, pp. 319-324, 2000.
- [74] X.Sun and Q.Yong, "The Roles and Applications of Molybdenum Element in Low Alloy Steels," in *International Seminar on Applications of Mo in Steels*, Beijing, 2010.
- [75] J.H.Jang, Y.U.Heo, C.H.Lee, H.K.D.H.Bhadeshia and D.W.Suh, "Interphase Precipitation in Ti-Nb and Ti-Nb-Mo Bearing Steel," *Materials Science and Technology*, vol. 29, no. 3, pp. 309-313, 2013.
- [76] H.Mohrbacher, X.Sun, Q.Yong and H.Dong, "MoNb-Based Alloying Concepts for Low-Carbon Bainitic Steels," in *Advanced Steels-The Recent Scenario in Steel*

- Science and Technology*, H. Y. Y.Weng, Ed., Springer, 2011, pp. 289-301.
- [77] J.S.Hinton, "Laboratory Simulation of Microstructural Evolution in AISI 430 Ferritic Stainless Steel during the Steckel Mill Process," Sheffield, 2006.
- [78] E.Valdes and C.M.Sellars, "Influence of Roughing Rolling Passes on Kinetics of Strain Induced Precipitation of Nb(C,N)," *Materials Science and Technology*, vol. 7, pp. 622-630, 1991.
- [79] M.J.White and W.S.Owen, "Effects of Vanadium and Nitrogen on Recovery and Recrystallization during and After Hot-Working some HSLA Steels," *Metallurgical Transactions A*, vol. 11A, pp. 597-604, 1980.
- [80] L.J.Cuddy, "Grain refinement of Nb Steels by Control of Recrystallization During Hot Rolling," *Metallurgical Transactions A*, vol. 15A, pp. 87-98, 1984.
- [81] R.M.Pothes, R.L.Higginson and E.J.Palmiere, "Complex Precipitation Behaviour in a Microalloyed Plate Steel," *Scripta mater.*, vol. 44, pp. 147-151, 2001.
- [82] R.Wang, C.I.Garcia, M.Hua, K.Cho, H.Zhang and A.J.Deardo, "Microstructure and Precipitation Behavior of Nb, Ti Complex Microalloyed Steel Produced by Compact Strip Processing," *ISIJ International*, vol. 46, no. 9, pp. 1345-1353, 2006.
- [83] T.Furuhara, J.Yamaguchi, N.Sugita, G.Miyamoto and T.Maki, "Nucleation of Proeutectoid Ferrite on Complex Precipitates in Austenite," *ISIJ International*, vol. 43, no. 10, pp. 1630-1639, 2003.
- [84] S.Q.Yuan and G.L.Liang, "Dissolving Behaviour of Second Phase Particles in Nb-Ti Microalloyed Steel," *Materials Letters*, vol. 63, pp. 2324-2326, 2009.
- [85] J.S.Park and Y.K.Lee, "Determination of Nb(C,N) Dissolution Temperature by Electrical Resistivity Measurement in a Low-carbon Microalloyed Steel," *Scripta Materialia*, vol. 56, p. 225-228, 2007.
- [86] J.G.Jung, J.S.Park, J.Kim and Y.K.Lee, "Carbide Precipitation Kinetics in Austenite of a Nb-Ti-V Microalloyed Steel," *Materials Science and Engineering A*, vol. 528, p. 5529-5535, 2011.
- [87] M.J.Crooks, A.J.Garratt-Reed, J.B.Vander-Sande and W.S.Owen, "Precipitation and Recrystallization in Some Vanadium and Vanadium-Niobium Microalloyed Steels," *Metallurgical Transactions A*, vol. 12A, pp. 1999-2013, 1981.
- [88] E.J.Palmiere, C.I.Garcia and A.J.DeArdo, "The Influence of Niobium Supersaturation in Austenite on the Static Recrystallization Behavior of Microalloyed Steels," *Metallurgical and Materials Transactions A*, vol. 27A, pp. 951-960, 1996.
- [89] T.Katajarinne, M.Somani, P.Karjalainen and D.Porter, "Evolution of Non-uniform Grain Structure during Hot Deformation of a Nb-Ti Microalloyed Steel,"

- Revista De Metalurgia*, vol. 40, pp. 329-334, 2004.
- [90] N.Z.Gutierrez, M.I.Luppo and C.A.Danon, "Heterogeneous Austenite Grain Growth in ASTM A213–T91 Steel," *ISIJ International*, vol. 47, no. 8, p. 178–1187, 2007.
- [91] C.M.Enloe, K.O.Findley, C.M.Parish, M.K.Miller, B.C.De-Cooman and J.G.Speer, "Compositional Evolution of Microalloy Carbonitrides in a Mo-Bearing Microalloyed Steel," *Scripta Materialia*, vol. 68, pp. 55-58, 2013.
- [92] S.Vervynckt, K.Verbeke, P.Thibaux and Y.Houbaert, "Recrystallization–Precipitation Interaction during Austenite Hot Deformation of a Nb Microalloyed Steel," *Materials Science and Engineering A*, vol. 528, p. 5519–5528, 2011.
- [93] S.H.M.Anijdan and S.Yue, "The Effect of Cooling Rate, and Cool Deformation Through Strain-Induced Transformation, on Microstructural Evolution and Mechanical Properties of Microalloyed Steels," *Metallurgical and Materials Transactions A*, vol. 43A, pp. 1140-1162, 2012.
- [94] Y.C.Liu, F.Sommer and E.J.Mittemeijer, "Abnormal Austenite–Ferrite Transformation Behaviour in Substitutional Fe-Based Alloys," *Acta Materialia*, vol. 51, pp. 507-519, 2003.
- [95] T.Furuhashi, T.Yamaguchi, G.Miyamoto and T.Maki, "Incomplete Transformation of Upper Bainite in Nb Bearing Low Carbon Steels," *Materials Science and Technology*, vol. 26, no. 4, pp. 392-397, 2010.
- [96] A.Zarei-Hanzak and S.Yue, "Ferrite Formation Characteristics in Si-Mn TRIP Steels," *ISIJ International*, vol. 37, no. 6, pp. 583-589, 1997.
- [97] H.J.Kestenbach, "Dispersion Hardening by Niobium Carbonitride Precipitation in Ferrite," *Materials Science and Technology*, vol. 13, pp. 731-739, 1997.
- [98] H.W.Yen, P.Y.Chen, C.Y.Huang and J.R.Yang, "Interphase Precipitation of Nanometer-Sized Carbides in a Titanium–Molybdenum-Bearing Low-Carbon Steel," *Acta Materialia*, vol. 59, p. 6264–6274, 2011.
- [99] H.K.D.H.Bhadeshia, "A Personal Commentary on ‘Transformation of Austenite at Constant Subcritical Temperatures’," *Metallurgical and Materials Transactions A*, vol. 41A, pp. 1351-1390, 2010.
- [100] Y.Ohmori, H.Ohtani and T.Kunitake, "The Bainite in Low Carbon Alloy High Strength Steels," *Transactions ISIJ*, vol. 11, pp. 250-259, 1971.
- [101] B.L.Bramfitt and J.G.Speer, "A Perspective on the Morphology of Bainite," *Metallurgical Transactions A*, vol. 21A, pp. 817-829, 1990.
- [102] L.C.D.Fielding, "The Bainite Controversy," *Materials Science and Technology*, vol. 29, no. 4, pp. 383-399, 2013.



- [103] H.K.D.H.Bhadeshia, "Some Phase Transformations in Steels," *Materials Science and Technology*, vol. 15, pp. 22-29, 1999.
- [104] H.J.Jun, S.H.Park, S.D.Choi and C.G.Park, "Decomposition of Retained Austenite during Coiling Process of Hot Rolled TRIP-Aided Steels," *Materials Science and Engineering A*, vol. 379, pp. 204-209, 2004.
- [105] Y.Tomita, "Effect of Bainitic Transformation on Microstructure of Si-Mn Steel," *Journal of Materials Science*, vol. 29, pp. 2605-2610, 1994.
- [106] A.Zarei-Hanzaki, P.D.Hodgson and S.Yue, "The Influence of Bainite on Retained Austenite Characteristics in Si-Mn TRIP Steels," *ISIJ International*, vol. 35, no. 1, pp. 79-85, 1995.
- [107] Z.Lawrynowicz, "Carbon Partitioning during Bainite Transformation in Low Alloy Steels," *Materials Science and Technology*, vol. 18, pp. 1322-1324, 2002.
- [108] D.Quidort and Y.Brechet, "The Role of Carbon on the Kinetics of Bainite Transformation in Steels," *Scripta Materialia*, vol. 47, pp. 151-156, 2002.
- [109] I.Zuazo and S.Cobo, "Low Temperature Precipitation in Nb-Added Si- and Si Free Bainitic Steels," *Materials Science Forum*, Vols. 706-709, pp. 2384-2389, 2012.
- [110] S.Hashimoto, S.Ikeda, K.I.Sugimoto and S.Miyake, "Effects of Nb and Mo Addition to 0.2%C–1.5%Si–1.5%Mn Steel on Mechanical Properties of Hot Rolled TRIP-aided Steel Sheets," *ISIJ International*, vol. 44, no. 9, pp. 1590-1598, 2004.
- [111] S.Matsuda and Y.Okamura, "The Later Stage of Reverse Transformation in Low-Carbon Low Alloy Steel," *Transactions ISIJ*, vol. 14, pp. 444-449, 1974.
- [112] R.R.Mohanty, O.A.Girina and N.M.Fonstein, "Effect of Heating Rate on the Austenite Formation in Low-Carbon High-Strength Steels Annealed in the Intercritical Region," *Metallurgical and Materials Transactions A*, vol. 42A, pp. 3680-3690, 2011.
- [113] G.A.Roberts and R.F.Mehl, "The Mechanism and The Rate of Formation of Austenite from Ferrite-Cementite Aggregates," *Transactions of the ASM*, vol. 31, pp. 613-650, 1943.
- [114] R.Homma, "Studies on Austenite Grain of 3.5%Ni-Cr-Mo-V Steel," *Transactions ISIJ*, vol. 14, pp. 434-443, 1974.
- [115] G.R.Speich, V.A.Demarest and R.L.Miller, "Formation of Austenite during Intercritical Annealing of Dual-Phase Steels," *Metallurgical Transactions A*, vol. 12A, pp. 1419-1428, 1981.
- [116] H.Azizi-Alizamini, M.Militzer and W.J.Poole, "Austenite Formation in Plain Low-Carbon Steels," *Metallurgical and Materials Transactions A*, vol. 42A, p.

1544, 2011.

- [117] [Online]. Available: <http://www.immpetus.group.shef.ac.uk>.
- [118] A.J.Lacey, M.S.Loveday, G.J.Mahon, B.Roebeck, C.M.Sellars and M.R.VanDerWinden, "Measuring Flow Stress in Hot Plane Strain Compression Tests," 2002.
- [119] J.Z.Silva, "Microstructural Evolution of a Multiphase Steel Microalloyed with Vanadium," 2009.
- [120] S.H.Magner, R. Angelis, W.N.Weins and J.D.Makinson, "A Historical Review of Retained Austenite and Its Measurement by X-ray Diffraction," *Advances in X-ray Analysis*, vol. 45, pp. 92-97, 2002.
- [121] [Online]. Available: [http://www.dur.ac.uk/john.evans/topas\\_academic/topas\\_main.htm](http://www.dur.ac.uk/john.evans/topas_academic/topas_main.htm).
- [122] [Online]. Available: <http://icsd.cds.rsc.org/>.
- [123] *Standard Practice for X-Ray Determination of Retained Austenite in Steel with Near Random Crystallographic Orientation*, 2003.
- [124] B.B.He, Two-Dimensional X-ray Diffraction, John Wiley & Sons, 2009.
- [125] B.L.Bramfitt and A.O.Benscoter, Metallographer's Guide, Practices and Procedures for Irons and Steels, ASM International, 2002.
- [126] [Online]. Available: <http://www.crystalmaker.com/>.
- [127] D.B.Williams and C.B.Carter, Transmission Electron Microscopy A Textbook for Materials Science, Second ed., Springer Science+ Business, 2009.
- [128] W.E.Stumpf and C.M.Sellars, "Measurement of Particle Density and Volume Fraction from Extraction Replicas," *Metallography*, vol. 1, pp. 25-34, 1968.
- [129] M.D.Meyer, D.Vanderschueren, K.D.Blauwe and B.C.De-Cooman, "The Characterization of Retained Austenite in TRIP Steels by X-ray Diffraction," in *Mechanical Working and Steel Processing Conference*, 1999.
- [130] Ch.Liu, Zh.Zhao and S.D.Bhole, "Lathlike Upper Bainite in a Silicon Steel," *Materials Science and Engineering A*, vol. 434, pp. 289-293, 2006.
- [131] J.Ch.Hell, M.Dehtmas, G.Geandier, N.Gey, S.Allain, A.Hazotte and J.P.Chateau, "Influence of the Austempering Temperature on the Microstructure and Crystallography of a Carbide-Free Bainitic Steel," *Solid State Phenomena*, Vols. 172-174, pp. 797-802, 2011.
- [132] D.J.Dyson and B.Holmes, "Effect of Alloying Additions on The Lattice Parameter of Austenite," *Journal of The Iron and Steel Institute*, vol. 208, pp. 469-474, 1970.

- [133] H.W.King, "Quantitative Size-Factors for Metallic Solid Solutions," *Journal of Materials Science*, vol. 1, pp. 79-90, 1966.
- [134] S.S.Babu, J.W.Elmer, S.A.David and M.A.Quintana, "In Situ Observations of Non-equilibrium Austenite Formation during Weld Solidification of an Fe–C–Al–Mn Low-Alloy Steel," *Proceedings of the Royal Society of London. Series A: Mathematical, Physical and Engineering Sciences*, vol. 458, pp. 811-821, 2002.
- [135] S.S.Babu, E.D.Specht, S.A.David, E.Karapetrova, P.Zschack, M.Peet and H.K.D.H.Bhadeshia, "In-Situ Observations of Lattice Parameter Fluctuations in Austenite and Transformation to Bainite," *Metallurgical and Materials Transactions A*, vol. 36A, pp. 3281-3289, 2005.
- [136] F.G.Caballero, H.W.Yen, M.K.Miller, J.R.Yang, J.Cornide and C.Garcia-Mateo, "Complementary Use of Transmission Electron Microscopy and Atom Probe Tomography for the Examination of Plastic Accommodation in Nanocrystalline Bainitic Steels," *Acta Materialia*, vol. 59, p. 6117–6123, 2011.
- [137] F.G.Caballero, M.K.Miller, S.S.Babu and C.Garcia-Mateo, "Atomic Scale Observations of Bainite Transformation in a High Carbon High Silicon Steel," *Acta Materialia*, vol. 55, p. 381–390, 2007.
- [138] I.B.Timokhina, P.D.Hodgson and E.V.Pereloma, "Transmission Electron Microscopy Characterization of the Bake-Hardening Behavior of Transformation-Induced Plasticity and Dual-Phase Steels," *Metallurgical and Materials Transactions A*, vol. 38A, pp. 2442-2454, 2007.
- [139] I.B.Timokhina, M.Enomoto, M.K.Miller and E.V.Pereloma, "Microstructure-Property Relationship in the Thermomechanically Processed C-Mn-Si-Nb-Al-(Mo) Transformation-Induced Plasticity Steels Before and After Prestraining and Bake Hardening Treatment," *Metallurgical and Materials Transactions A*, vol. 43A, pp. 2473-2483, 2012.
- [140] K.Hausmann, D.Krizan, K.Spiradek-Hahn, A.Pichler and E.Werner, "The Influence of Nb on Transformation Behavior and Mechanical Properties of TRIP-Assisted Bainitic–Ferritic Sheet Steels," *Materials Science & Engineering A*, vol. 588, p. 142–150, 2013.
- [141] I.B.Timokhina, P.D.Hodgson and E.V.Pereloma, "Effect of Deformation Schedule on the Microstructure and Mechanical Properties of a Thermomechanically Processed C-Mn-Si Transformation-Induced Plasticity Steel," *Metallurgical and Materials Transactions A*, vol. 34A, pp. 1599-1609, 2003.
- [142] S.Zaefferer, J.Ohlert and W.Bleck, "A Study of Microstructure, Transformation Mechanisms and Correlation between Microstructure and Mechanical Properties of a Low Alloyed TRIP Steel," *Acta Materialia*, vol. 52, p. 2765–2778, 2004.
- [143] Ch.Feng, H.Sh.Fang, B.Zh.Bai and Y.K.Zheng, "Microstructure and Mechanical Properties of FGBA/BG Air Cooling Bainitic Steels Containing Niobium,"

- International Journal of Minerals, Metallurgy and Materials*, vol. 17, no. 4, pp. 429-434, 2010.
- [144] F.Chun, F.H.Sheng, Zh.Yan-kang and B.Bing-zhe, "Mn-Series Low-Carbon Air-Cooled Bainitic Steel Containing Niobium of 0.02%," *Journal of Iron and Steel Research, International*, vol. 17, no. 4, pp. 53-58, 2010.
- [145] R.A.Farrar, Z.Zhang, S.R.Bannister and G.S.Barritte, "The Effect of Prior Austenite Grain Size on the Transformation Behaviour of C-Mn-Ni Weld Metal," *Journal of Materials Science*, vol. 28, pp. 1385-1390, 1993.
- [146] R.A.Farrar and P.L.Harrison, "Review Acicular Ferrite in Carbon-manganese Weld Metals: An Overview," *Journal of Materials Science*, vol. 22, pp. 3812-3820, 1987.
- [147] K.He and D.V.Edmonds, "Formation of Acicular Ferrite and Influence of Vanadium Alloying," *Materials Science and Technology*, vol. 18, pp. 289-296, 2002.
- [148] K.I.Sugimoto, J.Sakaguchi, T.Iida and T.Kashima, "Stretch-Flangeability of a High-strength TRIP Type Bainitic Sheet Steel," *ISIJ International*, vol. 40, no. 9, pp. 920-926, 2000.
- [149] E.Emadoddin, "Effect of Cold Rolling on Annealing Behavior and Retained Austenite Characteristics of Multiphase CMnSi Steel," *ISIJ International*, vol. 53, p. 330-336, 2013.
- [150] M.Hamzeh, A.Kermanpur and A.Najafizadeh, "Fabrication of the Ultrafine-Grained Ferrite with Good Resistance to Grain Growth and Evaluation of Its Tensile Properties," *Materials Science & Engineering A*, vol. 593, pp. 24-30, 2014.
- [151] S. Nedjada, Y. Moghaddam, A. Vazirabadia, H.Shirazib and M. Ahmadabadi, "Grain Refinement by Cold Deformation and Recrystallization of Bainite and Acicular Ferrite Structures of C-Mn Steels," *Materials Science and Engineering A*, vol. 528, p. 1521-1526, 2011.
- [152] R.Abbaschian, L.Abbaschian and R. Hill, *Physical Metallurgy Principles*, Fourth Edition ed., Cengage Learning, 2009.
- [153] F.J.Humphreys and M.Hatherly, *Recrystallization and Related Annealing Phenomena*, Second, Ed., Elsevier, 2004.
- [154] R.Ueji, N.Tsuji, Y.Minamino and Y.Koizumi, "Ultragrain Refinement of Plain Low Carbon Steel by Cold-Rolling and Annealing of Martensite," *Acta Materialia*, vol. 50, p. 4177-4189, 2002.
- [155] J.Kobayashi, D.Ina, N.Yoshikawa and K.I.Sugimoto, "Effects of the Addition of Cr, Mo and Ni on the Microstructure and Retained Austenite Characteristics of 0.2% C-Si-Mn-Nb Ultrahigh-strength TRIP-aided Bainitic Ferrite Steels," *ISIJ*

- International*, vol. 52, no. 10, p. 1894–1901, 2012.
- [156] T.N.Baker, “Review-Processes, Microstructure and Properties of Vanadium Microalloyed Steels,” *Materials Science and Technology*, vol. 25, no. 9, pp. 1083–1107, 2009.
- [157] N.K.Balliger and R.W.K.Honeycombe, “The Effect of Nitrogen on Precipitation and Transformation Kinetics in Vanadium Steels,” *Metallurgical Transactions A*, vol. 11A, no. 421–429, 1980.
- [158] D.A.Porter, K.E.Easterling and M.Y.Sherif, *Phase Transformations in Metals and Alloys*, Third ed., CRC press, 2009.
- [159] R.D.K.Misra, H.Zheng, K.M.Wu and L.P.Karjalainen, “Niobium-Containing Quenching and Partitioning Processed Ultrahigh Strength Martensite–Austenite Dual Phase Steels,” *Materials Science & Engineering A*, vol. 579, p. 188–193, 2013.
- [160] L.A.J.Garvie, A.J.Craven and R.Brydson, "Use of Electron-Energy Loss Near-Edge Fine Structure in the Study of Minerals," *American Mineralogist*, vol. 79, pp. 411–425, 1994.
- [161] K.Miyata, T.Omura, T.Kushida and Y.Komizo, “Coarsening Kinetics of Multicomponent MC-Type Carbides in High-Strength Low-Alloy Steels,” *Metallurgical and Materials Transactions A*, vol. 34A, pp. 1565–1573, 2003.
- [162] R.D.K.Misra, H.Nathani, J.E.Hartmann and F.Siciliano, “Microstructural Evolution in a New 770MPa Hot Rolled Nb–Ti Microalloyed Steel,” *Materials Science and Engineering A*, vol. 394, pp. 339–352, 2005.
- [163] S.Shanmugam, M.Tanniru, R.D.K.Misra, D.Panda and S.Jansto, “Precipitation in V Bearing Microalloyed Steel Containing Low Concentrations of Ti and Nb,” *Materials Science and Technology*, vol. 21, no. 8, pp. 883–892, 2005.
- [164] W.Bleck and F.Gerdemann, "Improved Mechanical Properties by Control of Bainite Transformation," *Materials and Manufacturing Processes*, vol. 26, pp. 43–50, 2011.
- [165] J.Kobayashi, D.Ina, A.Futamura and K.I.Sugimoto, "Fracture Toughness of an Advanced Ultrahigh-strength TRIP-aided Steel," *ISIJ International*, vol. 54, no. 4, p. 955–962, 2014.
- [166] E.Keehan, L.Karlsson, H.O.Andren and H.K.D.H.Bhadeshia, "New Developments with C-Mn-Ni High-Strength Steel Weld Metals, Part A — Microstructure," *Welding Research*, vol. 85, no. 9, pp. 200–210, 2006.
- [167] E.Kozeschnik and H.K.D.H.Bhadeshia, "Influence of Silicon on Cementite Precipitation in Steels," *Materials Science and Technology*, vol. 24, no. 3, pp. 343–347, 2008.

- [168] A.Zarei-Hanzaki, P.D.Hodgson and S.Yue, "Hot Detormation Characteristics ot Si-Mn TRIP Steels with and without Nb Microalloy Additions," *ISIJ International*, vol. 35, no. 3, pp. 324-331, 1995.
- [169] J.S.Park and Y.K.Lee, "Nb(C,N) Precipitation Kinetics in the Bainite Region of a Low-Carbon Nb-Microalloyed Steel," *Scripta Materialia*, vol. 57, pp. 109-112, 2007.
- [170] J.Kim, J.G.Jung, D.H.Kim and Y.K.Lee, "The Kinetics of Nb(C,N) Precipitation during the Isothermal Austenite to Ferrite Transformation in a Low-carbon Nb-microalloyed Steel," *Acta Materialia*, vol. 61, p. 7437–7443, 2013.
- [171] J.J.Jonas, "Dynamic Recrystallization-Scientific Curiosity or Industrial Tool?," *Materials Science and Engineering, A*, vol. 184, pp. 155-165, 1994.
- [172] G.Fitzsimons, K.Titto, R.Fix and A.J.DeArdo, "Precipitation of Nb(CN) during High Strain Rate Compression Testing of a 0.07 Pct Nb-Bearing Austenite," *Metallurgical Transactions A*, vol. 15A, pp. 241-243, 1984.
- [173] C.M.Sellars, "From Trial and Error to Computer Modelling of Thermomechanical Processing," *Ironmaking and Steelmaking*, vol. 38, no. 4, pp. 250-257, 2011 .
- [174] Q.Furnemont, M.Kempf, P.J.Jacques, M.Goken and F.Delannay, "On the Measurement of the Nanohardness of the Constitutive Phases of TRIP-Assisted Multiphase Steels," *Materials Science and Engineering A*, vol. 328, pp. 26-32, 2002.

## Appendix A. Analysis and Corrections of PSC Data

The outputs of PSC testing were the load, displacement and temperature. These were recorded by specific PC-based software which is designed for the TMC machine at the University of Sheffield. The stress-strain curves were plotted after corrections based on the Measurement Good Practice Guide No. 27 [118]. To analyze and correct the raw data the following parameters were taken into consideration:

- 1- Origin correction
- 2- Machine compliance
- 3- Breadth spread correction
- 4- Friction correction
- 5- Equivalent stress-strain
- 5- Thermal condition

In this Appendix the method of analysis and correction are explained briefly, however, further details can be found in [118].

Table A.1, Nomenclature [118].

Symbol	Designation	Unit
$C_b$	Breadth spread coefficient	-
$b_f$	Final average breadth of test piece	mm
$b_0$	Initial breadth of test piece	mm
$h_f$	Final average thickness of test piece	mm
$h_0$	Initial thickness of test piece	mm
$S$	Instantaneous stress	$N/mm^2$
$w$	Platen width	mm
$\alpha_t$	Thermal coefficient of expansion, i.e.0.000012	$^{\circ}C^{-1}$
$\mu$	Coefficient of friction	-
$Z_0$	A position where frictional condition change from sticking to sliding	-
$b$	Instantaneous breadth	mm
$R$	The Universal gas constant	$J/(mol.K)$
$\epsilon$	True strain	-
$k$	Shear flow stress	$N/mm^2$



**Origin correction** corresponds to the zero position of the specimen regarding the thermal conditions at higher temperatures, which result in the expansion of the specimen. The correction is based on shifting the curve along the X-axis to the origin point (0,0). Therefore, the tool displacement will be equal to the specimen displacement (Fig. A.1).

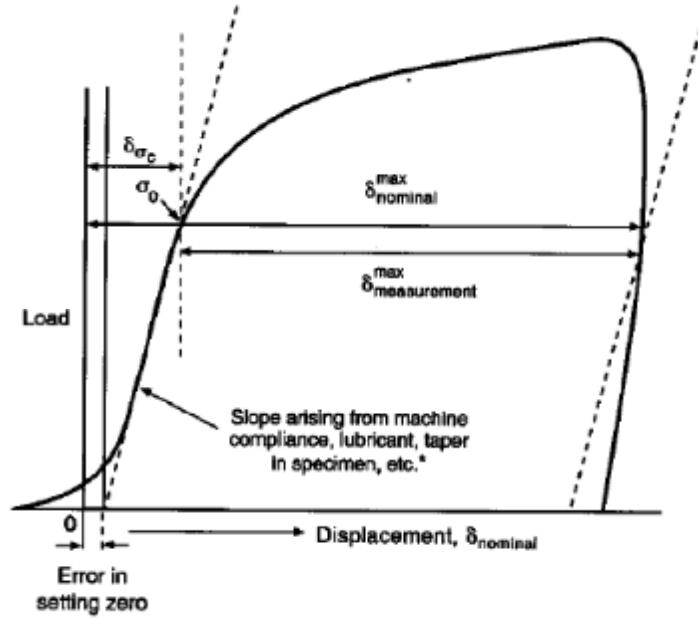


Fig. A.1, Schematic diagram of load-displacement illustrating origin correction [118].

**Machine compliance** is concerned with the effect of machine elastic deformation on the slope of the load-displacement curves. A slight drift in the slope of curves due to this effect was corrected from the reported results about the stiffness of the TMC machine in literature i.e. 410kN/mm (Fig. A.1) [118].

**Breath spread** corresponds to the effect of lateral deformation of the specimen under load which changes the contact area between the tools and specimen. The breadth spread coefficient was calculated instantaneously by the empirical formula suggested in [118]. Subsequently, using the instantaneous breadth spreading of the deformation zone the stress was calculated. The relationship between the instantaneous stress and breadth spreading coefficient is given as below.

$$C_b = \frac{(b_f / b_0) - 1}{1 - (h_f / h_0)^{0.5}} \quad (\text{A.1})$$

$$b = b_0(1 + C_b - C_b(h_f / h_0)^{0.5}) \quad (\text{A.2})$$

where

$h = h_0$  - the final corrected tool displacement

In this way, the effect of temperature on the breadth spread and height was measured from the instantaneous temperature recorded using the embedded thermocouple in the specimen. The equations below show the relationship between the temperature ( $T$  °K) and breadth spread:

$$h_h = h_f + a_t h_f (T - T_0) \quad (\text{A.3})$$

$$b_h = b_f + a_t b_f (T - T_0) \quad (\text{A.4})$$

From these equations the instantaneous contact area can be calculated to measure the stress according to the following equation:

$$\text{Stress} = \frac{\text{Load}}{wh} \quad (\text{A.5})$$

**Friction correction** was also carried out by measuring  $Z_0$  from the equation below:

$$Z_0 = \left[ \frac{h}{2m} \right] \text{Ln} \left[ \frac{1}{2m} \right] \quad (\text{A.6})$$

The thermomechanical practices in this work involve three different deformation temperatures which could be effective on the frictional condition. As Sellars et al. suggested, the value of 0.3 was considered as the coefficient of friction between specimen and tools in TMC machine [118]. In order to measure the shear stress, it was important to predict the frictional condition between the specimen and tools either as sliding friction or partial sticking friction or sticking friction. Thus;

Condition 1: If  $2Z_0 > w$ , the frictional condition will be as a sliding friction:

$$\frac{\text{Stress}}{2k} = \frac{1}{bw} \left[ \frac{2h^2}{m^2} + \frac{(b-w)h}{m} \right] \left[ \exp\left(\frac{mw}{h}\right) - 1 \right] - \frac{2h}{mb} \quad (\text{A.7})$$

Condition 2: If  $w > 2Z_0 > 0$ , the frictional condition will be as partial sticking:

$$\begin{aligned} \frac{Stress}{2k} = & \frac{h}{mv} \left[ \frac{1}{2m} - 1 \right] + \frac{(w/2) - z_0}{mv} + \frac{[(w/2) - z_0]^2}{hw} \\ & + \frac{1}{mb} \left( \frac{2z_0^2}{w} - z_0 - \frac{2hz_0}{mv} + \frac{h}{2m} - h + \frac{h^2}{wm^2} - \frac{2h^2}{mv} \right) + \frac{1}{hb} \left( z_0^2 - \frac{4z_0^3}{3w} - \frac{w^2}{12} \right) \end{aligned} \quad (A.8)$$

Condition 3: If  $0 > 2Z_0$ , the frictional condition will be as sticking friction:

$$\frac{Stress}{2k} = 1 + \frac{w}{4h} - \frac{w^2}{12hb} \quad (A.9)$$

Moreover, the equivalent stress was calculated by the following equation:

$$\text{Equivalent stress} = 2k / f' \quad (A.10)$$

where  $f'$  stands for the correction factor which is  $f' = \bar{\epsilon} / \epsilon_3$  and  $k$  represents the shear stress. The equivalent strain can be calculated from the lateral spread using the equation below:

$$\bar{\epsilon} = 2\sqrt{(e_2^2 + e_2e_3 + e_3^2)/3} \quad (A.11)$$

and

$$\epsilon_2 = \ln(b/b_0) \quad (A.12)$$

and

$$\epsilon_3 = \ln(h/h_0) \quad (A.13)$$

The equivalent true stress-strain flow curves are corrected for deformation temperature. The influence of thermal condition on the calculations is determined at isothermal temperature for each deformation stage using the following equation:

$$\text{Stress}_{\text{iso}} = \text{stress} + \frac{340(\text{kJmol}^{-1})}{0.045\epsilon^{-0.126}R} \left( \frac{1}{T_{\text{iso}}} - \frac{1}{T_{\text{ins tan tan eous}}} \right) \quad (A.14)$$